# Control of Whirling Vibrations in BTA Deep Hole Boring Process using Fuzzy Logic Modeling and Active Suppression Technique

Hussien Al-Wedyan

A Thesis

in

The Department

of

Mechanical & Industrial Engineering

Presented in Partial Fulfillment of the Requirements for the Degree of

Doctor of Philosophy

at

Concordia University
Montreal, Quebec, Canada
April 2004

*Your file Votre référence*
*ISBN: 0-612-90373-7*
*Our file Notre référence*
*ISBN: 0-612-90373-7*

CONCORDIA UNIVERSITY
SCHOOL OF GRADUATE STUDIES

This is to certify that the thesis prepared

By: **Hussien Al-Wedyan**

Entitled: **Control of Whirring Vibrations in BTA Deep Hole Boring Process using Fuzzy Logic Modeling and Active Suppression Technique**

and submitted in partial fulfillment of the requirements for the degree of

DOCTOR OF PHILOSOPHY (Mechanical Engineering)

complies with the regulations of the University and meets the accepted standards with respect to originality and quality.

Signed by the final examining committee:

Dr. E. Doedel _____ Chair

Dr. H. Attia _____ External Examiner

Dr. F. Haghighat _____ External to Program

Dr. H. Hong _____ Examiner

Dr. R. Sedaghati _____ Examiner

Dr. R. Bhat _____ Thesis Co-Supervisor

Dr. K. Demirli _____ Thesis Co-Supervisor

Approved by _____
Dr. K. Demirli, Graduate Program Director

APR 26 2004
_____ 2004

_____
Dr. N. Esmail
Dean of Engineering & Computer Science

# ABSTRACT

## CONTROL OF WHIRLING VIBRATIONS IN BTA DEEP HOLE BORING PROCESS USING FUZZY LOGIC MODELING AND ACTIVE SUPPRESSION TECHNIQUE

Hussien M. Al Wedyan, Ph.D.

Concordia University

Need for increased productivity has motivated interest in drilling equipment for high speed and high precision drilling. However, long drills exhibit aggressive and self-excited vibrations known as whirling motions. These vibrations deteriorate the outcome drilled surface qualities, i.e., finish, geometrical dimensioning and tolerances. Deep hole boring is the most complex and expensive drilling operation in terms of expertise needed, operating conditions and size.

The present research is to study the whirling vibrations of the boring bar workpiece system in the BTA deep hole boring process. After a review of the literature, a set of objectives is outlined for the thesis. The objectives are to formulate an analytical model, which will include the self-excited motion caused by the internal cutting forces in the Z and Y directions and the active suppression forces used to counteract the cutting forces. This model will be used to carry out simulation studies on the whirling vibrations of the

boring bar-workpiece system and to carry out some experiments in order to validate the analytical model.

In view of the large number of machining parameters that influence the system dynamics and the resulting surface finish, geometrical dimensioning and tolerancing on the workpiece, a fuzzy logic model is proposed for off line modeling. Such a model will be used to examine the results obtained in the experiments and to predict the best parametric combinations that will provide the required surface finish. This will constitute an open loop control of the vibrations.

An active vibration suppression is carried out to reduce the whirling motion of the boring bar-workpiece system, which in turn will improve the surface finish. Two electrodynamic shakers are used in Z-Y plane to overcome the displacement of the boring bar while drilling.

The experimental investigations are carried out in the deep hole boring laboratory. Instrumentation involving proximity pickups, oscillator, amplifiers and demodulator are used to measure the displacement response and the orbital motion of the boring bar-workpiece system, and two electrodynamic shakers to suppress the motion. The surface roughness, straightness and circularity are measured which are related to the whirling vibrations and the machining parameters.

I dedicate this thesis to my beloved parents …

# ACKNOWLEDGEMENTS

Many different people have made this thesis possible, none more so than my supervisors, Dr. Rama Bhat and Dr. Kudret Demirli. I am deeply grateful for all their support and encouragement during the course of the work. I would like to thank the administrative and technical support staff in the mechanical and industrial engineering department, John Elliott, Brian Cooper, Gilles Huard, Juan Alfarai, and Danny Juras.

Thanks go to Dr. Serafettin Engin for his help in giving me the opportunity to do the surface irregularity measurements at Pratt and Whitney Company.

I am indebted to my cousin and my flatmate who are my best friends, Khalid Alwidyan and Alaa Al Hawari; their friendship has been treasured and shall not be forgotten.

The financial support of Al-Balqa Applied University (BAU) in Jordan is gratefully acknowledged.

I am indebted to my colleagues and friends during the course of this research, Dr. Mohammad Molhim, Dr. Muhanad Al-Atta, Dr. Medhat Bahr, Dr. Mamoun Medraj, Dr. Muntasser Tahat, Ali Jawarneh, Murad El-Shibly, Omer Banimelhem, Imad Khazali, Minnie Ritchardson, Panagiota Karava, and Kathy McAleese for their constant help and encouragement.

I also want to thank my father and my mother, who are anxiously awaiting the completion of this thesis. Thanks go to my brothers and sisters Mohammad, Ali, Hassan, Fatina, Nadia, Samar, Lara and Lora for their deep love, encouragement, support and help during my study.

Thanks to Montreal for making me feel at home.

## TABLE OF CONTENTS

## CHAPTER 3 EXPERIMENTAL MEASUREMENT OF WHIRLING VIBRATIONS

## CHAPTER 4 SURFACE ROUGHNESS, GEOMETRIC DIMENSIONING AND TOLERANCING IN DEEP HOLE MACHINING PROCESS

## CHAPTER 5 FUZZY SETS AND FUZZY SYSTEMS

# LIST OF FIGURES

# LIST OF TABLES

# LIST OF SYMBOLS

| Symbol | Description | Units |
|---|---|---|
| $A_1, A_2$ | Cross section area of the boring bar and workpiece | [$m^2$] |
| $d_o, d_i$ | Outside and inside diameter of the boring bar | [m] |
| $d_w$ | Diameter of the workpiece | [m] |
| E | Young's modulus | [$N/m^2$] |
| $I_1, I_2$ | Area moment of cross section of the boring bar and workpiece | [$m^4$] |
| $M_1$ | Mass per unit length of the boring bar assembly | [Kg/m] |
| $M_2$ | Mass per unit length of the workpiece assembly | [Kg/m] |
| t | Time | [sec] |
| $W_1(x,t)$ | Displacement of the boring bar to the left of the stuffing box | [m] |
| $W_2(x,t)$ | Displacement of the boring bar to the right of the stuffing box | [m] |
| $W_3(x,t)$ | Displacement of the workpiece | [m] |
| $\gamma$ | Weight density of the boring bar | [$N/m^3$] |
| $\eta(t)$ | Generalized co-ordinate | |
| $\omega_n$ | Natural frequency of the system | [Hz] |
| $\Omega$ | Angular velocity of the boring bar | [Hz] |

| | | |
|---|---|---|
| BTA | Boring Trepanning Association | |
| CLA | Center line average | |
| $R_a$ | Arithmetic mean derivation | [μm] |
| RMS ($R_q$) | The root mean square average | [μm] |

# CHAPTER 1

# INTRODUCTION AND LITRATURE REVIEW

In this chapter an introduction to the general field of deep hole boring process, followed by a summary of prior work done related to the thesis topic is presented. The thesis objectives are then formulated and the scope of the present work is described.

## 1.1 Introduction

Deep hole boring process is used to drill holes with large length to diameter ratios, normally above 10, while seeking better surface finish, good roundness and straightness. The process is usually subject to the following hole requirements: diameter of the bored hole, the depth of the bored hole, the characteristics of the hole surface, the dimension, parallelism, and straightness. Due to the fact that the boring bar-cutting head combination is slender which is highly needed to produce holes with different diameter to length ratios as shown in Fig. 1.1, deep hole machining is considered to be one of the hardest and the most complex of all hole drilling operations. In deep hole boring process, the boring bar and the workpiece are subject to disturbances such as chattering vibrations.

The accuracy, size, parallelism and other surface integrity characteristics of deep holes deteriorate while drilling due to high length to diameter ratio of the boring bar. Deep hole boring process is used extensively to drill long holes in aircraft components and auto parts that demand high precision.

## 1.2 Historical background

It is found that deep hole drilling operations were used to produce gun barrels in the 16-th –18- th centuries. The first gun-boring machine was invented around 1600-1800. The cutter head was fixed at the end of a boring bar, which was rotated by animals, and the feed downward was given to the gun barrel. Verbrugger and Ziegler produced the first boring machine in 1700s, with a massive construction. The axis of rotation of the gun was horizontal and the feed was given to the boring bar. Since then, the development of deep boring operation has been taking place until today.

## 1.3 Description and principle of operation

The machine that is used for this study is a (15-20) HP Schearer HPD 631 lathe, which is retrofitted for deep-hole drilling as shown in Fig. 1.1. In order to have variable speed of rotation and feed drive control, the drive motor was replaced with 15 KW variable speed AC motor and the feed motor was replaced with 5 KW variable speed AC motor. The optimum running efficiency by the motors are obtained using an AC inverter, which provides the required Volts/Hertz ratio.

The main driving components in the deep hole boring machine which are used in the experiment are the cutting tool drive unit, the pressure head unit, and the workpiece unit.

**(a) Cutting tool drive unit:** This drive unit mainly consists of two variable speed motors in order to control the feed rate and the speed of rotation of the boring bar. The desired rotation speed is applied to the boring bar and the feed motion is applied to the whole

drive unit, which slides along the machine bed. The boring bar is clamped onto the spindle drive unit. In order to minimize the runout of the spindle, a high precision bearing is used.

**(b) Pressure head:** The main function of the pressure head is to provide a cutting fluid supply to the drill while operating. It is also used as initial support to the tool by means of the starting bush, which is mounted on the pressure head; also the pressure head gives a good support and centering for the workpiece using a chamfered reception plate mounted on high precision bearings installed in the pressure head. The pressure head can be moved to fit different sizes of workpieces. During drilling operations the pressure head is locked at its position ensuring that no oil leakage occurs at the workpiece-pressure head reception plate.

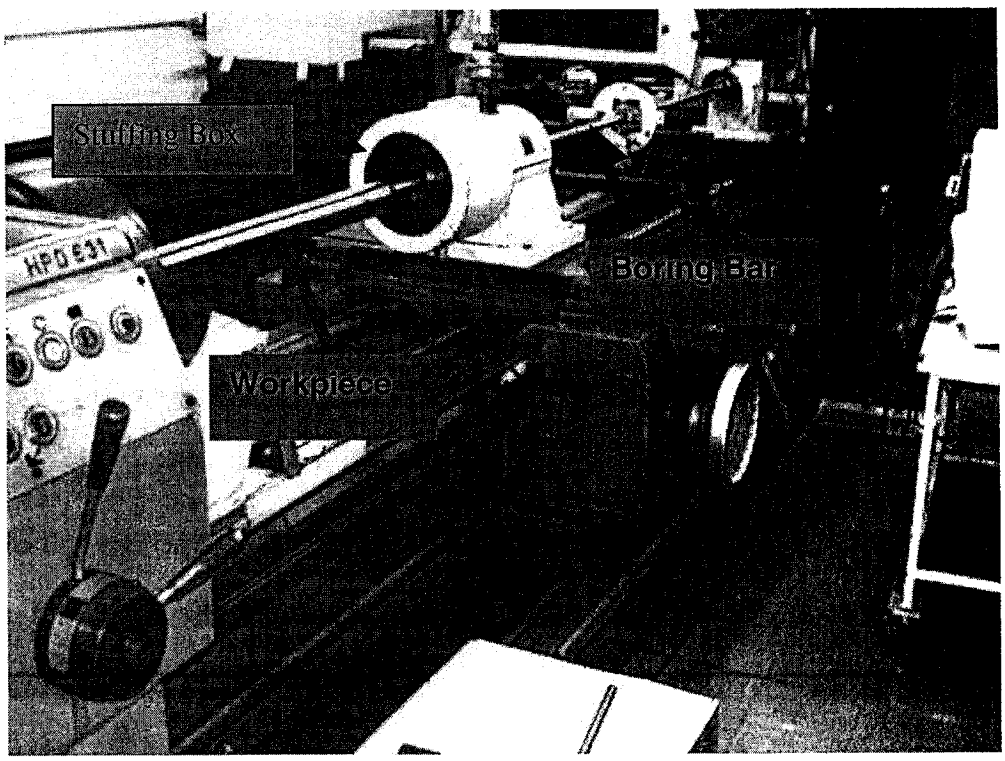


Fig. 1.1: Deep hole drilling machine

## 1.4 Survey of previous work

Many aspects of the deep hole boring operations were studied in the past few years concerning machining and cutting theory, vibration analysis and dynamic characteristics, control strategy and many other concerning surface integrity as a result of machining. In the following review, the most relevant work on the various aspects of the thesis work is presented. The reviews were done on chatter vibrations in drilling, surface roughness irregularities, geometrical dimensioning and tolerancing, fuzzy models and active vibration suppression of motion in rotating machinery. Based on the previous literature, the motivation for this study and the objectives of this thesis are presented.

### (a) Chatter vibrations in drilling

Chatter vibrations are self-excited vibrations encountered in machining operations. A part of the constant power supply to the machine is converted into vibratory power during the machining operation, which sets up sustained vibrations in the tool and the workpiece. Over the last twenty years, there have been increased research efforts to investigate the chatter vibration.

#### -Chatter as a self excited vibration in drilling

The regenerative vibration effect was investigated by Bayly et al. [1]. Their model was used to study cutting and rubbing forces in a chisel drilling edge in addition to tool vibration, which causes error in the hole size or, "roundness error" of the drilled piece.

Statistical process planning was used to describe the relationship between the machining parameters and the quality of the bored surface by Weinert et al. [2]. During the process of deep hole boring, linear and nonlinear phenomena occur. Also undesirable vibrations are initiated due to slender BTA drills having larger length to diameter ratio with low torsional and bending stiffnesses. A mechanism of torsional chatter was investigated experimentally by Bayly et al. [3], and analysis was carried out in the frequency domain to find the chatter frequencies and boundaries of stability. The engagement and disengagement is highly nonlinear during drilling process and is highly dynamic.

A mathematical model was presented by Batzer et al. [4] for a chisel drill with a zero helix angle to determine the displacement of the assumed rigid tool and rigid workpiece, where they consider only the axial vibrations and ignore the transverse motion. They used a single degree of freedom model that was solved numerically to find the chip thickness and the time lag for the chip formation. Cutting tests were done to verify the results. Keraita, et al. [5] theoretically correlated the acoustic emission during cutting to the workpiece-tool geometry and the cutting conditions. They showed that the instability of cutting or chatter is due to combination of structure, cutting conditions and tool geometry. Litak et al. [6] theoretically investigated the chaotic harmful chatter vibrations, which caused instabilities during cutting process.

The roundness error in reaming due to regenerative vibration was investigated by Bayly et al. [7] by using a quasi static model. It is shown that the tool with N teeth caused holes with N+1 or N-1 "lobes" which are related directly to the forward and backward whirl

motion. Huang et al. [8] used the acoustic emission to detect and measure the air vibration during cutting process, which gives a general idea about the tool breakage. They constructed a regression model to follow up the tool breakage while cutting. The method is validated experimentally. Kovcic [9] used the tool geometry, rake angle and shear angle and the feed rate to propose a nonlinear model to investigate chatter vibrations. The mechanism of chatter vibration was studied experimentally by Marui et al. [10] using six different spindle-workpiece combinations having different properties. They found that the phase lag between the forces and chatter displacement is related to the energy induced by chatter.

**-Whirling vibration in the chisel drill**

Whirling vibrations were experimentally measured by Fuji et al. [11] in order to investigate how the whirling vibrations developed in the chisel drill. They used three different chisel drills with different web thicknesses. Fuji et al. [12] studied the interactions among the effect of drill geometry and drill flank, in starting whirling and developing it, where they find also that the flank surface of the cutting edge is responsible for damping the vibration. Fuji et al. [13] also investigated the whirling vibrations in a workpiece having a pilot hole, where they find out that whirling motion is a regenerative vibration caused by cutting forces and friction while drilling.

**-Effect of cutting parameters and tool geometry on chatter development and surface integrity**

Edhi et al. [14] carried out an experimental study to show that chatter vibration is developed during penetration. A new chatter model was developed which is responsible for supplying and dissipating energy in the system. The dynamic response of BTA deep hole boring tool was measured experimentally and statistically investigated by Weinert et al. [15]. They show that disturbances like chatter and spiraling caused roundness and straightness errors in the bored workpiece due to high length to diameter ratio of the boring bar. Landers et al. [16] proposed a new chatter analysis, which combines forces and workpiece structure to include the nonlinearities of cutting forces by varying cutting parameters (speed, feed and depth of cut). This model was verified experimentally. Marui et al. [17] investigated experimentally the effect of the cutting parameters on the cutting system dynamic behavior. Under different cutting conditions the phase lag between cutting forces and vibration displacement was investigated. Marui et al. [18] found theoretically that the chatter vibration is generated due to the phase lag between cutting forces and vibration displacement. Ema et al. [19] carried out an experimental investigation on long drills with different lengths and special mass added to them. The results showed that chatter is a self-induced vibration and the frequency of chatter is equal to the bending natural frequency of the drill.

Atabey et al. [20] presented two models, which open the door to investigate the effect of insert geometry and the cutting parameters, speed, feed, depth of cut, boring forces and torque on chatter vibrations. These parameters are considered essential foundations to

investigate both forced and chatter vibrations in boring process. The variable chip geometry was modeled in their study as a function of tool geometry and cutting parameters. Experimental investigation to validate the model was carried out at different speeds, feeds and depths of cut. Atabey et al. [21] also presented a mathematical model for the cutting forces as a function of cutting parameters, tool geometry, chip load and cutting edge contact length. In that model, they attempted to study the process faults such as axial and radial run outs. Experimental validation of the model was also carried out. Vafaei [22] conducted experiments to monitor the X and Y vibrations of a twist drill using spectral analysis. The ARMA approach (auto-regression moving average) was used and proved to be an effective tool in vibration monitoring. Won-Soo Yun et al. [23] developed a virtual machining system in milling operations. They simulated the cutting process in two dimensional pocket milling. Surface error was estimated under different cutting conditions. Off line feed rate scheduling also was done based on mechanistic cutting forces model.

Elwardany et al. [24] monitored tool failure in twist drill by calculating the Kurtosis value in the transverse and axial vibrations. Also, they monitored the vibration power spectra of the signal in both directions to detect the breakage event. Experimental studies were conducted to verify the ability of monitoring features using this practical method. Smith et al. [25] investigated different models in milling process starting from the simple model using only a static view of the tool and increasing the complexity by including the effect of the time varying force, the position of the tool helix, the tool deflection and the

surface error generated. The simulated models could predict the quality of the milling process by means of surface errors.

Montgomery et al. [26] presented an improved structural dynamic model for a tool and workpiece separately in a milling process. The vibrations of the milling cutter and workpiece were modeled which allows the prediction of the force and surface finish under dynamic cutting conditions. The simulated model was validated by experimental studies. Matsumito et al. [27] experimentally investigated the effect of two machining processes, cutting and grinding, on the fatigue strength of hardened AISI 4340. The residual stresses distribution in addition to surface structure and surface profiles were also determined. Kolarits et al. [28] presented a mechanistic model for predicting the force in end milling when some of the cutting parameters (speed and feed rate) changed while cutting. The simulated model with experimental results was able to predict the surface geometry and the tool run out.

**-Vibration in turning operation**

Minis et al. [29] presented an improved method based on the interrupted cutting in turning in order to identify the structural dynamic behavior from input-output measurements. The three force components were measured at the same time in addition to the tool accelerations. As a result of that they found that the value of the critical depth of cut for chatter-free cutting is strongly affected by the damping presented in the structure. Minis et al. [30] also experimentally determined the dynamics of metal cutting in turning operations, which enable a direct determination of the cutting transfer

functions from input-output measurements. An external force was applied on the base plate of a specially designed stiff force dynamometer rigidly mounted on the machine tool's turret to measure the cutting force. The measurements of the tool displacement and the corresponding cutting force are uncoupled from the machine tool structural dynamics. Minis et al [31] generalized the linear stability theory for chatter in turning operations. Experimental measurements for the dynamics of the machine tool structure and the cutting process were used from previously measured actual cutting conditions. The proposed investigations were applied to the orthogonal turning, where the cutting edge of the tool is perpendicular to the feed direction. The predicted critical depth of cut was in good agreement with the measured values.

**-Dynamic of endrill operation**

Rahman et al. [32] evaluated the performance of a new type of drill (the endrill), which is a cross between a twist drill, and an endmill. The investigations were carried out to study the effects of its cutting conditions on the drilling forces, surface errors and the hole runout. It was found that the endrills produced good surface finish and good quality holes (less oversize error) under proper cutting parameters (speed, feed and flow rate). General equations of the drill torque and thrust were derived from the experimental results. Lee [33] investigated, mathematically and experimentally, the twist drill wandering motion. The model was used to explain the formation of a polygonal hole during initial penetration of drilling. The initial penetration process was observed by measuring the displacement of the drill in two radial directions.

**-BTA deep hole machining**

Zhang et al. [34] carried out theoretical and experimental investigations on the boring machining system. The dynamic characteristics of the process were formulated in state space. Special attention was paid to the tangential vibration of the boring process. As the depth of cut was continuously increased, the large tangential vibration was built up. Kojic [35] made a theoretical and experimental investigation on the BTA deep hole tool support in the machined zone. He studied the influence of various tool design parameters on the effective geometry involved in drilling. He showed that changing of various parameters at the tool design affects the hole oversizing. In his model, he showed that the inherent features of the design are to bend the boring bar even if it is initially straight. Therefore the author proposed to integrate a spherical joint in the tool drive spindle assembly, which would compensate for the angular misalignment in the clamping element, which would affect the tool performance. He carried out a signal analysis under real operating conditions with a scope on the boring bar lateral movements and the drilling forces. Alata [36] used Taguchi method for statistical techniques to find the conditions that are close to the optimum in BTA drilling operations. This statistical technique was applied to investigate the surface parameters in BTA drilling. Experimental studies were carried out on the Bell mouth formation at the beginning of drilling.

Koganti [37] developed an analytical formulation of the tool cutting force system in BTA drilling tool with staggered cutters in order to optimize the tool design to maintain equal guide pad reactions. Different boundary conditions were suggested at the cutting

tool-workpiece contact ends. The transverse free vibrations of cutting tool-boring bar are predicted for different boundary conditions.

Torabi [38] suggested an improved version of BTA Deep hole drilling tools with staggered disposable carbide inserts. He proved, experimentally, that it has small hole size capability, less hole roundness error and better surface roughness finish. Gessesse [39] studied the stability of BTA deep hole machining process. He carried out experiments to show that spiraling occurs while drilling. He suggested to modify the tool to prevent spiraling and hole roundness errors. The modification consisted of placing an additional pad near the circle land of the cutting tool. Chandrashekhar [40] conducted analytical and experimental investigations in BTA deep hole drilling. He carried out stochastic modeling of the resultant force system and its influence on the dynamics of the process. The main investigation was to study the type of cutting forces that occur at the interaction point between the cutting tool and workpiece system.

**(b) Surface roughness, geometrical dimensioning and tolerancing**

Under ideal conditions, the machined surface should be smooth with perfect circularity resulting in a straight-drilled hole. However, due to the chatter vibrations, clearances misalignments, unbalances of rotating parts and forces, the drilled holes will not be perfect.

**-Surface roughness**

Hecker et al. [41] determined the arithmetic mean surface roughness in grinding taking into consideration the undeformed chip thickness based on probabilistic method. The material property, the kinematic conditions and the wheel structure were considered in predicting the surface roughness. As a result of the investigation, an expression for the surface roughness was presented. The model was verified experimentally. Hassui et al. [42] investigated the surface roughness in AISI 52100 tempered steel in cylindrical grinding. The input variables considered in the experiment were the dressing overlap ratio, the spark out time and the workpiece velocity. The outputs were the roughness and roundness errors and the vibration in the process. It was found that the vibration level affected the workpiece roughness and roundness. Muralikrishnan et al. [43] developed a surface finish toolbox for manufacturing and machining process. They used groups of collected data of surface profile of machined parts to train a neural network. The resulting clusters were examined and analyzed for further studies in the way to develop this procedure.

Rech et al. [44] investigated the effects of surface cutting parameters such as speed, feed and tool wear, on the case hardened 27MnCr5 gear conebrakes on the outcome surface roughness. In the paper, the technical limitations due to this roughness are pointed out in mass productions. Salisbury et al. [45] investigated the geometrical and kinematical generation of the surface roughness in grinding. The effects of the process parameters (table speed, wheel speed, the wheel topography and the original workpiece surface topography) were taken into account. The model was verified experimentally.

Lee et al. [46] presented theoretically the effect of surface roughness in the alignment process of the mating parts. It was found that the level of alignment precision decreased with an increase in the roughness if the workpiece surface material was hard; the effect was not as significant as the geometrical effect in multiple-station processes. Experiments were carried out to validate the mathematical model. Jang et al. [47] presented a technique to evaluate, online, the quality of machining process in hard turning. The correlation between surface roughness and cutting vibration was established as the first step towards a final model. They utilized the relative cutting vibrations between the cutting tool and the workpiece during operation. Experiments were conducted using inductance pick-ups and specific vibration components, for different cutting parameters (feed, speed and depth). It showed that the roughness of the surface had specific frequency components without the chatter, which was determined by feed marks and were almost close to the natural frequency of the cutting tool structure. The simulated technique showed a good agreement with the experimental results.

Zhang et al. [48] presented a model to correlate the surface finish parameters with the conditions and the workpiece material. As a result of the correlation they were able to generate a 3-dimensional texture of the machined surface. The idea behind this model was that the random excitation originated from the non-homogeneity of the distribution of the micro-hardness of the workpiece material. The model was verified experimentally. Zhang et al. [49] also presented a methodology to dynamically generate the surface topography under the random excitation using computer simulation as a continuation of their previous study. The method was based on the tool vibration along with the tool

geometrical motion to produce the surface profile. They found both analytically and experimentally that the effect of spiral trajectory of tool geometrical motion decayed when using small feed rate, and the random excitation system was the main source of surface texture generation.

**-Geometrical dimensioning and size variation**

Zhu et al. [50] came up with a new model to evaluate cylindricity in mechanical parts. The proposed model used measurement points obtained from a coordinate measuring machine. By a signing point-to-surface distance function, they were able to derive the increment of the surface with respect to the differential motion of the surface. The developed method was compared with the four basic methods used to evaluate cylindricity error. The model was simple and easy to implement and computationally efficient. Dhanish [51] presented a new model to calculate the circularity error from coordinate data. The model was compared to the basic model used to evaluate circularity such as the minimum zone method. The model was proved to give a minimum value for circularity error.

Astakhov [52] investigated the formation of most common surface irregularities that occurred at the initial, unstable stage of gun drilling and the formation of bell mouth. The study revealed the main design features that affects this kind of irregularities and gave some design recommendations. The role of the clearance in the starting bush is included also, in order to reduce the irregularities. Astakhov [53] also investigated the mechanism of bell mouth formations at the second stage of drilling after the gundrill's cutting edge is fully engaged in cutting. The main focus in this study was on the design parameters of the

gundrill such as, the flank relief angle of the outer cutting edge, the location of the rake face and the design of the supporting area. Some practical suggestions in the design parameters were presented to reduce the bell mouth.

Ko et al. [54] presented a virtual machining system in the four flute end milling. The effect of the cutting forces on the uncut chip thickness and the size of the machined part were investigated. The simulation studies showed that the virtual machining system could predict better than the previous model in terms of cutting forces and the size error. Cho et al. [55] addressed the effect of roundness error in two mating parts. As a result of the investigation, they developed a systematic model for assigning circularity error to meet certain limits in two mating parts, or the circularity tolerance, in order to ensure positioning accuracy in transition assembly fit. The simulated model showed a good agreement with the experimental results. Fung et al. [56] described with experimental proofs, a methodology for online measurement of roundness error in taper turning. The online error measurements of the roundness were compensated online using two dimensional piezo-actuated tool movements. They showed, experimentally, that using this method resulted in an improvement of 42-47 % in roundness error.

Chou et al. [57] developed a method to assist circularity or to reduce roundness error of machined parts in three dimensions. The proposed approach was based on identifying the obliqueness of the cylindrical features under test and then eliminating its influence on the departure from circularity from the measured points. Following this approach, the roundness of the object could be assessed more accurately. Cho et al. [58] proposed a harmonic roundness model for machined specimens using Fourier series expansions.

Also, they established a relationship between the radial error motions of a spindle and the resultant part profile, which was used then to give physical meaning to the proposed roundness error generated by the harmonics. Carrying out experiments for both turning and cylindrical grinding processes they verified the proposed model.

Jywe et al. [59] presented three simple mathematical models, taking into consideration the method used to choose the exact control points which were constructed to evaluate the analytical solution of the minimum circumscribed circle, the maximum inscribed circle and the minimum zone circle by solving the simultaneous linear algebraic equations. Through some examples, this method was proved to have better accuracy than the least square method. Furness et al. [60] statically analyzed the hole quality or surface irregularities in drilling using twist drills. The effect of the cutting parameters, feed and speed on the outcome roundness error, location error, angularity error and hole oversize, were examined using a full factorial analysis of variance. The experimental results showed that feed and speed have a small error effect on the hole quality, but the hole location was not affected by that. This meant that the production rates could be increased without sacrificing the hole quality, without affecting drill breakage, force, torque and power limits and drill wear.

Shawky et al. [61] developed an online technique to evaluate the workpiece geometrical dimensioning in turning operations. Their technique was based on the idea of using three non-contacting proximity pickups to determine the runout of the bar in turning and to eliminate this error using the spectral analysis and error separation method. Also, they

provided an analytical technique to determine the cylindricity tolerance of the workpiece based on the experimental data collected. The technique could provide a useful basis for further research in the area of intelligent machines and real time geometric adaptive control.

Gessesse et al. [62] experimentally investigated the spiraling formation in machined hole in BTA deep-hole drilling process. They found that spiraling was caused by defects in the tool geometry, radial oversize, and when the lateral natural frequency of the boring bar cutting tool assembly was five cycles per second, relative to the workpiece. Also, they noticed that spiraling only occurred in five lobes. The experiments were repeated a number of times to confirm the validity of these observations. Starbuck [63] developed software to remove unwanted features in machined hole for roundness measurements, such as asperities caused by contamination from air borne particles or other debris from the environment, or discontinuities in the surface such as holes or particles stuck from the cutting tool. These kinds of features affected the accuracy of roundness measurements and removing them was crucial.

Parsons et al. [64] developed software for the measurement of surface roughness and geometrical parameters such as roundness error. The idea was to use a touch screen and related surface functions and color graphic icons (window) that described the surface to complete the measurement process. The software was user friendly and was easy to understand because it presented only specific questions that were related to the current measurements. Cogun [65] developed a correlation between the deviation errors in the

form of roundness and cylindricity errors, based on a number of published data and investigations, and the International Standards Organization (ISO) tolerances. This investigation helped to choose the size tolerance for roundness and cylindricity errors when certain workpiece accuracy was highly needed. The correlations were verified by a number of measurements.

Shiraishi et al. [66] established a control on dimension and surface roughness in turning operations. They aimed to produce a smooth surface by removing local irregularities and to keep the size deflection within a certain tolerance. The control results showed an improvement of surface with dimensional accuracies based on optical measurements. Ema et al. [67] investigated the hole accuracy and size tolerances using a new type of twist drill with three major cutting edges, three chisel edges and three flutes. They showed, using the new drill, that no whirling vibrations occurred unlike in drills with two major cutting edges. As a result of that, hole roundness, straightness and cylindricity were more accurate.

Kim [68] presented a compensatory control strategy to improve form accuracy, like cylindricity. The technique was based on the idea of taking error model, which was the tool wear in online measurements, and then forecasting the error of the cutting point in order to compensate for it using piezoelectric actuators. The model was verified experimentally through online cutting using in-process gauging and actuators. Rao et al. [69] studied the accuracy and surface finish in BTA deep-hole drilling process. Experiments were carried out on EN-9 steel under different cutting conditions (speed,

feed and depth of cut). The main focus was the size variation, strength, roundness and surface finish. They showed that the effect of speed was to produce a wide variation of size, and the effect of feed was to produce oversize or undersize holes depending on the feed value. Further, roundness and straightness increased with speed due to instability of the system. The roundness was high at entry due to instability at the beginning of drilling. A better finish was achieved at high speeds of cut.

Kim et al. [70] presented a mathematical model of an alignment error, and examined the effect of each alignment error on overall system accuracy. A compensation scheme was suggested to improve the accuracy in the process. They noticed that if there were no alignment errors, the signal on the photosensor would be a perfect circle and the most affecting factor was the angular misalignment of the laser beam. Kim et al. [71] also developed a forecasting control to improve workpiece roundness in cylindrical grinding. They identified the spindle radial error as a dominant error source.

**(c) Fuzzy model**

Machining process is affected by several parameters such as speed, feed, depth of cut (tool penetration) and balance conditions of rotating parts etc. The machined surface quality is a highly nonlinear function of these parameters. In view of the associated uncertainties, either a statistical analysis or a fuzzy logic model is suitable to predict the outcome for specific machining parameters set initially. A fuzzy logic approach is employed in this study and a review of the past work in this area is given below.

**- Fuzzy modeling from numerical data**

Dweiri et al. [72] presented a technique in fuzzy modeling of a CNC down milling machining process. After machining different specimens under different cutting conditions (feed, speed and depth of cut), they were tested for surface quality by means of arithmetic surface roughness, Ra. The model was based on the idea of setting up the fuzzy rules by using fuzzy grid partitioning. Surface responses were obtained and the optimum cutting parameters were determined. The resulting best cutting parameters were tested and gave good results.

Yang [73] presented an automated procedure to select the best material and processing parameters for composite materials. A multiple neural network was used with an algorithm that was employed to identify the holes and calculate the complexity of the surfaces. For each specific material a genetic algorithm was assigned to select the best operating parameters. The optimum parameters process was determined by checking the good qualities of the surfaces generated. The proposed model was very convenient to model other complex systems.

Demirli et al. [74] developed higher fuzzy model identification, using subtractive clustering. The main idea was to automatically generate the fuzzy rules and to determine the best clustering parameters that will model the system with minimum fuzzy rules. The model was used to model highly nonlinear systems and gave very good results. Ying Ho [75] proposed a model to predict the surface roughness of a test specimen in turning operations using computer vision. The main idea was to use an adaptive neuro fuzzy

inference system (ANFIS) to obtain a relation between the different cutting parameters (feed, speed and depth of cut) and the surface roughness. The results were tested experimentally and showed very good prediction accuracy.

Jaulent et al. [76] presented a fuzzy logic model for the uncertainties due to the use of clinical practice guidelines (CPGs), which help the physician in their decision-making in giving a best classification procedure. The rate of the recommendation is based on the strength of recommendations for the patient under consideration. An 86.6% of agreement was noticed between the proposed model and the classical decision tree. Also, the variability of close characteristics of the 82 patients under study with mild to moderate hypertension was reduced.

Alwedyan et al. [77] presented a technique for modeling Alumic-79 in CNC milling operation under different cutting conditions. They used higher order subtractive clustering based on first order Sugeno fuzzy model to automatically generate the rules. Then the model with the minimum number of rules associated with the root mean square error was considered. The chosen model was then tuned to make more accurate modeling by using ANFIS. The tuned fuzzy model was able to reproduce the actual behavior of the system under study. Alata et al. [78] carried out an experiment in deep hole boring process taking into account two inputs, the speed and the feed rate. The specimens were tested for the surface roughness. An enumerative search was done for the input-output data to find the optimum clustering parameters. The Fuzzy model was able to reproduce

the actual behavior of the system under study. Hence the operator, using this model, can predict the surface quality for a given input parameters.

Lou et al. [79] presented a fuzzy modeling technique from a limited experimental data. Their model was based on the idea of assuming a set of linear models in the THEN part (the consequent part). Model reliability was assured by using a t-test based nonlinear analysis after each fuzzy implication was developed. The efficiency of the proposed model was demonstrated by applying it to two industrial processes. Abonyi et al. [80] presented an algorithm for fuzzy modeling and control to identify the laboratory liquid level process. The main idea was to use the past known behavior of the system such as, stability, maximal or minimal static gain and to translate this knowledge into inequality constraints on the consequent parameters of the THEN part. They found that when this proposed model was applied, not only the physically justified models were obtained, but the total performance model-based controller improved also in case no prior knowledge was involved in the process.

Bontempi et al. [81] presented, theoretically and experimentally, a model selection approach for local learning. The focus in this paper was on the automatic query by query to select the structural parameters. In the model, and for each query, a different model candidate was first generated, assessed and then selected. The learning algorithm was based on the recursive least squares algorithm to generate the local models. While selecting the best model, it takes all the strategy and local combinations of the most promising models are explored. The experimental results proved that the resulting model

is able to compete with the state of the art approaches. Wu et al. [82] proposed an architectural and learning approach, dynamical fuzzy neural networks (D-FNN) based on Takagi-Sugeno-Kang (TSK) approach. In the model, a hierarchical online self-organizing approach was utilized. The efficiency of the model was proved by its capability to delete or add neurons dynamically in addition to its learning speed. The model was verified experimentally and a comparison with other learning algorithms was carried out. The results showed high competing performance and efficiency.

Hashmi et al. [83] presented a technique using fuzzy logic modeling approach to select the best cutting conditions that matches with material properties and cutting tool type. The model was based on the relationship that exists between any specific material (say its hardness) as an input and the corresponding cutting speed, and feedrate as outputs. The resulting model showed a very good correlation between the machining data handbook and the fuzzy logic model. Ali et al. [84] presented a complex fuzzy model to predict the surface finish of a ground component. They introduced in the model 16 variables, which are the most effective variables on surface finish. The model was constructed of three layers fuzzy model to correlate the variables with the surface roughness by means of Fuzzy IF –THEN rules based on experimental measurements. The effectiveness, simplicity and superior modeling of nonlinearity in the model was verified by working out an example.

Bontempi et al. [85] presented a toolbox for neuro fuzzy modeling identification and data analysis. The theory of the model was to use Takagi-Sugeno fuzzy architecture. The

initialization of the architecture was provided by a hyper-ellipsoidal fuzzy clustering procedure. The axis of the ellipsoid (eigen vectors of the scatter matrix) was used to initialize the parameters of the consequent parts (the THEN part). The cluster centers were projected on the input domain to initialize the centers of the antecedent part of the model. The efficiency and simplicity of the model were illustrated by an example. This toolbox was found to be efficient in data training and identification process of complex functions.

Kim [86] presented a technique for automatic generation of membership functions for numerical data based on entropy minimization for screening analogue values. Minimum entropy clustering decisions were introduced to make partitioning in the space and to derive the membership functions and fuzzy rules. The partition point (the entropy minimum point) was used to decide the range of membership functions along with the rule weight determination. A numerical example was presented to illustrate the algorithm. Berini et al. [87] discussed the idea of deffuzifying the neuro fuzzy model. Based on the available data, the neural-fuzzy model had the capacity of automatic self-tuning of the structures and parameters. Two main things in the paper were made clear, the linguistic translation of a numerical mapping and the powerful multi-local model black-box approximator. Duch et al. [88] presented a technique to automatically extract rules from training data using backpropgation algorithm. The idea was based on adding an additional term to the cost function that forced the weight values to be +1, -1 or zero. Auxiliary constraints were added to ensure the training process using maximal number of zero weights, which will yield a minimal number of logical rules extracted by weight analysis. The attractive feature of this technique was its ability to add additional neurons

in case there were exceptions to the rules. The algorithm was applied to the mushrooms classification data set, which included 8124 vectors. The model was able to perform a better approximation with smaller number of rules. Pedrycz [89] presented an effective and attractive model in dealing with numerical data training. The model dealt with the data as families and not as a single model. The model was based on the nature of the distribution rather than their function orientation. The model was able to trigger and aggregate using relevant mechanisms, which assured a good interaction between these models. The model was simulated using different examples to show its effectiveness.

Suharyanta et al. [90] used fuzzy rules capability to generate rules in a reservoir where imperfect stream flow of data condition occurred. The fuzzy model was able to produce an operation policy for a single reservoir designed under imperfect data conditions. The technique was applied to Wadaslintang reservoir in central Java, Indonesia. The model gave a more straightforward analysis than conventional methods.

Lee et al. [91] developed a corner-matching algorithm that minimized the amount of calculation using fuzzy logic model. The model recognized the corner of the model object and the corner of the scene to initialize the model. A matched segment list was extracted which was used then to calculate the transformation between object of the model and the scene. To find out the uncertainties of the features from the recognized results, an outer tuning scheme of the fuzzy rules was introduced. An experiment was conducted for an image of real components where the position and orientation of the object was recognized effectively.

**-Fuzzy C-mean clustering**

Stutz et al. [92] presented an extension of the fuzzy C-mean clustering (FCM) by using a mix of different prototypes in the clustering procedure. Previously known constraints helped in integrating into the clustering algorithm by using constraint prototype. In the paper, two modification models of FCM were presented, in addition to the constraints. The locations or the geometry dependencies between clusters could be involved into the clustering process. The model was applied to the classification of the traffic conditions by clearly identifying the clusters as "free flow", "dense traffic" and "traffic jam". Stutz [93] also presented two modifications of the FCM. A partial supervision of the clustering by labeling data points and determining the number of clusters by cluster merging was applied. The main idea was to combine the partial supervision and the cluster merging into one algorithm. The resulting approach was applied to the traffic data.

Ross et al [94] used a proposed fuzzy classification and clustering method to help in calculating the uncertainties in multi degree of freedom systems, by classification of the model data into partitions whose impact on the final uncertainties can be measured qualitatively. The fuzzy C-mean was acting as a confirmation of the behavior of the system once certain conditions of the system were known to lead to some well known behavior in vibration. The model also was quite useful in extracting information from modal data by determining the data structure.

**-Fuzzy models for a dynamic system**

Pyotsia [95] presented a fuzzy model to diagnose a system with a fuzzy reasoning in order to handle vagueness and inaccuracies. A description of the failure detection architecture was also presented. The proposed model aimed to give information about the failure analysis concept in dynamical systems. Bontempi [96] discussed modeling with uncertainty in a continuous dynamical system. He compared between using the probability approach, the conventional Monte Carlo, and the possibility approach (fuzzy logic system). In the paper he showed that using the probability approach may lead, in some cases, to an inaccurate outcome, making it more advisable to use the fuzzy logic model. Hence, a new algorithm using fuzzy logic was proposed for a numerical simulation to solve the dynamics of the system by means of differential equations. A comparison between probability and fuzzy logic approach with fuzzy models showed that the latter was more accurate.

**-Fuzzy control models**

Hsu et al. [97] used an adaptive fuzzy control in CNC machining process under different cutting conditions. The feed rate was varied to keep a constant cutting force. The idea was to adopt online scaling factors for cases with varied cutting parameters. Also, a reliable self-learning algorithm was proposed to achieve a good cutting performance by modeling an adaptive rule base taking into consideration a properly weighted performance measure. The experimental results showed a good sensitivity and robustness with the simulated results under variable cutting conditions. The main idea of the model was to maintain a constant force in the CNC machining process. Du et al. [98] presented

a study on tool condition monitoring such as, tool breakage, tool wear and chatter. Three components of the cutting force, the acceleration of the tool holder in two perpendicular directions and the spindle motion, were monitored. Fuzzy relations were then established between the tool conditions and the monitored quantities. A total of 396 cutting tests under 52 cutting conditions were carried out to validate the model. The results showed a 90% reliability of the proposed methodology for detecting tool conditions.

Zadeh [99] emphasized on the use of soft computing rather than hard computing. Soft computing proved to be more tolerant of imprecision, uncertainty and incomplete truth. An example was presented on the use of the basic idea of fuzzy logic modeling and identification and control. The role model of the fuzzy logic was the human mind.

**(d) Active vibration control**

Using fuzzy logic approach to arrive at the optimum machining parameters that will minimize the chatter vibrations and consequently improve the surface quality is an open loop control approach. Suppression of chatter vibrations can also be done using a feedback control approach such as active vibration control. In the following a review of active vibration control attempts to suppress chatter vibrations is presented.

**-Active control in drilling operation**

Xiao et al. [100] proposed a cutting vibration model to suppress the chatter vibration in turning without relying on the cutting tool geometry. The idea was to use an eddy current

sensor, which sensed the Y amplitude of the workpiece, and to use longitudinal vibration with electrostriction transducer on the cutting tool to compensate for the workpiece motion. The simulated results showed a very good agreement with the experimental ones. They also found that this technique of cutting tool chatter vibration is not affected by the tool geometry, in contrast to conventional cutting where the chatter is caused by a decrease in the rake angle and an increase in clearance angle.

Ismail et al. [101] presented online and offline chatter suppression in a five axis CNC machine. In online control they changed the spindle speed ramping to suite the dB level, while in offline control they increased the feed rate when the rotary axis underwent large increments. A combined scheme was also used to suppress the chatter motion. They found that the feed scheduling approach is more practical than the speed control where fast response is needed and cannot be readily implemented on most machining processes.

Zhou et al. [102] reviewed the techniques and methods used in dynamic modeling and analysis, to suppress the vibration in rotating machinery. The main problem in their approach was that a limited number of actuators were used to control a large number of vibration modes. Also, no systematic method was available to show the relationship between the estimation and control strategy, which is highly needed in active balancing and vibration control methods. It was concluded that active suppression can improve the product quality and improve fatigue life of the cutting machines. Dyer et al. [103] presented an optimal technique for multiple plane active balancing control to improve control robustness and modeling and estimation error. This optimal law was applied in

the laboratory for two plane active balancing of the rotor system using two balancing actuators to work with two eddy current proximity probes that measure the radial displacements in two orthogonal directions. The results from the experiment showed a good agreement with the proposed model.

Altintas et al. [104] presented, theoretically and experimentally, a technique to detect and suppress the chatter vibration in milling machines. In the experiment they used proximity sensor to check the displacement of the tool in one direction and to detect the chatter vibration level by means of measuring sound spectrum using a microphone. The cutting conditions, mainly speed of cut, was changed accordingly using a high performance and high torque delivery spindle drive system which could deliver speed oscillation to overcome the chatter produced in a wide range of amplitude and short time interval. Lin et al. [105] studied the effect of cutting speed of vibration control in face milling. They found that the self-excited vibration, resulting from constant speed of cut, which would limit the possible size of cut, could be suppressed by continuously varying the speed of cut. The simulation model and the experiments showed a good agreement.

Kim et al. [106] investigated, analytically and experimentally, the design of a viscoelastic dynamic damper in turning operations. They found that it is relatively simple to build an optimum viscoelastic damper with excellent capability of vibration absorption to suppress the machine chatter under different cutting conditions.

**-Active control in structures and rotating machinery**

Agnes et al. [107] presented the effect of nonlinear electrical shunts on the performance of piezoelectric absorbers for linear systems. The electrical shunt, which is a cubic and quadratic element, is coupled to the structure using the piezoelectric effect. The shunt was turned near a structural mode and it caused the mechanical energy to be transformed to electrical energy and to be dissipated by the resistance elements in the shunt as in damped vibration absorbers. The main idea was to see the effect of a small nonlinearity on the performance of piezoelectric absorber. It was found that the performance of the absorber could degrade without the designer's knowledge. Yellin et al. [108] developed an analytical model for active constraint layer (ACL), which would be used to predict theoretically the performance of a self-sensing active constraint layer (SACL) damping for an Euler-Bernoulli beam. They found that, carrying out this comparison, the (SACL) was a real and feasible method to control an elastic beam. The theoretical model, which predicts the first and second modes for SACL, was verified experimentally to show the ability of predicting the frequency response of these beams.

Palazzolo et al. [109] used the active vibration control by means of piezoelectric actuators in rotating machines. They used two eddy current sensors and two stacks of piezoelectric ceramic disks. The theory was developed and a number of experiments were carried out to verify the theory, which was able to effectively suppress unbalance response and vibrations. Palazzolo et al. [110] also used piezoelectric pushers in rotor bearing systems in view of its lightweight rather than using heavy electric shakers. They presented an analytical technique, which extended quadratic regulator, and derivative feed back

control methods. The experiments were conducted on the NASA test rig as preliminary verification of the related theory. Two active theories were under study to treat the internal displacement of the piezoelectric pushers. The uncoupled velocity-feed back theory was tested by comparing with the experimental results. Palazzolo et al. [111] presented an optimal control theory to decrease rotor vibrations due to sudden imbalance such as blade loss. The associated Riccati equation was solved to obtain the system gain matrix. Then a relationship between the number of sensors and the number of modes used in the model were investigated. The experimental results showed that the orbital vibration has been reduced from 0.45 mm to 0.1 mm and the maximum actuater force was 100 N.

Bennighaf et al. [112] investigated the active vibration control in a distributed system with a moving support, i.e. a plate attached to a moving rigid beam. They designed a control to mitigate the effect of the moving support on the absolute motion of the system and another minimized the remaining absolute motion. An experiment was conducted to verify the model and showed a very good agreement, indicating that the model duplicated the dynamic characteristics of the system very closely.

## 1.5 Research Goals

The whirling and chatter vibrations encountered in the deep hole machining process are due to the inherent nature of the process itself involving long and flexible boring bars, the cutting forces and the unbalance. Consequently, the machined surface will suffer from unwanted roughness, deviation from roundness and straightness. The main objective of the present study is to suppress such vibrations, in order to improve the surface quality,

which would involve modeling the system, identification of optimum cutting parameters and control of unwanted vibrations.

In this study, comprehensive approach is proposed to study the whirling vibrations, in a continuous boring bar-cutting head assembly by considering the boring bar and the workpiece as one single system with self exciting cutting forces acting internally at the interaction point. The resulting problem involves nonhomogeneous boundary conditions with homogenous equations. The approach followed transforms the problem into nonhomogeneous equations with homogeneous boundary conditions.

The mathematical model will include the active suppression forces in the Y and Z directions and simulations of the model will be carried out with the forces acting on the boring bar-workpiece system. Optimum machining parameters are identified using fuzzy logic relations between the machining parameters and the quality of the machined surface. Active vibration experiment is carried out to suppress excessive vibrations in the boring bar and at the cutting tool and to validate the simulated model.

The specific objectives of the present thesis study are:

1. Theoretically investigate the whirling motion by proposing a new model for the excitation with non-homogenous boundary conditions.
2. Experimentally investigate:
    i. Whirling motion of the boring bar-cutting head system.
    ii. Whirling motion of the boring bar-cutting head assembly at the beginning of drilling process.

iii. Whirling motion of the boring bar-cutting head assembly under different cutting parameters.

3. Theoretically determine the mode shapes of the boring bar-cutting head-workpiece assembly, and also experimentally determine the natural frequencies of the boring bar-cutting head assembly.
4. Investigate surface irregularities such as roughness, straightness, roundness and cylindricity under different cutting conditions.
5. Build a fuzzy model system that will predict the optimum cutting parameters to minimize surface irregularities in geometrical dimensioning and tolerancing such as roundness, straightness and cylindricity and surface roughness.
6. Active vibration control experiment with two electrodynamic shakers to directly suppress the whirling motion of the boring bar.

-**The main contributions in the thesis are**: Formulation of an innovative cutting force model in order to obtain orbital response of the tool workpiece system for the self-excited motion and the active suppression forces in the Y and Z direction to counteract the cutting forces. A comprehensive experimental study of the surface irregularities under different cutting conditions in order to demonstrate that at any cutting parameters the whirl motion and the resulting surface irregularities will vary for different tool penetrations. Design and testing of the fuzzy logic model relating finished surface, geometrical dimensioning and tolerancing with machining parameters. Implementation of active suppression technique in order to reduce the whirling motion using electrodynamic shakers and the validation of analytical model.

## 1.6 Scope of Work

The first chapter of the thesis provides a basic working principle of the deep-hole boring process, a survey of previous work done related to the thesis project and proposes thesis objectives. The second chapter focuses on the mathematical modeling of the whirling motion in deep hole boring process. In the mathematical model, a general modified approach is proposed by introducing the system excitation in the form of an internally forced relative motion between two members within the system. This involves nonhomogeneous boundary conditions with homogeneous equations. The modified approach will transform the problem into nonhomogeneous equations with homogenous boundary conditions. In our case, the forces transmitted from the boring-bar to the workpiece while drilling consists of a component corresponding to the mean transmitted power plus a fluctuating component of a dynamic origin. This excitation that produces the latter originates from within the complete system of the boring bar-workpiece assembly and the nature of the drilling process. The special feature that characterizes the present problem is that the excitation forces are applied at an internal point linking the two subsystems, the boring bar and the workpiece. The whirling motion of the boring bar was obtained at different locations of the boring bar-workpiece assembly.

In the third chapter, an experimental set up is developed to validate the proposed mathematical model. The experiments contain three parts. The first part considers the whirling motion of the boring bar alone without the cutting torque, under the action of unbalance force at different rotational speeds, say, low, medium and high speeds of

rotation. The second part studies the whirling motion of the boring bar at different speeds of rotation at the beginning of cutting process. The third part varies the cutting parameters in order to obtain the whirling motion of the boring bar at each combination of cutting parameters. The effect of the whirling motion of the boring bar on the outcome surface irregularities, geometrical dimensioning and tolerancing is presented in chapter 4. The focus in this chapter is on the RMS values of roughness, roundness, cylindricity and straightness errors.

The effect of the whirling motion of the boring bar on the outcome surface quality shows the need to have optimum combination of cutting parameters. A new Fuzzy logic technique is proposed to obtain the best cutting parameters to give better surface quality in chapter 5. In chapter 5, an offline technique is proposed to eliminate the effect of whirling motion to get better surface quality using subtractive clustering technique and adaptive-neuro-fuzzy inference system (ANFIS).

In chapter 6, an active vibration control of the whirling motion of the boring bar is implemented. In the experiment, two electrodynamic shakers are used in the Y and Z directions to suppress the whirling motion. The suppression of the whirling motion has been done at three speeds of rotation of the boring bar (1040, 1237, 1440 rpm) under no cutting loads and one experiment while drilling at a speed of 1040 rpm, feed of 71 mm/min and flow rate of 20 G/min. The surface roughness was investigated before and after applying the active suppression forces. The conclusions and suggestion for future work are presented in chapter 7.

# CHAPTER 2

# MATHEMATICAL MODELING OF THE WHIRLING MOTION IN DEEP HOLE-BORING PROCESS

As mentioned in the previous chapter, suppression of vibrations in deep hole boring process in order to improve the machined surface quality is the main objective of this thesis. In order to understand the dynamics of the boring bar workpiece system, a mathematical model is formulated to start with. The mathematical model is used to carry out analytical and simulation studies of the whirling motion in deep hole-boring process. In this chapter, the mathematical modeling of the deep hole boring will begin with modeling the boring bar alone. The model for the boring bar-workpiece system is then introduced with internal cutting forces at the interaction point. The control forces introduced by two electrodynamic shakers to counteract the vibration of the system that is required for the active vibration control, to be discussed in chapter 6 is also included in the analytical model developed. The natural frequencies and the mode shapes of the boring bar and the boring bar-workpiece assembly are calculated. The whirling motion of the system at any point of the boring bar and the workpiece is established. The derived model is validated experimentally.

## 2.1 Mathematical modeling of the boring bar

Deep hole boring process is used to bore holes with usually high length to diameter ratios seeking better surface finish, good roundness and straightness. The process usually depends upon the following hole requirements: diameter and the depth of the bored hole, the characteristic of the hole surface, the dimension, correctness, parallelism and straightness. A photograph of the deep hole machining facility is shown in Fig. 2.1. The system is subjected to disturbances such as chattering vibrations during operation. Despite the abundance of studies done in this field, chatter vibrations are still not fully understood. Whirling motion is vibration in 3 dimensions, which affect the geometrical accuracy and the surface quality of the bored piece. Deep hole boring process is used extensively to drill expensive workpieces and hence process precision is of prime importance. To achieve the best process performance with the aim of minimizing the risk of the workpiece damage, a comprehensive investigation of the dynamics involved in the process, both analytically and experimentally, is highly important.

To achieve our purpose in this thesis we will start by establishing the mathematical model of the boring bar alone, and then that of the boring bar-workpiece system. The whirling motion of the system is then simulated at different sections of the system.

The cutting head portion of the boring bar is shown in Fig. 2.2 with the stuffing box. Fig. 2.3 shows the model for the boring bar with two distinct regions. During the machining process, depending upon the degree of stability, the boring bar with the cutting tool attached to it can be considered subjected to different end conditions.

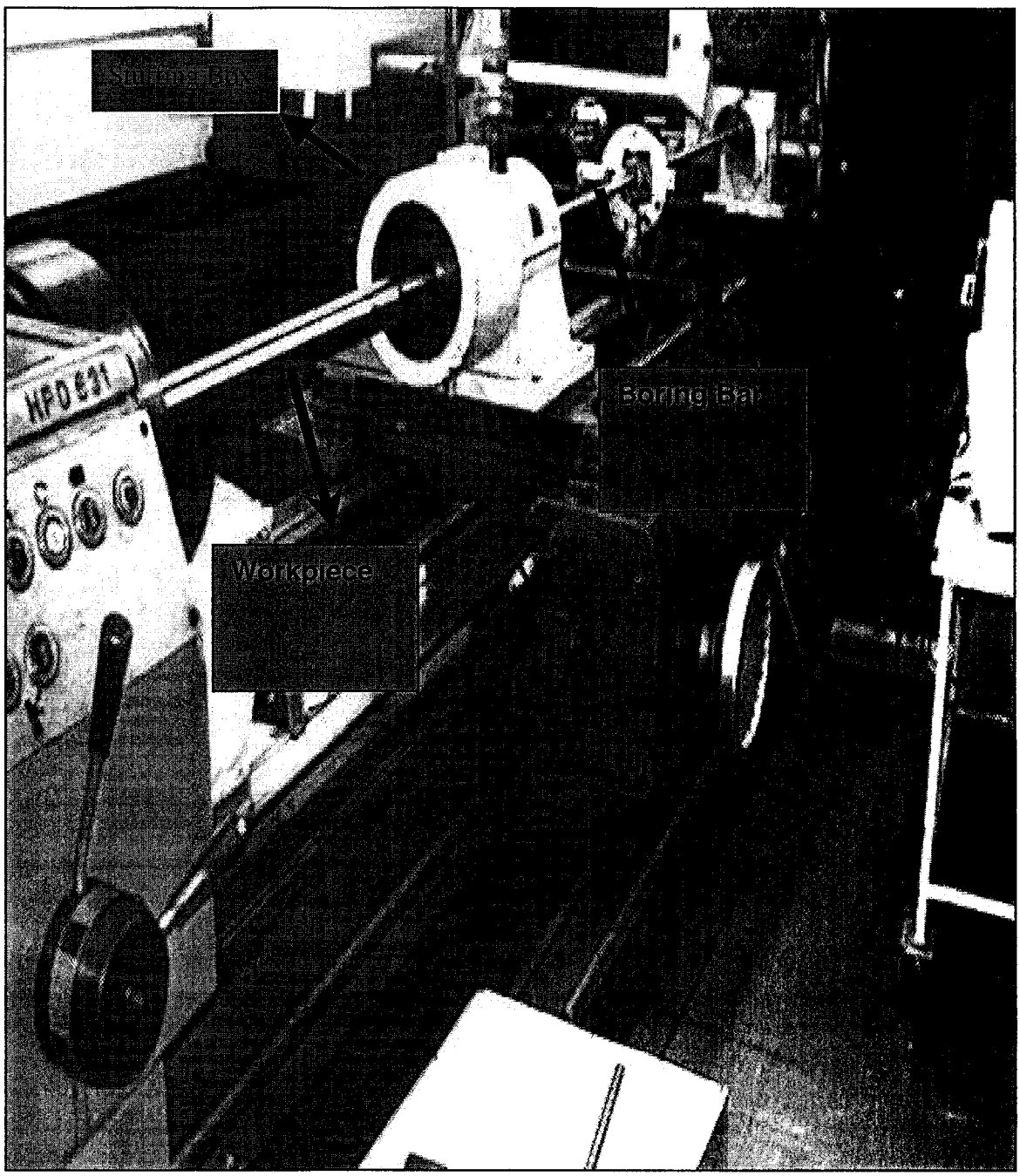


Fig 2.1: The boring bar, the workpiece and the stuffing box in BTA deep hole boring machine.

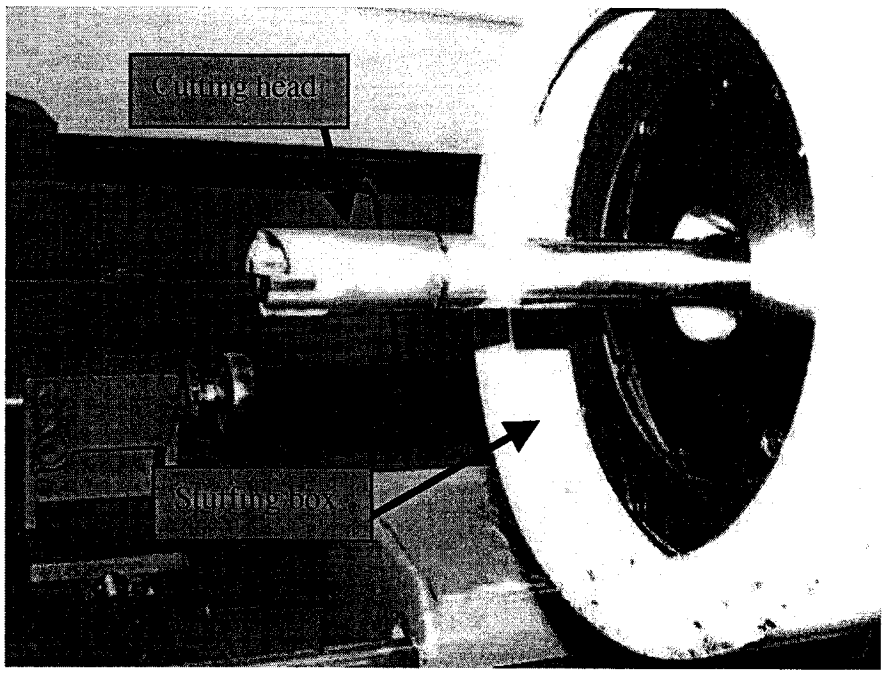


Fig. 2.2: The deep hole boring cutting head.

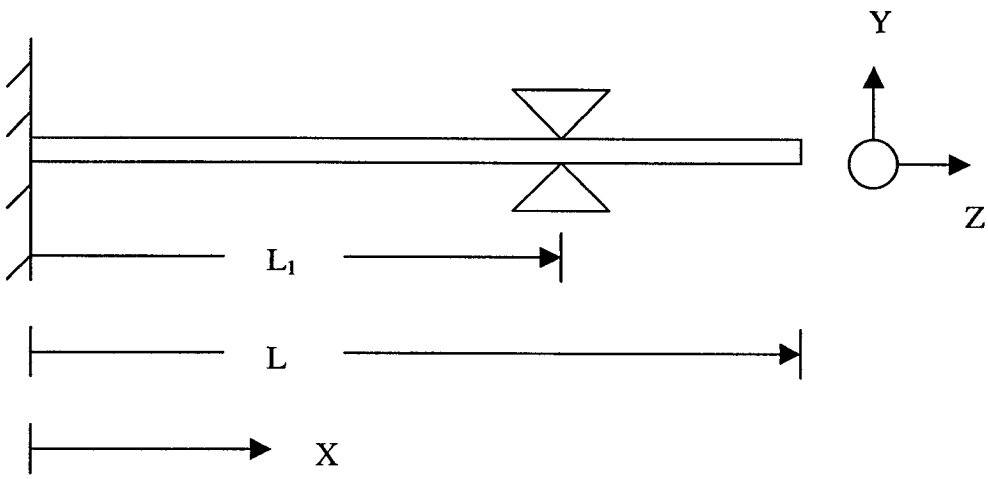


Fig. 2.3: Boring bar assembly.

A mathematical model of the boring bar system is suggested on the basis of the following: First, the boring bar is considered as a continuous beam clamped at the driver end. Second, an intermediate support is provided to the boring bar by the

pressure head and proper type of stuffing box provided at the contact point, so that a simple support condition is assumed at the contact point. The boring bar system will be considered as a multi-span beam as in Fig. 2.3 and the transverse vibrations of the multi-span beam are studied initially. When the boring bar undergoes a transverse vibration, the governing partial differential equation is given by:

$$EI\frac{\partial^4 W_y(X,t)}{\partial X^4}+M\frac{\partial^2 W_y(X,t)}{\partial t^2}=0, \tag{2.1}$$

$$EI\frac{\partial^4 W_z(X,t)}{\partial X^4}+M\frac{\partial^2 W_z(X,t)}{\partial t^2}=0,$$

where,

$M$ , $W_y$ , $W_z$ , respectively are:

$M_1$ , $W_{1y}$ , $W_{1z}$ *in* $0 < X < L_1$

$M_2$ , $W_{2y}$ , $W_{2z}$ *in* $L_1 < X < L$

$M = \frac{\gamma}{g}A$ is the mass per unit length of the boring bar and is assumed to be uniform. EI is the bending rigidity of the material. The solution of the above equation is obtained by the separation of variables technique where we assume:

$$W_y(X,t)=\varsigma_y(X)P_y(t)$$
$$W_z(X,t)=\varsigma_z(X)P_z(t) \tag{2.2}$$

Substituting Eq. (2.2) into Eq. (2.1), the motion in the Y direction results in

$$\varsigma_{jy}''''(X) - \beta^4 \varsigma_{jy}(X) = 0, \quad j = 1,2 \tag{2.3}$$

and

$$\ddot{P}_y(t) + \omega^2 P_y(t) = 0, \tag{2.4}$$

where,

$\beta_i^4 = \dfrac{\omega^2 L_i^4 M_i}{EI}$, $i = 1, 2$ in the two regions.

The solution of Eq. (2.3) for the two regions are expressed as:

$$\varsigma_{1y}(X) = A_1 \cos\beta_1 X + A_2 \sin\beta_1 X + A_3 \cosh\beta_1 X + A_4 \sinh\beta_1 X \qquad 0 < X < L_1 \tag{2.5}$$

$$\varsigma_{2y}(X) = A_5 \cos\beta_2 X + A_6 \sin\beta_2 X + A_7 \cosh\beta_2 X + A_8 \sinh\beta_2 X \qquad L_1 < X < L \tag{2.6}$$

and the solution of Eq. (2.4) is of the form

$$P_y(t) = F\cos\omega t + Q\sin\omega t \tag{2.7}$$

The constants $A_1, A_2, \ldots, A_8$ are evaluated using the following boundary conditions:

$$\varsigma_{1y}(0) = 0.0 \qquad (a) \qquad \varsigma'_{1y}(L_1) = \varsigma'_{2y}(L_1) \qquad (e)$$

$$\varsigma'_{1y}(0) = 0.0, \qquad (b) \qquad \varsigma''_{1y}(L_1) = -\varsigma''_{2y}(L_1) \qquad (f) \qquad (2.8)$$

$$\varsigma_{1y}(L_1) = 0.0 \qquad (c) \qquad \varsigma''_{2y}(L) = 0.0 \qquad (g)$$

$$\varsigma_{2y}(L_1) = 0.0 \qquad (d) \qquad \varsigma'''_{2y}(L) = 0.0 \qquad (h)$$

Substituting the boundary conditions into the equations will end up with 8 equations in terms of the 8 constants $A_i, i = 1,\ldots,8$ as $[C]\{A\} = \{0\}$. The determinant of the coefficient matrix will give us the frequency equation.

$$|C| = \begin{vmatrix} 1 & 0 & 1 & 0 & 0 & 0 & 0 & 0 \\ 0 & 1 & 0 & 1 & 0 & 0 & 0 & 0 \\ c_{31} & c_{32} & c_{33} & c_{34} & 0 & 0 & 0 & 0 \\ 0 & 0 & 0 & 0 & c_{45} & c_{46} & c_{47} & c_{48} \\ -c_{51} & c_{52} & c_{53} & c_{54} & c_{55} & -c_{56} & -c_{57} & -c_{58} \\ -c_{61} & -c_{62} & c_{63} & c_{64} & -c_{65} & -c_{66} & c_{67} & c_{68} \\ 0 & 0 & 0 & 0 & c_{75} & -c_{76} & c_{77} & c_{78} \\ 0 & 0 & 0 & 0 & -c_{85} & -c_{86} & c_{87} & c_{88} \end{vmatrix}$$

where,

$$c_{31} = \cos(\beta_1 L_1), c_{32} = \sin(\beta_1 L_1),\ c_{33} = \cos(\beta_1 L_1),\ c_{34} = \sinh(\beta_1 L_1)$$

$$c_{45} = \cos(\beta_1 L_1), c_{46} = \sin(\beta_1 L_1),\ c_{47} = \cosh(\beta_1 L_1),\ c_{48} = \sinh(\beta_1 L_1)$$

$$c_{51} = -\sin(\beta_1 L_1),\ c_{52} = \cos(\beta_1 L_1),\ c_{53} = \sinh(\beta_1 L_1),\ c_{54} = \cosh(\beta_1 L_1)$$

$$c_{55} = \sin(\beta_1 L_1),\ c_{56} = -\cos(\beta_1 L_1),\ c_{57} = -\sinh(\beta_1 L_1),\ c_{58} = -\cosh(\beta_1 L_1)$$

$$c_{61} = -\cos(\beta_1 L_1), c_{62} = -\sin(\beta_1 L_1), c_{63} = \cosh(\beta_1 L_1), c_{64} = \sinh(\beta_1 L_1)$$

$$c_{65} = -\cos(\beta_1 L_1), c_{66} = -\sin(\beta_1 L_1),\ c_{67} = \cosh(\beta_1 L_1), c_{68} = \sinh(\beta_1 L_1)$$

$$c_{75} = \sin(\beta_2 L), c_{76} = -\cos(\beta_2 L), c_{77} = \sinh(\beta_2 L),\ c_{78} = \cosh(\beta_2 L)$$

$$c_{85} = -\cos(\beta_2 L), c_{86} = -\sin(\beta_2 L), c_{87} = \cosh(\beta_2 L), c_{88} = \sinh(\beta_2 L)$$

In order to get a nontrivial solution the determinant $|C| = 0$. Fig. 2.4 shows a plot of the frequency equation against ($\omega$).

In order to obtain the roots of the frequency equation, and hence the natural frequencies. The following table provides the calculated natural frequencies for the system under study. The first five natural frequencies are presented in table 2.1 at L1=1.25 and L=2.5.

Solution of Eq. (2.3) for the motion in the Z direction will also yield the natural frequencies and normal modes, which are identical to those, obtained above for the Y direction.

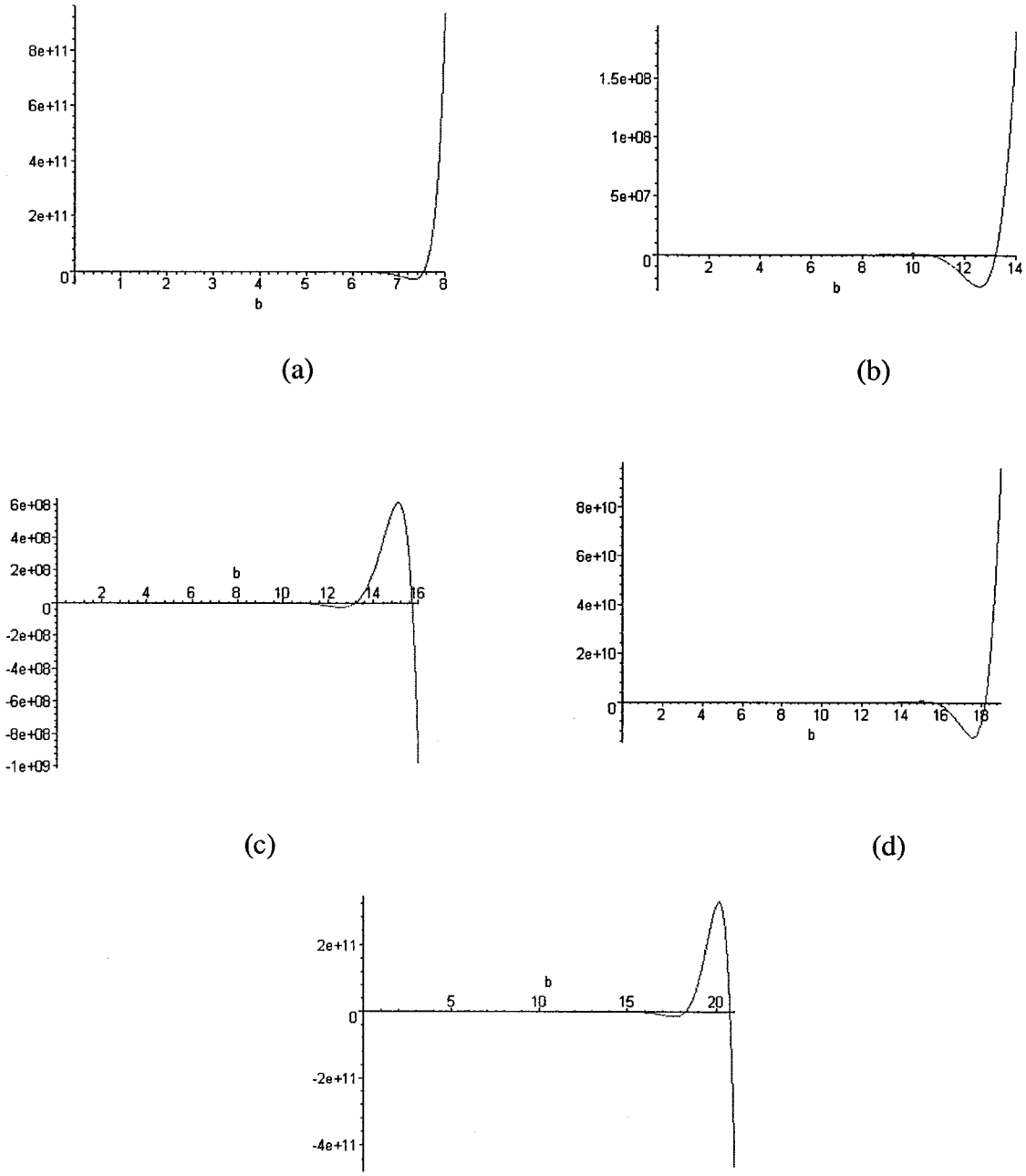


Fig. 2.4: Frequency equation plot with ( $b = \sqrt{\omega_n}$ rad/sec) vs. (Amplitude μm) for the first five roots of the frequency equation.

Table 2.1: The first five natural frequencies of the boring bar system.

| Natural frequency number | $\omega_n$ (Hz) |
|---|---|
| 1 | 9.149 |
| 2 | 27.745 |
| 3 | 39.25 |
| 4 | 52.745 |
| 5 | 69.22 |

## 2.3 Mathematical modeling of the boring bar-workpiece assembly

This model has an intermediate simple support for the boring bar as shown in Fig. 2.5. During the machining process, the interaction point between the cutting tool head and the workpiece is shown in Fig. 2.5. Continuity conditions are assumed for the deflection, slope, and moment at the interaction point, and shear force increases with the addition of the cutting force there.

The boring bar is considered as a continuous beam clamped at the bar driver while the workpiece is clamped at its end. Hence, we can consider the boring bar-workpiece system as a multi-span beam and the transverse vibration of this beam in the Y-Z plane has the following governing partial differential equation in the Y and Z directions as:

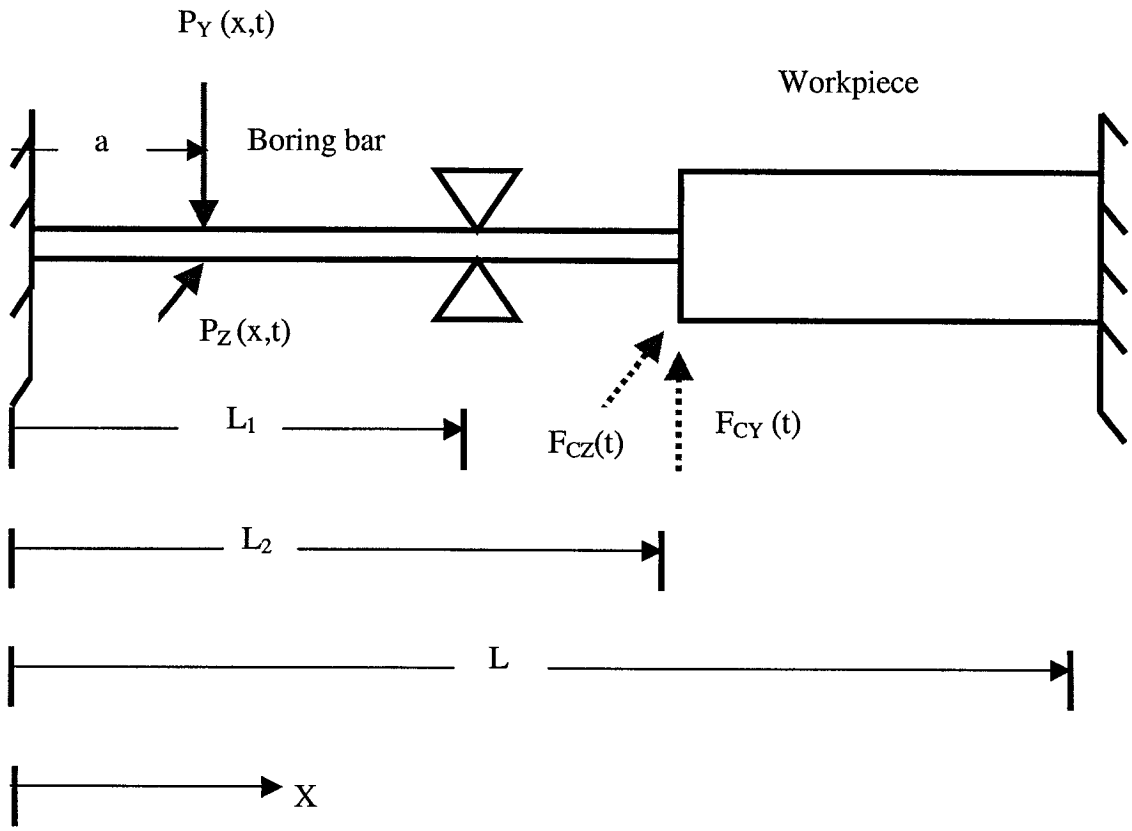


Fig. 2.5: Boring bar-workpiece assembly with the cutting forces and control forces.

$$EI \frac{\partial^4 W_y}{\partial X^4}(X,t) + M \frac{\partial^2 W_y}{\partial t^2}(X,t) = F_y(t) \tag{2.9}$$

and

$$EI \frac{\partial^4 W_z}{\partial X^4}(X,t) + M \frac{\partial^2 W_z}{\partial t^2}(X,t) = F_z(t) \tag{2.10}$$

where:

$I$ , $M$ , $W_y$ , $W_z$ , $F_y$ and $F_z$ , respectively, are:

$I_1, M_1, W_{1y}, W_{1z}, P_y$ and $P_z$, in $0 \langle X \langle L_1$

$I_2, M_2, W_{2y}, W_{2z}, 0$ and $0$, in $L_1 \langle X \langle L_2$

$I_3, M_3, W_{3y}, W_{3z}, 0$ and $0$, in $L_2 \langle X \langle L$

Further,

$$M_1 = \frac{\gamma}{g} A_1$$

$$M_2 = \frac{\gamma}{g} A_2$$

$$M_3 = \frac{\gamma}{g} A_3$$

$$I_1 = \frac{\pi}{64}\left(d_\circ^{\,4} - d_i^{\,4}\right) \quad and \quad A_1 = \frac{\pi}{4}\left(d_\circ^{\,2} - d_i^{\,2}\right) ,$$

$$I_2 = \frac{\pi}{64}\left(d_\circ^{\,4} - d_i^{\,4}\right) \quad and \quad A_2 = \frac{\pi}{4}\left(d_\circ^{\,2} - d_i^{\,2}\right) , \; I_3 = \frac{\pi}{64} d_w^{\,4} \quad and \quad A_3 = \frac{\pi}{4} d_w^{\,2}$$

The boundary conditions are:

$$W_{1y}(0,t)=0.0 \quad \text{(a)} \qquad W'_{2y}(L_2,t) = W'_{3y}(L_2,t) \quad \text{(h)}$$

$$W'_{1y}(0,t)=0.0 \quad \text{(b)} \qquad W''_{2y}(L_2,t) = -W''_{3y}(L_2,t) \quad \text{(i)}$$

$$W_{1y}(L_1,t)=0.0 \quad \text{(c)} \qquad EI_2\, W'''_{2y}(L_2,t) = -EI_3\, W'''_{3y}(L_2,t) - F_{cy}(t) \quad \text{(j)}$$

$$W_{2y}(L_1,t)=0.0 \quad \text{(d)} \qquad W_{3y}(L,t)=0.0 \quad \text{(k)}$$

$$W'_{1y}(L_1,t) = W'_{2y}(L_1,t) \quad \text{(e)} \qquad W'_{3y}(L,t)=0.0 \quad \text{(l)}$$

$$W''_{1y}(L_1,t) = -W''_{2y}(L_1,t) \quad \text{(f)}$$

$$W_{2y}(L_2,t) = W_{3y}(L_2,t) \quad \text{(g)} \qquad (2.11)$$

$$W_{1z}(0,t)=0.0 \quad \text{(a)} \qquad W'_{2z}(L_2,t) = W'_{3z}(L_2,t) \quad \text{(h)}$$

$$W'_{1z}(0,t)=0.0 \quad \text{(b)} \qquad W''_{2z}(L_2,t) = -W''_{3z}(L_2,t) \quad \text{(i)}$$

$$W_{1z}(L_1,t)=0.0 \quad \text{(c)} \qquad EI_2\, W'''_{2z}(L_2,t) = -EI_3\, W'''_{3z}(L_2,t) - F_{cz}(t) \quad \text{(j)}$$

$$W_{2z}(L_1,t)=0.0 \quad \text{(d)} \qquad W_{3z}(L,t)=0.0 \quad \text{(k)}$$

$$W'_{1z}(L_1,t) = W'_{2z}(L_1,t) \quad \text{(e)} \qquad W'_{3z}(L,t)=0.0 \quad \text{(l)}$$

$$W''_{1z}(L_1,t) = -W''_{2z}(L_1,t) \quad \text{(f)}$$

$$W_{2z}(L_2,t) = W_{3z}(L_2,t) \quad \text{(g)} \qquad (2.12)$$

The system is subjected to nonhomogeneous boundary conditions or time-dependent boundary conditions as given in Eqs. (2.11j) and Eqs. (2.12j). A modified approach will be used to transform this problem into a problem consisting of nonhomogeneous

differential equations with homogeneous boundary conditions which will be solved by modal analysis. To this end let us assume a solution of the boundary-value problem described by the equations of motion above in the Y and Z directions in the form:

$$
\begin{aligned}
&W_{1y}(x,t) = v_{1y}(x,t) && 0 < X < L_1 \\
&W_{2y}(x,t) = v_{2y}(x,t) + g_2(x)F_{cy}(t) && L_1 < X < L_2 \\
&W_{3y}(x,t) = v_{3y}(x,t) + g_3(x)F_{cy}(t) && L_2 < X < L \\
&W_{1z}(x,t) = v_{1z}(x,t) && 0 < X < L_1 \\
&W_{2z}(x,t) = v_{2z}(x,t) + g_2(x)F_{cz}(t) && L_1 < X < L_2 \\
&W_{3z}(x,t) = v_{3z}(x,t) + g_3(x)F_{cz}(t) && L_2 < X < L
\end{aligned}
\qquad (2.13), (2.14)
$$

The functions $g_2(x)$ and $g_3(x)$ are chosen to render the boundary conditions for the variables $v_{1y}(x,t), v_{2y}(x,t), v_{3y}(x,t)$ and $v_{1z}(x,t), v_{2z}(x,t), v_{3z}(x,t)$ homogeneous.

The functions $g_2(x)$ and $g_3(x)$ are not unique and several choices may be acceptable [113]. The second step is to introduce the boundary conditions of the current problem into equations (2.13) and (2.14). Consider Eq. (2.11 j):

$$
\rho_2 v_{2y}'''(L_2,t) + v_{3y}'''(L_2,t) = -F_{cy}(t)\left[\rho_2 g_2'''(L_2) + g_3'''(L_2) + \frac{1}{EI_3}\right] \qquad (2.15)
$$

For the right hand side of Eq. (2.15) to be zero:

$$\rho_2 g_2'''(L_2) + g_3'''(L_2) + \frac{1}{EI_3} = 0, \quad \text{or}$$

$$\rho_2 g_2'''(L_2) + g_3'''(L_2) = \frac{-1}{EI_3} \tag{2.16}$$

with the other boundary conditions:

$$g_2(L_1) = 0, \qquad \text{corresponding to (2.3 d)}$$

$$g_2'(L_1) = 0, \qquad \text{corresponding to (2.3 e)}$$

$$g_2''(L_1) = 0, \qquad \text{corresponding to (2.3 f)}$$

$$g_3(L_2) - g_2(L_2) = 0 \qquad \text{corresponding to (2.3 g)}$$

$$g_3'(L_2) - g_2'(L_2) = 0 \qquad \text{corresponding to (2.3 h)}$$

$$g_3''(L_2) + g_2''(L_2) = 0 \qquad \text{corresponding to (2.3 i)}$$

$$g_3(L) = 0, \qquad \text{corresponding to (2.3 k)}$$

$$g_3'(L) = 0 \qquad \text{corresponding to (2.3 l)} \tag{2.17}$$

At this stage let us assume that:

$$g_2'''(X) = D_1 X + D_2 \tag{2.18}$$

Substitute Eq. (2.18) into Eq. (2.16), the following equation is obtained:

$$g_3'''(X) = -\left(\frac{1}{EI_3} + \rho_2 (D_1 X + D_2)\right) \tag{2.19}$$

From Eqs. (2.18) and (2.19) we obtain:

$$g_2(X) = \frac{X^4}{24} D_1 + \frac{X^3}{6} D_2 + \frac{X^2}{2} D_3 + X D_4 + D_5 \tag{2.20}$$

$$g_3(X) = \frac{-X^3}{6EI_3} - \rho_2 \left( \frac{X^4}{24} D_1 + \frac{X^3}{6} D_2 \right) + \frac{X^2}{2} D_6 + X D_7 + D_8 \tag{2.21}$$

where the constants $D_1$ $D_2$ ,$D_3$ ,$D_4$ $D_5$ ,$D_6$ ,$D_7$ $D_8$ are evaluated by applying the set of boundary conditions in Eq. (2.17). The values of these constants are presented in table 2.2.

Table 2.2: Values for the constants of integration for $g_1(x)$ and $g_2(x)$.

| Constant | Value |
|---|---|
| $D_1$ | 0.1723 |
| $D_2$ | -0.4032 |
| $D_3$ | 0.4551 |
| $D_4$ | -0.3339 |
| $D_5$ | 0.1803 |

Table 2: Values for the constants of integration for $g_1(x)$ and $g_2(x)$, (cont'd).

| Constant | Value |
|---|---|
| $D_6$ | 0.0113 |
| $D_7$ | 0.0374 |
| $D_8$ | 0.0571 |

Now introducing Eqs. (2.13) and (2.14) in Eqs. (2.9) and (2.10), respectively, we obtain a set of nonhomogeneous differential equations.

In the Y direction:

$$EI\, v_y''''(x,t) + M\ \ddot{v}_y(x,t) = F_y(t) \tag{2.22}$$

where

$$F_y(t) = P_y(t)\ \delta(x-a) \quad and\ I = I_1,\ M = M_1 \qquad 0 < X < L_1$$

$$= -EI\ g_2''''(x) F_{cy}(t) - M\ g_2(x) \ddot{F}_{cy}(t) \quad and\ I = I_2,\ M = M_2 \qquad L_1 < X < L_2$$

$$= -EI\ g_3''''(x) F_{cy}(t) - M\ g_3(x) \ddot{F}_{cy}(t) \quad and\ I = I_3,\ M = M_3 \qquad L_2 < X < L$$

and in Z direction we have:

$$EI\, v_z''''(x,t) + M\ \ddot{v}_z(x,t) = F_z(t) \tag{2.23}$$

where

$$F_z(t) = P_z(t)\ \delta(x-a) \text{ and } I = I_1,\ M = M_1 \qquad 0\langle X\langle L_1$$

$$= -EI\ g_2''''(x)F_{cz}(t) - M\ g_2(x)\ddot{F}_{cz}(t) \text{ and } I = I_2,\ M = M_2 \qquad L_1\langle X\langle L_2$$

$$= -EI\ g_3''''(x)F_{cz}(t) - M\ g_3(x)\ddot{F}_{cz}(t) \text{ and } I = I_3,\ M = M_3 \qquad L_2\langle X\langle L$$

At this stage we will assume that all the forces equal to zero and solve the homogeneous equations to find the natural frequencies with the corresponding eigen functions for the following system of equations:

$$EI\ v_y''''(x,t) + M\ \ddot{v}_y(x,t) = 0 \tag{2.24}$$

$$EI\ v_z''''(x,t) + M\ \ddot{v}_z(x,t) = 0 \tag{2.25}$$

Under free vibration conditions, we assume:

$$v_y(x,t) = V_y(x)\ e^{i\omega t} \tag{2.26}$$

$$v_z(x,t) = V_z(x)\ e^{i\omega t} \tag{2.27}$$

Consider $\overline{X} = \frac{X}{L}$, then $\frac{d}{dX} = \frac{d}{d\overline{X}}\frac{1}{L}$, and accordingly we have

$$v_y''''(\overline{X}) - \beta^4 v_y(\overline{X}) = 0 \tag{2.28}$$

$$v_z''''(\overline{X}) - \beta^4 v_z(\overline{X}) = 0 \tag{2.29}$$

where,

$$\beta^4 = \frac{\omega^2 M \bar{L}^4}{E I}, \text{ becomes}$$

$$\beta_1^4 = \frac{\omega^2 M_1 \bar{L}_1^4}{E I_1}, \qquad 0 \langle \bar{X} \langle \bar{L}_1$$

$$\beta_2^4 = \frac{\omega^2 M_2 \bar{L}_2^4}{E I_2}, \qquad \bar{L}_1 \langle \bar{X} \langle \bar{L}_2$$

$$\beta_3^4 = \frac{\omega^2 M_3 \bar{L}^4}{E I_3}, \qquad \bar{L}_2 \langle \bar{X} \langle 1$$

$$\bar{L}_1 = \frac{L_1}{L}, \quad \bar{L}_2 = \frac{L_2}{L}, \quad \bar{L} = \frac{L}{L} = 1$$

The solutions in the three regions are:

$$v_{1y}(\bar{x}) = A_1 \cos\beta_1 \bar{X} + A_2 \sin\beta_1 \bar{X} + A_3 \cosh\beta_1 \bar{X} + A_4 \sinh\beta_1 \bar{X}, \quad 0 \langle X \langle \bar{L}_1$$

$$v_{2y}(\bar{x}) = A_5 \cos\beta_2 \bar{X} + A_6 \sin\beta_2 \bar{X} + A_7 \cosh\beta_2 \bar{X} + A_8 \sinh\beta_2 \bar{X}, \; \bar{L}_1 \langle X \langle \bar{L}_2 \qquad (2.30)$$

$$v_{3y}(\bar{x}) = A_9 \cos\beta_3 \bar{X} + A_{10} \sin\beta_3 \bar{X} + A_{11} \cosh\beta_3 \bar{X} + A_{12} \sinh\beta_3 \bar{X}, \; \bar{L}_2 \langle X \langle 1$$

and in the Z direction:

$$v_{1z}(\bar{x}) = B_1 \cos\beta_1 \bar{X} + B_2 \sin\beta_1 \bar{X} + B_3 \cosh\beta_1 \bar{X} + B_4 \sinh\beta_1 \bar{X}, \quad 0 \langle X \langle \bar{L}_1$$

$$v_{2z}(\bar{x}) = B_5 \cos\beta_2 \bar{X} + B_6 \sin\beta_2 \bar{X} + B_7 \cosh\beta_2 \bar{X} + B_8 \sinh\beta_2 \bar{X}, \; \bar{L}_1 \langle X \langle \bar{L}_2 \qquad (2.31)$$

$$v_{3z}(\bar{x}) = B_9 \cos\beta_3 \bar{X} + B_{10} \sin\beta_3 \bar{X} + B_{11} \cosh\beta_3 \bar{X} + B_{12} \sinh\beta_3 \bar{X}, \; \bar{L}_2 \langle X \langle 1$$

Further,

$$\beta_j^4 = \frac{\omega^2 \bar{L}_j^4 M_j}{(E\,I)_j}$$

$$\omega = \left(\frac{\beta_j}{\bar{L}_j}\right)^2 \left[\frac{(EI)_j}{M_j}\right]^{1/2}$$

$$\beta_{1i}^4 = \omega_i^2 \frac{\alpha_1 \lambda_1}{\rho_1} \frac{M_2 \bar{L}_2^4}{(EI)_2},\ \beta_{2i}^4 = \omega_i^2 \frac{M_2 \bar{L}_2^4}{(EI)_2},\ \beta_{3i}^4 = \omega_i^2 \frac{\rho_3 \alpha_1 \lambda_1}{\lambda_3 \alpha_2 \rho_1} \frac{M_2 \bar{L}_2^4}{(EI)_2}$$

or

$$\beta_{1i}^4 = \omega_i^2 C_1 \frac{M_2 \bar{L}_2^4}{(EI)_2},\ \beta_{2i}^4 = \omega_i^2 \frac{M_2 \bar{L}_2^4}{(EI)_2},\ \beta_{3i}^4 = \omega_i^2 C_2 \frac{M_2 \bar{L}_2^4}{(EI)_2}$$

where:

$$\rho_1 = \frac{(EI)_1}{(EI)_2}, \rho_2 = \frac{(EI)_2}{(EI)_3}, \rho_3 = \frac{(EI)_1}{(EI)_3}$$

$$\alpha_1 = \frac{M_1}{M_2}, \alpha_2 = \frac{M_2}{M_3}, \alpha_3 = \frac{M_1}{M_3}, \text{ and } \lambda_1 = \frac{\bar{L}_1^4}{\bar{L}_2^4}, \lambda_2 = \frac{\bar{L}_2^4}{\bar{L}_3^4}, \lambda_3 = \frac{\bar{L}_1^4}{\bar{L}_3^4},$$

$v_{1y}(\bar{X})$, $v_{2y}(\bar{X})$ $\varsigma_{3y}(\bar{X})$ in the Y direction and $v_{1z}(\bar{X})$, $v_{2z}(\bar{X})$ and $v_{3z}(\bar{X})$ in the Z direction have to satisfy the conditions that their respective fourth derivatives are equal to a constant multiplied by the functions. All the constants $A_i$ *and* $B_i, i = 1,\ldots,12$ are evaluated using the following boundary conditions in the Y direction:

$$v_{1y}(0,t) = 0.0 \quad \text{(a)} \qquad v'_{2y}(\bar{L}_2,t) = v'_{3y}(\bar{L}_2,t) \quad \text{(h)}$$

$$v'_{1y}(0,t) = 0.0 \quad \text{(b)} \qquad v''_{2y}(\bar{L}_2,t) = -v''_{3y}(\bar{L}_2,t) \quad \text{(i)}$$

$$v_{1y}(\bar{L}_1,t) = 0.0 \quad \text{(c)} \qquad v'''_{2y}(\bar{L}_2,t) = -v'''_{3y}(\bar{L}_2,t) \quad \text{(j)}$$

$$v_{2y}(\bar{L}_1,t) = 0.0 \quad \text{(d)} \qquad v_{3y}(\bar{L},t) = 0.0 \quad \text{(k)}$$

$$v'_{1y}(\bar{L}_1,t) = v'_{2y}(\bar{L}_1,t) \quad \text{(e)} \qquad v'_{3y}(\bar{L},t) = 0.0 \quad \text{(l)}$$

$$v''_{1y}(\bar{L}_1,t) = -v''_{2y}(\bar{L}_1,t) \quad \text{(f)}$$

$$v_{2y}(\bar{L}_2,t) = v_{3y}(\bar{L}_2,t) \quad \text{(g)} \qquad (2.32)$$

$$v_{1z}(0,t) = 0.0 \quad \text{(a)} \qquad v'_{2z}(\bar{L}_2,t) = v'_{3z}(\bar{L}_2,t) \quad \text{(h)}$$

$$v'_{1z}(0,t) = 0.0 \quad \text{(b)} \qquad v''_{2z}(\bar{L}_2,t) = -v''_{3z}(\bar{L}_2,t) \quad \text{(i)}$$

$$v_{1z}(\bar{L}_1,t) = 0.0 \quad \text{(c)} \qquad v'''_{2z}(\bar{L}_2,t) = -v'''_{3z}(\bar{L}_2,t) \quad \text{(j)}$$

$$v_{2z}(\bar{L}_1,t) = 0.0 \quad \text{(d)} \qquad v_{3z}(\bar{L},t) = 0.0 \quad \text{(k)}$$

$$v'_{1z}(\bar{L}_1,t) = v'_{2z}(\bar{L}_1,t) \quad \text{(e)} \qquad v'_{3z}(\bar{L},t) = 0.0 \quad \text{(l)}$$

$$v''_{1z}(\bar{L}_1,t) = -v''_{2z}(\bar{L}_1,t) \quad \text{(f)}$$

$$v_{2z}(\bar{L}_2,t) = v_{3z}(\bar{L}_2,t) \quad \text{(g)} \qquad (2.33)$$

After obtaining the 12 equations we arrange them in a matrix form with $\overline{L}_1 = 0.559, \overline{L}_2 = 0.842$ *and* $\overline{L} = 1$.

From Eqs. (2.32a) and (2.32b), it is found that $A_1 = -A_3$ and $A_2 = -A_4$, respectively. The same for Eqs. (2.33a) and (2.33b), it is found that $B_1 = -B_3$ and $B_2 = -B_4$, respectively.

These equations are written in the form:

$$[G]_{10\,X\,10}\{A\}_{10\,X\,1} = \{0\} \quad \text{and} \quad [H]_{10\,X\,10}\{B\}_{10\,X\,1} = \{0\} \tag{2.34}$$

For a nontrivial solutions $|G| = 0$ , $|H| = 0$. Any one will give the characteristic equation, where $|G|$ and $|H|$ are the determinant of the coefficient matrices $[G]$ *and* $[H]$ respectively.

$$|Y| = \begin{vmatrix} g_{11} & g_{12} & 0 & 0 & 0 & 0 & 0 & 0 & 0 & 0 \\ g_{21} & g_{22} & -g_{23} & -g_{24} & g_{25} & g_{26} & 0 & 0 & 0 & 0 \\ g_{31} & g_{32} & g_{33} & -g_{34} & -g_{35} & -g_{36} & 0 & 0 & 0 & 0 \\ 0 & 0 & g_{43} & g_{44} & g_{45} & g_{46} & -g_{47} & -g_{48} & -g_{49} & -g_{410} \\ 0 & 0 & -g_{53} & g_{54} & g_{55} & g_{56} & g_{57} & -g_{58} & -g_{59} & -g_{510} \\ 0 & 0 & g_{63} & g_{64} & g_{65} & g_{66} & -g_{67} & -g_{68} & g_{69} & g_{610} \\ 0 & 0 & g_{73} & -g_{74} & g_{75} & g_{76} & g_{77} & -g_{78} & g_{79} & g_{710} \\ 0 & 0 & g_{83} & g_{84} & g_{85} & g_{86} & 0 & 0 & 0 & 0 \\ 0 & 0 & 0 & 0 & 0 & 0 & g_{97} & g_{98} & g_{99} & g_{910} \\ 0 & 0 & 0 & 0 & 0 & 0 & -g_{107} & g_{108} & g_{109} & g_{1010} \end{vmatrix}, \text{ where,}$$

$g_{11} = \cosh(\overline{C}_1 \overline{L}_1 a) - \cos(\overline{C}_1 \overline{L}_1 a)$, $g_{12} = \sinh(\overline{C}_1 L_1 a) - \sin(\overline{C}_1 \overline{L}_1 a)$,

$g_{21} = \cosh(\overline{C}_1 \overline{L}_1 a) + \cos(\overline{C}_1 \overline{L}_1 a)$, $g_{22} = \sin(\overline{C}_1 \overline{L}_1 a) + \sinh(\overline{C}_1 \overline{L}_1 a)$,

$g_{23} = \cos(\overline{C}_2 \overline{L}_1 a)$, $g_{24} = \sin(\overline{C}_2 \overline{L}_1 a)$, $g_{25} = \cosh(\overline{C}_2 \overline{L}_1 a)$,

$g_{26} = \sinh(\overline{C}_2 \overline{L}_1 a)$, $g_{31} = \sinh(\overline{C}_1 \overline{L}_1 a) + \sin(\overline{C}_1 \overline{L}_1 a)$, $g_{32} = \cosh(\overline{C}_1 \overline{L}_1 a) - \cos(\overline{C}_1 \overline{L}_1 a)$,

$g_{33} = \sin(\overline{C}_2 \overline{L}_1 a)$, $g_{34} = \cos(\overline{C}_2 \overline{L}_1 a)$, $g_{35} = \sinh(\overline{C}_2 \overline{L}_1 a)$,

$g_{36} = \cosh(\overline{C}_2 \overline{L}_1 a)$, $g_{43} = \cos(\overline{C}_2 \overline{L}_2 a)$, $g_{44} = \sin(\overline{C}_2 \overline{L}_2 a)$,

$g_{45} = \cosh(\overline{C}_2 \overline{L}_2 a)$, $g_{46} = \sinh(\overline{C}_2 \overline{L}_2 a)$, $g_{47} = \cos(\overline{C}_3 \overline{L}_2 a)$,

$g_{48} = \sin(\overline{C}_3 \overline{L}_2 a)$, $g_{49} = \cosh(\overline{C}_3 \overline{L}_2 a)$, $g_{410} = \sinh(\overline{C}_3 \overline{L}_2 a)$,

$g_{53} = \sin(\overline{C}_2 \overline{L}_2 a)$, $g_{54} = \cos(\overline{C}_2 \overline{L}_2 a)$, $g_{55} = \sinh(\overline{C}_2 \overline{L}_2 a)$,

$g_{56} = \cosh(\overline{C}_2 \overline{L}_2 a)$, $g_{57} = \sin(\overline{C}_3 \overline{L}_2 a)$, $g_{58} = \cos(\overline{C}_3 \overline{L}_2 a)$,

$g_{59} = \sinh(\overline{C}_3 \overline{L}_2 a)$, $g_{510} = \cosh(\overline{C}_3 \overline{L}_2 a)$, $g_{63} = \cos(\overline{C}_2 \overline{L}_2 a)$,

$g_{64} = \sin(\overline{C}_2 \overline{L}_2 a)$, $g_{65} = \cosh(\overline{C}_2 \overline{L}_2 a)$, $g_{66} = \sinh(\overline{C}_2 \overline{L}_2 a)$,

$g_{67} = \cos(\overline{C}_3 \overline{L}_2 a)$, $g_{68} = \sin(\overline{C}_3 \overline{L}_2 a)$, $g_{69} = \cosh(\overline{C}_3 \overline{L}_2 a)$,

$g_{610} = \sinh(\overline{C}_3 \overline{L}_2 a)$, $g_{73} = \sin(\overline{C}_2 \overline{L}_2 a)$, $g_{74} = \cos(\overline{C}_2 \overline{L}_2 a)$,

$g_{75} = \sinh(\overline{C}_2 \overline{L}_2 a)$, $g_{76} = \cosh(\overline{C}_2 \overline{L}_2 a)$, $g_{77} = \sin(\overline{C}_3 \overline{L}_2 a)$,

$g_{78} = \cos(\overline{C}_3 \overline{L}_2 a)$, $g_{79} = \sinh(\overline{C}_3 \overline{L}_2 a)$, $g_{710} = \cosh(\overline{C}_3 \overline{L}_2 a)$,

$$g_{83} = \cos(\bar{C}_2 \bar{L}_1 a),\ g_{84} = \sin(\bar{C}_2 \bar{L}_1 a), g_{85} = \cosh(\bar{C}_2 \bar{L}_1 a),$$

$$g_{86} = \sinh(\bar{C}_2 \bar{L}_1 a),\ g_{97} = \cos(\bar{C}_3 \bar{L} a),\ g_{98} = \sin(\bar{C}_3 \bar{L} r),$$

$$g_{99} = \cosh(\bar{C}_3 \bar{L} a), g_{910} = \sinh(\bar{C}_3 \bar{L} a),\ g_{107} = \sin(\bar{C}_3 \bar{L} a),$$

$$g_{108} = \cos(\bar{C}_3 \bar{L} a),\ a_{109} = \sinh(\bar{C}_3 \bar{L} a),\ a_{1010} = \cosh(\bar{C}_3 \bar{L} a),$$

In the above, the quantities $\bar{C}_i$ are:

$$\bar{C}_1 = \left( C_1 \frac{M_2 \bar{L}_2^4}{(EI)_2} \right)^{1/4},\ \bar{C}_2 = \left( \frac{M_2 \bar{L}_2^4}{(EI)_2} \right)^{1/4},\ \bar{C}_3 = \left( C_2 \frac{M_2 \bar{L}_2^4}{(EI)_2} \right)^{1/4},\ a = \sqrt{\omega_n}$$

Plotting the frequency equation against $a = \sqrt{\omega_n}$ will give us the roots of the frequency equation for the first five natural frequencies of the Cutting Tool-Boring Bar-Workpiece Assembly as shown in Fig. 2.6. Table 2.3 presents the first five natural frequencies.

Table 2.3: The first five natural frequencies of the boring bar-workpiece system.

| Natural frequency number | $\omega_n$ (Hz) |
|---|---|
| 1 | 11.235 |
| 2 | 25.280 |
| 3 | 53.863 |
| 4 | 88.612 |
| 5 | 93.254 |

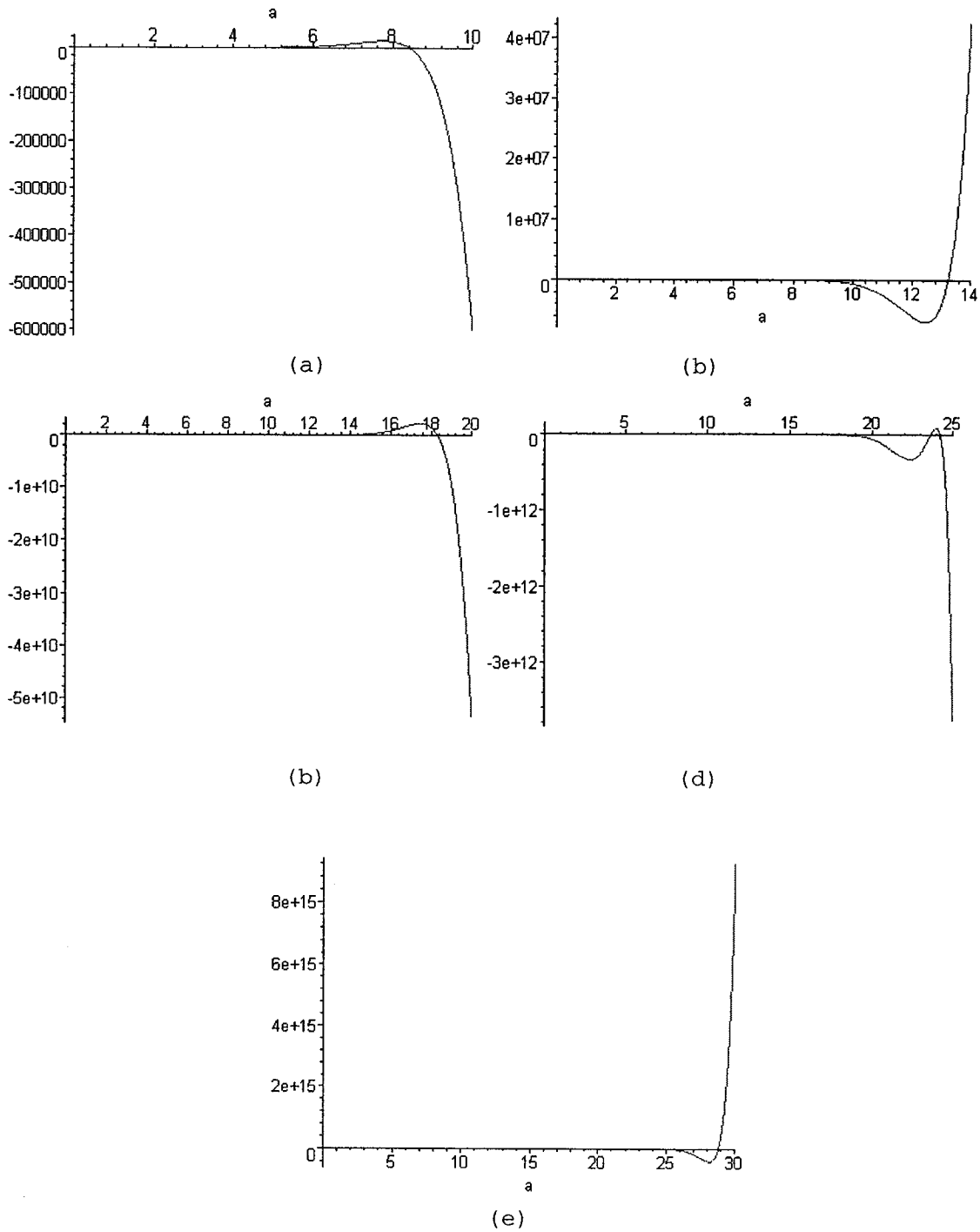


Fig. 2.6: Frequency equation plot with ( $a = \sqrt{\omega_n}$ rad/sec) vs. (Amplitude μm) for the first five roots of the frequency equation.

The normal modes corresponding to these natural frequencies are:

$$v_{1yi}(\bar{x}) = \bar{A}_3(\cosh\beta_{1i}\bar{X} - \cos\beta_{1i}\bar{X}) - \sin\beta_{1i}\bar{X} + \sinh\beta_{1i}\bar{X}$$

$$v_{2yi}(\bar{x}) = \bar{A}_5\cos\beta_{2i}\bar{X} + \bar{A}_6\sin\beta_{2i}\bar{X} + \bar{A}_7\cosh\beta_{2i}\bar{X} + \bar{A}_8\sinh\beta_{2i}\bar{X} \qquad (2.35)$$

$$v_{3yi}(\bar{x}) = \bar{A}_9\cos\beta_{2i}\bar{X} + \bar{A}_{10}\sin\beta_{2i}\bar{X} + \bar{A}_{11}\cosh\beta_{2i}\bar{X} + \bar{A}_{12}\sinh\beta_{2i}\bar{X}$$

$$v_{1zi}(\bar{x}) = \bar{B}_3(\cosh\beta_{1i}\bar{X} - \cos\beta_{1i}\bar{X}) - \sin\beta_{1i}\bar{X} + \sinh\beta_{1i}\bar{X}$$

$$v_{2zi}(\bar{x}) = \bar{B}_5\cos\beta_{2i}\bar{X} + \bar{B}_6\sin\beta_{2i}\bar{X} + \bar{B}_7\cosh\beta_2\bar{X} + \bar{B}_8\sinh\beta_{2i}\bar{X} \qquad (2.36)$$

$$v_{3zi}(\bar{x}) = \bar{B}_9\cos\beta_{3i}\bar{X} + \bar{B}_{10}\sin\beta_{3i}\bar{X} + \bar{B}_{11}\cosh\beta_{3i}\bar{X} + \bar{B}_{12}\sinh\beta_{3i}\bar{X}$$

The values for $\bar{A}_i$ *and* $\bar{B}_i$ , $i = 3,5,...,12$ are presented in Table 2.3.

Table 2.4: The arbitrary constants for the normal modes at the first five natural frequencies.

| | $\omega_1$ | $\omega_2$ | $\omega_3$ | $\omega_4$ | $\omega_5$ |
|---|---|---|---|---|---|
| $\bar{A}_3$ , $\bar{B}_3$ | -0.0908 | -0.2037 | -0.4286 | -0.6893 | -0.7374 |
| $\bar{A}_5$ , $\bar{B}_5$ | 1.5703 | 1.1701 | -0.8996 | 0.0313 | -0.2971 |
| $\bar{A}_6$ , $\bar{B}_6$ | -0.9189 | 1.1507 | -0.3758 | 0.5280 | 0.4780 |
| $\bar{A}_7$ , $\bar{B}_7$ | -2.2355 | -8.1567 | -67.9999 | -662.3000 | -710.7308 |
| $\bar{A}_8$ , $\bar{B}_8$ | 2.8708 | 8.3050 | 68.0048 | 662.3000 | 710.7308 |
| $\bar{A}_9$ , $\bar{B}_9$ | -0.0125 | -0.1034 | -0.4449 | -0.4875 | -0.4726 |
| $\bar{A}_{10}$ , $\bar{B}_{10}$ | 1.8644 | 1.8197 | 1.2021 | 0.3080 | 0.2349 |
| $\bar{A}_{11}$ , $\bar{B}_{11}$ | -0.0054 | -0.0723 | -0.3149 | 0.4626 | 0.7224 |
| $\bar{A}_{12}$ , $\bar{B}_{12}$ | -1.7543 | -1.3410 | -0.2369 | -0.5921 | -0.8355 |

Going back to the main equations in the Y direction:

$$EI\, v_y''''(\bar{x},t) + M\ \ddot{v}_y(\bar{x},t) = F_y(t) \tag{2.37}$$

where

$$F_y(t) = P_y(t)\ \delta(\bar{x}-\bar{a}) \text{ and } I = I_1,\ M = M_1 \qquad 0 \langle \bar{X} \langle \bar{L}_1$$

$$= -EI\ g_2''''(\bar{x}) F_{cy}(t) - M\ g_2(\bar{x}) \ddot{F}_{cy}(t) \text{ and } I = I_2,\ M = M_2 \qquad \bar{L}_1 \langle \bar{X} \langle \bar{L}_2$$

$$= -EI\ g_3''''(\bar{x}) F_{cy}(t) - M\ g_3(\bar{x}) \ddot{F}_{cy}(t) \text{ and } I = I_3,\ M = M_3 \qquad \bar{L}_2 \langle \bar{X} \langle 1$$

and in Z direction we have:

$$EI\, v_z''''(\bar{x},t) + M\ \ddot{v}_z(\bar{x},t) = F_z(t) \tag{2.38}$$

where

$$F_z(t) = P_z(t)\ \delta(\bar{x}-\bar{a}) \text{ and } I = I_1,\ M = M_1 \qquad 0 \langle \bar{X} \langle \bar{L}_1$$

$$= -EI\ g_2''''(\bar{x}) F_{cz}(t) - M\ g_2(\bar{x}) \ddot{F}_{cz}(t) \text{ and } I = I_2,\ M = M_2 \qquad \bar{L}_1 \langle \bar{X} \langle \bar{L}_2$$

$$= -EI\ g_3''''(\bar{x}) F_{cz}(t) - M\ g_3(\bar{x}) \ddot{F}_{cz}(t) \text{ and } I = I_3,\ M = M_3 \qquad \bar{L}_2 \langle \bar{X} \langle 1$$

In order to solve the nonhomogeneous differential Eq. (2.37) and Eq. (2.38), assume the solution in terms of normal modes:

$$v_y(\bar{x},t)=\sum_{n=1}^{\infty} v_{yn}(\bar{x})\eta_{yn}(t)$$

$$v_z(\bar{x},t)=\sum_{n=1}^{\infty} v_{zn}(\bar{x})\eta_{zn}(t) \tag{2.39}$$

Introduce Eq. (2.39) into Eq. (2.37) in the Y direction we obtain:

$$\sum_{n=1}^{\infty}\left(\eta_{yn}(t)v''''_{yn}(\bar{x})+\ddot{\eta}_{yn}(t)\frac{M}{EI}v_{yn}(\bar{x})\right)=F_y(t) \tag{2.40}$$

where

$$F_y(t)=\frac{P_y(t)\ \delta(\bar{x}-\bar{a})}{EI}\ \text{and } I=I_1,\ M=M_1 \qquad 0\langle\bar{X}\langle\bar{L}_1$$

$$=-EI\ g_2''''(\bar{x})F_{cy}(t)-M\ g_2(\bar{x})\ddot{F}_{cy}(t)\ \text{and } I=I_2,\ M=M_2 \qquad \bar{L}_1\langle\bar{X}\langle\bar{L}_2$$

$$=-EI\ g_3''''(\bar{x})F_{cy}(t)-M\ g_3(\bar{x})\ddot{F}_{cy}(t)\ \text{and } I=I_3,\ M=M_3 \qquad \bar{L}_2\langle\bar{X}\langle 1$$

and introduce Eq. (2.39) into Eq. (2.38) in the Z direction, we obtain:

$$\sum_{n=1}^{\infty}\left(\eta_{zn}(t)v''''_{zn}(\bar{x})+\ddot{\eta}_{zn}(t)\frac{M}{EI}v_{zn}(\bar{x})\right)=F_z(t) \tag{2.41}$$

where

$$F_z(t) = \frac{P_z(t)\ \delta(\bar{x}-\bar{a})}{EI} \quad \text{and } I = I_1,\ M = M_1 \qquad 0 \langle \bar{X} \langle \bar{L}_1$$

$$= -EI\ g_2''''(\bar{x}) F_{cz}(t) - M\ g_2(\bar{x}) \ddot{F}_{cz}(t) \text{ and } I = I_2,\ M = M_2 \quad \bar{L}_1 \langle \bar{X} \langle \bar{L}_2$$

$$= -EI\ g_3''''(\bar{x}) F_{cz}(t) - M\ g_3(\bar{x}) \ddot{F}_{cz}(t) \text{ and } I = I_3,\ M = M_3 \quad \bar{L}_2 \langle \bar{X} \langle 1$$

and since $v_{1yn}(\bar{x}), v_{2yn}(\bar{x}), v_{3yn}(\bar{x})$ and $v_{1zn}(\bar{x}), v_{2zn}(\bar{x}), v_{3zn}(\bar{x})$ and $\omega_n$ satisfies Eqs. (2.28) and (2.29), Eqs. (2.40) and (2.41) can be written as, first in the Y direction:

$$\sum_{n=1}^{\infty} \left( \left( \ddot{\eta}_{yn}(t) + \omega_n^2 \eta_{yn}(t) \right) \frac{M}{EI} v_{yn}(\bar{x}) \right) = F_y(t) \tag{2.42}$$

where

$$F_y(t) = \frac{P_y(t)\ \delta(\bar{x}-\bar{a})}{EI} \text{ and } I = I_1,\ M = M_1 \qquad 0 \langle \bar{X} \langle \bar{L}_1$$

$$= -\left[ g_2''''(\bar{x}) F_{cy}(t) + \frac{M}{EI} g_2(\bar{x}) \ddot{F}_{cy}(t) \right] \text{ and } I = I_2,\ M = M_2 \quad \bar{L}_1 \langle \bar{X} \langle \bar{L}_2$$

$$= -\left[ g_3''''(\bar{x}) F_{cy}(t) + \frac{M}{EI} g_3(\bar{x}) \ddot{F}_{cy}(t) \right] \text{ and } I = I_3,\ M = M_3 \quad \bar{L}_2 \langle \bar{X} \langle 1$$

and in the Z direction:

$$\sum_{n=1}^{\infty} \left( \left( \ddot{\eta}_{zn}(t) + \omega_n^2 \eta_{zn}(t) \right) \frac{M}{EI} v_{zn}(\bar{x}) \right) = F_z(t) \tag{2.43}$$

where,

$$F_z(t) = \frac{P_z(t)\ \delta(\bar{x}-\bar{a})}{EI} \quad \text{and } I = I_1,\ M = M_1 \qquad 0 \langle \bar{X} \langle \bar{L}_1$$

$$= -\left[ g_2''''(\bar{x}) F_{cz}(t) + \frac{M}{EI} g_2(\bar{x}) \ddot{F}_{cz}(t) \right] \quad \text{and } I = I_2,\ M = M_2 \quad \bar{L}_1 \langle \bar{X} \langle \bar{L}_2$$

$$= -\left[ g_3''''(\bar{x}) F_{cz}(t) + \frac{M}{EI} g_3(\bar{x}) \ddot{F}_{cz}(t) \right] \quad \text{and } I = I_3,\ M = M_3 \quad \bar{L}_2 \langle \bar{X} \langle 1$$

To find the solution in the three regions, we have to uncouple these equations using the orthogonal property and integrate with respect to $\bar{X}$ over the domain. The orthogonal property is as follows:

$$\int_0^{\bar{L}_1} v_{1yn}(\bar{x}) v_{1ym}(\bar{x})\, d\bar{x} + \int_{\bar{L}_1}^{\bar{L}_2} v_{2yn}(\bar{x}) v_{2ym}(\bar{x})\, d\bar{x} + \int_{\bar{L}_2}^{1} v_{3yn}(\bar{x}) v_{3ym}(\bar{x})\, d\bar{x} = \alpha_{nm}, \text{if } m = n$$

$$\int_0^{\bar{L}_1} v_{1yn}(\bar{x}) v_{1ym}(\bar{x})\, d\bar{x} + \int_{\bar{L}_1}^{\bar{L}_2} v_{2yn}(\bar{x}) v_{2ym}(\bar{x})\, d\bar{x} + \int_{\bar{L}_2}^{1} v_{3yn}(\bar{x}) v_{3ym}(\bar{x})\, d\bar{x} = 0, \text{ if } m \neq n$$

$$\int_0^{\bar{L}_1} v_{1zn}(\bar{x}) v_{1zm}(\bar{x})\, d\bar{x} + \int_{\bar{L}_1}^{\bar{L}_2} v_{2zn}(\bar{x}) v_{2zm}(\bar{x})\, d\bar{x} + \int_{\bar{L}_2}^{1} v_{3zn}(\bar{x}) v_{3zm}(\bar{x})\, d\bar{x} = \alpha_{nm}, \text{if } m = n$$

$$\int_0^{\bar{L}_1} v_{1zn}(\bar{x}) v_{1zm}(\bar{x})\, d\bar{x} + \int_{\bar{L}_1}^{\bar{L}_2} v_{2zn}(\bar{x}) v_{2zm}(\bar{x})\, d\bar{x} + \int_{\bar{L}_2}^{1} v_{3zn}(\bar{x}) v_{3zm}(\bar{x})\, d\bar{x} = 0, \text{ if } m \neq n$$

Hence, we obtain an infinite set of uncoupled ordinary differential equations in Y direction for the three regions of the beam:

$$\ddot{\eta}_{yi}(t)+2\varsigma\beta_{1i}^2\eta_{yi}(t)+\beta_{1i}^4\eta_{yi}(t)=N_{yi}(t)$$

$$\ddot{\eta}_{yi}(t)+2\varsigma\beta_{2i}^2\dot{\eta}_{yi}(t)+\beta_{2i}^4\eta_{yi}(t)=N_{yi}(t) \qquad (2.44)$$

$$\ddot{\eta}_{yi}(t)+2\varsigma\beta_{3i}^2\dot{\eta}_{yi}(t)+\beta_{3i}^4\eta_{yi}(t)=N_{yi}(t)$$

Similarly in Z direction:

$$\ddot{\eta}_{zi}(t)+2\varsigma\beta_{1i}^2\eta_{zi}(t)+\beta_{1i}^4\eta_{zi}(t)=N_{zi}(t)$$

$$\ddot{\eta}_{zi}(t)+2\varsigma\beta_{2i}^2\dot{\eta}_{zi}(t)+\beta_{2i}^4\eta_{zi}(t)=N_{zi}(t) \qquad (2.45)$$

$$\ddot{\eta}_{zi}(t)+2\varsigma\beta_{3i}^2\dot{\eta}_{zi}(t)+\beta_{3i}^4\eta_{zi}(t)=N_{zi}(t)$$

where,

$$N_{yi}(t)=F_y(t)\left[\int_0^{\bar{L}_1} v_{1yi}(\bar{x})\,d\bar{x}+\int_{\bar{L}_1}^{\bar{L}_2} v_{2yi}(\bar{x})\,d\bar{x}+\int_{\bar{L}_2}^{1} v_{3yi}(\bar{x})\,d\bar{x}\right]$$

$$N_{zi}(t)=F_z(t)\left[\int_0^{\bar{L}_1} v_{1zi}(\bar{x})\,d\bar{x}+\int_{\bar{L}_1}^{\bar{L}_2} v_{2zi}(\bar{x})\,d\bar{x}+\int_{\bar{L}_2}^{1} v_{3zi}(\bar{x})\,d\bar{x}\right]$$

$$F_y(t)=\frac{1}{EI}v_{1yi}(\bar{a})P_y(t) \text{ and } I=I_1,\ M=M_1 \qquad 0\langle\bar{X}\langle\bar{L}_1$$

$$=-\left[G_{2yi}^{*}F_{cy}(t)+G_{2yi}\ddot{F}_{cy}(t)\right] \text{ and } I=I_2,\ M=M_2 \qquad \bar{L}_1\langle\bar{X}\langle\bar{L}_2$$

$$=-\left[G_{3yi}^{*}F_{cy}(t)+G_{3yi}\ddot{F}_{cy}(t)\right] \text{ and } I=I_3,\ M=M_3 \qquad \bar{L}_2\langle\bar{X}\langle 1$$

$$F_z(t) = \frac{1}{EI} v_{1zi}(\bar{a}) P_z(t) \quad \text{and } I = I_1,\ M = M_1 \qquad 0 \langle \bar{X} \langle \bar{L}_1$$

$$= -\left[G^*_{2zi} F_{cy}(t) + G_{2zi} \ddot{F}_{cz}(t)\right] \text{ and } I = I_2,\ M = M_2 \qquad \bar{L}_1 \langle \bar{X} \langle \bar{L}_2$$

$$= -\left[G^*_{3zi} F_{cz}(t) + G_{3zi} \ddot{F}_{cz}(t)\right] \text{ and } I = I_3,\ M = M_3 \qquad \bar{L}_2 \langle \bar{X} \langle 1$$

Further,

$$G^*_{2yi} = \int_{\bar{L}_1}^{\bar{L}_2} v_{2yi}(\bar{x}) g_2''''(\bar{x}) d\bar{x}$$

$$G_{2yi} = \int_{\bar{L}_1}^{\bar{L}_2} v_{2yi}(\bar{x}) \frac{M_2}{EI_2} g_2(\bar{x}) d\bar{x}$$

$$G^*_{3yi} = \int_{\bar{L}_2}^{1} v_{3yi}(\bar{x}) g_3''''(\bar{x}) d\bar{x}$$

$$G_{3yi} = \int_{\bar{L}_2}^{1} v_{3yi}(\bar{x}) \frac{M_3}{EI_3} g_3(\bar{x}) d\bar{x}$$

$$G^*_{2zi} = \int_{\bar{L}_1}^{\bar{L}_2} v_{2zi}(\bar{x}) g_2''''(\bar{x}) d\bar{x}$$

$$G_{2zi} = \int_{\bar{L}_1}^{\bar{L}_2} v_{2zi}(\bar{x}) \frac{M_2}{EI_2} g_2(\bar{x}) d\bar{x}$$

$$G^*_{3zi} = \int_{\bar{L}_2}^{1} v_{3zi}(\bar{x}) g_3''''(\bar{x}) d\bar{x}$$

$$G_{3zi} = \int_{\bar{L}_2}^{1} v_{3zi}(\bar{x}) \frac{M_3}{EI_3} g_3(\bar{x}) d\bar{x}$$

$$P_y(t) = P_{0y} \cos(\omega t + \theta)$$

$$P_z(t) = P_{0z} \sin(\omega t + \theta)$$

$$F_{cy}(t) = \bar{F}_c + F_{c0} \cos(\omega t)$$

$$F_{cz}(t) = \bar{F}_c + F_{c0} \sin(\omega t)$$

At this time it is assumed that there are no external forces, i.e., $P_y(t) = P_z(t) = 0$, before applying the active suppression forces. The solution will be given only for the self-excited motion of the boring bar-workpiece system. A continuation of the model with the active control forces is presented in chapter 6. The force terms will be in the form of:

$$F_y(t) = 0 \quad \text{and } I = I_1, M = M_1 \qquad 0 \langle \bar{X} \langle \bar{L}_1$$

$$= -\left[G^*_{2yi} F_{cy}(t) + G_{2yi} \ddot{F}_{cy}(t)\right] \quad \text{and } I = I_2, M = M_2 \qquad \bar{L}_1 \langle \bar{X} \langle \bar{L}_2$$

$$= -\left[G^*_{3yi} F_{cy}(t) + G_{3yi} \ddot{F}_{cy}(t)\right] \quad \text{and } I = I_3, M = M_3 \qquad \bar{L}_2 \langle \bar{X} \langle 1$$

$$F_z(t) = 0 \quad \text{and } I = I_1, M = M_1 \qquad 0 \langle \bar{X} \langle \bar{L}_1$$

$$= -\left[G^*_{2zi} F_{cy}(t) + G_{2zi} \ddot{F}_{cz}(t)\right] \quad \text{and } I = I_2, M = M_2 \qquad \bar{L}_1 \langle \bar{X} \langle \bar{L}_2$$

$$= -\left[G^*_{3zi} F_{cz}(t) + G_{3zi} \ddot{F}_{cz}(t)\right] \quad \text{and } I = I_3, M = M_3 \qquad \bar{L}_2 \langle \bar{X} \langle 1$$

The solution for the set of equations in Y direction Eqs. (2.44) and (2.45) will be done by the convolution integral or superposition integral. It is based on the superposition of the responses of the system to a sequence of impulses. Let the variable of integration is ($\tau$) between the limits of integration (0) and (t) and the elemental impulse is $N_n(\tau)\, d\tau$. So the complete solution for these equations with zero initial conditions is:

$$\eta_{yi}(t) = \left( \frac{1}{\omega_i} \int_0^t N_{yi}(\tau) e^{-\varsigma w_i (t-\tau)} \sin \omega_i (t-\tau) d\tau \right)$$

$$\eta_{zi}(t) = \left( \frac{1}{\omega_i} \int_0^t N_{zi}(\tau) e^{-\varsigma w_i (t-\tau)} \sin \omega_i (t-\tau) d\tau \right) \qquad (2.46)$$

The complete solution for the current problem is as follows:

$$W_{1y}(\bar{x},t) = \sum_{i=1}^{\infty} v_{1yi}(\bar{x}) \left( \frac{1}{\omega_i} \int_0^t N_{yi}(\tau) e^{-\varsigma w_i (t-\tau)} \sin \omega_i (t-\tau) d\tau \right) \qquad 0 < \bar{X} < \bar{L}_1$$

$$W_{2y}(\bar{x},t) = \sum_{i=1}^{\infty} v_{2yi}(\bar{x}) \left( \frac{1}{\omega_i} \int_0^t N_{yi}(\tau) e^{-\varsigma w_i (t-\tau)} \sin \omega_i (t-\tau) d\tau \right)$$

$$+ g_2(\bar{x}) F_{cy}(t) \qquad \bar{L}_1 < \bar{X} < \bar{L}_2$$

$$W_{3y}(\bar{x},t) = \sum_{n=1}^{\infty} v_{3yi}(\bar{x}) \left( \frac{1}{\omega_i} \int_0^t N_{yi}(\tau) e^{-\varsigma w_i (t-\tau)} \sin \omega_i (t-\tau) d\tau \right)$$

$$+ g_3(\bar{x}) F_{cy}(t) \qquad \bar{L}_2 < \bar{X} < 1$$

and in the Z direction

$$W_{1z}(\bar{x},t)=\sum_{i=1}^{\infty} v_{1zi}(\bar{x})\left(\frac{1}{\omega_i}\int_0^t N_{zi}(\tau)e^{-\varsigma w_i(t-\tau)}\sin\omega_i(t-\tau)d\tau\right) \qquad 0\langle \bar{X}\langle \bar{L}_1$$

$$W_{2z}(\bar{x},t)=\sum_{i=1}^{\infty} v_{2zi}(\bar{x})\left(\frac{1}{\omega_i}\int_0^t N_{zi}(\tau)e^{-\varsigma w_i(t-\tau)}\sin\omega_i(t-\tau)d\tau\right)$$

$$+ g_2(\bar{x})F_{cz}(t) \qquad \bar{L}_1\langle \bar{X}\langle \bar{L}_2$$

$$W_{3z}(\bar{x},t)=\sum_{n=1}^{\infty} v_{3zi}(\bar{x})\left(\frac{1}{\omega_i}\int_0^t N_{zi}(\tau)e^{-\varsigma w_i(t-\tau)}\sin\omega_i(t-\tau)d\tau\right)$$

$$+ g_3(\bar{x})F_{cz}(t) \qquad \bar{L}_2\langle \bar{X}\langle 1$$

Substituting the forces in the solution in the Y directions:

$$W_{1y}(\bar{x},t)=\sum_{i=1}^{\infty} v_{1yi}(\bar{x})\left(\frac{1}{\omega_i}\int_0^t \begin{pmatrix} -\left[G^*_{2yi}F_{cy}(\tau)+G_{2yi}\ddot{F}_{cy}(\tau)\right] \\ -\left[G^*_{3yi}F_{cy}(\tau)+G_{3yi}\ddot{F}_{cy}(\tau)\right] \end{pmatrix} e^{-\varsigma w_i(t-\tau)}\sin\omega_i(t-\tau)d\tau\right),$$

in the range of $0\langle \bar{X}\langle \bar{L}_1$

$$W_{2y}(\bar{x},t)=\sum_{i=1}^{\infty} v_{2yi}(\bar{x})\left(\frac{1}{\omega_i}\int_0^t \begin{pmatrix} -\left[G^*_{2yi}F_{cy}(\tau)+G_{2yi}\ddot{F}_{cy}(\tau)\right] \\ -\left[G^*_{3yi}F_{cy}(\tau)+G_{3yi}\ddot{F}_{cy}(\tau)\right] \end{pmatrix} e^{-\varsigma w_i(t-\tau)}\sin\omega_i(t-\tau)d\tau\right),$$

$$+ g_2(\bar{x})F_{cy}(t)\text{, in the range of } \bar{L}_1\langle \bar{X}\langle \bar{L}_2$$

$$W_{3y}(\bar{x},t)=\sum_{i=1}^{\infty} v_{3yi}(\bar{x})\left(\frac{1}{\omega_i}\int_0^t \begin{pmatrix} -\left[G^*_{2yi}F_{cy}(\tau)+G_{2yi}\ddot{F}_{cy}(\tau)\right] \\ -\left[G^*_{3yi}F_{cy}(\tau)+G_{3yi}\ddot{F}_{cy}(\tau)\right] \end{pmatrix} e^{-\varsigma w_i(t-\tau)}\sin\omega_i(t-\tau)d\tau\right),$$

$$+ g_3(\bar{x})F_{cy}(t),\quad \text{in the range of } \bar{L}_2\langle \bar{X}\langle 1$$

And in the Z direction :

$$W_{1z}(\bar{x},t)=\sum_{i=1}^{\infty}v_{1zi}(\bar{x})\left(\frac{1}{\omega_i}\int_0^t\begin{pmatrix}-\left[G^*_{2zi}F_{cz}(\tau)+G_{2zi}\ddot{F}_{cz}(\tau)\right]\\ \\ -\left[G^*_{3zi}F_{cz}(\tau)+G_{3zi}\ddot{F}_{cz}(\tau)\right]\end{pmatrix}e^{-\varsigma w_i(t-\tau)}\sin\omega_i(t-\tau)d\tau\right),$$

in the range of $0\langle\bar{X}\langle\bar{L}_1$

$$W_{2z}(\bar{x},t)=\sum_{i=1}^{\infty}v_{2zi}(\bar{x})\left(\frac{1}{\omega_i}\int_0^t\begin{pmatrix}-\left[G^*_{2zi}F_{cz}(\tau)+G_{2zi}\ddot{F}_{cz}(\tau)\right]\\ \\ -\left[G^*_{3zi}F_{cz}(\tau)+G_{3zi}\ddot{F}_{cz}(\tau)\right]\end{pmatrix}e^{-\varsigma w_i(t-\tau)}\sin\omega_i(t-\tau)d\tau\right),$$

$+g_2(\bar{x})F_{cz}(t)$, in the range of $\bar{L}_1\langle\bar{X}\langle\bar{L}_2$

$$W_{3z}(\bar{x},t)=\sum_{i=1}^{\infty}v_{3zi}(\bar{x})\left(\frac{1}{\omega_i}\int_0^t\begin{pmatrix}-\left[G^*_{2zi}F_{cz}(\tau)+G_{2zi}\ddot{F}_{cz}(\tau)\right]\\ \\ -\left[G^*_{3zi}F_{cz}(\tau)+G_{3zi}\ddot{F}_{cz}(\tau)\right]\end{pmatrix}e^{-\varsigma w_i(t-\tau)}\sin\omega_i(t-\tau)d\tau\right),$$

$+g_3(\bar{x})F_{cz}(t)$, in the range of $\bar{L}_2\langle\bar{X}\langle 1$

In order to arrive to the final formula for the solution, the integrals in Appendix A are used:

The first and fourth integral formulas will be used in chapter 6, which corresponds to the control force of electrodynamic shaker. It is seen from those integrals that the final solution will have a transient and steady state solution. The transient solution will die out after a while, and we are interested in the steady state solution of the current problem. The steady state solution for the self-excited motion at $\omega = 60$ rad/sec below the first natural frequency, is plotted in Fig. 2.7 and 2.8. Fig. 2.7 and 2.8 show a plot of the Y and Z signals for the boring bar-workpiece system and the whirl motion at $\bar{L}_1 = 0.41$ respectively. Fig. 2.9 is a one-figure plot of the system at $\bar{L}_1 = 0.41$, $\bar{L}_2 = 0.81$ and $\bar{L} = 0.91$.

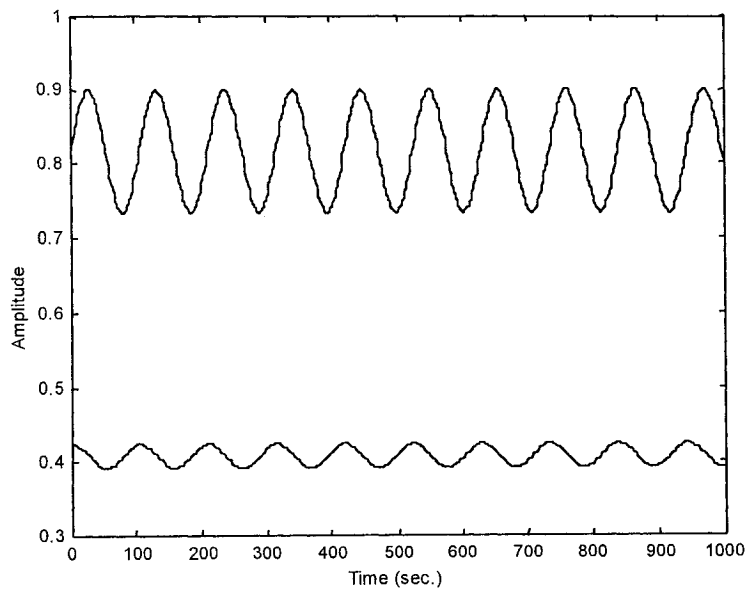


Fig. 2.7: The Y (___) and Z (.....) signals for the boring bar-workpiece system at $\omega = 60$ rad/sec in $0 < \bar{X} < \bar{L}_1$ at $\bar{L}_1 = 0.41$.

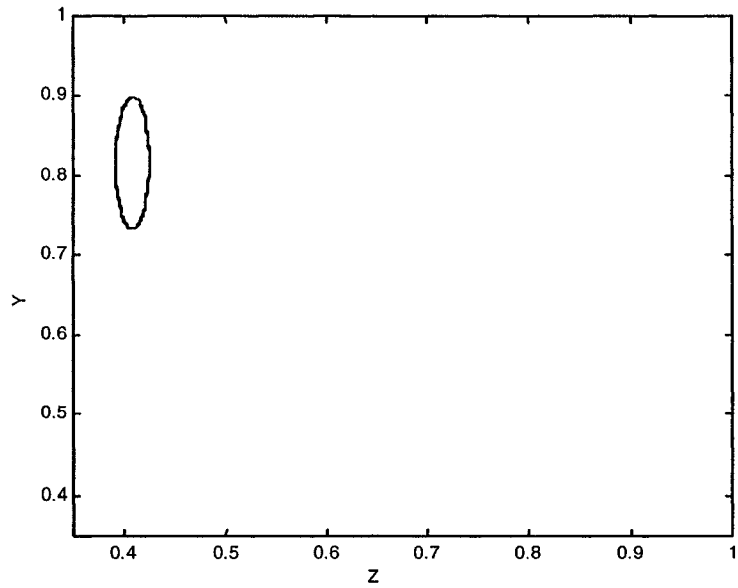


Fig. 2.8: The whirl motion for the boring bar-workpiece system in $0\langle \overline{X}\langle \overline{L}_1$ at $\overline{L}_1 = 0.41$.

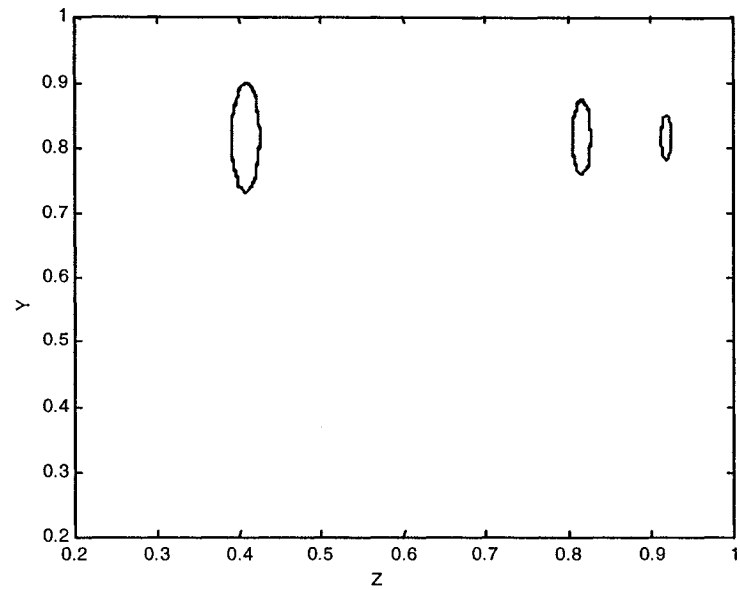


Fig. 2.9: The Z and Y signals for the boring bar-workpiece system in $0\langle \overline{X}\langle \overline{L}_1$, $\overline{L}_1\langle \overline{X}\langle \overline{L}_2$ and $\overline{L}_2\langle \overline{X}\langle 1$ at $\overline{L}_1 = 0.41$, $\overline{L}_2 = 0.81$ and $\overline{L} = 0.91$. respectively.

In this chapter, an analytical model is developed for the boring bar-workpiece system that includes the excitation and the control forces. The model considered the dynamics of the deep hole boring system based on a self-excited motion of the system. In the following, chapter 3 will show the experimental set up and the results to verify the mathematical model.

# CHAPTER 3

# EXPERIMENTAL MEASUREMENT OF WHIRLING MOTION IN DEEP HOLE BORING PROCESS

In the previous chapter, a complete mathematical model for the boring bar-workpiece system was established including the external forces acting upon the system. The model was able to predict the whirl motion at any section of the boring bar-workpiece system. In this chapter, whirling vibrations in deep hole machining process are measured experimentally. Three parts of experiment were carried out at low, medium and high rotational speeds. The first experiment was for the boring bar alone, the second experiment was drilling with feed rate and the third one was with the cutting parameters varied while drilling.

## 3.1 Experimental set-up, Description and Instruments:

The whirling motion of deep hole boring-cutting head system is investigated experimentally. None of the previous studies concerning vibrations and chatter in the deep hole boring system dealt with the whirling vibrations of the boring bar-cutting head system, at the initial stage of drilling operations and during the machining process. Non-contacting type proximity pickups were used to measure the whirling motion of the boring bar. An electronic package with labview software was used to obtain the whirl

orbit of the boring bar as shown in Fig. 3.1, 3.2 and 3.3. The labview program and the specifications of the sensors are given in appendix A. The experiments were conducted to validate the analytical predictions of whirling vibrations of the rotating boring bar-cutting head system described in chapter 2. The boring bar is a flexible circular, hollow shaft, clamped at one end and simply supported by the stuffing box in the middle and the other end is coupled with the workpiece to be bored. It is driven by a variable speed motor to control the speed of cut. Two non-contacting type displacement transducers, (Master for vertical displacement and Slave for the horizontal displacement) which operate using eddy current principle, are used to measure whirl amplitudes. The whirl orbit was detected using data acquisition system (DAQ) along with labview computer software.

### 3.1.1 Displacement transducers

The proximity pickups or the non-contacting displacement transducers are used to measure the transverse motion of the boring bar (displacement along Y and Z directions). As the boring bar rotates relative to the sensors during the boring process, the eddy current developed starts modulating the oscillator voltage signal which is demodulated to provide an output signal proportional to the displacement. This displacement signal can be recorded and analyzed. The output of this transducer is a time varying continuous voltage analogous to the quantity being measured and a scale factor or a calibration constant will determine the value of the measured quantity. This will be discussed in the next section.

Kaman Instrumentation Displacement Measuring System Model KD-2310 was used to make the precision non-contact displacement measurements in the experiment. The system includes a sensor, a 3 m coaxial cable and a signal conditioning electronics package. This system uses the principle of impedance variation caused by eddy currents induced in a conductive metal target.

The coupling between a coil in the sensor and a target is dependent upon their displacement or the gap between them. The output voltage of the system is proportional to the distance between the face of the sensor and any metallic target.

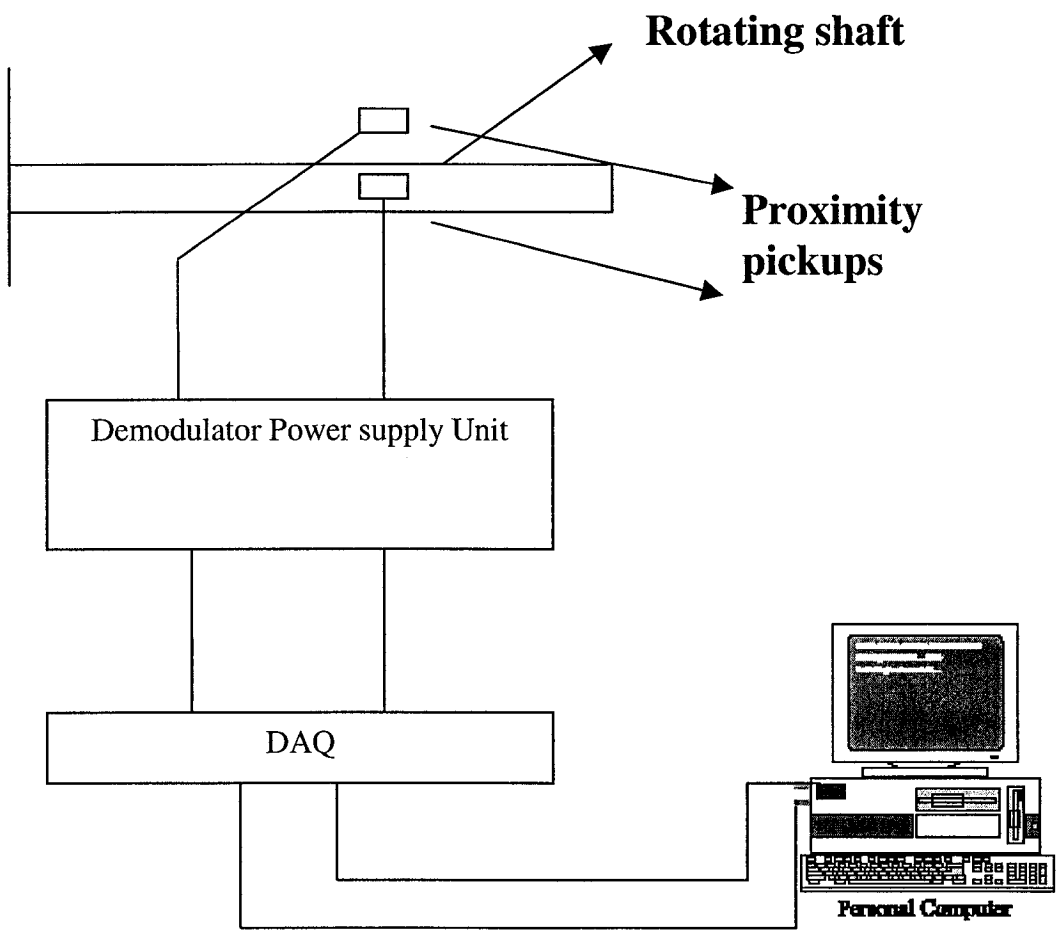


Fig. 3.1: Schematic presentation of experimental setup.

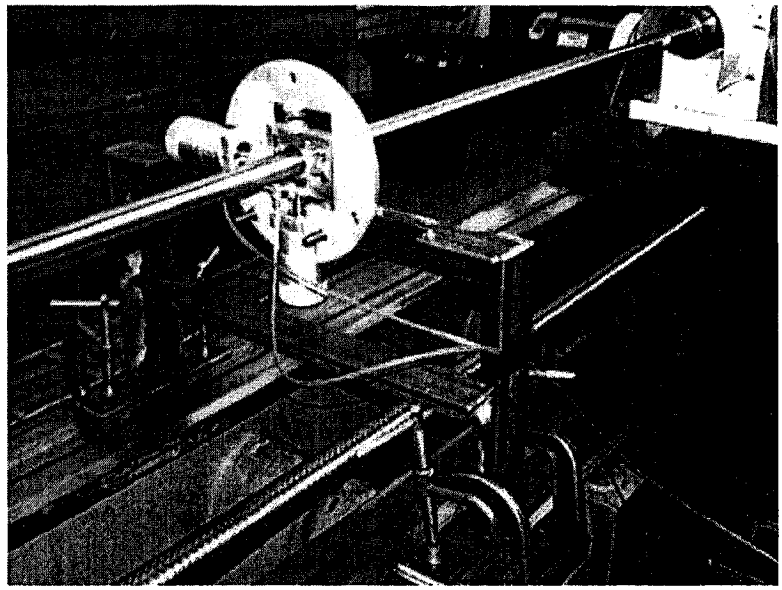

Fig. 3.2: The frame and the two measuring sensors

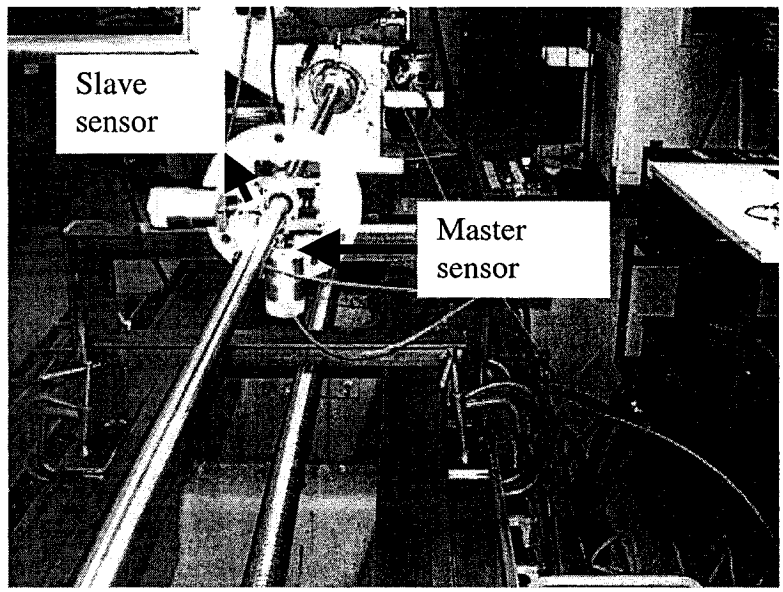


Fig. 3.3: The frame and the two measuring sensors.

KD-2310 systems are most stable when the target is near the face of the sensor. Also, the sensitivity to the cable movement, dielectric constant, magnetic field, etc., is the greatest

when the target is at full-scale displacement. Parallelism between the target and the sensor is acceptable as long as it does not exceed 15 degrees.

### 3.1.2 Data acquisition system (DAQ)

The specifications of the DAQ card used in the experiment are found in appendix A. The devices can scan multiple channels at the same maximum rate as their single-channel rate. In this experiment we have two channels and the scan rate was 1000 scans per second for each channel.

## 3.2 Experimental investigations

The following experiments were carried out:

1- Part-1: Measurement of the whirl orbits of the boring bar–cutting head assembly while rotating freely at different speeds; low, medium and high. Also the natural frequencies of the boring bar were determined.

2- Part-2: Measurement of the whirl orbits of the boring bar-cutting head-workpiece interaction at different speeds of rotation, at the beginning of drilling operation.

3- Part-3: Measurement of the whirl orbits under different cutting parameters of feed, speed and flow rate of the coolant fluid and the tool penetration.

Part-3 will be followed by a surface roughness investigation to study the effect of the cutting parameters on the whirl orbit as well as the surface irregularity. Surface roughness was then be modeled by fuzzy logic analysis to get the best cutting parameters associated with the minimum surface irregularities.

### 3.2.1 Proximity pickups installation and calibration

Two proximity sensors were mounted to measure the unbalance response amplitude in both Z and Y directions at a point where the boring bar is moving at a constant velocity. Once the proximity pickups were installed they were calibrated for the machining operation. The bipolar output calibration procedure (Kaman Instrumentation manual) was carried out. The output voltage ranges from a negative voltage for the first half of the measuring range to a positive output for the second half of the range. The calibration procedures are as follows:

1- Position the target using the micrometer support to give the total distance between the sensor and the target to be equal to the specified full-scale displacement needed for the sensor. Adjust the linearity control until the output is equal to the needed output reading.

2- Position the target so that it is at one-half of the desired full-scale and adjust the zero control until the output reads zero.

3- Position the target at its nearest point to the sensor and adjust the gain control until the output reads the desired negative voltage reading.

4- Move the target to its farthest point from the sensor. Read the output voltage and note the difference between the actual and the needed reading. Adjust the linearity until the output reads the needed voltage level.

5- Repeat steps 2 through 5 as many times as necessary until the needed output voltage at each point is reached.

After calibration, the voltage and distance relation are plotted, and an equation that represents this curve is obtained. Fig.'s 3.4 and 3.5 below are for the master and slave sensors.

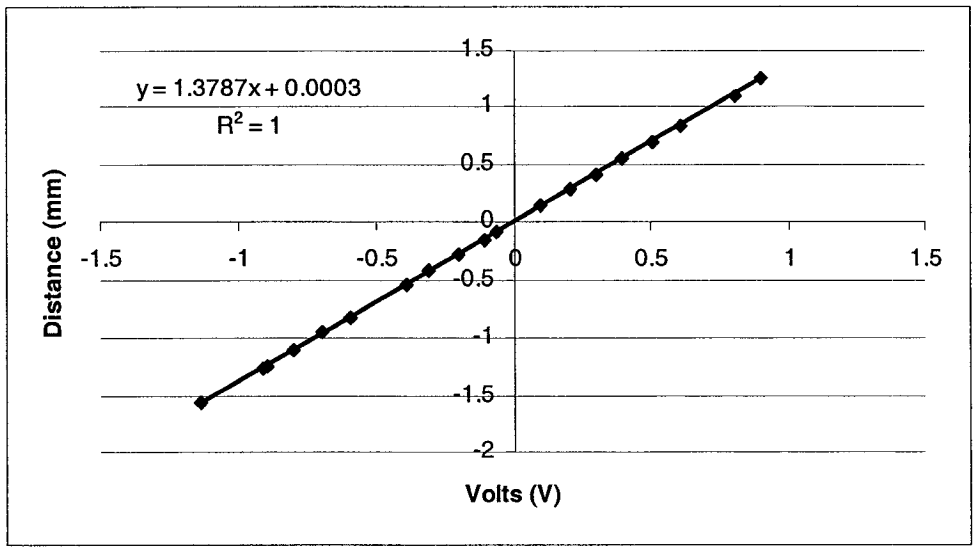


Fig. 3.4: The master calibration with y = 1.3787 x + 0.0003

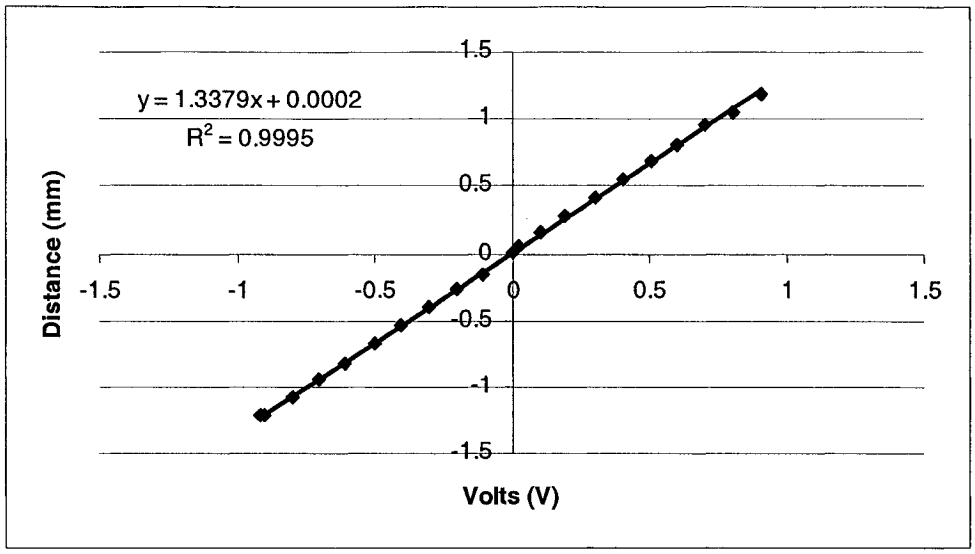


Fig. 3.5: The slave calibration with y = 1.3379x + 0.0002

## 3.3 Experimental results and discussion

The signals sensed by the master (vertical direction) and the slave (horizontal direction) sensors are routed into the data acquisition package, which consists of demodulators, data acquisition card and a computer with a labview software to capture the signals and analyze them.

### 3.3.1 Part-1: Measurement of the whirling motion of the boring bar rotating freely under different speeds of rotation

The orbital motion of the boring bar assembly is caused by many factors such as the straightness error of the shaft which introduces the centrifugal force, the anisotropic shaft stiffnesses in the Y and Z directions or the anisotropic support properties. The whirling

vibration arises because of the existence of some physical phenomenon, which introduces force that cause radial deflection. Such self-excited vibrations adversely affect the surface quality and can cause destruction and damage to the system since the synchronous whirling due to self-excited vibrations induces alternating stresses in the rotating element which will lead to fatigue failure. The experiment will be carried out at different speeds: 120, 240, 480, 600, 1000 and 1440 rpm.

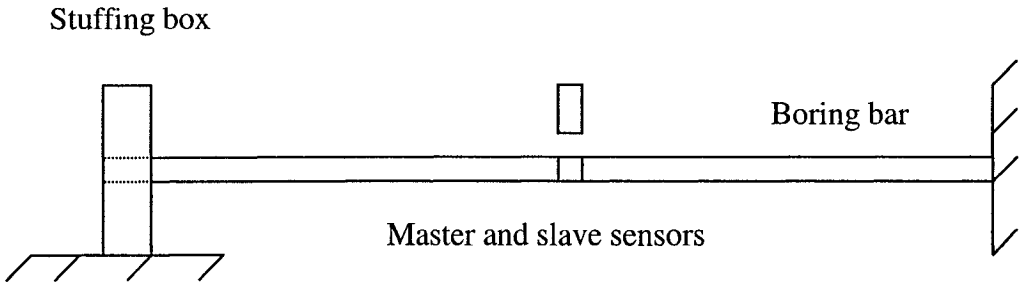


Fig. 3.6: Part-1: Schematic of the boring bar rotating freely.

Fig. 3.6 and 3.7 shows the schematic set-up of the experiment done on the boring bar at different rotational speeds.

At a speed of 120 rpm, the whirl major length is around 400 μm as shown in Fig. 3.8. Both signals coming from the master and slave sensors are plotted in Fig. 3.9. The signals from the master and slave sensors corresponding to one cycle are shown in Fig. 3.10 and the associated whirl orbit is shown in Fig. 3.11.

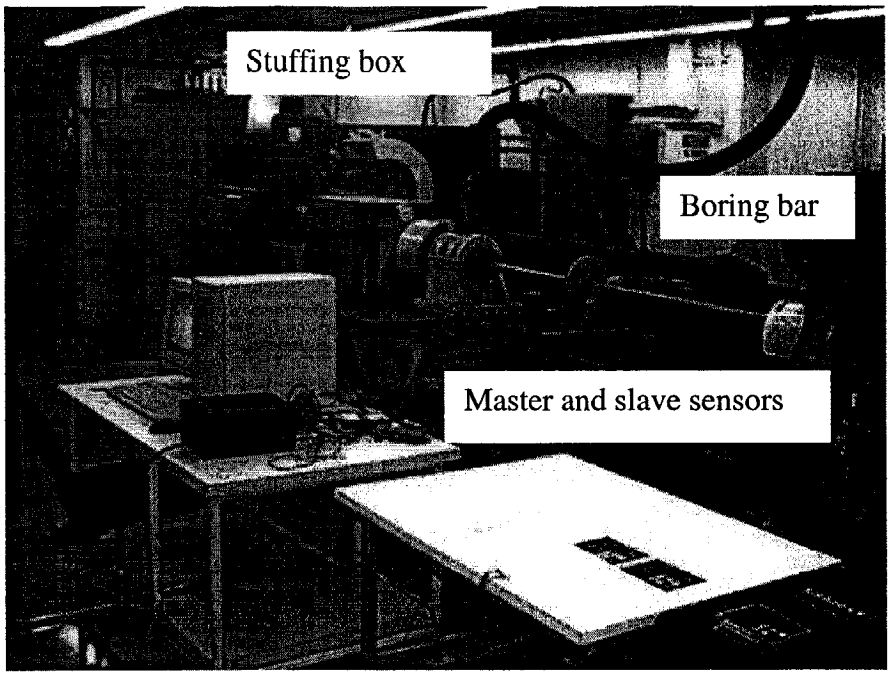


Fig. 3.7: Part-1: Picture of the boring bar rotating freely.

When the speed increases to 240 rpm the whirl major radius is almost the same as that at 120 rpm, as shown in Fig. 3.12. The signals from the two sensors are shown in the Fig. 3.13 for 240 rpm. Increasing the speed to 480 rpm we can see that the shaft has two lobes due to many factors, such as the stiffness of the shaft along the Y and Z coordinate, and vibrations from the gears as in Fig. 3.14. The two signals from the sensors are shown in Fig. 3.15. Increasing the speed to 600 rpm, the major radius is 470 μm as in Fig. 3.16 and the two signals from the sensors are shown in Fig. 3.17.

At a speed of 1000 rpm the major axis of the whirl orbit increases to 550 μm and it seams to be more stable as in Fig. 3.18 and 3.19. Figs. 3.20 and 3.21 show the signals from the two sensors at a speed of 1200 rpm where the ellipse is getting bigger. Figs. 3.22 and 3.23 show the whirl orbit at a speed of 1359 rpm and the radius also is getting bigger.

Figs. 3.24 and 3.25 show the signals from the two sensors, at a speed of 1440 rpm, which is the maximum rotational speed of the boring bar. In this case the ellipse seems to be more clear and more stable with a major axis of 900 μm. The two signals from the master and slave sensors corresponding to one cycle are shown in Fig 3.26 and the associated whirl orbit is shown in Fig. 3.27.

The first and second computed natural frequencies for the boring bar alone is 9.149 Hz and 27.745 Hz, respectively, and the first and second natural frequencies obtained experimentally were in the range of (8.5-10.38) and (30.36-31.13) Hz, respectively, as will be seen in section 4.3.1. Since the rotational speeds of 120, 240 and 480 were below the first natural frequency the whirl amplitude was increasing with speed. The rest of the rotational speeds were below the second natural frequency.

As mentioned before the whirling motion is the result of the rotation of the drill about its center line as the boring bar rotates. In the following figures, one cycle of the boring bar is plotted under different speeds. The geometric center under zero rotation is shown in the Fig. 3.28. The rest of the Figures (3.29-3.36) are for different speeds of rotation, 120, 240, 480, 600, 1000, 1200, 1359 and 1440 rpm's.

From all these figures it is shown that the center of the bar is rotating in a clockwise manner around the geometric center. The boring bar is rotating also in a clockwise sense. It could be concluded that we have forward whirling motion as the whirling motion is in the same direction as that of the boring bar.

Table 3.1 summarizes of the major amplitude of the boring bar associated with its rotation speed.

Table. 3.1: The bar rotational speed associated with the major whirl ellipse amplitude.

| Rotational speed (rpm) | Major amplitude of the whirling ellipse (μm) |
|---|---|
| 120 | 400 |
| 240 | 410 |
| 480 | 500 |
| 600 | 470 |
| 1000 | 550 |
| 1200 | 600 |
| 1359 | 810 |
| 1440 | 900 |

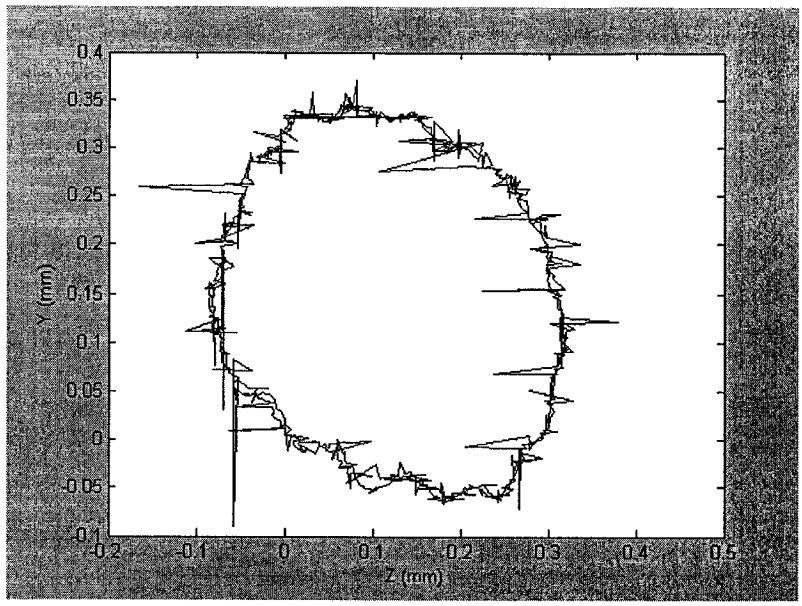


Fig. 3.8: Whirl orbit at speed of 120 rpm.

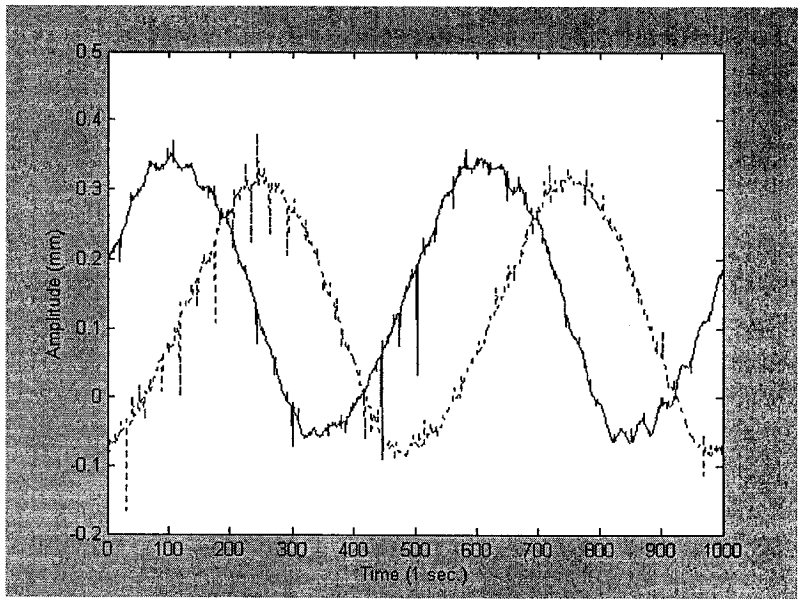


Fig. 3.9: The master (dot line) and the slave (continuous line) at speed of 120 rpm.

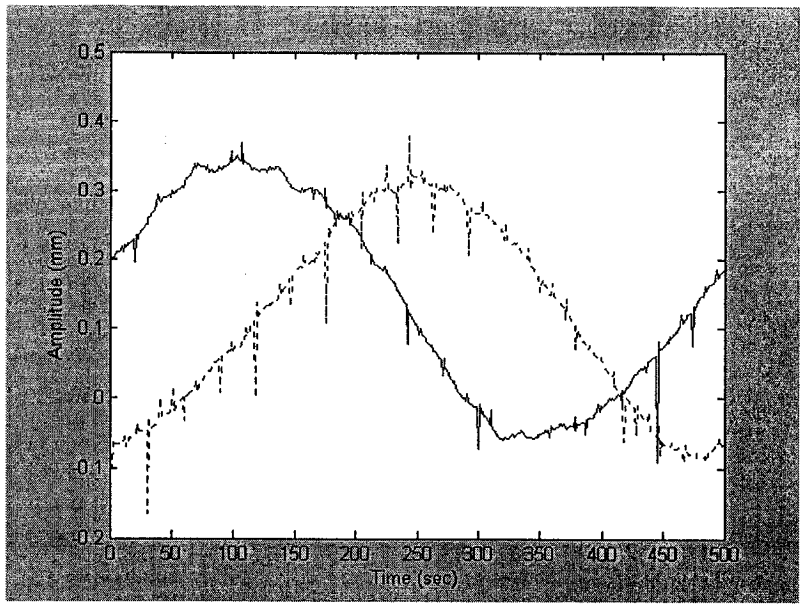


Fig. 3.10: One cycle signal from the master and slave sensors at speed of 120 rpm.

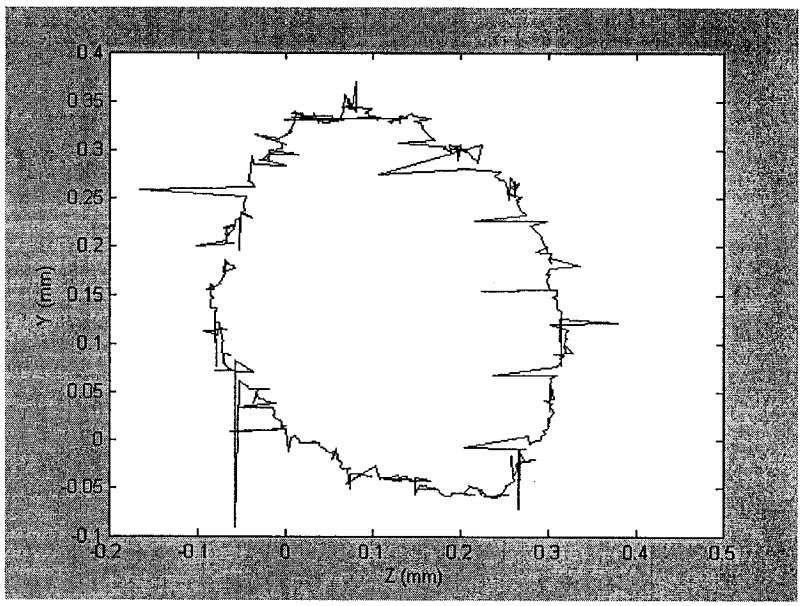


Fig. 3.11: One cycle whirl orbit at speed of 120 rpm.

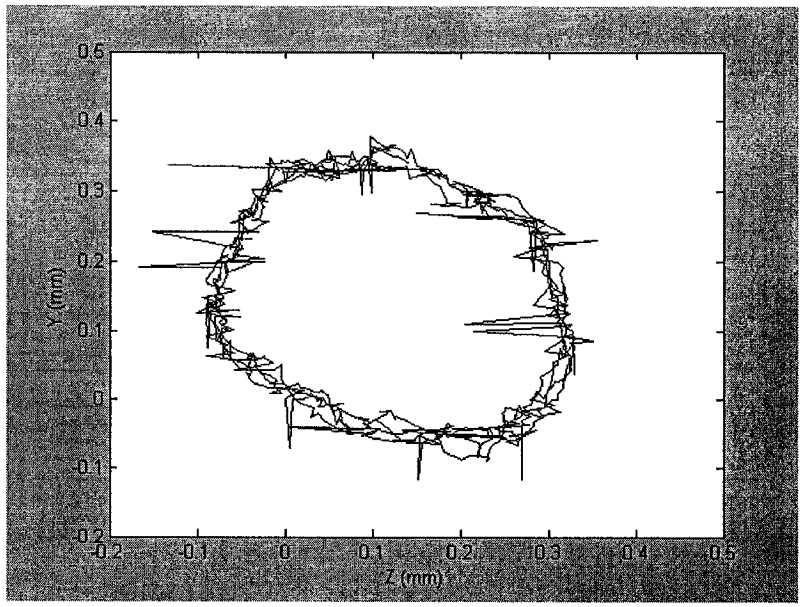


Fig. 3.12: Whirl orbit at speed of 240 rpm.

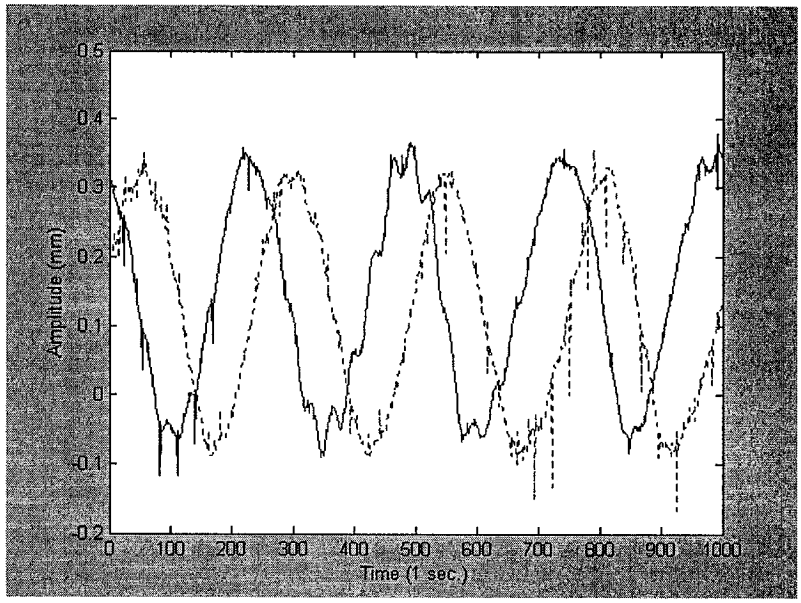


Fig. 3.13: The master (dot line) and the slave (continuous line) at speed of 240 rpm.

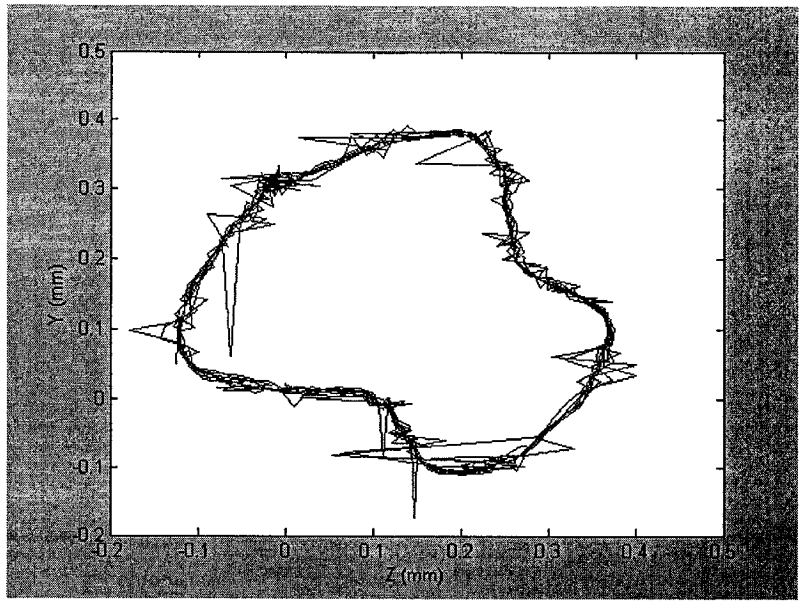


Fig. 3.14: Whirl orbit at speed of 480 rpm.

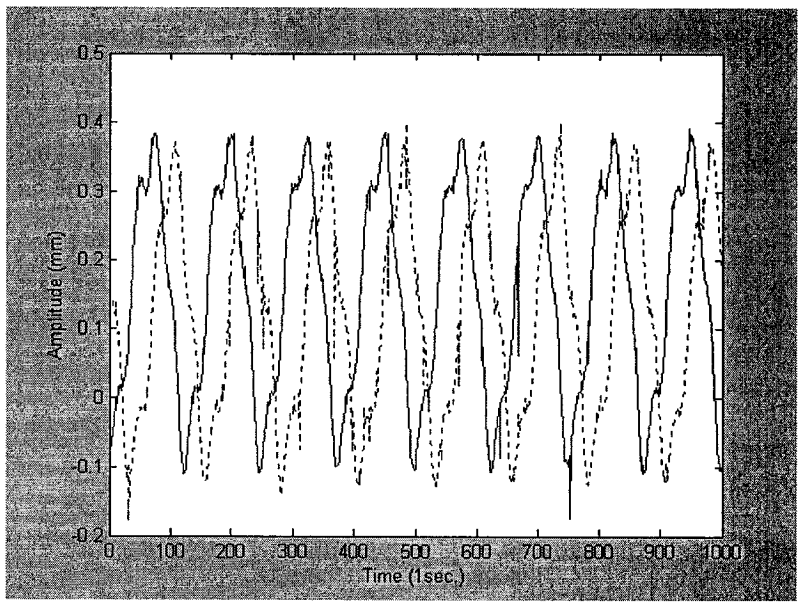


Fig. 3.15: The master (dot line) and the slave (continuous line) at speed of 480 rpm.

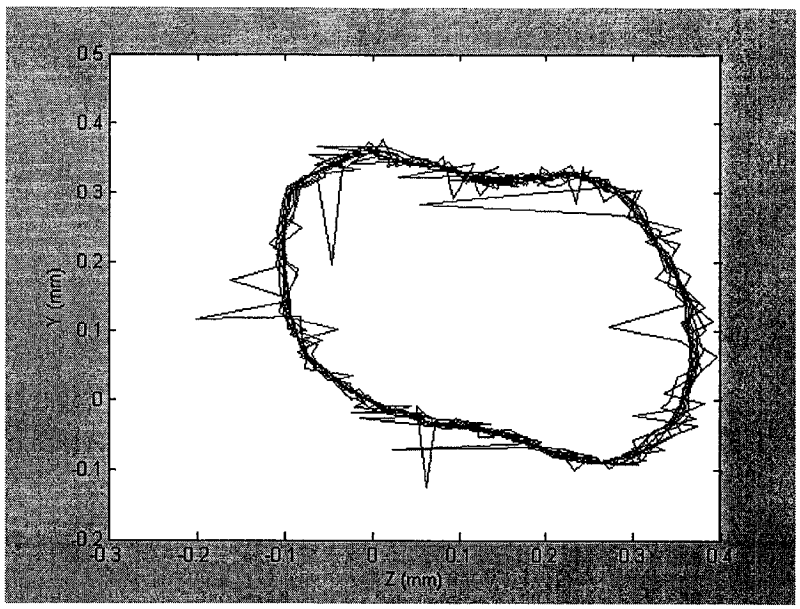


Fig. 3.16: Whirl orbit at speed of 600 rpm.

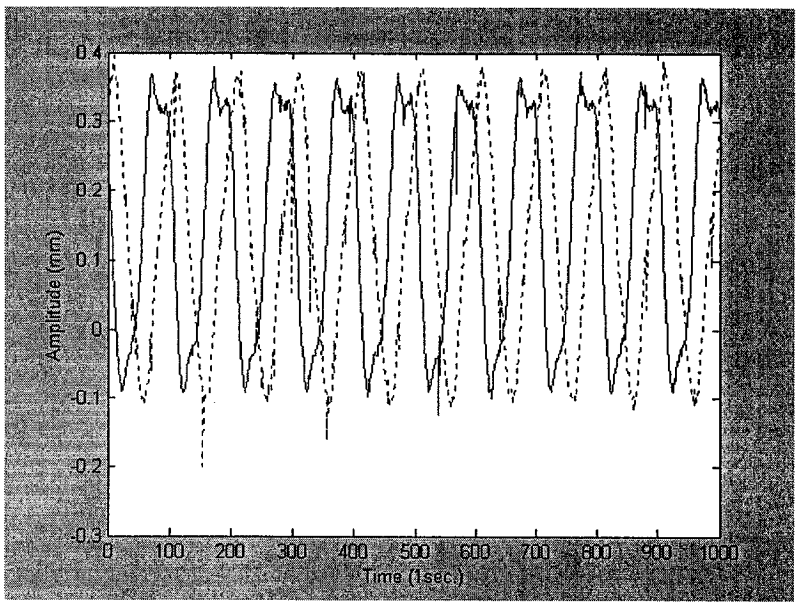


Fig. 3.17: The master (dot line) and the slave (continuous line) at speed of 600 rpm.

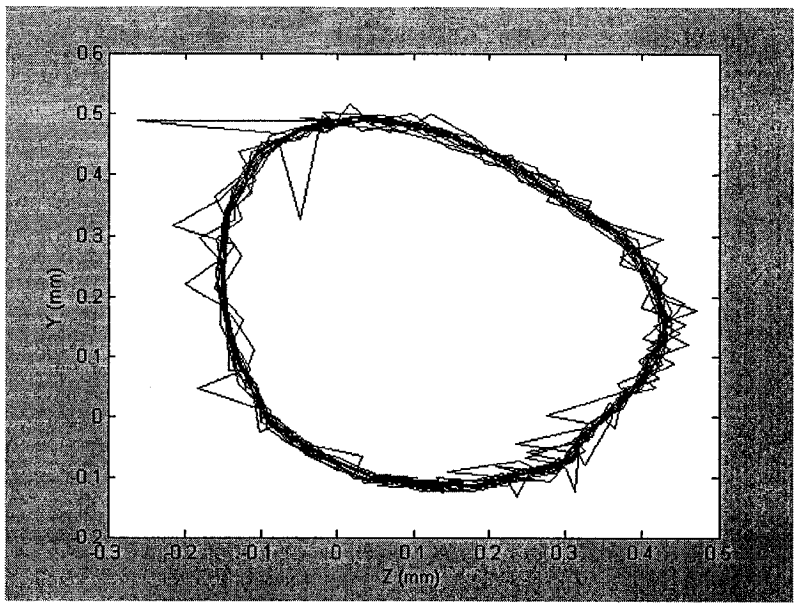


Fig. 3.18: Whirl orbit at speed of 1000 rpm.

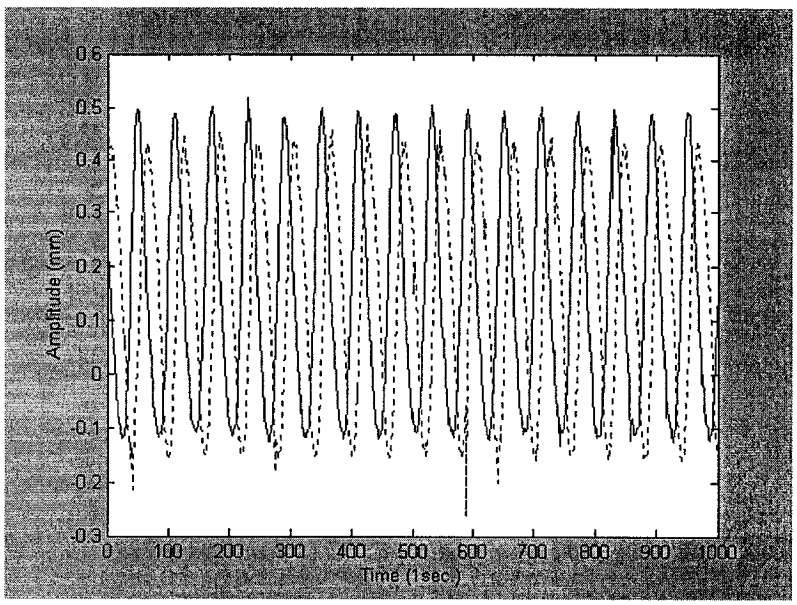


Fig. 3.19: The master (dot line) and the slave (continuous line) at speed of 1000 rpm.

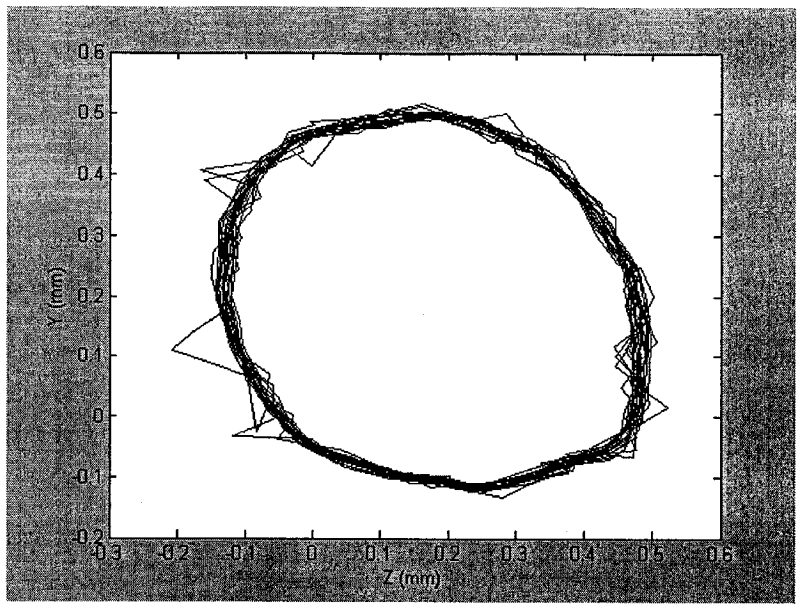


Fig. 3.20: Whirl orbit at speed of 1200 rpm.

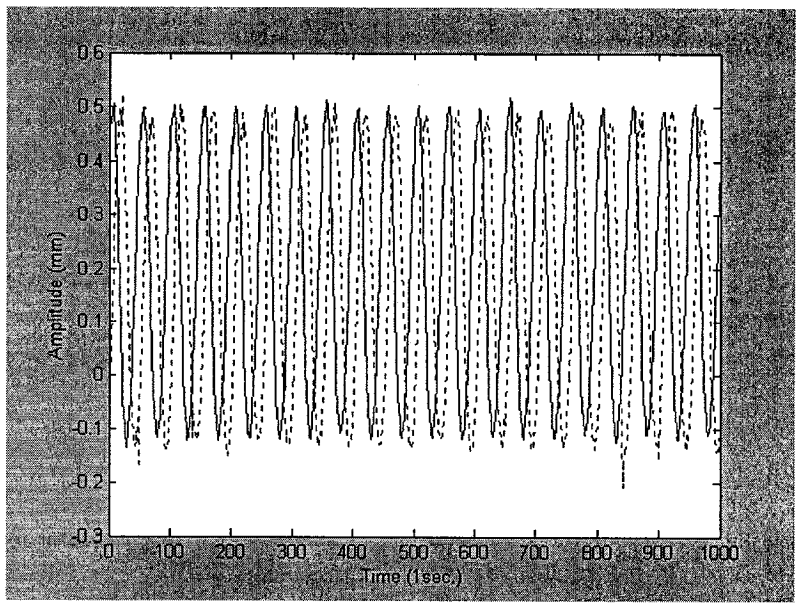


Fig. 3.21: The master (dot line) and the slave (continuous line) at speed of 1200 rpm.

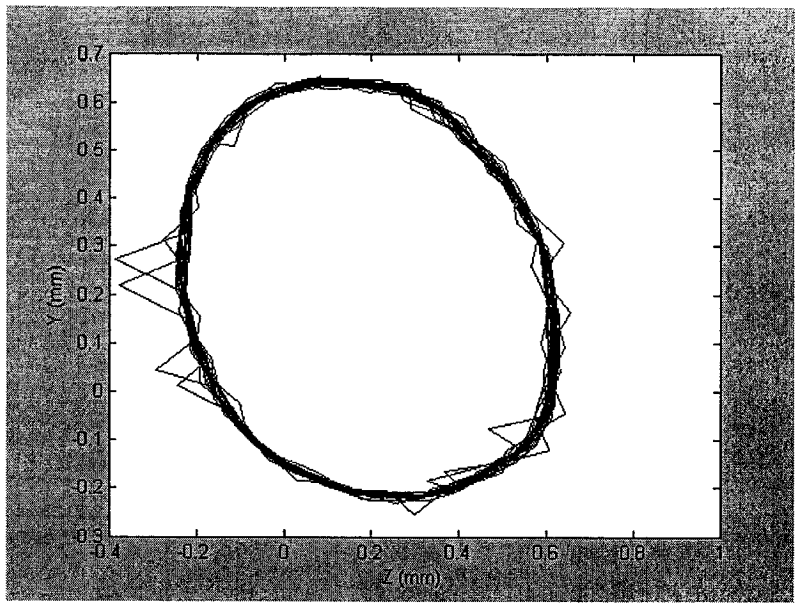


Fig. 3.22: Whirl orbit at speed of 1359 rpm.

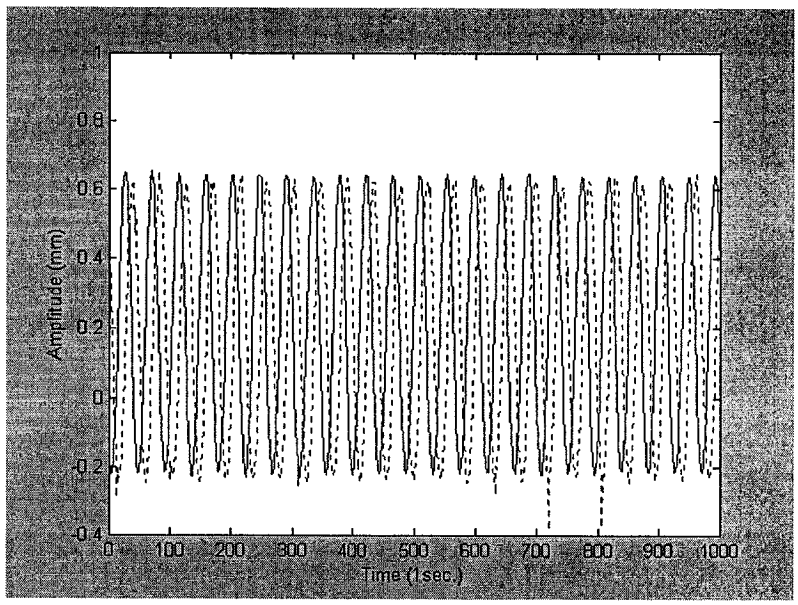


Fig. 3.23: The master (dot line) and the slave (continuous line) at speed of 1359 rpm.

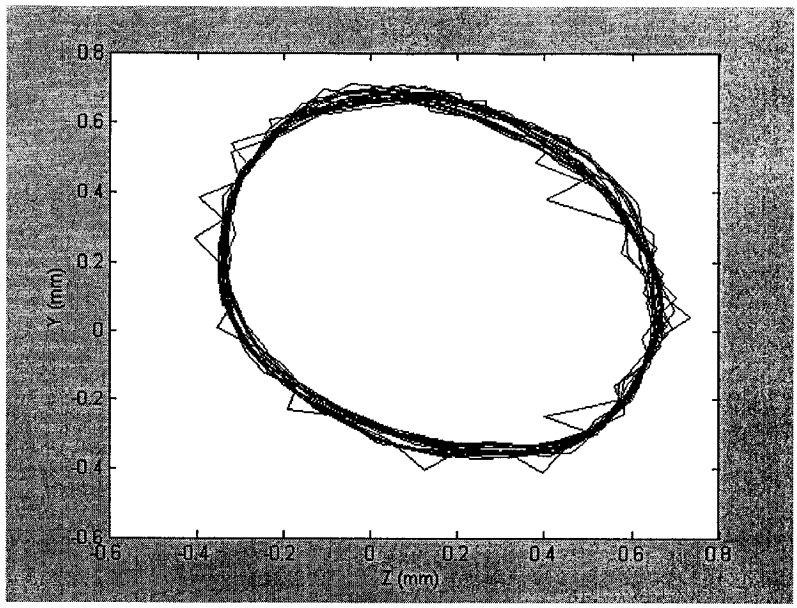


Fig. 3.24: Whirl orbit at speed of 1440 rpm.

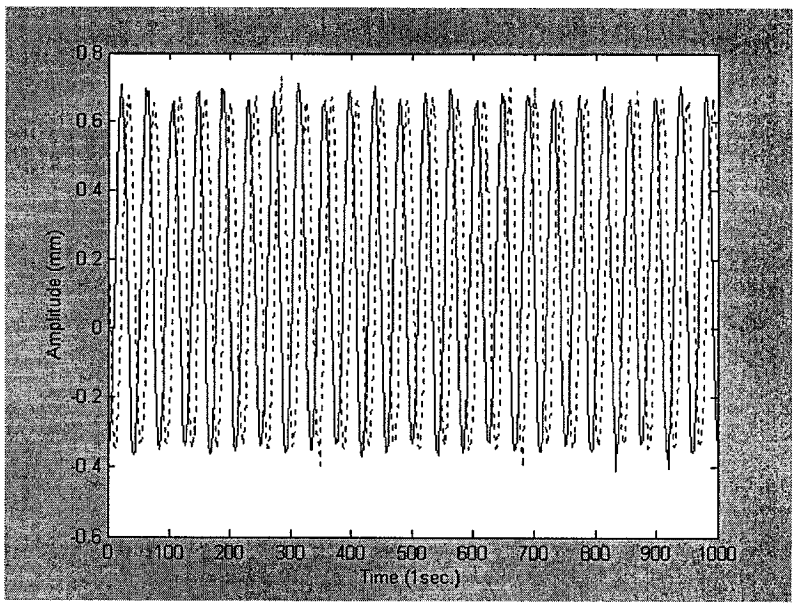


Fig. 3.25: The master (dot line) and the slave (continuous line) at speed of 1440 rpm.

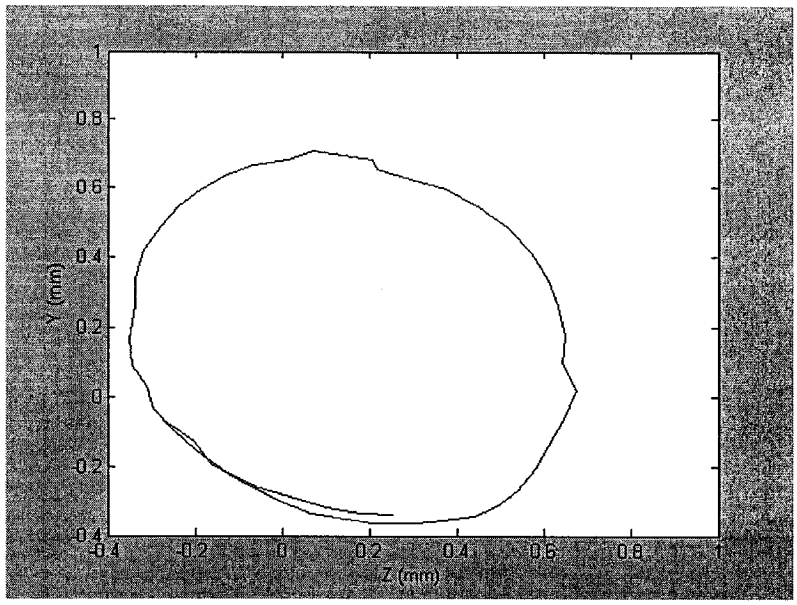


Fig. 3.26: One cycle whirl orbit at speed of 1440 rpm.

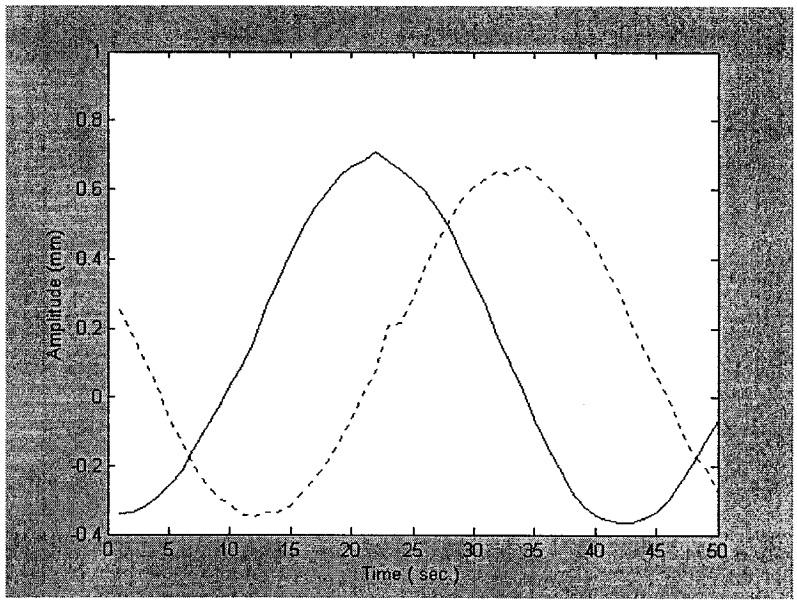


Fig. 3.27: One cycle signal from the master and slave sensors at speed of 120 rpm.

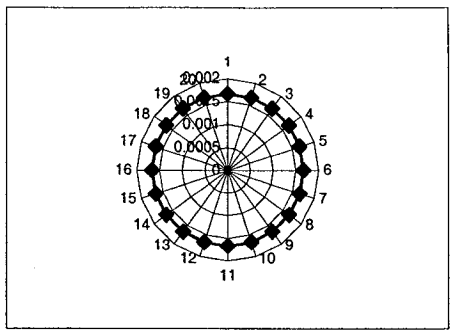


Fig. 3.28: The geometric center of the boring bar under zero rpm.

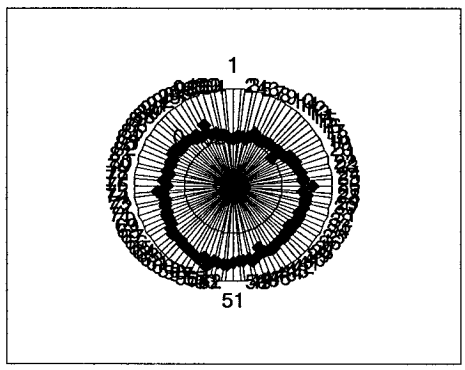


Fig. 3.29: The location of the boring bar at speed of 120 rpm.

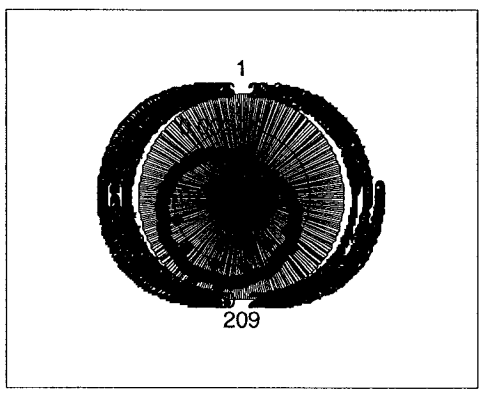


Fig. 3.30: The location of the boring bar at speed of 240 rpm.

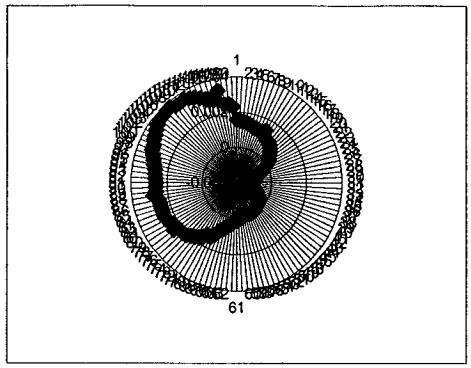


Fig. 3.31: The location of the boring bar at speed of 480 rpm.

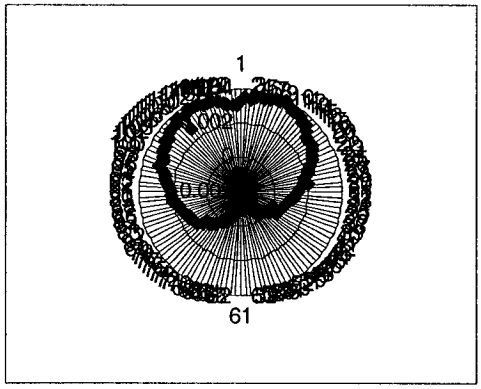


Fig. 3.32: The location of the boring bar at speed of 600 rpm.

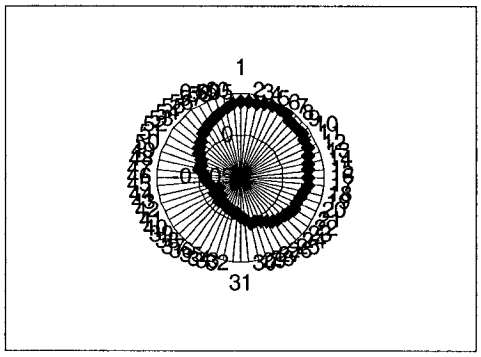


Fig. 3.33: The location of the boring bar at speed of 1000 rpm.

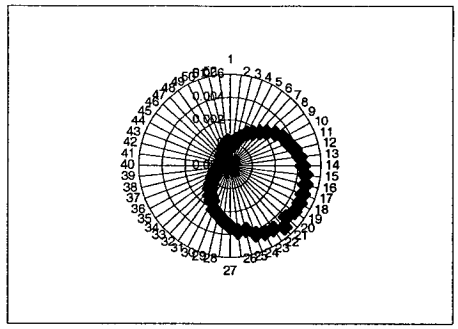

Fig. 3.34: The location of the boring bar at speed of 1200 rpm

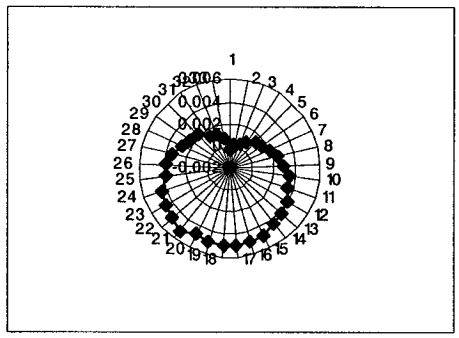

Fig. 3.35: The location of the boring bar at speed of 1359 rpm.

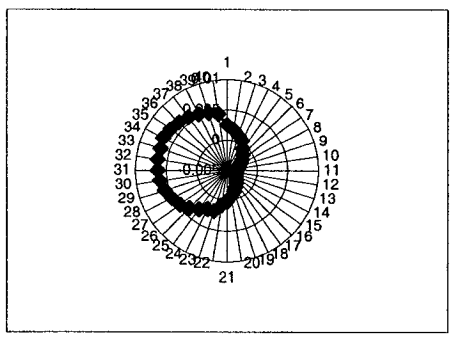

Fig. 3.36: The location of the boring bar at speed of 1440 rpm.

### 3.3.2 Part-2: Measurement of the whirling motion of the boring bar at the beginning of drilling operation

The cutting head is supported by the work piece and a small feed is provided because rotating the boring bar without giving some feed will damage the cutting head. The experiments are carried out at high speeds of rotation in order to overcome the resistance of the work piece. The investigation speeds were 1200, 1280, 1359 and 1440 rpm as shown in Fig. 3.37 and 3.38.

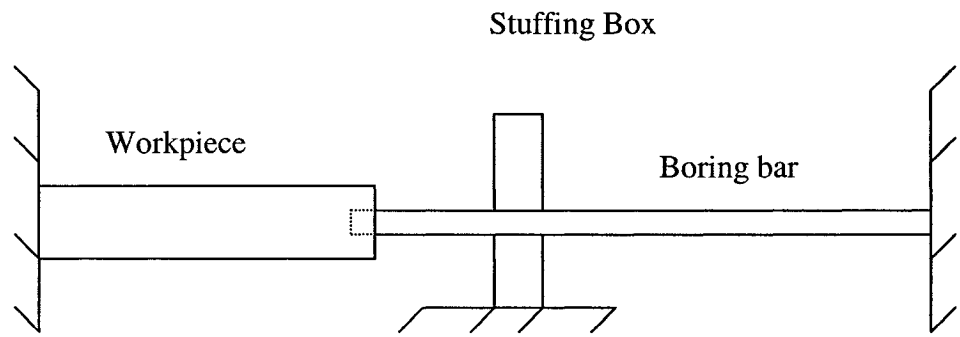


Fig. 3.37: Part 2: Schematic representation the experiment at different speeds of rotation.

The minimum speed used to start cutting was 1200 rpm. As shown in Fig. 3.39 the whirl diameter was approximately 1000 μm and the signals from the master and slave are plotted in Fig. 3.40. Increasing the speed to 1280 rpm, the corresponding whirl mode shown in Fig. 3.41, seems to be more stable with a diameter equal to 900 μm. The corresponding master and slave signals are shown in Fig. 3.42. At speed equal to 1359

rpm the whirl diameter decreased to 895 μm as in Fig. 3.43 and the two signals are shown in Fig. 3.44. For the maximum speed of 1440 rpm, the whirl mode

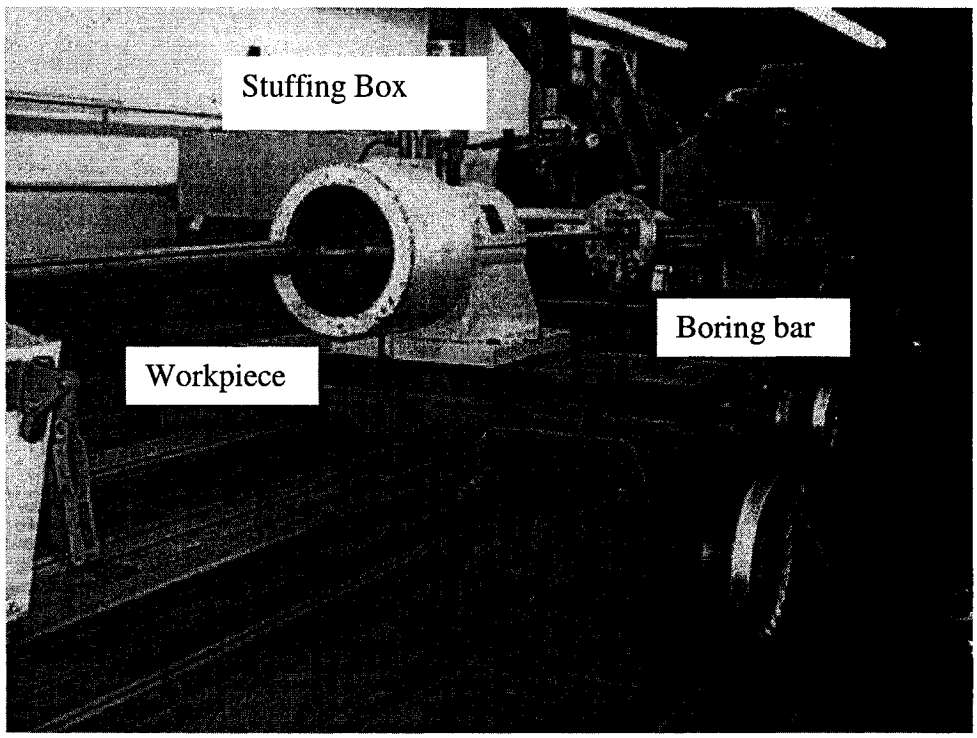


Fig. 3.38: Part 2: Picture of the experiment done at different speeds of rotation.

seems to be more and more stable with a diameter equal to 710 μm as in Fig. 3.45 and the two signals are shown in Fig. 3.46. The reason for the reduced whirl diameter may be due to more stability when the speed is increased while cutting. Also a small feed was given during the experiments, and hence the whirl mode was not measured at the same point for the four speeds. The first and second computed natural frequencies for the boring bar-workpiece system are 11.23 Hz and 25.28 Hz, respectively. The first and second natural frequencies obtained experimentally were in the range of 8.43-11.41 and 20-24.51 Hz, respectively, as will be seen in section 4.3.1. The 1200 rpm was far away from the first

natural frequency and close to the second natural frequency as will be seen in section 3.4.1. The speed 1280, 1359 and 1440 rpm were below the second computed value and in the range of the experimentally obtained natural frequency. Table 3.2 summarizes the rotational speed with the major amplitudes of the elliptical whirl orbit of the boring bar.

Table. 3.2: The bar rotational speed associated with the major whirl ellipse amplitude for experiment part 2.

| Rotational speed (rpm) | Major amplitude of the whirling ellipse (μm) |
|---|---|
| 1200 | 1000 |
| 1280 | 980 |
| 1359 | 895 |
| 1440 | 710 |

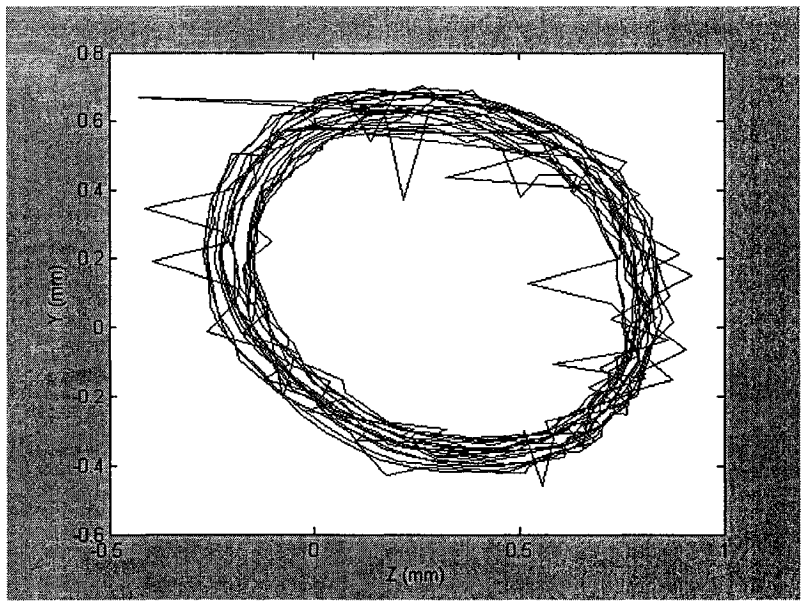


Fig. 3.39: Whirl orbit at speed of 1200 rpm

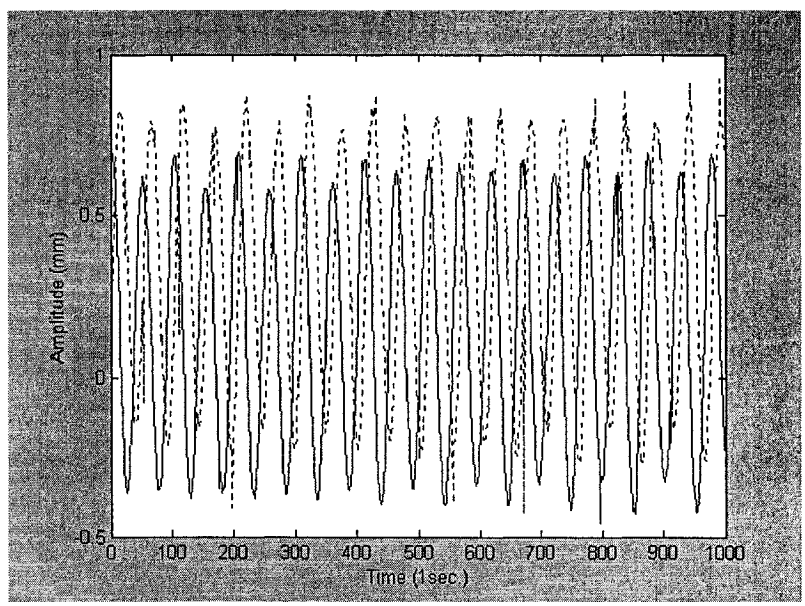


Fig. 3.40: The master (dot line) and the slave (continuous line) at speed of 1200 rpm.

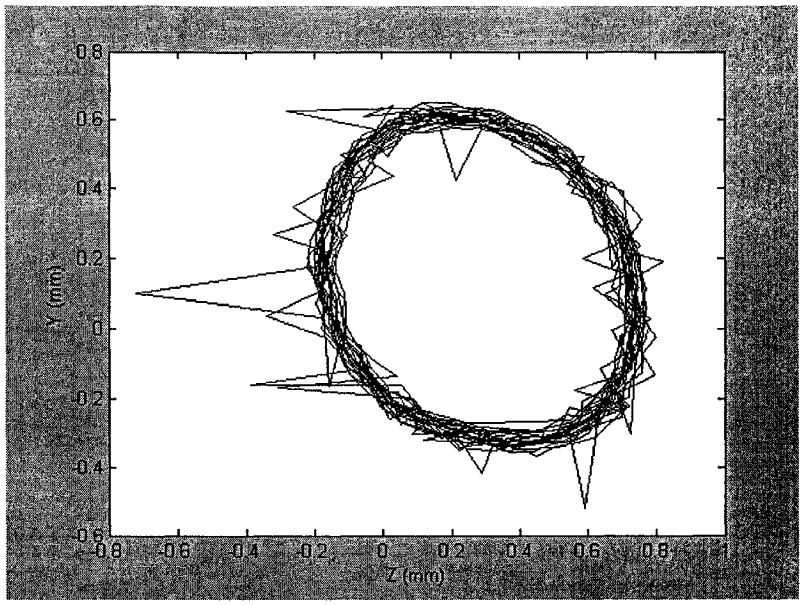


Fig. 3.41: Whirl orbit at speed of 1280 rpm.

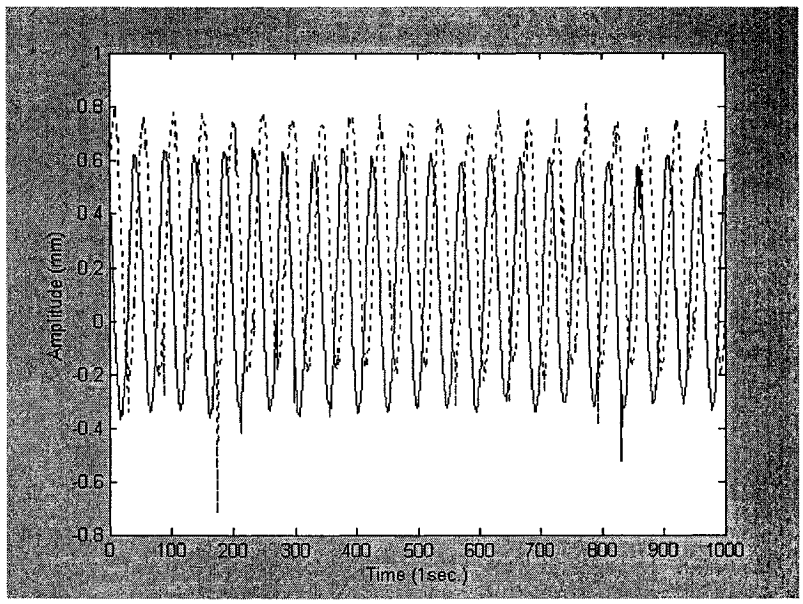


Fig. 3.42: The master (dot line) and the slave (continuous line) at speed of 1280 rpm.

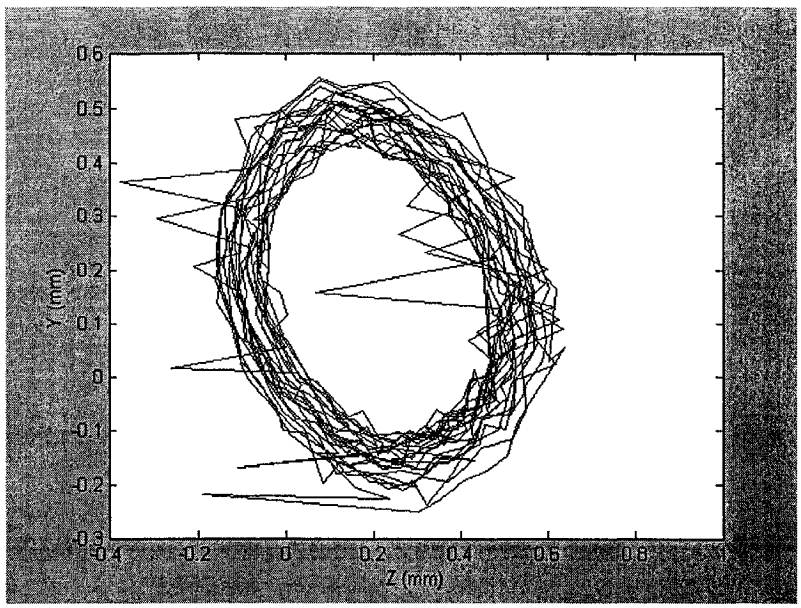


Fig. 3.43: Whirl orbit at speed of 1359 rpm.

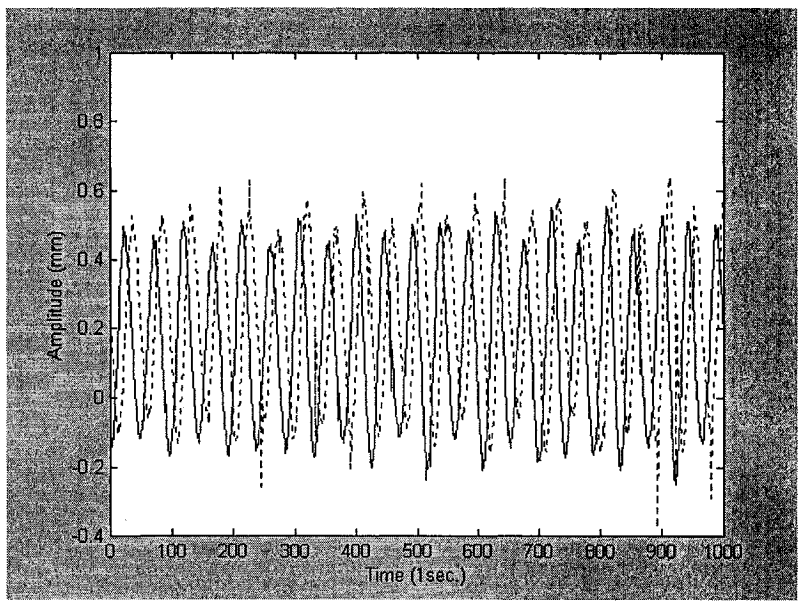


Fig. 3.44: The master (dot line) and the slave (continuous line) at speed of 1359 rpm.

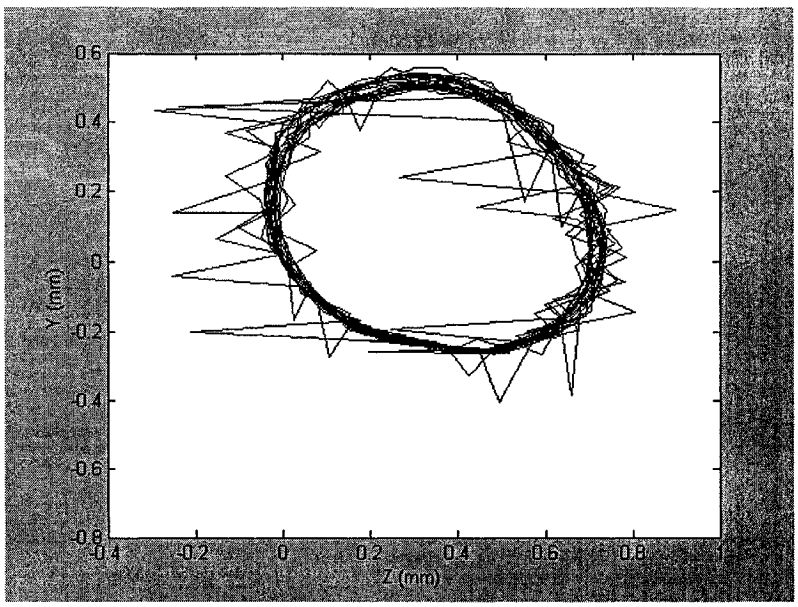


Fig. 3.45: Whirl orbit at speed of 1440 rpm.

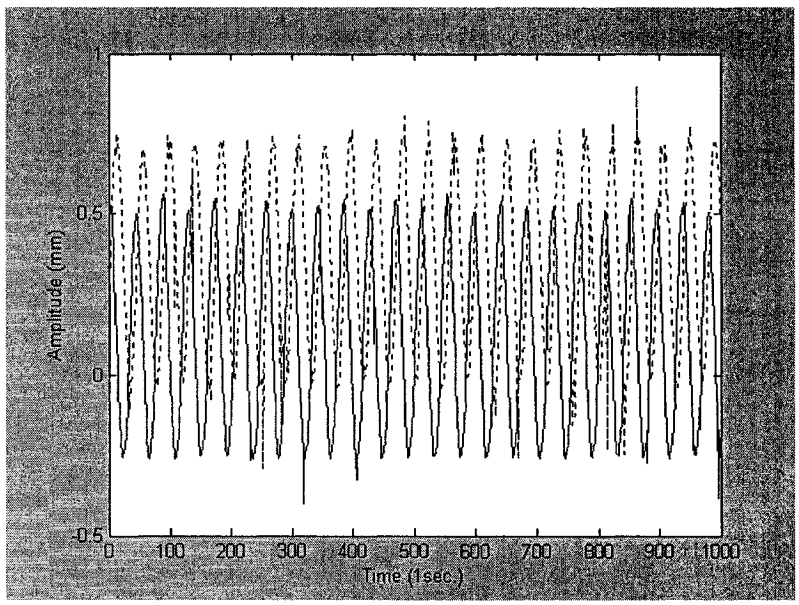


Fig. 3.46: The master (dot line) and the slave (continuous line) at speed of 1440 rpm.

## 3.4 Frequency response domain

The measured time-domain data is also converted to frequency domain data via Fourier transform. A frequency analysis of the signals will show the natural frequencies of the boring-bar cutting head assembly. Under steady state conditions, the response will be a periodic or non-periodic process and hence can be represented by a Fourier series. If one of those frequencies is close to the resonant frequency of the vibrating system then the corresponding oscillations may be the dominant part of the response. The discrete Fourier transform is:

$$F_K = \frac{1}{N}\sum_{n=0}^{N-1}\left\{x_n \exp\left(-i\frac{2\pi}{N}n\right)\right\},$$

where

N is the number of time domain samples,

n is the time domain sample index

### 3.4.1 Power spectral density

The power spectral density, (PSD), is the amount of *power* per unit (*density*) of frequency (*spectral*) as a function of the frequency. The power spectral density, PSD, describes how the power (or variance) of a process is distributed over the frequency range. Mathematically, it is defined as the Fourier transform of the autocorrelation of the

process. An equivalent definition of PSD is the squared modulus of the Fourier transform of the process, scaled by a proper constant term. The power spectral density S(f) for a discrete Fourier transform is defined as :

$$S(f) = \lim_{N\to\infty} \frac{1}{T} F_N \times F_N^*$$

where the asterisk denotes complex conjugate. The nature of the representation of the Fourier series in this way becomes clear if we think of it as a superposition of sinusoidal oscillations of all possible frequencies.

### 3.4.1.1 Frequency response for part-1

In order to analyze the signals in the frequency domain, the Fourier transform of the data from the two sensors are obtained and then the power spectral density for both of them are obtained. In Fig.3.47, there are spectral peaks at 6.9714 Hz and at 30.632 Hz. The actual heights depend on the magnitude of excitation. The area beneath each peak however is quantitatively useful and represents the energy of the signal. In Fig. 3.48, there are three spectral peaks at 4.19 Hz, 8.50 Hz and 31.13 Hz. In Fig. 3.49, the first spectral peak is at 8.29 Hz; the second is at 16.9987 Hz, the third at 24.90 Hz, the fourth at 32.01 Hz and the fifth is at 40.15. In Fig. 3.50, the spectral peaks are at 10.38 Hz, 20.9 Hz and at 30.632 Hz. In Fig. 3.51 the first spectral peak is at 16.89 Hz, the second is at 32.12 Hz and the third is at 50. 17 Hz. In Fig. 3.52 which is the frequency analysis of the

signal at speed of 1200 rpm there are spectral peaks at 20.90 Hz, 32.2 Hz, 40.17 Hz, 50.17 Hz and 60 Hz. In Fig. 3.53 there are spectral peaks at 23.74 Hz, 45.60 Hz, and 67 Hz. For Fig. 3.54, there are four peaks at 24.33 Hz, at 32. 21 Hz, at 48.60 Hz, and at 72.35 Hz. Table 3.3 summarizes the spectral peaks for part-1. Table 3.4 lists the first and second natural frequencies both, computed and experimentally obtained.

Table 3.3: The spectral peaks for part-1.

| Spectral peaks (Hz) | | | | | |
|---|---|---|---|---|---|
| Figure number | 1st | 2nd | 3rd | 4th | 5th |
| 3.47 | 6.9714 | 32.632 | ---- | ---- | ---- |
| 3.48 | 4.19 | 8.5 | 31.13 | ---- | ---- |
| 3.49 | 8.29 | 16.9987 | 24.9 | 32.01 | 40.15 |
| 3.5 | 10.38 | 20.9 | 30.632 | ---- | ---- |
| 3.51 | 16.89 | 32.12 | 50.17 | ---- | ---- |
| 3.52 | 20.9 | 32.2 | 40.17 | 50.17 | 60 |
| 3.53 | 23.74 | 45.6 | 67 | ---- | ---- |
| 3.54 | 24.33 | 32.21 | 48.6 | 72.35 | ---- |

Table 3.4: The first and second computed and experimentally obtained natural frequencies for part-1.

| Natural frequencies ($\omega_n$) | Computed (Hz) | Experimentally obtained (Hz) |
|---|---|---|
| $\omega_1$ | 9.149 | (8.5 – 10.38) |
| $\omega_2$ | 27.745 | (30.63 – 31.13) |

### 3.4.1.2 Frequency response for part-2

Frequency response at the beginning of the boring process is shown in Fig. 3.55 where there are five spectral peaks, at 11.06 Hz, at 20.25 Hz, at 29.67 Hz, at 58.82 Hz and at 78.34 Hz. In Fig. 3.56 there are six spectral peak at 8.43 Hz, 21.92 Hz, 31.12 Hz, 35.34 Hz, 42 Hz and 63.70 Hz. In Fig. 3.57 there are seven spectral peaks at 12.76 Hz, 22.22 Hz, 32.13 Hz, 44.17 Hz, 65.76 Hz, and 307.94 Hz. In Fig. 3.58 there are six spectral peaks at 11.41 Hz, 24.51 Hz, 32.91 Hz, at 47.077 Hz, 70.08 Hz and at 93.33 Hz. From these Figure's we notice that the maximum spectral peak is at the first natural frequency of the system. Table 3.5 lists the first and second natural frequencies, both computed and experimentally obtained. Table 3.6 summarizes the spectral peaks for part-2.

Table 3.5: The first and second computed and experimentally obtained natural frequencies for part-2.

| Natural frequencies ($\omega_n$) | Computed (Hz) | Experimentally obtained (Hz) |
|---|---|---|
| $\omega_1$ | 11.23 | (8.43 – 12.76) |
| $\omega_2$ | 25.28 | (20.25 – 24.51) |

Table 3.6: The spectral peaks for part-2.

| | Spectral peaks (Hz) | | | | | |
|---|---|---|---|---|---|---|
| Figure number | 1st | 2nd | 3rd | 4th | 5th | ---- |
| 3.55 | 11.06 | 20.25 | 29.67 | 58.82 | 78.34 | ---- |
| 3.56 | 8.43 | 21.92 | 31.12 | 35.34 | 42 | 63.7 |
| 3.57 | 12.76 | 22.22 | 32.13 | 44.17 | 65.76 | 307.44 |
| 3.58 | 11.41 | 24.51 | 32.91 | 47.077 | 70.08 | 93.33 |

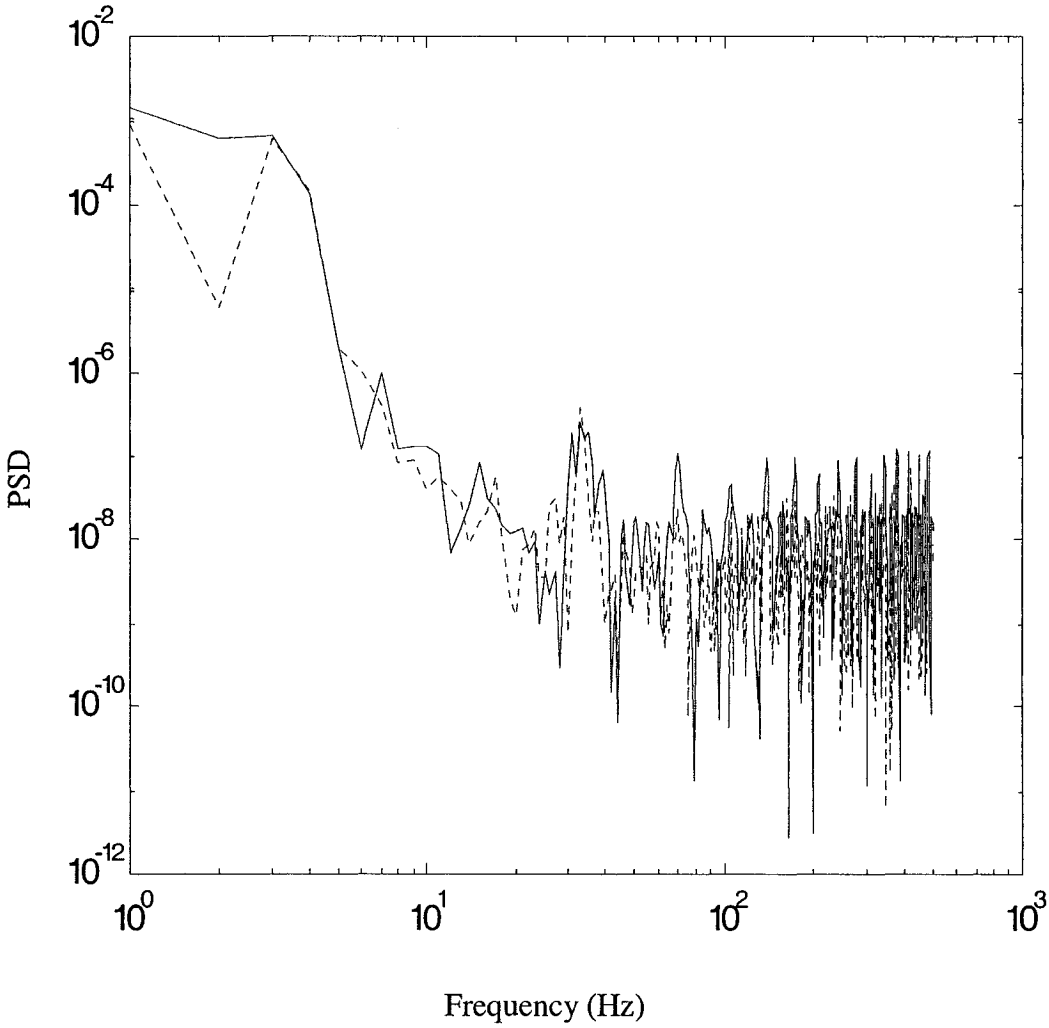


Fig.3.47: Amplitude Spectral Density for speed of 120 rpm for the master and slave signals.

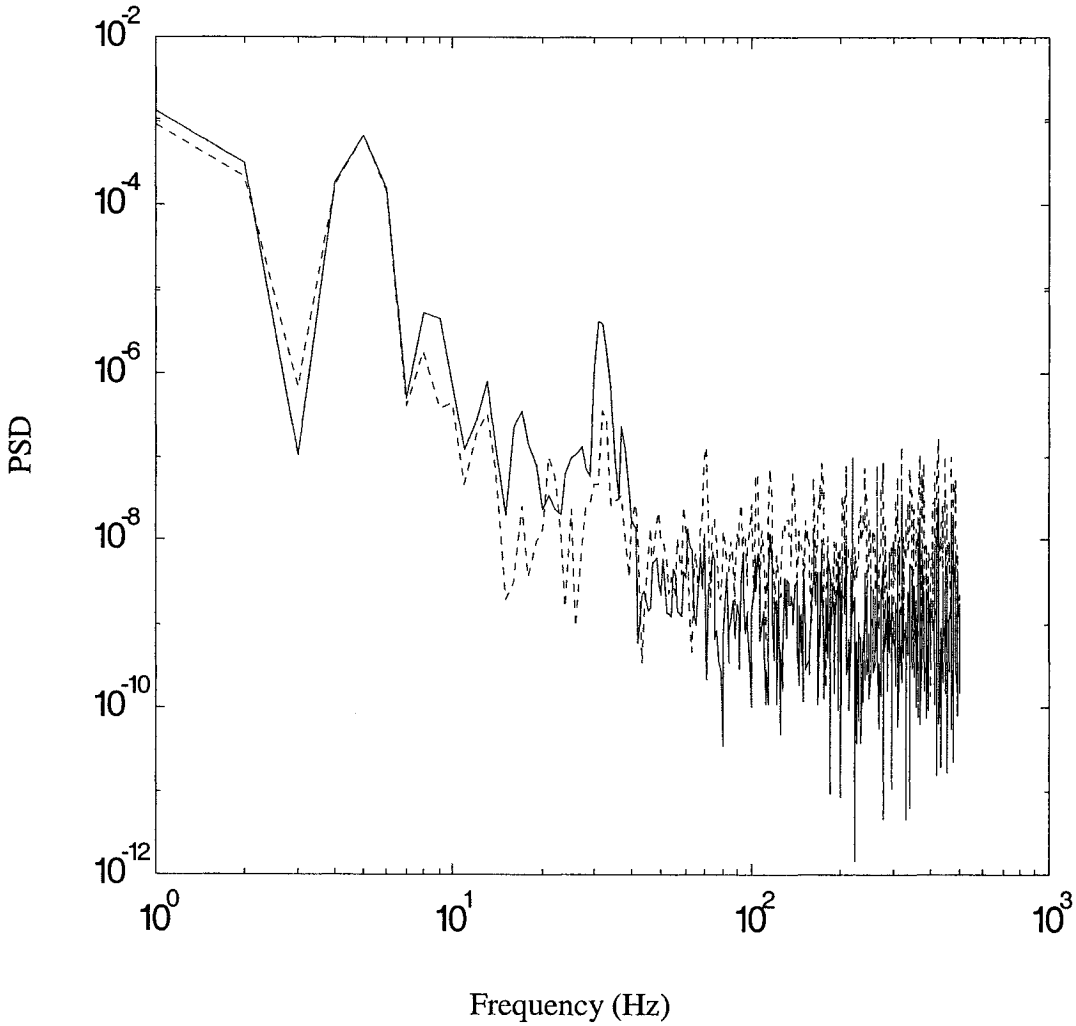


Fig.3.48: Amplitude Spectral Density for speed of 240 rpm, for the two signals.

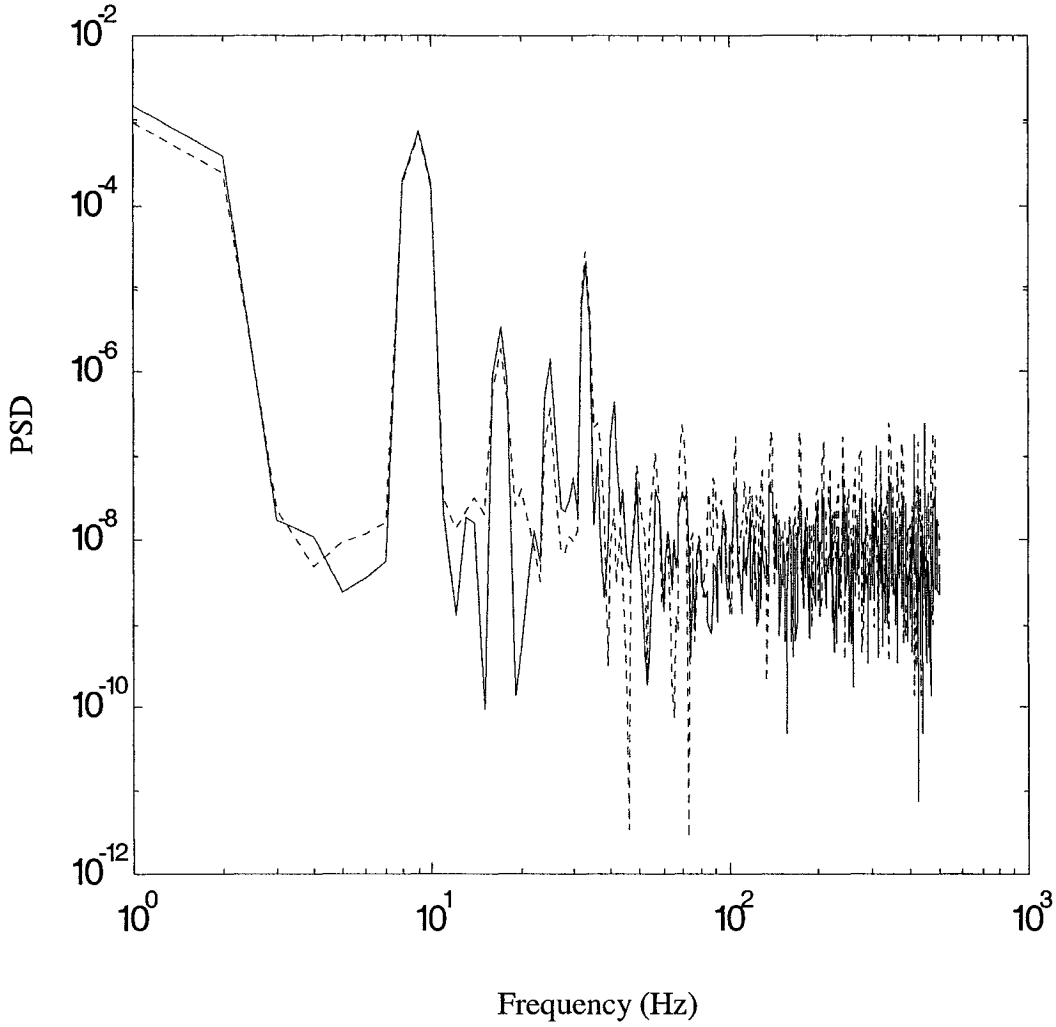


Fig. 3.49: Amplitude Spectral Density for speed of 480 rpm.

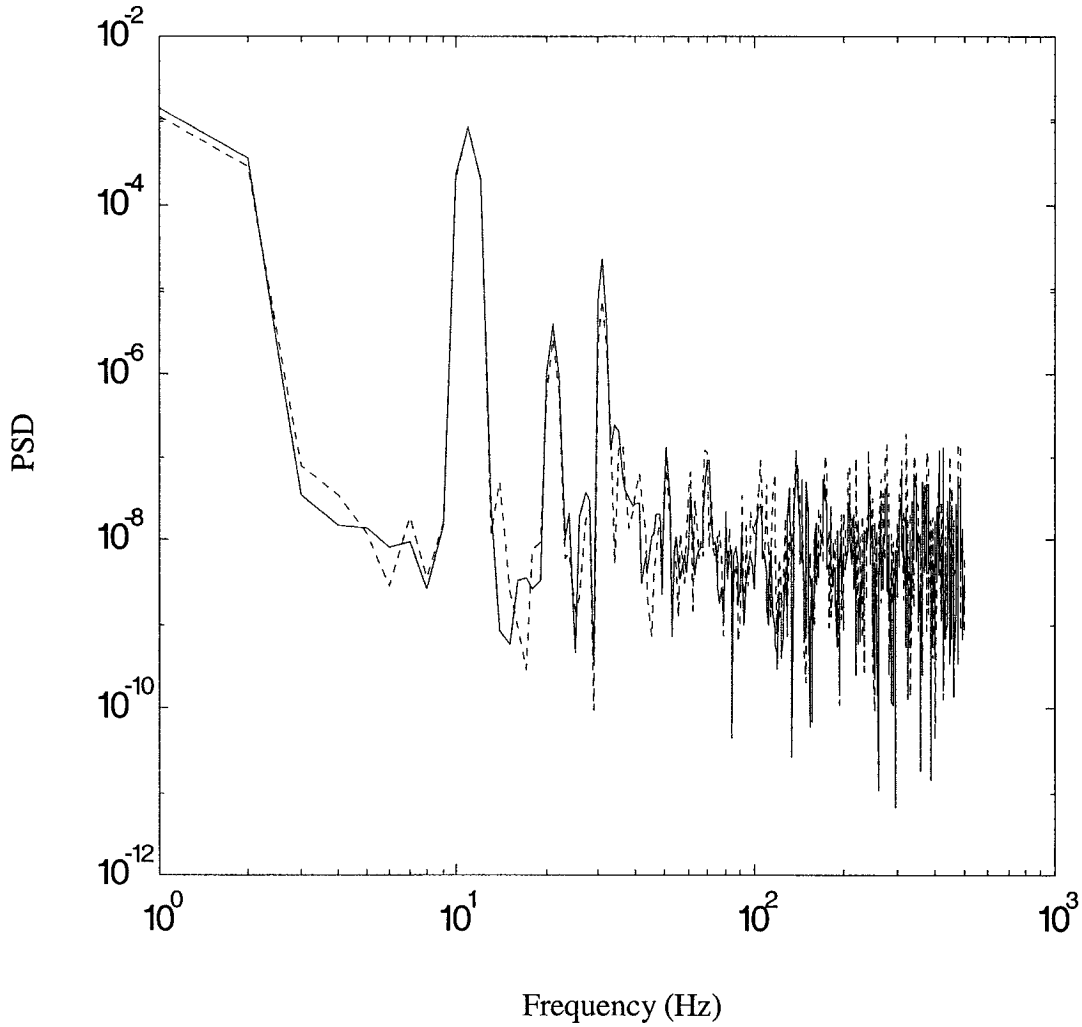


Fig. 3.50: Amplitude Spectral Density for speed of 600 rpm.

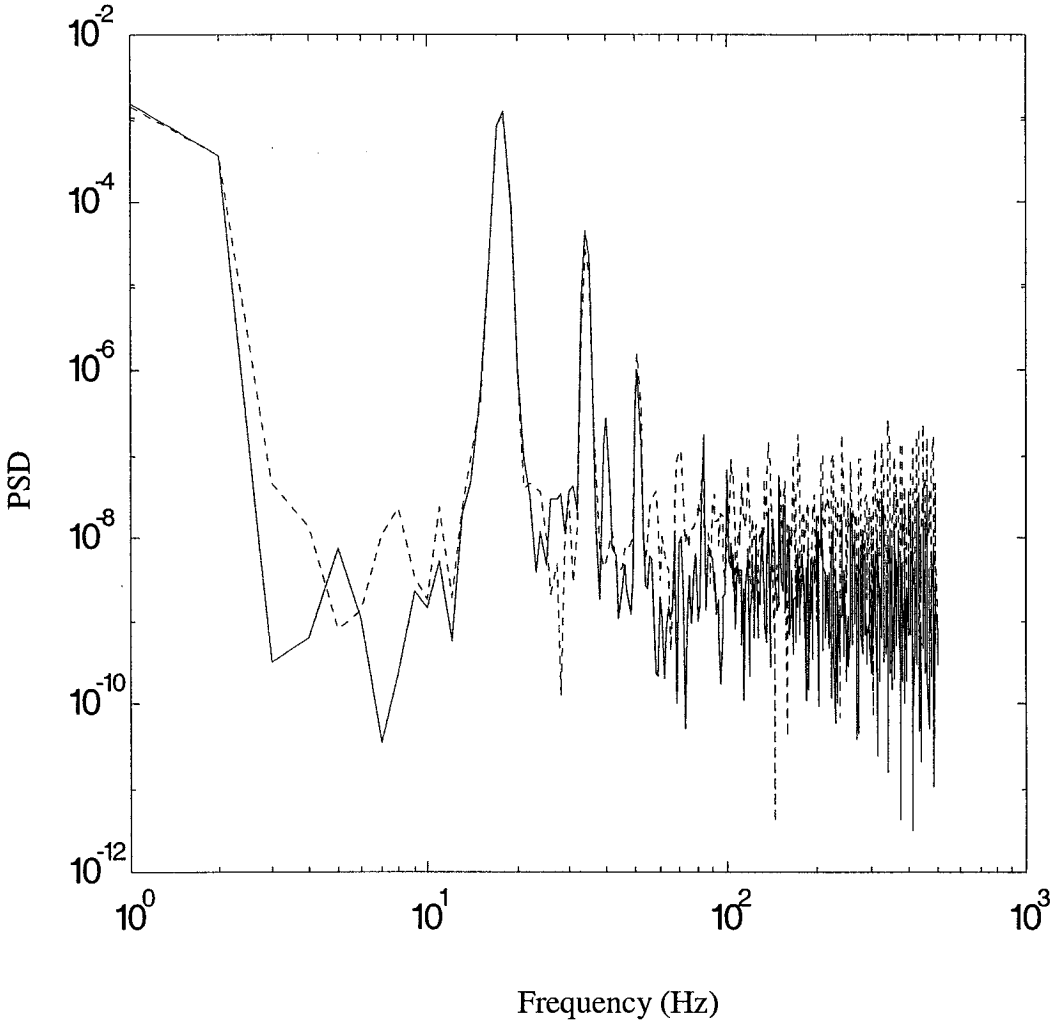


Fig.3.51: Amplitude Spectral Density for speed of 1000 rpm.

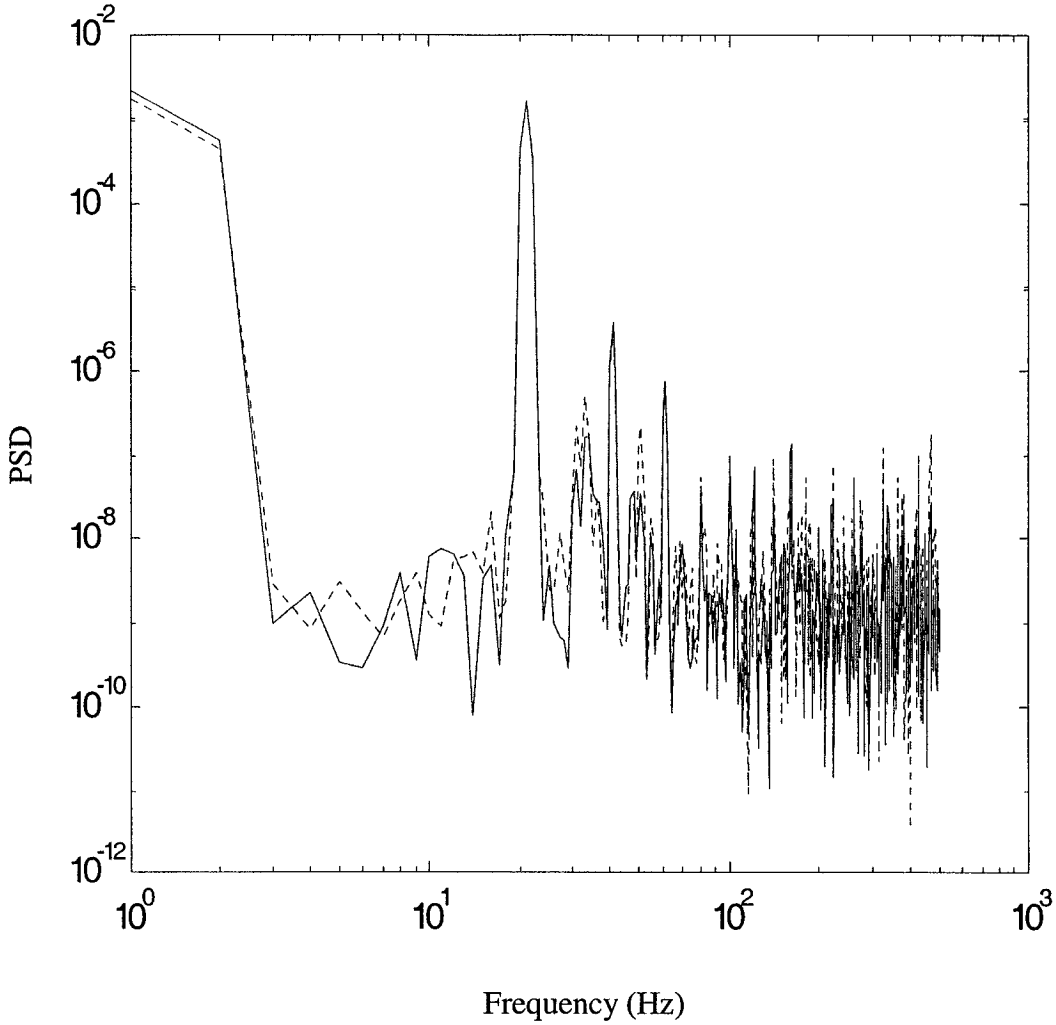


Fig. 3.52: Amplitude Spectral Density for speed of 1200 rpm.

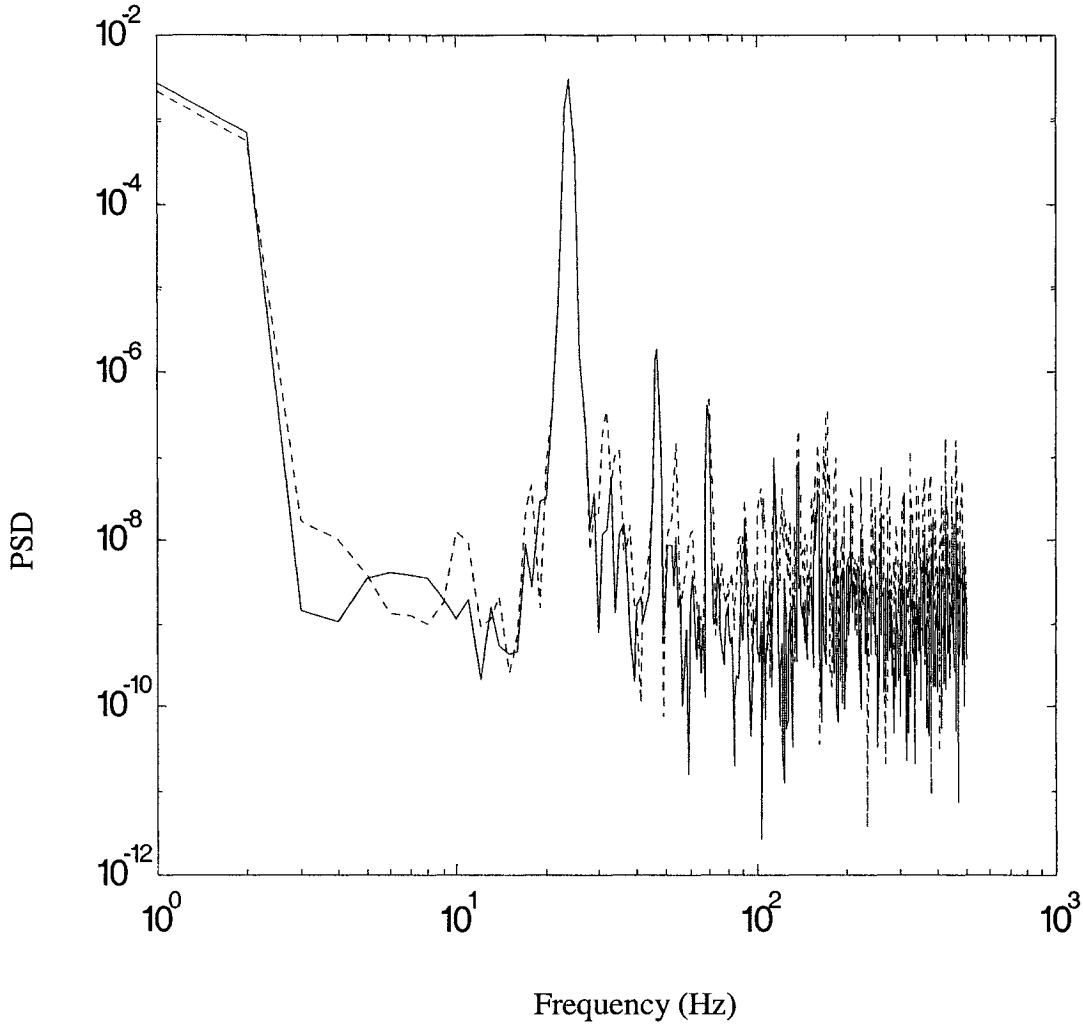


Fig. 3.53: Amplitude Spectral Density for speed of 1359 rpm.

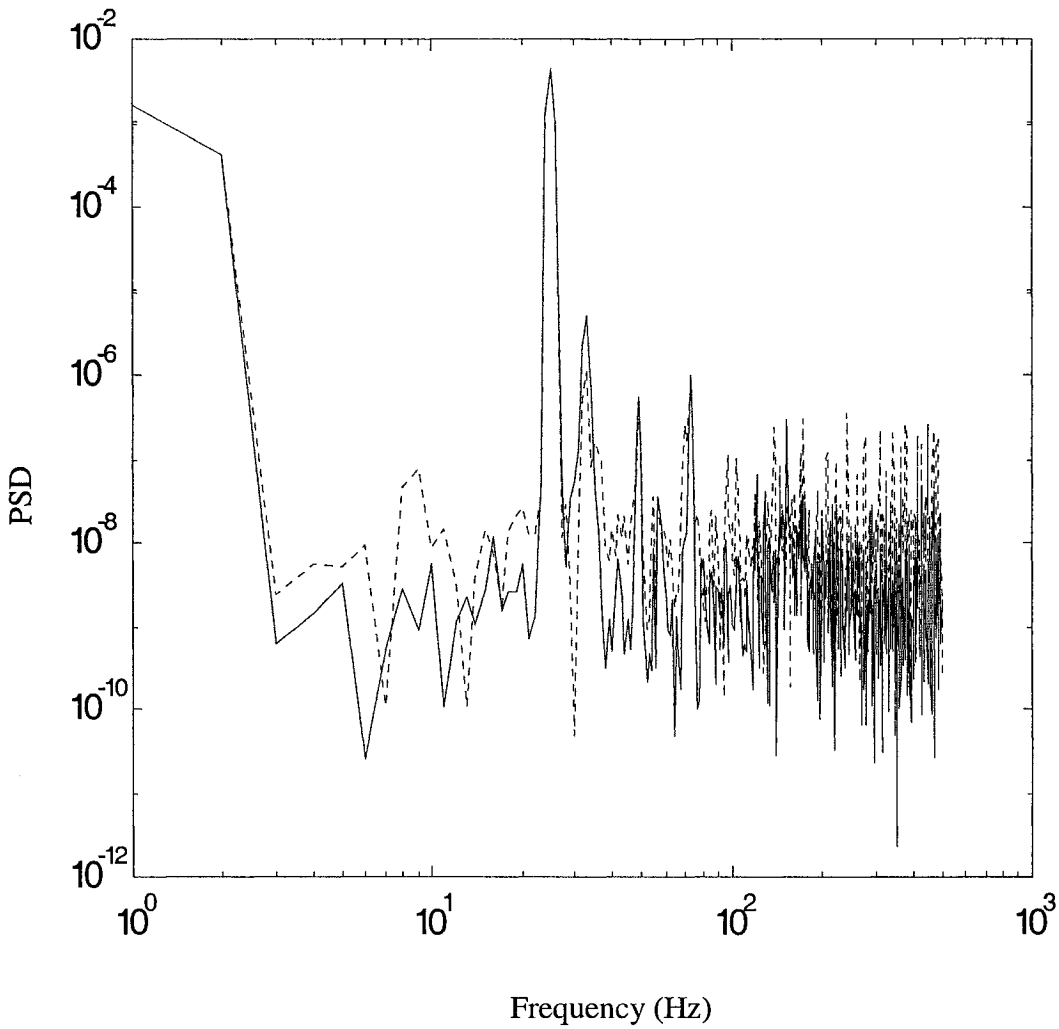


Fig.3.54: Amplitude Spectral Density for speed of 1440 rpm.

**Part-2:**

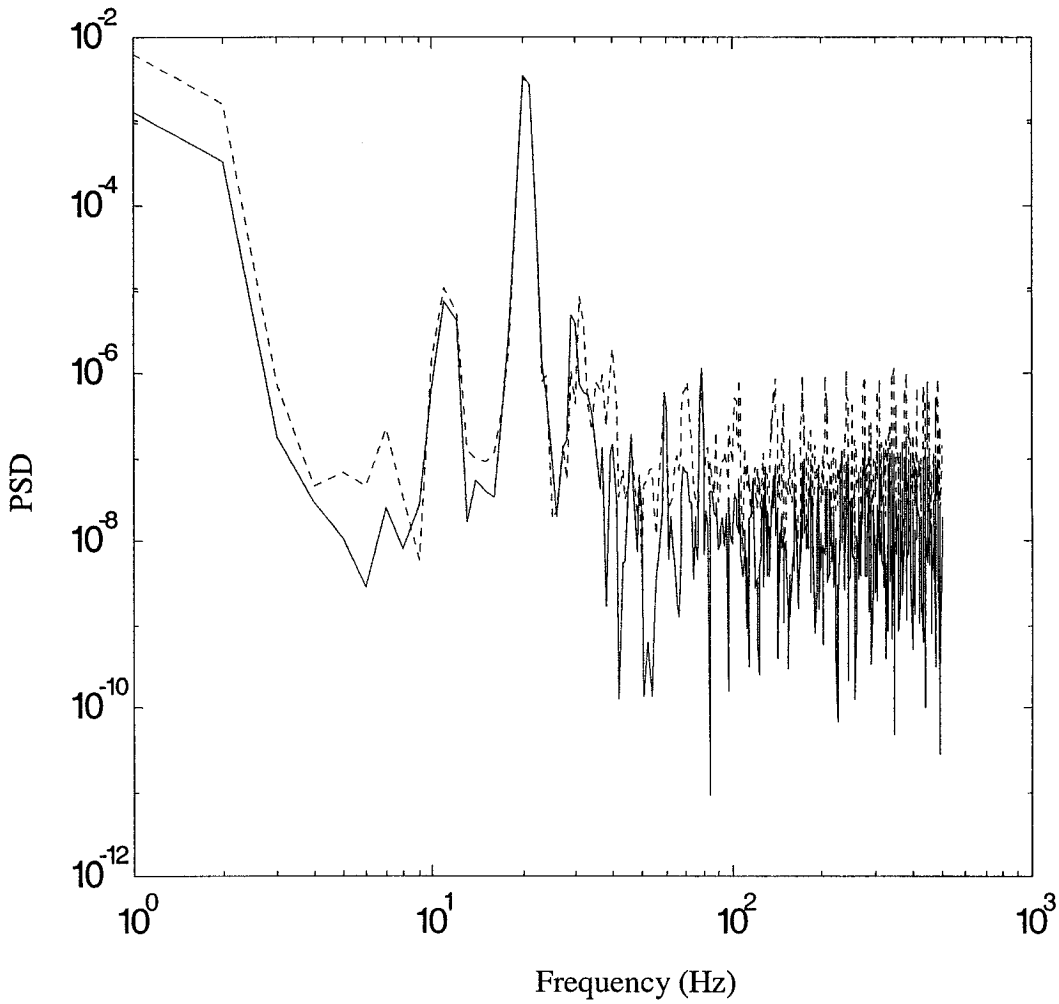


Fig.3.55: Amplitude Spectral Density for speed of 1200 rpm.

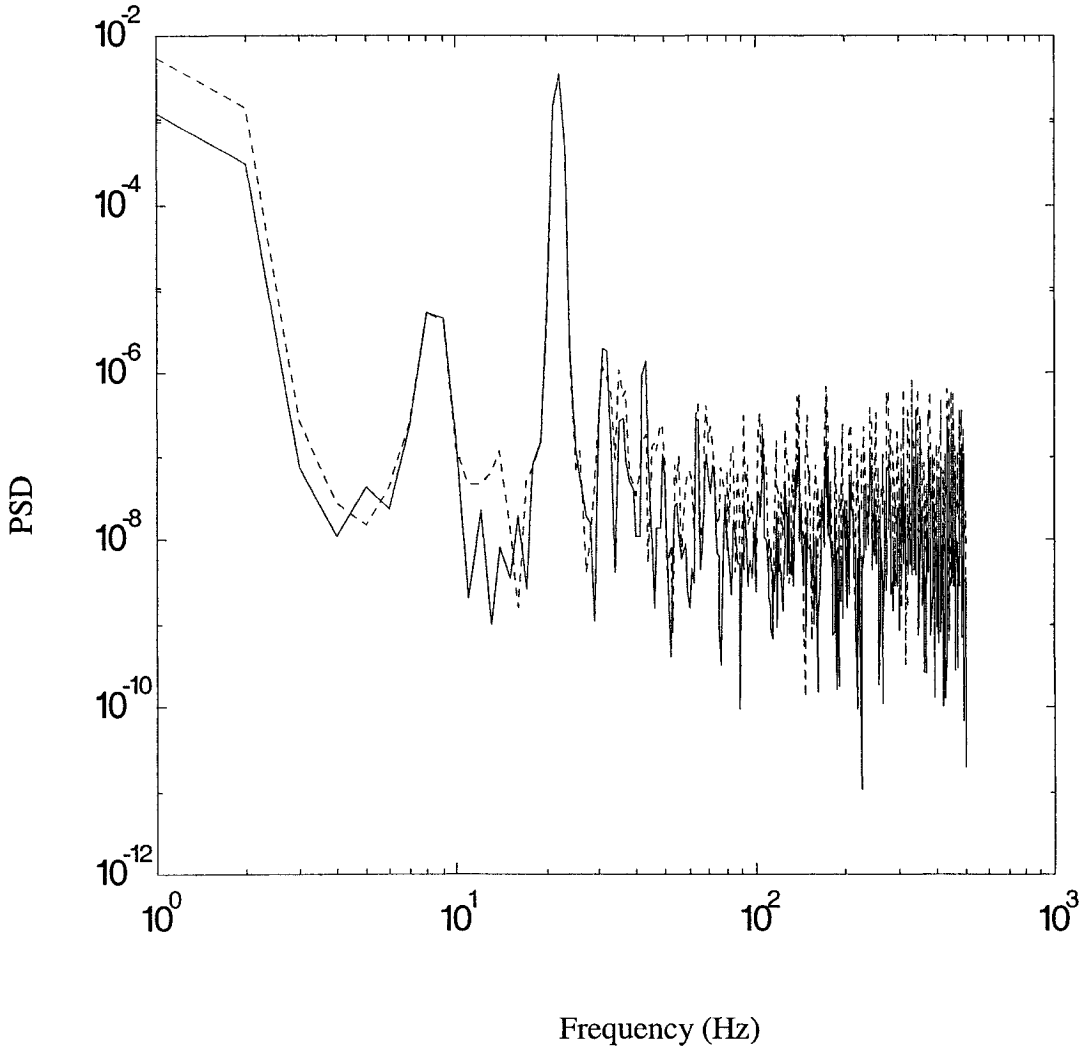


Fig.3.56: Amplitude Spectral Density for speed of 1280 rpm.

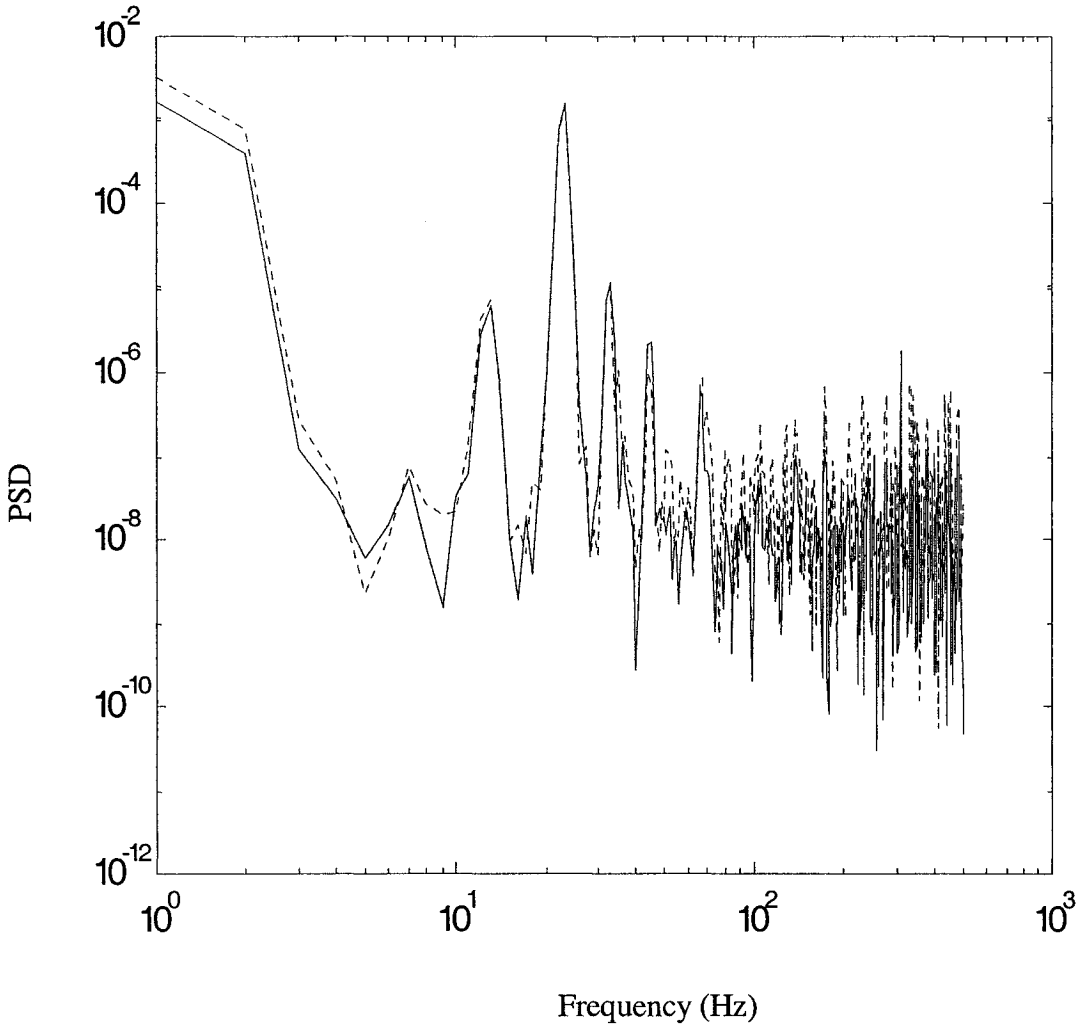


Fig.3.57: Amplitude Spectral Density for speed of 1359 rpm.

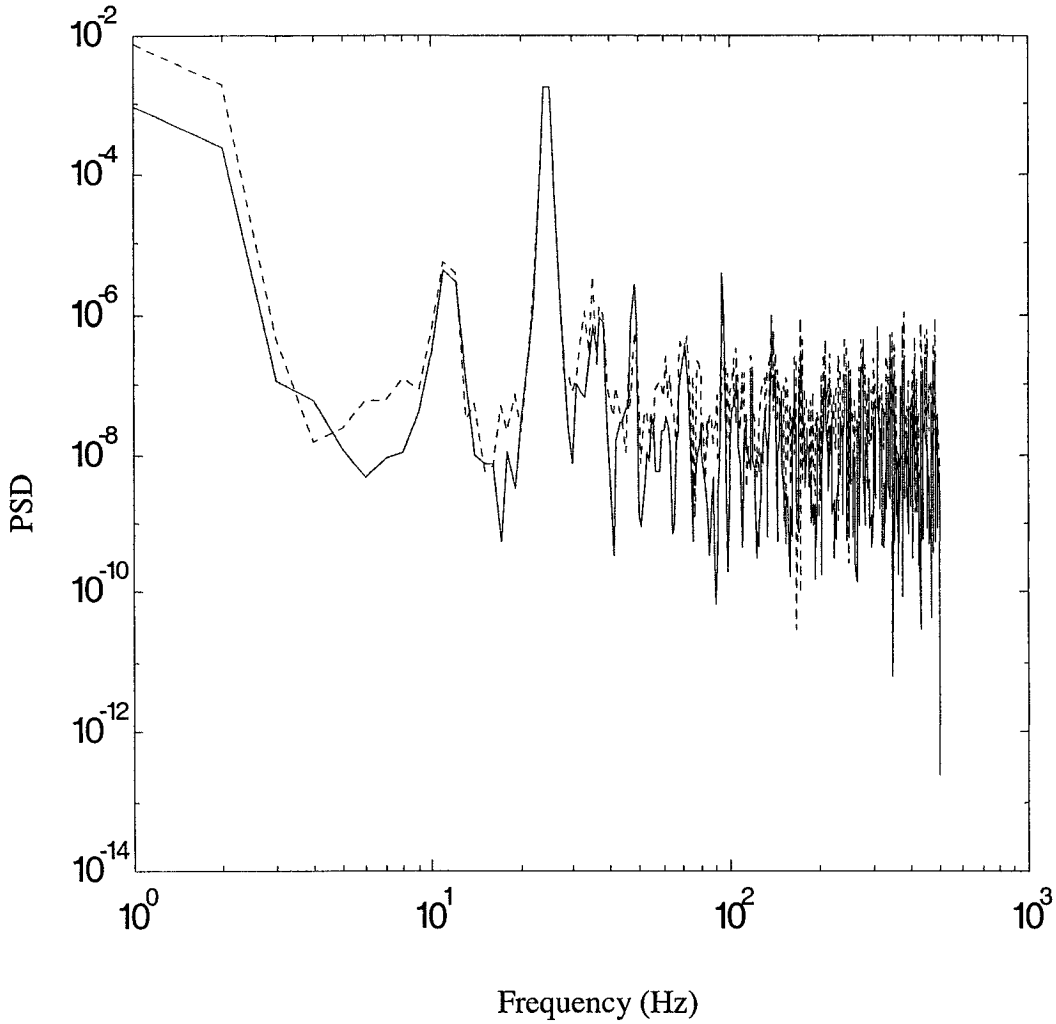


Fig.3.58: Amplitude Spectral Density for speed of 1440 rpm.

## 3.5 Part-3: Measurement of the whirling motion of the boring-bar-workpiece assembly under different cutting parameters

As mentioned before, the hole making operation usually depends upon the following requirements: diameter of the hole; depth of the hole; quality of the hole surface; size, accuracy and parallelism and straightness. Machining holes of high length-to-diameter ratios to high standards of size, parallelism, straightness and surface finish, has always presented problems. Hole straightness deteriorates when the hole length to diameter ratio exceeds 10. One of the most significant technological advances made during the past thirty years to help solve the above-mentioned problems has been the development of hole machining with self-piloting tools.

In the next chapter some observations of surface integrity in deep hole drilling process will be discussed for part three of the experiment to examine the effect of varying the cutting parameters on the outcome surface finish.

### 3.7.1 Experimental procedures for part-3

When it is difficult to establish a mathematical solution between several parameters contributing to an output process, a statistical relation between such independent and dependent parameters can be established. In such cases it is necessary to collect an appropriate set of data to analyze it statistically, or using other techniques such as fuzzy model approach in order to get the best objective conclusions. All the factors in the

experiment will be varied simultaneously or sequentially in order to collect such data. The experiment under study may be characterized by several inputs and several important output parameters, however; they are chosen in an optimum fashion. Such parameters should be effective in our study and should be easily measured. Each input variable has a certain range of variation, which can be determined through experience or as a result of other studies.

Experiments were carried out using BTA system solid boring head of 25.4 mm diameter. The material of the work piece was medium carbon steel. Tests were repeated for different cutting parameters (cutting speed, feed and cutting fluid flow rate) at different lengths of cut or tool penetration on the surface roughness and geometrical dimensioning and tolerancing of the machined hole in BTA drilling. The choice of the optimized parameters and the selection of the involved factors and the range of each factors were done and a series of tests were carried out to collect the data in each test. The collected data was evaluated using fuzzy logic model, analyzed and finally optimized.

The system can be represented mathematically using a fuzzy model with the aid of the neural network system. To get the best number of rules that will describe the system, subtractive clustering technique was employed and the initial membership function was tuned by ANFIS. Then the surface response of the system was plotted. From these plots it was possible to get the optimum parameters to minimize the surface irregularities. The matrix is as shown in table 3.7.

Table 3.7: Different cutting parameters for part-3 of the experiment.

| Speed (rev/min) | Feed (mm/min) | Flow rate (G/min) | Specimen no. | Location (length) mm (Inch) | At the Same length |
|---|---|---|---|---|---|
| 1040 | 71 | 20 | 1 | 76.2 (3) | 1,7,8,13,19,25 |
| 1040 | 117 | 20 | 2 | 228.6 (9) | 2,9,14,20,26 |
| 1040 | 173 | 20 | 3 | 381 (15) | 3,10,15,21,27 |
| 1240 | 71 | 20 | 4 | 533.4 (21) | 4,11,16,22 |
| 1240 | 117 | 20 | 5 | 685.8 (27) | 5,12,17,23 |
| 1240 | 173 | 20 | 6 | 838.2 (33) | 6,18,24 |
| 1440 | 71 | 20 | 7 | 76.2 (3) | |
| 1440 | 117 | 20 | 8 | 76.2 (3) | |
| 1440 | 173 | 20 | 9 | 228.6 (9) | |
| 1040 | 71 | 30 | 10 | 381 (15) | |
| 1040 | 117 | 30 | 11 | 533.4 (21) | |
| 1040 | 173 | 30 | 12 | 685.8 (27) | |
| 1240 | 71 | 30 | 13 | 76.2 (3) | |
| 1240 | 117 | 30 | 14 | 228.6 (9) | |
| 1240 | 173 | 30 | 15 | 381 (15) | |
| 1440 | 71 | 30 | 16 | 533.4 (21) | |
| 1440 | 117 | 30 | 17 | 685.8 (27) | |
| 1440 | 173 | 30 | 18 | 838.2 (33) | |
| 1040 | 71 | 40 | 19 | 76.2 (3) | |
| 1040 | 117 | 40 | 20 | 228.6 (9) | |
| 1040 | 173 | 40 | 21 | 381 (15) | |
| 1240 | 71 | 40 | 22 | 533.4 (21) | |
| 1240 | 117 | 40 | 23 | 685.8 (27) | |
| 1240 | 173 | 40 | 24 | 838.2 (33) | |
| 1440 | 71 | 40 | 25 | 76.2 (3) | |
| 1440 | 117 | 40 | 26 | 228.6 (9) | |
| 1440 | 173 | 40 | 27 | 381 (15) | |

In this chapter, experiments were carried out in order to verify the analytical model. Chapter 4 will investigate the effect of whirling vibration of the boring bar on the outcome surface irregularities and geometrical dimensioning and tolerancing in BTA deep hole boring process under different cutting conditions.

# CHAPTER 4

# SURFACE ROUGHNESS AND GEOMETRIC DIMENSIONING AND TOLERANCING IN DEEP HOLE MACHINING PROCESS

The previous chapter described the experiments that were carried out by varying the cutting parameters in order to study their effect on the whirling motion and on the outcome surface irregularities. In this chapter, the cutting parameters (speed, feed and flow rate) were varied at different lengths of cut or tool penetration. The whirling motion will be plotted for each cutting parameter combination. Some surface irregularities will be investigated in order to study the effect of whirling motion in deteriorating the surface quality and tolerancing.

## 4.1 Some observations of surface integrity in deep hole drilling

Surface integrity is defined as the inherent or enhanced condition of a surface produced in machining or other surface generation operation. The term surface integrity has become widely accepted and is now used extensively in technical literature. Four of the most important surface and geometric parameters [42,43,69] under this study are:

### 1- Roundness.

## 2- Cylindricity

## 3- Straightness

## 4- Surface roughness

Each of them will be explained, studied and discussed through specimens taken from an actual experiment.

### 4.1.1 Roundness:

Perfect **roundness** is very important in order to have smooth relative rotational motions among engineering components. First, the circular cross section is the most frequently used basic shape in engineering design [117]. Secondly, the quality of roundness affects the exact functioning of most kinds of machinery. In view of the above, the conditions of roundness quality, external and internal, require the most attention in any form or shape measurement. Roundness is the condition of revolution as in cylinder, cone and sphere where all points of the surface intersected by any plane (1) have to be perpendicular to a common axis or should pass through a common center equidistant from the axis or center, [45,116].

**(a) Roundness tolerance**

A roundness tolerance gives an idea about the tolerance zone that is bounded by two coplanar concentric circles in that plane within which the actual surface elements must lie

[116,117]. A roundness tolerance zone is established relative to the actual size of the part when measured at the surface periphery at any cross section perpendicular (normal) to the longitudinal axis. It should be noted here that roundness tolerance applies only at the cross-sectional point of measurement, and is relative to the size at that section. Therefore, a cylindrical part with roundness tolerance control could taper or otherwise vary in its surface control within its size tolerance range, yet still meet roundness requirements if it is within the roundness tolerance zone at that cross section, as we will see in the experimental results.

The tolerance zone is established relative to the part size at any cross section along the surface. In other wards the part size is first determined and then its roundness is defined as a refinement of the part form relative to that size. It should also be noted that the roundness tolerance is a form control of a single part element as it compares to a perfect counterpart of itself.

**(b) Checking roundness**

In order to check the roundness, the part surface periphery should be related to the geometry of a perfect circular form, which is constructed about a reference axis. The method used here is an electronic talyround (Taylor Hobson Talyround 262, Fig. 4.1) where the part rotates in the roundness test between 2-6 rpm with a 2 mm stylus head diameter. While the specimen rotates, the stylus scans around the internal hole of the specimen at specified cross section as the specimen is perfectly mounted on an accurate spindle. The traced profile is magnified and plotted in a polar plot. This enlarged scanned profile is then compared with a transparent overlay gage, which includes circles at

different radii. The final basis of comparison is the specimen at certain intersection (like the 152.4 mm (6 in) specimen in our case) with a reference circle on a polar graph. There are four types of reference circles used for comparison [115]. The least square circle, the minimum zone circle, minimum circumscribed circle and the maximum inscribed circle. In our measurement we used both the least square circle and the minimum zone circle as references.

**1. Least Square Reference Circle**

The Least Squares circle is a circle fitted on to the profile to be measured where the sum of areas inside this circle are equal to the sum of the areas outside the circle as shown in Fig.4.2, [115,116]. An example at one intersection of a specimen is done below to illustrate this method. The specimen used for the example is machined at speed of 1040 rpm, feed of 117 mm/min and flow rate of 20 G/min at 88.9 mm (3.5 inch) length of cut. The out of roundness value is the difference between the maximum and minimum radial departure from the reference circle center.

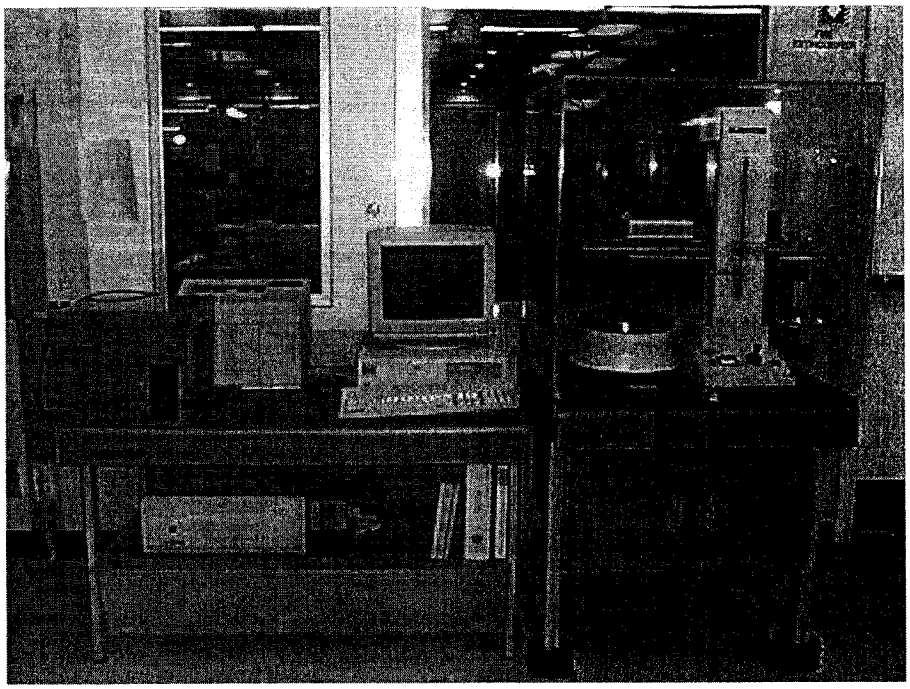

Fig. 4.1: Talyround 262, Horizontal and Vertical Straightness, Roundness, & Cylindricity measurement [120].

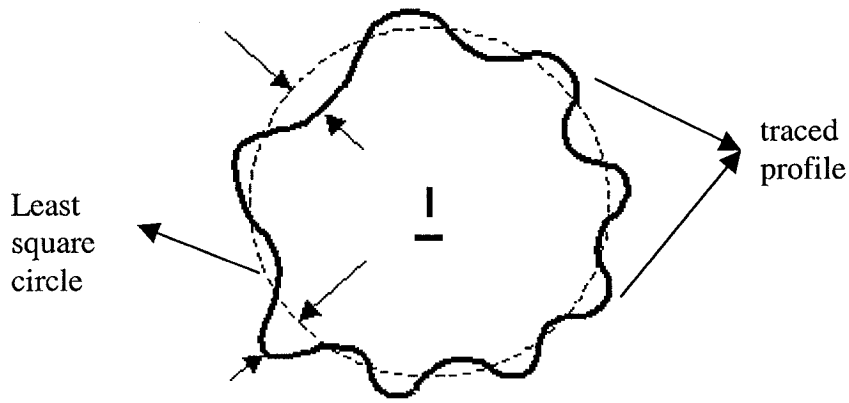


Fig.4.2: A traced profile with a least square reference circle [120].

**2. Minimum Zone Circle**

The minimum zone circle is defined as two concentric circles positioned to just enclose the measured profile such that their radial departure is a minimum. The roundness value is then given as their radial separation, or the peak to valley difference from a reference circle used. The reference circle that is used in our roundness value is shown in Fig. 4.3.

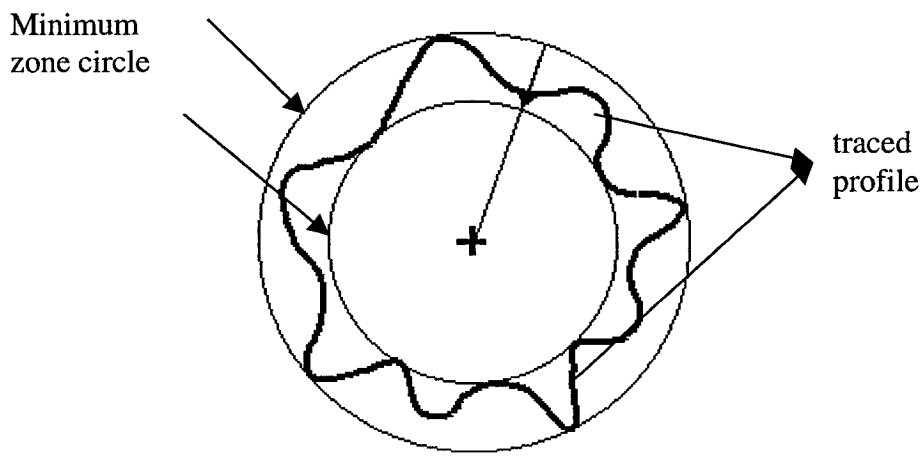


Fig.4.3: A traced profile with a minimum zone reference circle [118].

These two types of circles explained above are the most commonly used references.

**- Least square reference circle calculation:**

The procedure followed to calculate the least square circle from a scanned profile is presented below. The traced section corresponding to the specimen at a speed of 1040 rpm, feed of 117 mm/min and flow rate of 20 G/min at 88.9 mm (3.5 inch) length of cut

is used for this purpose. As seen in the traced profile, 18 radial ordinates are drawn relative to the center of the chart and numbered 1 to 18 as shown in Fig. 4.4. The rectangular coordinates of the point of intersection between each ordinate are measured with respect to the x and y axes, taking the sign into account. These are tabulated, as shown in table 4.1, and the values of $\sum x$ and $\sum y$ are used to establish the center of the least squares circle with respect to the center of the chart. The radial distance between each point of intersection and the least squares center may now be measured and used to calculate the radius of the least squares circle (see A6 in Appendix A). The roundness error is determined on the basis of the maximum peak to least squares circle plus maximum valley to least squares circle. This value, in the example, equals to 19.34 $\mu$m (76.0 $\mu$in).

From table 4.1 it is found out that:

$$a = \frac{2\sum x}{18} = \frac{2\times 274.99}{18} = 7.7597\,\mu m\ (30.55\ \mu in)$$

$$b = \frac{2\sum y}{18} = \frac{2\times -340.76}{18} = 9.6164\ \mu m (-37.86 \mu in)$$

$$R = \frac{\sum r}{18} = \frac{4171.09}{18} = 58.856\ \mu m (231.72\ \mu in)$$

where a and b are the least square rectangular coordinates of the center and R is the radius. Hence, we have 58.856 $\mu$m (231.72 $\mu$in) LSC (least squares centre).

Table 4.1: Calculation of least squares center and radius.

| Position | X ($\mu$in) | Y ($\mu$in) | r ($\mu$in) |
|---|---|---|---|
| 1 | 0 | 201.92 | 201.92 |
| 2 | 86.53 | 226.92 | 240.38 |
| 3 | 165.38 | 40 | 257.69 |
| 4 | 225 | 128.84 | 259.61 |
| 5 | 246.15 | 51.92 | 251.92 |
| 6 | 246.15 | 0 | 246.15 |
| 7 | 217.3 | -46.15 | 232.69 |
| 8 | 169.23 | -134.61 | 215.38 |
| 9 | 113.46 | -157.69 | 196.15 |
| 10 | 73.07 | -184.61 | 198.07 |
| 11 | 0 | -203.84 | 203.84 |
| 12 | -84.61 | -211.53 | 228.84 |
| 13 | -165.38 | -200 | 253.84 |
| 14 | -219.23 | -126.92 | 257.69 |
| 15 | -259.61 | -50 | 263.46 |
| 16 | -238.46 | 50 | 244.23 |
| 17 | -192.3 | 115.38 | 225 |
| 18 | -107.69 | 159.61 | 194.23 |
| Sum | 274.99 | -340.76 | 4171.09 |

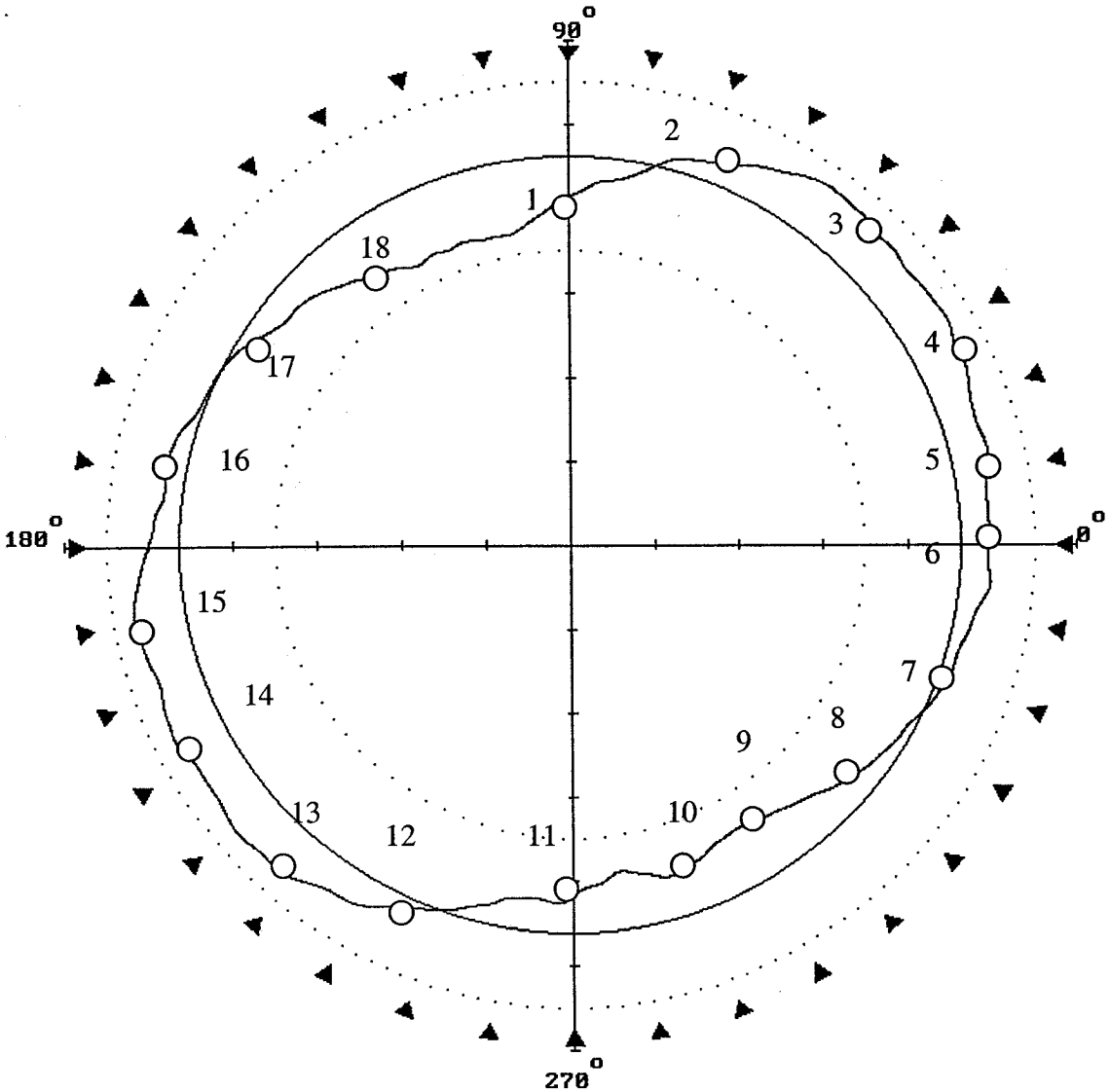


Fig. 4.4: Roundness test diagram at one intersection for one specimen

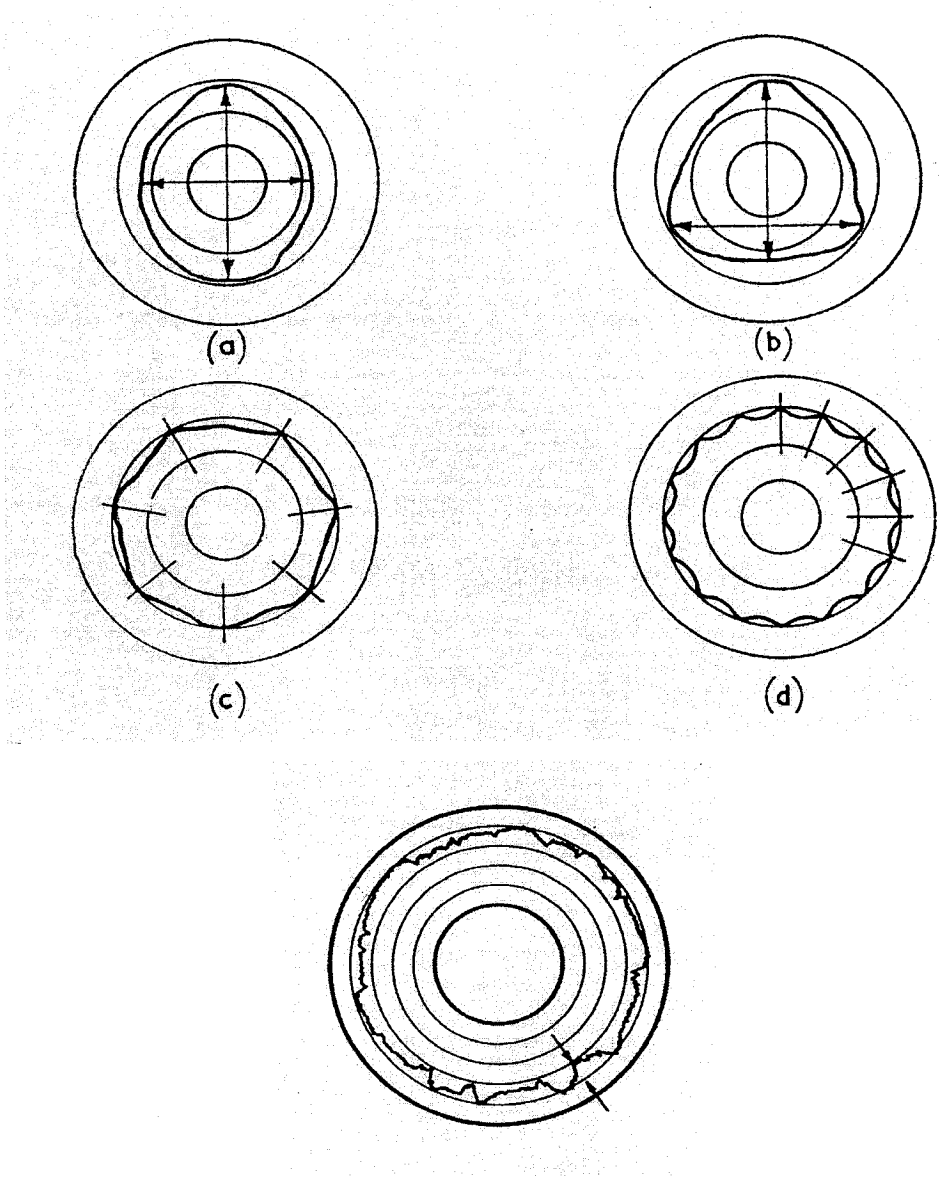


Fig. 4.5: Out of roundness modes- predominant characteristics (a) Ovality with unequal and approximately orthogonal axis, (b) 3-lobed out of roundness, (c) Odd number of undulations of approximately equal spacing, 7-lobed out of roundness, (d) A lobing situation with higher frequency, and (e) Random irregularities [116].

The predominant characteristics of the out of roundness modes are shown in Fig. 4.5. The out of roundness could be a combination of these different modes i.e. two lobed with random irregularities.

### 4.1.2 Cylindricity

Cylindricity is the condition on a surface of revolution in which all elements form a cylinder, or it is a condition of a surface in which all points of the surface are the same distance from a common axis [65, 119]. The cylindricity tolerance is a composite control of form that includes circularity (roundness), and parallelism of the surface elements of a cylindrical feature. A cylindricity tolerance specifies a tolerance zone confined to the annular space between two concentric cylinders within which the surface must lie. Cylindricity tolerancing can be applied only to cylindrical forms.

It should be noted here that a cylindricity tolerance simultaneously controls roundness, straightness and parallelism of the elements of the cylindrical surface. A cylindricity tolerance applies to the entire cylindrical surface as opposed to the cross-sectional or diametral measurement considered in roundness. Also, in measuring cylindricity, the concentric cylinders defining the tolerance zone are always based on the size of the part produced. It should be noted here that the cylindricity tolerance must always be contained within the part size tolerance range. The cylindricity tolerance cannot exceed the size tolerance limits. As will be seen in the following examples, the cylindricity tolerance zone is established relative to the part size wherever it may fall in its size tolerance range.

The cylindricity tolerance is a form control of a surface element as it compares to a perfect matching part of itself.

Cylindricity values are becoming more important in the measurement of components particularly as an aid to improve the efficiency and cost effectiveness of systems. An example is the automotive fuel injection, where the need for high economy is demanding greater precision in different components. There are many ways of defining cylindricity of a component. A good example is the minimum zone method of analysis. This can be identified as the radial separation of 2 co-axial cylinders fitted to the total measured surface under test such that their radial difference is at a minimum. Fig. 4.6 is an example.

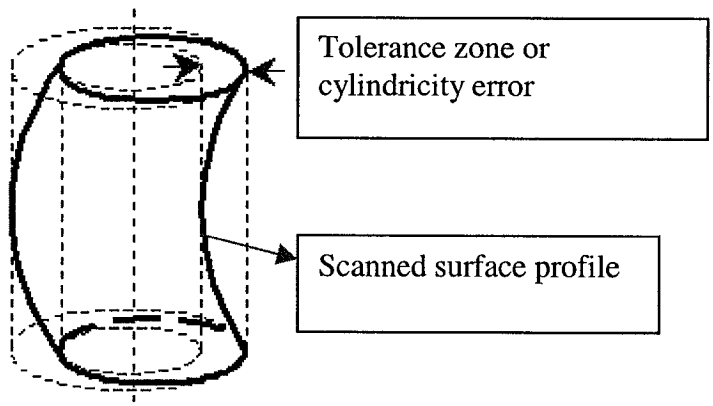


Fig. 4.6: Defining tolerance zone or cylindricity error value.

As in roundness where we have different types of reference circles for comparisons, for a cylinder we have a reference cylinder, which is a true cylinder fitted to the scanned data in order to measure the deviations from it. There are four internationally recognized reference cylinders. These are the least squares cylinder, minimum zone cylinder,

maximum inscribed and minimum circumscribed cylinders. These cylinders are explained in Appendix A.

### (a) Checking cylindricity

Cylindricity is checked or measured by the same basic techniques that are used to check roundness except that cylindricity involves a cylindrical tolerance zone of uniform thickness over the entire surface and is based on a single size reference. In roundness the measurements were at cross sections only, whereas in cylindricity, one must consider the entire surface as controlled by the one tolerance zone. It should be noted here that roundness tolerance applies only at the cross-sectional point of measurement, and is relative to the size at that section. Therefore, a cylindrical part with roundness tolerance control could taper or otherwise vary in its surface control within its size tolerance range, yet still meet roundness requirements if it is within the roundness tolerance at that cross section. Hence, the cylindricity error is taking into consideration the roundness error at different sections of the cylinder piece.

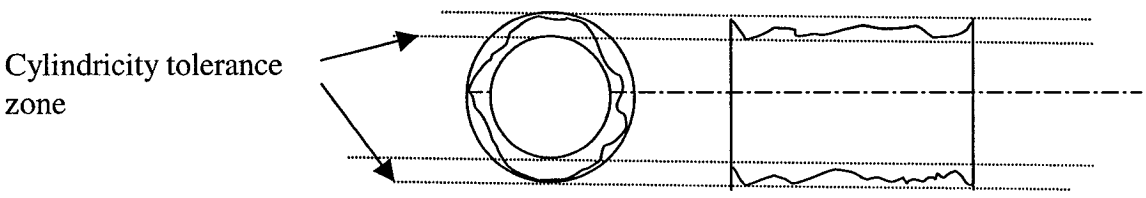


Fig. 4.7: Example of cylindricity error

As shown in Fig. 4.7, the feature must be within the specified tolerance of size and must lie between two concentric cylinders. Also from Fig. 4.7 it should be noted that in the

case of cylindricity unlike that of circularity, the tolerance applies simultaneously to both circular and longitudinal elements of the surface [116].

Cylindricity tolerances can be applied only to cylindrical surfaces, such as round holes and shafts. Errors of cylindricity may be caused by out-of-roundness such as ovality or lobing, by errors of straightness caused by bending or by diametral variation, by errors of parallelism, conicity or taper and by random irregularities from a real cylindrical form.

Finally, cylindricity is a powerful tool that combines data from multiple roundness profiles into a single geometric figure.

### 4.1.3 Straightness

Straightness is a condition where an element of a surface is a straight line. A straightness tolerance specifies a tolerance zone of uniform width along a straight line within which all points of the considered line must lie [117]. Straightness is a type of form control in which elements (usually longitudinal of a surface) are permitted to vary within the stated tolerance. Straightness tolerance is typically used as a form control of longitudinal elements of cylindrical or conical surfaces. A straightness requirement applies to the entire surface as controlled or measured in a single line movement in the direction (usually longitudinal) specified. The straightness tolerance zone reads, as "Each longitudinal element of this surface shall be straight within the tolerance zone specified". The straightness tolerance on a cylindrical part may be considered in combination with

other elements of form such as roundness and straightness, since "cylindricity" may provide more effective control. Fig. 4.8 is an illustration of straightness error.

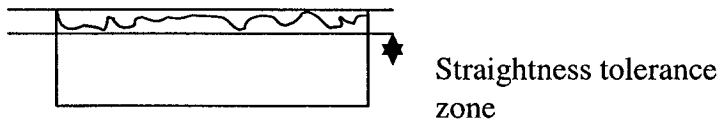


Fig. 4.8: Straightness tolerance zone example.

### 4.1.4 Roughness:

Surface metrology may be broadly defined as the measurement of the difference between what the surface actually is and what it is intended to be. Roughness is an average deviation from a mean center line [42, 50].

The measurement of surface roughness is defined by several international standards. These standards cover characteristics of the measurement equipment as well as defining the mathematical definition of the many parameters. A few important definitions are: Roughness, which is a quantitative measure of the process marks produced during the creation of the surface, i.e. machining and other factors such as the structure of the material. Waviness is a longer wavelength variation in surface away from its basic form (e.g. straight). Forms are the general shape of the surface, as seen in Fig. 4.9. The deviations from the desired form can be caused by many factors [42]. i.e. :

- The part being fixed very well or not

- Some inaccuracies of the guideways of the different machines used
- Stresses developed in the workpiece.

In order to measure these process marks, many methods have been used as described in references [42,44,69].

Initially simple analogue instruments were used, employing an amplifier, chart recorder and meter to give graphical and numerical output. With the arrival of mini-computers, over twenty years ago, numerical analysis of the information obtained became a possibility. Using this new technology a host of parameters became available. It is now commonplace for the filtering to be implemented by means of digital filter algorithms rather than through electronic circuits.

Every surface has some form of texture that takes the form of a series of peaks and valleys. These peaks and valleys vary in height and spacing and have properties that are a result of the way the surface was produced. For example, surfaces produced by cutting tools tend to have uniform spacing with defined cutting directions whilst those produced by grinding have random spacing.

In surface texture there are many factors that, when combined, characterize a surface's profile [116]. For example:

- The microstructure of the workpiece material
- The inherent action of the production process or the cutting tool
- The instability of the type of the cutting tool used on the workpiece material

- Errors in the machine tool slides
- Deformations in the components due to stresses

Surface, Waviness and Form are rarely found in isolation. Most surfaces are a combination of all three and it is usual to assess them separately. Roughness consists of finer irregularities in the surface texture usually including those irregularities, which result from the inherent action of a production process. These are considered to include traverse feed marks and other irregularities within the limits of the roughness-width cut off. Roughness width cut off is the greatest spacing of repetitive surface irregularities to be included in the measurement of average roughness height.

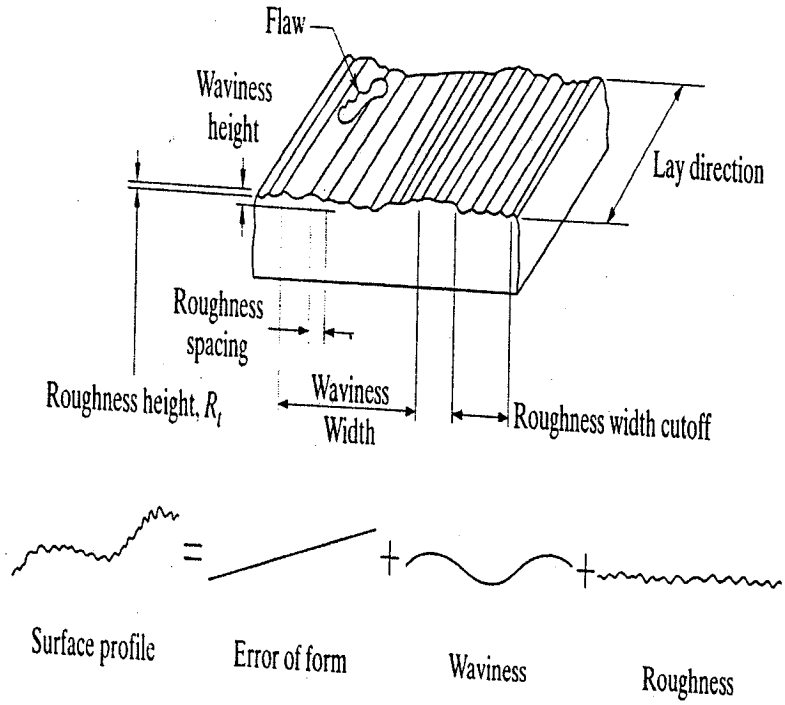


Fig. 4.9: Standard terminology to describe surface finish [116].

It is possible to give the surface texture a numerical value in one of several different ways. The following are the most commonly used values:

- Arithmetic Mean Deviation of the profile ($R_a$): Consider the roughness profile and place a straight line through it as shown in Fig. 4.10 such that for some evaluation length L the sum of the area above this line is equal to the sum of area below. This line is called the centerline. If we consider the center line as X-axis then let the roughness curve be defind by some function $f(x)$. The arithmetic mean deviation is the mean of $f(x)$ over the evaluation length L as shown in Fig. 4.11. It is called the center line average CLA and is given by the equation:

$$R_a = \frac{1}{L}\int_0^L f(x)\,dx \tag{4.1}$$

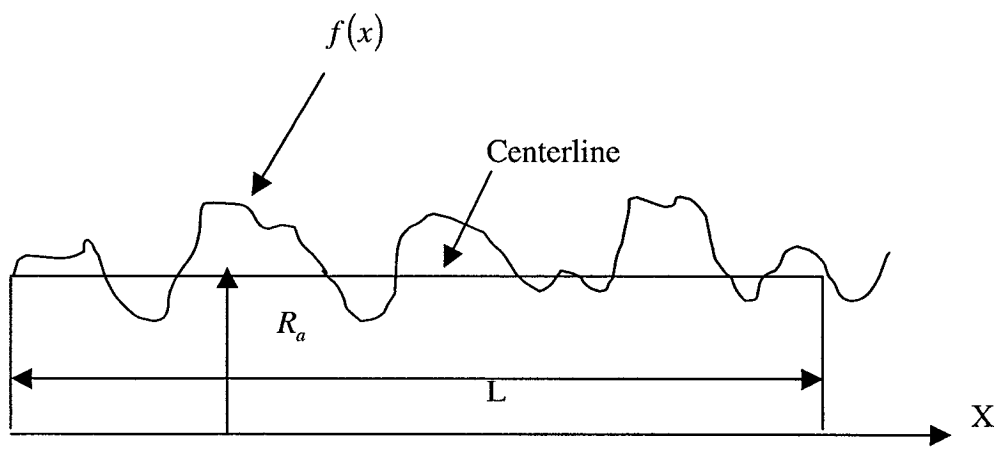


Fig. 4.10: center line of roughness profile

- The root mean square average ($R_q$ or RMS), is defined as :

$$R_q = \sqrt{\frac{1}{L}\int_0^L f^2(x)\ dx} \tag{4.2}$$

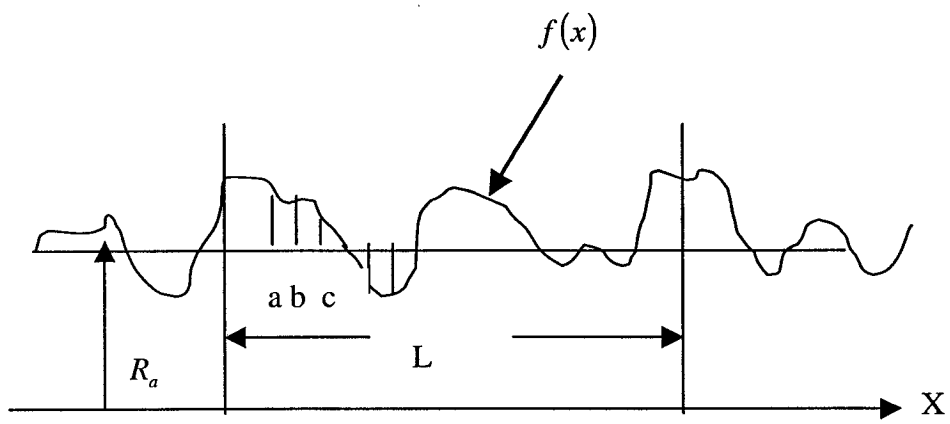


Fig. 4.11: Arithmetic average mean deviation of the roughness curve ($R_a$)

**(a) Measurement of roughness**

Roughness is measured using a stylus instrument. This measurement is based on the amplification of the movement of a finely pointed probe or stylus as it is moved across the surface. The essential features of such an instrument, a Mitutoyo SJ-400 surface roughness tester, is shown in Fig. 4.12. It consists of:

(a) a measuring head carrying a stylus with provision to magnify its vertical and horizontal movements.

(b) a means of traversing the measuring head across the surface to be measured. Mechanical means have been used for this.

(c) a means of providing a graphical representation and numerical values of the surface. The magnification of the stylus movement by electrical means to provide a graphical record, and the integration of the electrical output to provide a centerline average meter reading, is by far the most common technique used in surface-finish measuring instruments. The cut off distance that the stylus can travel in this kind of surface profilemeter is 13.3 mm. The cutoff is so important in that it should include 10 to 15 roughness irregularities as well as all surface waviness.

All kind of surface irregularities mentioned before such as geometrical dimensioning and tolerances (Roundness, Cylindricity and straightness) and surface roughness measurement were done on 27 specimens as seen in Fig. 4.13.

Each specimen is labeled D1, D2, and D3... D27, corresponding to a certain combination of cutting parameters, speed of cut, feed rate and flow rate at different depth of cut (tool penetration). Each specimen length is 152.4 mm (6 inches). These parameter combinations corresponding to each specimen are presented in table 4.2.

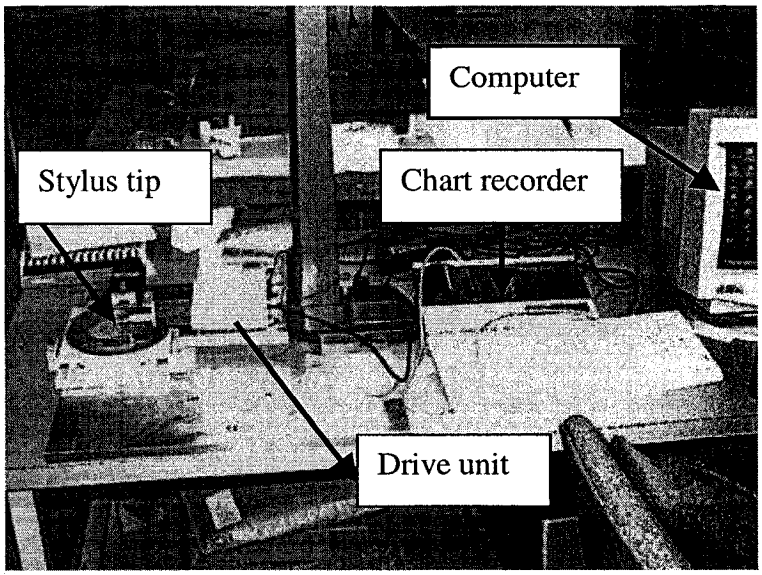


Fig.4.12: Mitutoyo SJ-400 surface roughness tester.

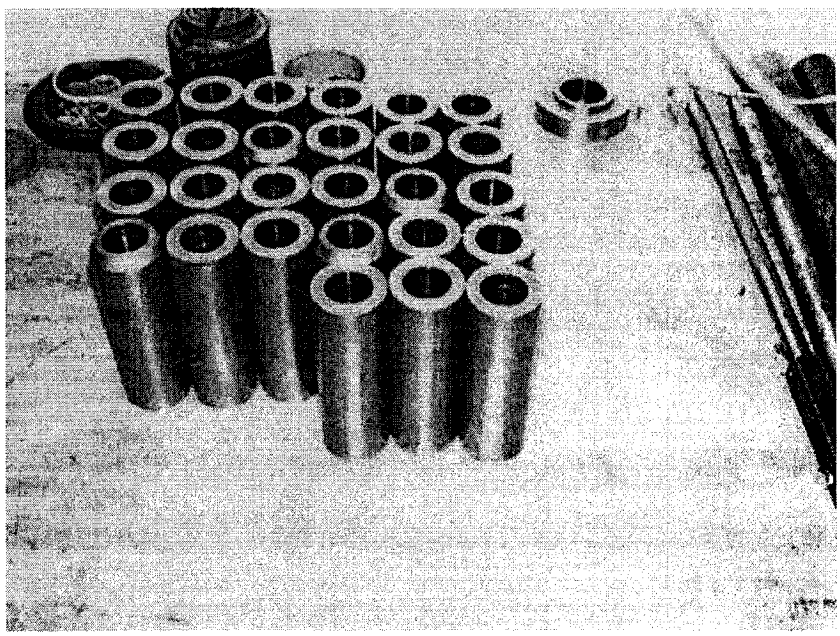

Fig. 4.13: The 27 specimens used for surface irregularity measurements.

For roundness measurement, the measurements were taken in the direction of drilling and up, at 12.7 mm, 38.1 mm, 63.5 mm, 88.9 mm, 114.3 mm and 139.7 mm (0.5 in, 1.5 in,

2.5 in, 3.5 in, 4.5 in and 5.5 in). For straightness the stylus scans one side of each specimen. For roughness evaluation, 8 measurements were taken following the direction of drilling.

Table 4.2: 27 specimens with different combinations of cutting parameters at different length of cut.

| Speed (rev/min) | Feed (mm/min) | Flow rate (G/min) | Specimen no. | Location (length) (Inch) | Location (length) (mm) |
|---|---|---|---|---|---|
| 1040 | 71 | 20 | D1 | 3 | 76.2 |
| 1040 | 117 | 20 | D2 | 9 | 228.6 |
| 1040 | 173 | 20 | D3 | 15 | 381 |
| 1240 | 71 | 20 | D4 | 21 | 533.4 |
| 1240 | 117 | 20 | D5 | 27 | 685.8 |
| 1240 | 173 | 20 | D6 | 33 | 838.2 |
| 1440 | 71 | 20 | D7 | 3 | 76.2 |
| 1440 | 117 | 20 | D8 | 3 | 76.2 |
| 1440 | 173 | 20 | D9 | 9 | 228.6 |
| 1040 | 71 | 30 | D10 | 15 | 381 |
| 1040 | 117 | 30 | D11 | 21 | 533.4 |
| 1040 | 173 | 30 | D12 | 27 | 685.8 |
| 1240 | 71 | 30 | D13 | 3 | 76.2 |
| 1240 | 117 | 30 | D14 | 9 | 228.6 |
| 1240 | 173 | 30 | D15 | 15 | 381 |
| 1440 | 71 | 30 | D16 | 21 | 533.4 |
| 1440 | 117 | 30 | D17 | 27 | 685.8 |
| 1440 | 173 | 30 | D18 | 33 | 838.2 |
| 1040 | 71 | 40 | D19 | 3 | 76.2 |
| 1040 | 117 | 40 | D20 | 9 | 228.6 |
| 1040 | 173 | 40 | D21 | 15 | 381 |
| 1240 | 71 | 40 | D22 | 21 | 533.4 |
| 1240 | 117 | 40 | D23 | 27 | 685.8 |
| 1240 | 173 | 40 | D24 | 33 | 838.2 |
| 1440 | 71 | 40 | D25 | 3 | 76.2 |
| 1440 | 117 | 40 | D26 | 9 | 228.6 |
| 1440 | 173 | 40 | D27 | 15 | 381 |

## 4.2 Effect of the whirling motion on machined surface

Each of the 27 specimens has a combination of certain cutting parameters at certain length of cut or tool penetration. The results at each length of cut are shown in the following sections. At different tool penetration i.e. 76.2 mm, 228.6 mm, 381 mm, 533.4 mm, 685.8 mm and 838.2 mm (3, 9, 15, 21, 27 and 33 inches) and the corresponding combinations are presented in a table. Each table summarizes the figures of the displacement in the Y and Z coordinates, the whirl ellipse of the boring bar and the first and second natural frequencies of the system.

As mentioned in the previous sections, there are predominant characteristics of certain modes of out-of-roundness. The roundness, cylindricity and straightness errors are also mentioned separately for each specimen. In addition to roundness, cylindricity involves the measurement of the straightness of the cylinder and the uniformity of the size of the cylinder throughout its length. Cylindricity and straightness were almost close in value in some specimens. The roundness shape is characterized by having random irregularities characterized by non-periodic occurrence of significant departures from the round forms and oval with unequal axis approximately perpendicular to each other and of essentially symmetrical position. Some of the specimens have two, three, four, five or seven out of roundness at different sections of the specimen. Tables 4.3, 4.4, 4.5, 4.6, 4.7 and 4.8 are a description of the observations at 76.2 mm, 228.6 mm, 381 mm, 533.4 mm, 685.8 mm and 838.2 mm of tool penetration.

## 4.2.1 Effect of the whirling motion at 76.2 mm length of cut

At 76.2 mm (3 in) the specimens are: D1, D7, D8, D13, D19 and D25. Table 4.3 is a summary of the observations at this tool penetration.

Table 4.3: A description of the main characteristics at a tool penetration of 76.2 mm (3 in).

| Tool penetration of 76.2 mm | Figure number | Speed (rpm) | Feed rate (mm/min) | Flow rate (G/min) |
|---|---|---|---|---|
| D1 | 4.14 | 1040 | 71 | 20 |
| | (a) | Displacement in the Y and Z coordinates | | |
| | (b) | Whirl ellipse | | |
| | (c) | Power spectral density (PSD) | | |
| First and second spectral peaks | | 17.94 Hz, 34.52 Hz | | |
| | 4.15 | Roundness characteristics | | Value ($\mu$m) |
| | (a) | Almost two lobed-out-of-roundness | | 0.028956 |
| | (b) | Random irregularities with ovality | | 0.044958 |
| | (c) | Oval | | 0.049276 |
| | (d) | Oval and irregular | | 0.049276 |
| | (e) | Random irregularities with ovality | | 0.044196 |
| | (f) | Almost true round | | 0.022352 |
| | (g) | Cylindricity error | | 0.204851 |
| | (h) | Straightness error | | 0.124968 |

Table 4.3: A description of the main characteristics at a tool penetration of 76.2 mm (3 in) (continued).

| Tool penetration of 76.2 mm | Figure number | Speed (rpm) | Feed rate (mm/min) | Flow rate (G/min) |
|---|---|---|---|---|
| D7 | 4.16 | 1440 | 71 | 20 |
| | (a) | Displacement in the Y and Z coordinates | | |
| | (b) | Whirl ellipse | | |
| | (c) | Power spectral density (PSD) | | |
| First and second spectral peaks | | 24.12 Hz, 33.70 Hz | | |
| | 4.17 | Roundness characteristics | | Value ($\mu$m) |
| | (a) | Almost two lobed-out-of-roundness | | 0.028956 |
| | (b) | Random irregularities with ovality | | 0.044958 |
| | (c) | Oval | | 0.049276 |
| | (d) | Oval and irregular | | 0.049276 |
| | (e) | Random irregularities with ovality | | 0.044196 |
| | (f) | Almost true round | | 0.022352 |
| | (g) | Cylindricity error | | 0.204851 |
| | (h) | Straightness error | | 0.124968 |
| D8 | 4.18 | 1440 | 117 | 20 |
| | (a) | Displacement in the Y and Z coordinates | | |
| | (b) | Whirl ellipse | | |
| | (c) | Power spectral density (PSD) | | |
| First and second spectral peaks | | 24.51 Hz, 32.64 Hz | | |
| | 4.19 | Roundness characteristics | | Value ($\mu$m) |
| | (a) | Oval with egg-shaped | | 0.027813 |
| | (b) | Random irregularities with ovality | | 0.046736 |
| | (c) | Random irregularities | | 0.038608 |
| | (d) | Almost true round | | 0.026035 |
| | (e) | Random irregularity | | 0.037084 |
| | (f) | Almost oval | | 0.026416 |
| | (g) | Cylindricity error | | 0.239522 |
| | (h) | Straightness error | | 0.121158 |

Table 4.3: A description of the main characteristics at a tool penetration of 76.2 mm (3 in) (continued).

| Tool penetration of 76.2 mm | Figure number | Speed (rpm) | Feed rate (mm/min) | Flow rate (G/min) |
|---|---|---|---|---|
| D13 | 4.20 | 1240 | 71 | 30 |
| | (a) | Displacement in the Y and Z coordinates | | |
| | (b) | Whirl ellipse | | |
| | (c) | Power spectral density (PSD) | | |
| First and second spectral peaks | | 20.90 Hz, 33.70 Hz | | |
| | 4.21 | Roundness characteristics | | Value ($\mu$m) |
| | (a) | Random irregularity | | 0.023012 |
| | (b) | 3-lobed out of run | | 0.038049 |
| | (c) | 3-lobed out of run | | 0.040386 |
| | (d) | 3-lobed out of run | | 0.044044 |
| | (e) | Random irregularity with interrupted surface | | 0.02987 |
| | (f) | 5-lobed out of run | | 0.029007 |
| | (g) | Cylindricity error | | 0.0235 |
| | (h) | Straightness error | | 0.08351 |
| D19 | 4.22 | 1040 | 71 | 40 |
| | (a) | Displacement in the Y and Z coordinates | | |
| | (b) | Whirl ellipse | | |
| | (c) | Power spectral density (PSD) | | |
| First and second spectral peaks | | 17.54 Hz, 35.35 Hz | | |
| | 4.23 | Roundness characteristics | | Value ($\mu$m) |
| | (a) | Almost ellipse shape | | 0.024486 |
| | (b) | 4-lobed out of run | | 0.045466 |
| | (c) | Random irregularities | | 0.028956 |
| | (d) | Almost true round | | 0.02225 |
| | (e) | 4-lobed out of run | | 0.047244 |
| | (f) | Random irregularities | | 0.031369 |
| | (g) | Cylindricity error | | 0.200152 |
| | (h) | Straightness error | | 0.138303 |

Table 4.3: A description of the main characteristics at a tool penetration of 76.2 mm (3 in) (continued).

| Tool penetration of 76.2 mm | Figure number | Speed (rpm) | Feed rate (mm/min) | Flow rate (G/min) |
|---|---|---|---|---|
| D25 | 4.24 | 1440 | 71 | 40 |
| | (a) | Displacement in the Y and Z coordinates | | |
| | (b) | Whirl ellipse | | |
| | (c) | Power spectral density (PSD) | | |
| First and second spectral peaks | | 24.91 Hz, 32.13 Hz | | |
| | 4.25 | Roundness characteristics | | Value ($\mu$m) |
| | (a) | Oval | | 0.036728 |
| | (b) | Oval | | 0.036779 |
| | (c) | Oval | | 0.025502 |
| | (d) | Oval | | 0.03744 |
| | (e) | Oval | | 0.041275 |
| | (f) | Random irregularities | | 0.03556 |
| | (g) | Cylindricity error | | 0.1002 |
| | (h) | Straightness error | | 0.09677 |

In Fig. 4.15(d) and (e) the roundness shape is characterized by random irregularities. These irregularities are significant departures from the round form.

Low amplitude undulations of high frequency, usually associated with surface roughness, were noticed especially at the last measurement in Fig. 4.19 (f).

In Fig. 4.21(b), high amplitude undulations in the contour of low frequency with interrupted surfaces were noticed in Fig. 4.19 (c), (d) and (e). In order to remove the residual effects caused by the stylus dropping down holes, some means of software

manipulation is required. There are many methods of using software to remove these residual errors. Some of these methods are automatic and capture the unwanted data by detection of the holes [61]. Another possible method is by manual means where the user selects the area for analysis.

In Fig. 4.21 (d) there are random irregularities with 3-lobed out of roundness. In Fig. 4.21 (f) there is an odd number of undulations (5 lobes) of almost similar spacing. In Fig. 4.23 (b) and (d) a medium and low amplitude of undulations of the contour were noticed.

Fig. 4.25 (a), (b), (c), and (d) are oval with one location of interrupted surface. For Fig. 4.25(f) there is a low amplitude of undulation of high frequency.

In Fig. 4.26, the roughness values along the specimen were shown for D1, 7,8,13,19 and 25. For D1, D8 and D25 the roughness was increasing along the specimen in the direction of drilling while for D7, D13 and D19 the roughness was decreasing. Fig. 4.27 and 4.28 are a one-figure plot of roundness and roughness, respectively, for the entire specimen at 3 inch to show the difference between them.

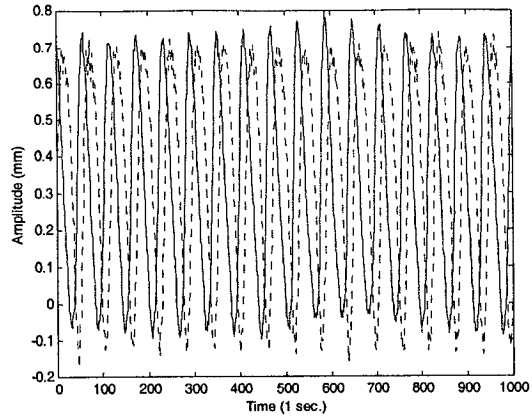


(a)

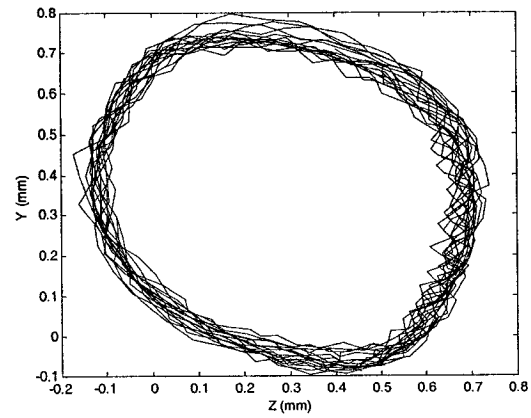


(b)

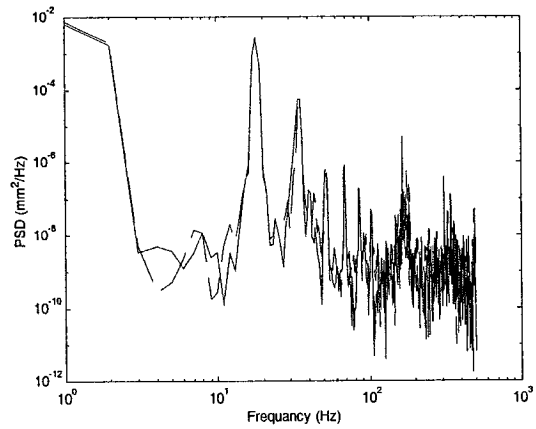


(c)

Fig. 4.14: The signal analysis of D1, (a) The two signals of master and slave sensors, (b) The whirl orbit and (c) the power spectral density of the signal.

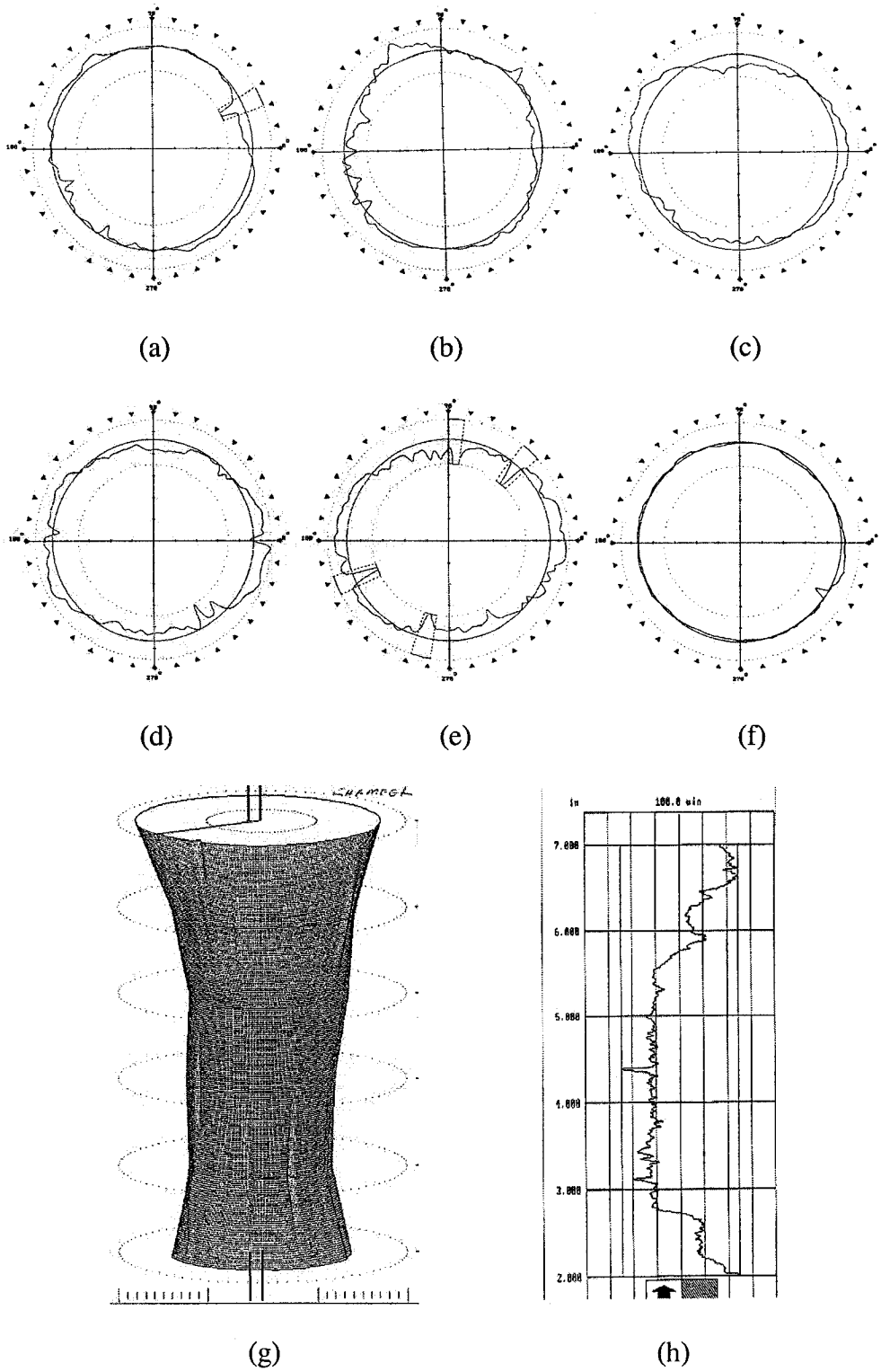


Fig. 4.15: Roundness for D1 from the direction of drilling in mm (a) at 12.7, (b) at 38.1, (c) at 50.8, (d) at 88.9, (e) at 114.3, (f) at 139.7, (g) cylindricity error and (h) Straightness.

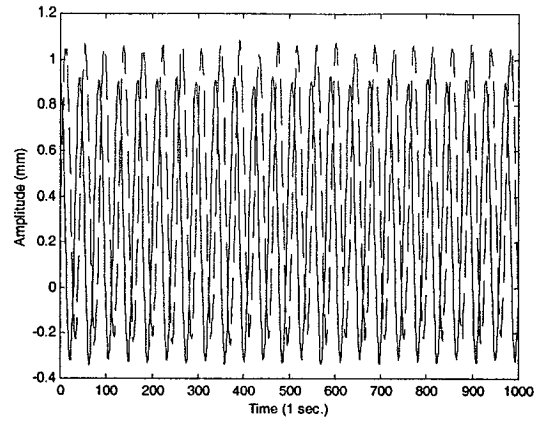


(a)

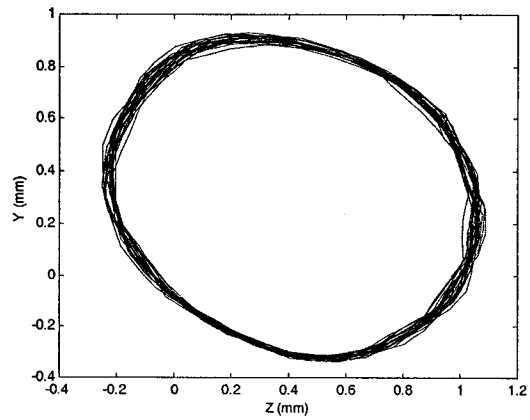


(b)

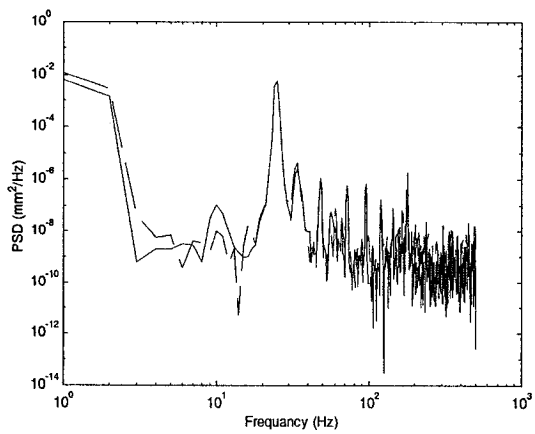


(c)

Fig. 4.16: The signal analysis of D7, (a) The two signals of master and slave sensors, (b) The whirl orbit and (c) the power spectral density of the signal.

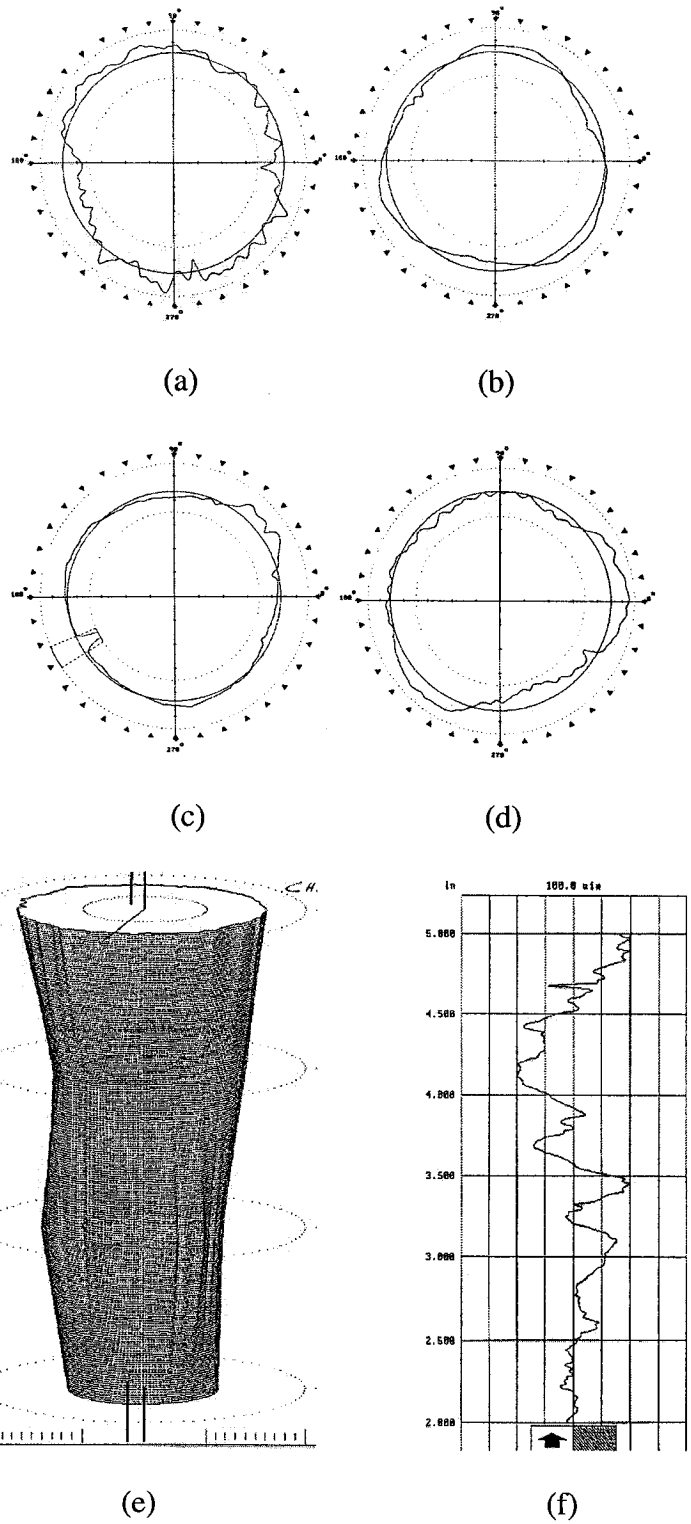


Fig. 4.17: Roundness for D7 from the direction of drilling in mm (a) at 12.7, (b) at 38.1, (c) at 50.8, (d) 88.9, (e) cylindricity and (h) Straightness errors.

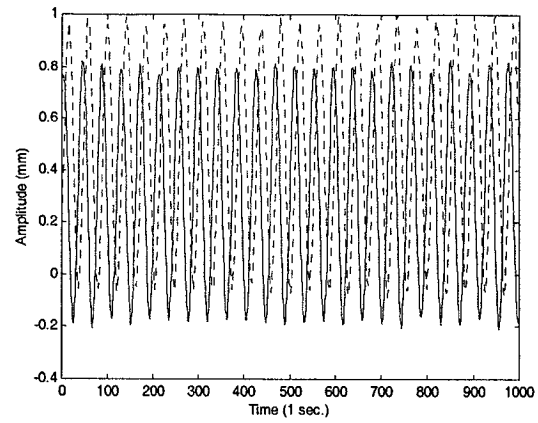


(a)

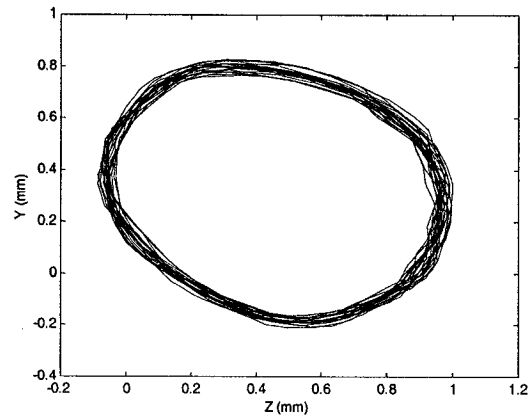


(b)

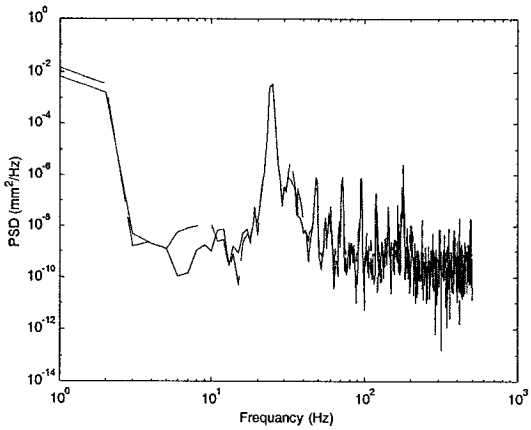


(c)

Fig. 4.18: The signal analysis of D8, (a) The two signals of master and slave sensors, (b) The whirl orbit and (c) the power spectral density of the signal.

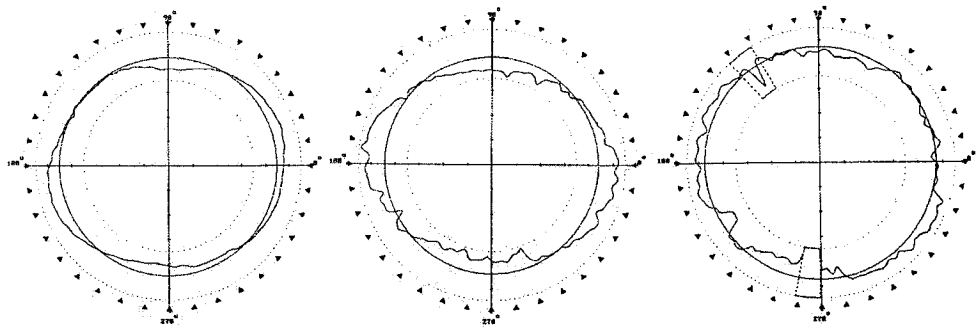

(a) (b) (c)

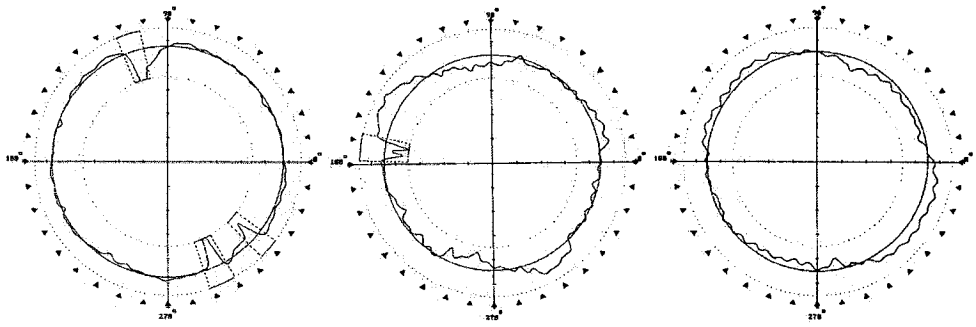

(d) (e) (f)

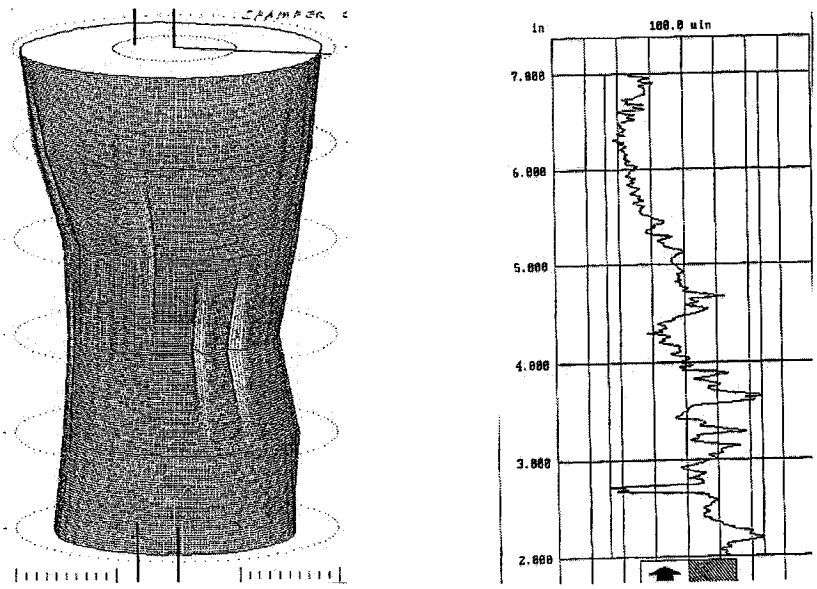


(g) (h)

Fig. 4.19: Roundness for D8 from the direction of drilling in mm (a) at 12.7, (b) at 38.1, (c) at 50.8, (d) at 88.9, (e) at 114.3, (f) at 139.7, (g) cylindricity error and (h) Straightness.

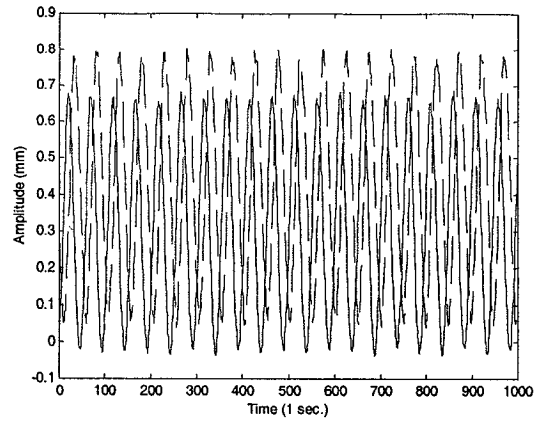


(a)

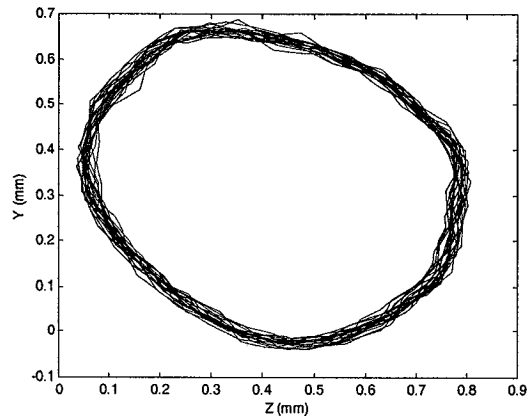


(b)

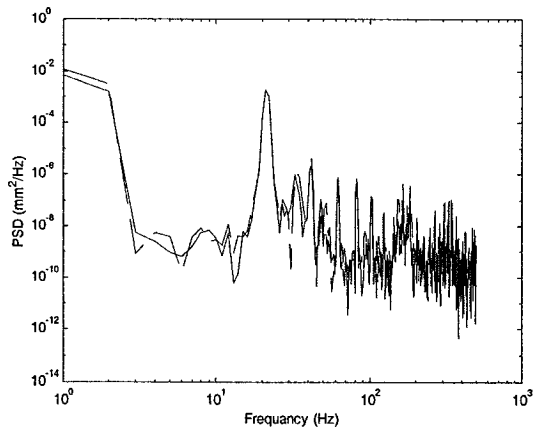


(c)

Fig. 4.20: The signal analysis of D13, (a) The two signals of master and slave sensors, (b) The whirl orbit and (c) the power spectral density of the signal.

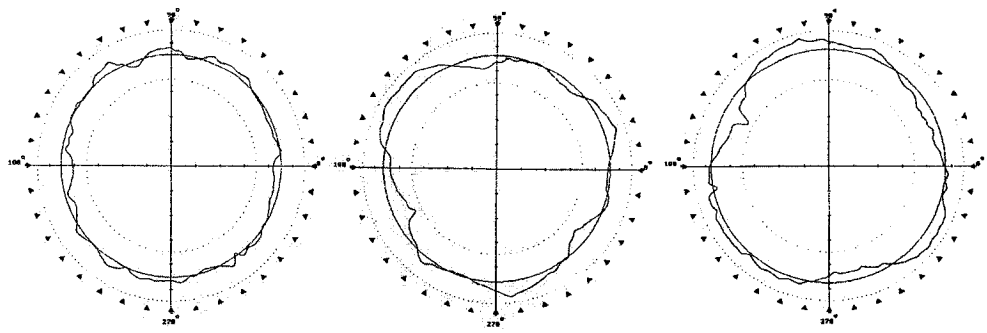

(a) (b) (c)

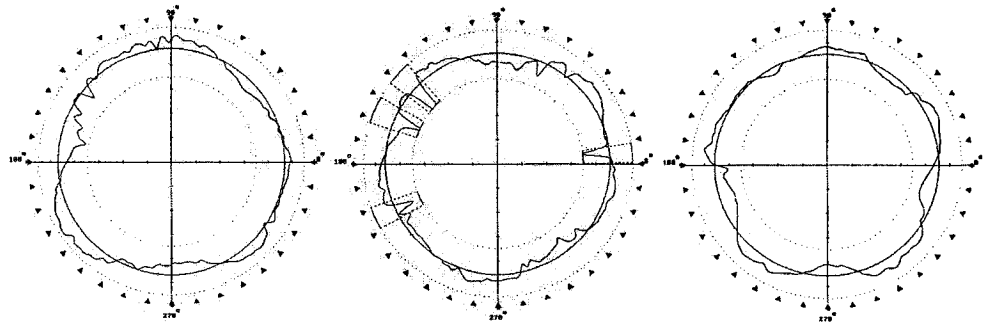

(d) (e) (f)

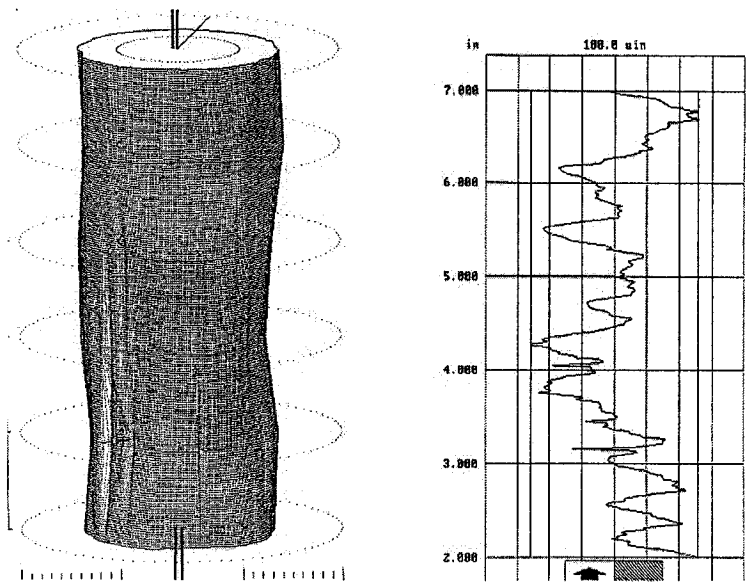


(g) (h)

Fig. 4.21: Roundness for D13 from the direction of drilling in mm (a) at 12.7, (b) at 38.1, (c) at 50.8, (d) at 88.9, (e) at 114.3, (f) at 139.7, (g) cylindricity error and (h) Straightness.

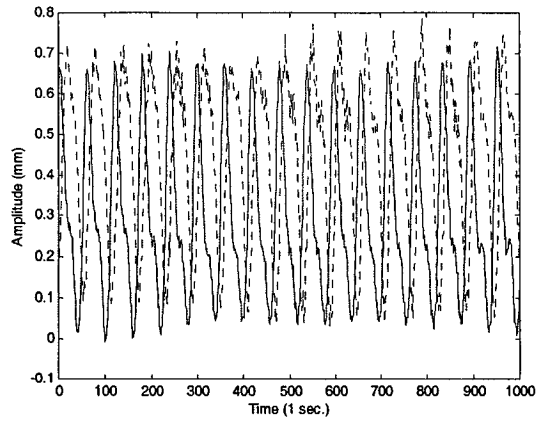


(a)

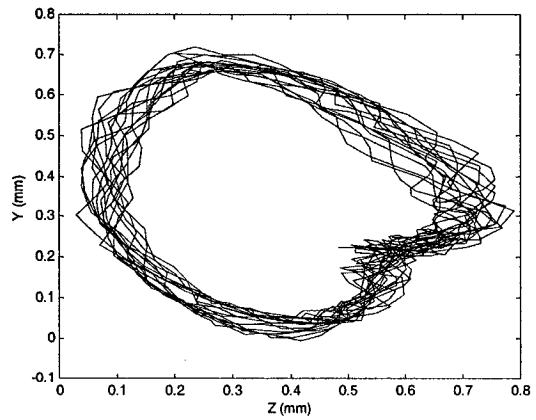


(b)

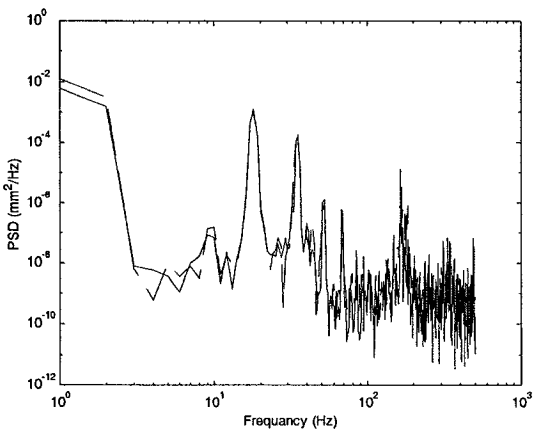


(c)

Fig. 4.22: The signal analysis of D19, (a) The two signals of master and slave sensors, (b) The whirl orbit and (c) the power spectral density of the signal.

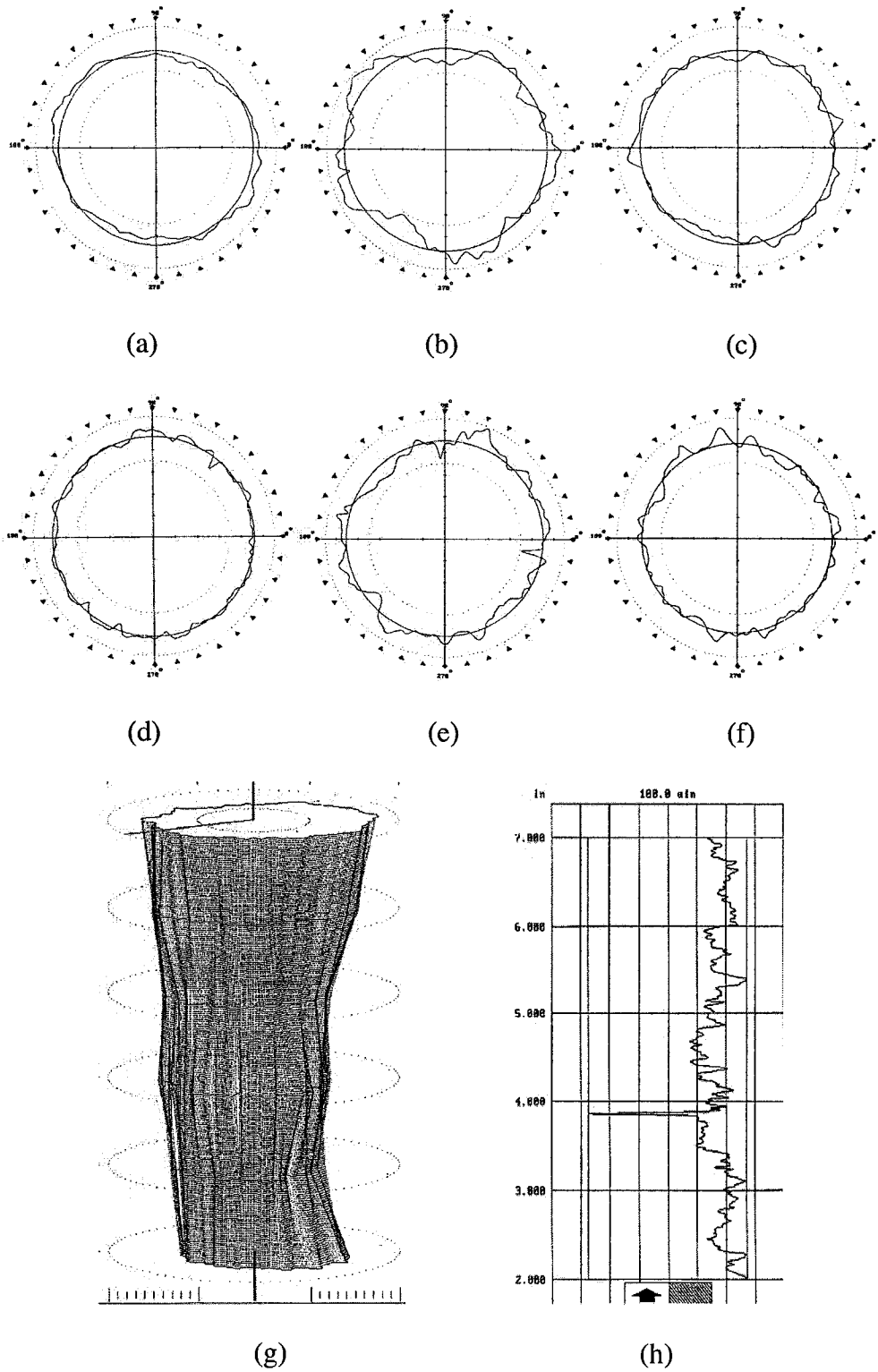


Fig. 4.23: Roundness for D19 from the direction of drilling in mm (a) at 12.7, (b) at 38.1, (c) at 50.8, (d) at 88.9, (e) at 114.3, (f) at 139.7, (g) cylindricity error and (h) Straightness.

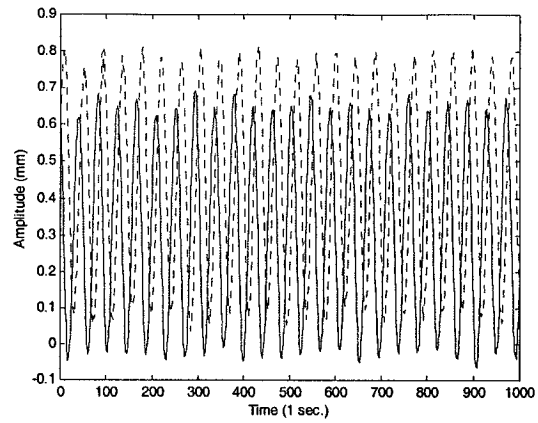


(a)

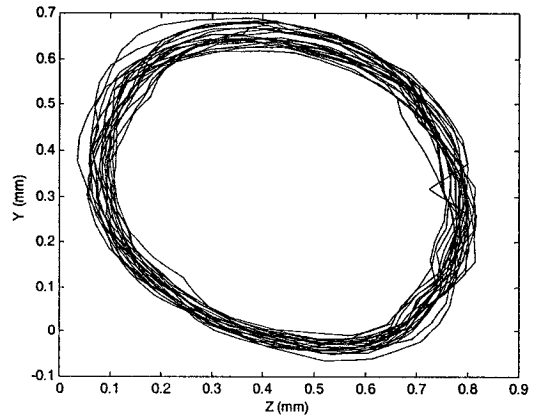


(b)

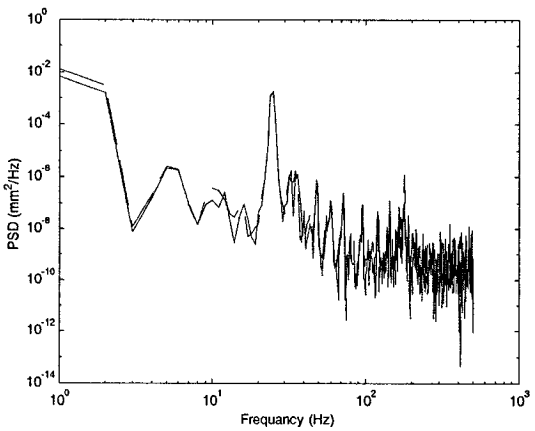


(c)

Fig. 4.24: The signal analysis of D25, (a) The two signals of master and slave sensors, (b) The whirl orbit and (c) the power spectral density of the signal.

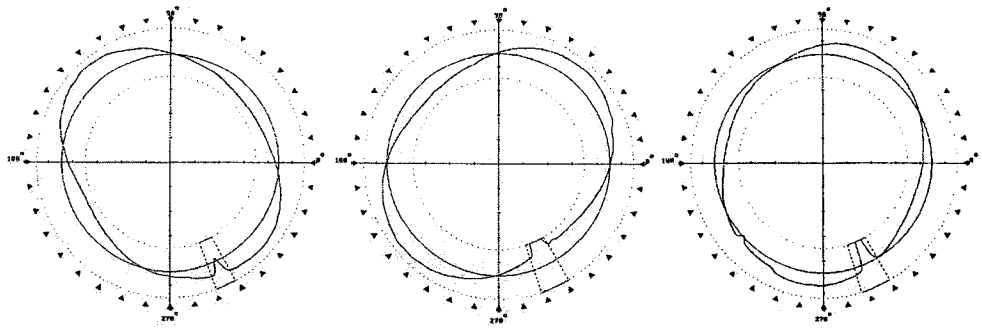

(a) (b) (c)

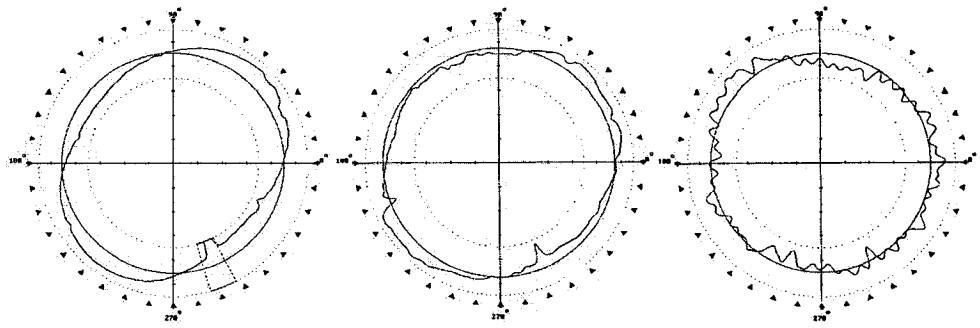

(d) (e) (f)

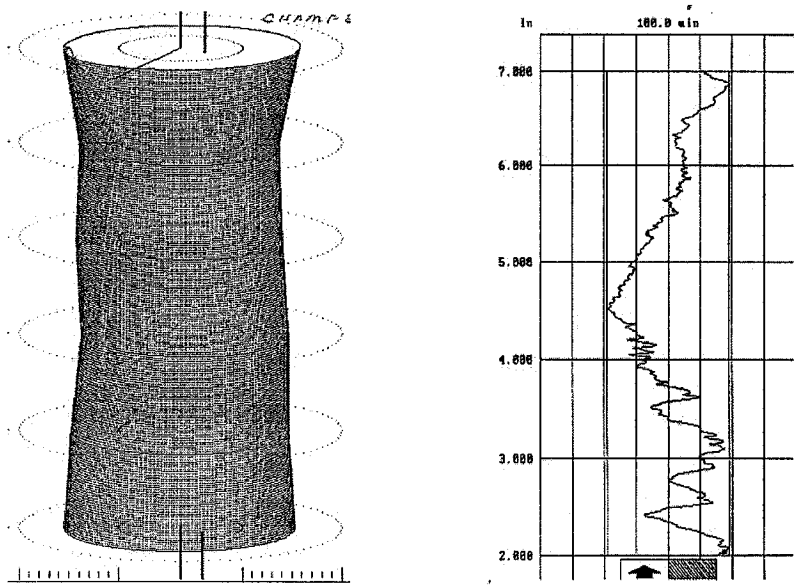


(g) (h)

Fig. 4.25: Roundness for D25 from the direction of drilling in mm (a) at 12.7, (b) at 38.1, (c) at 50.8, (d) at 88.9, (e) at 114.3, (f) at 139.7, (g) cylindricity error and (h) Straightness.

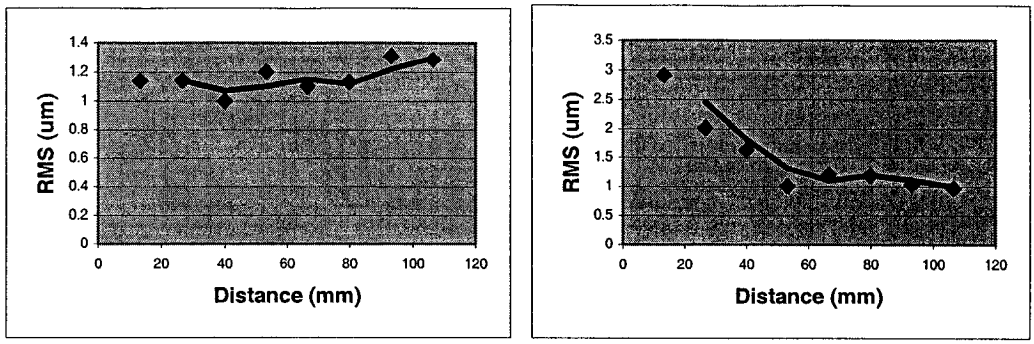


(a) (b)

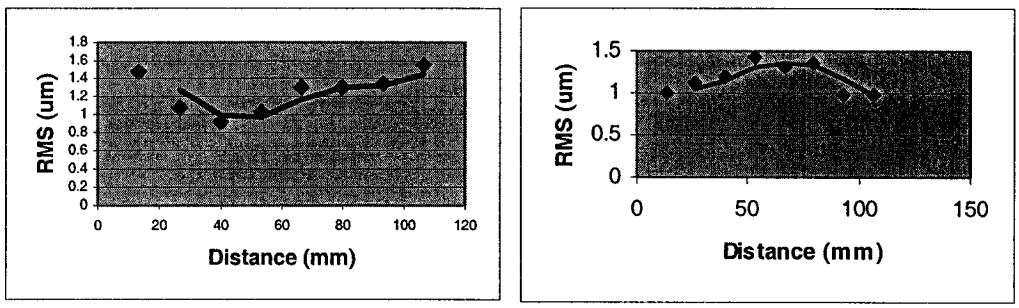


(c) (d)

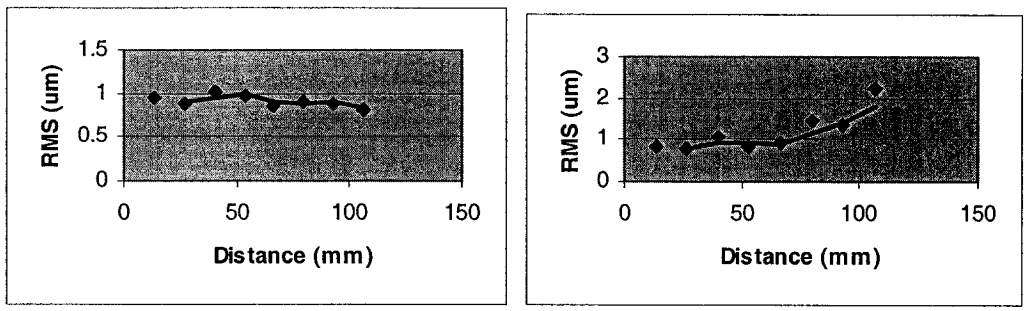


(e) (f)

Fig. 4.26: Roughness measurements (a) D1 (b) D7, (c) D8, (d) D13, (e) D19 and (f) D25.

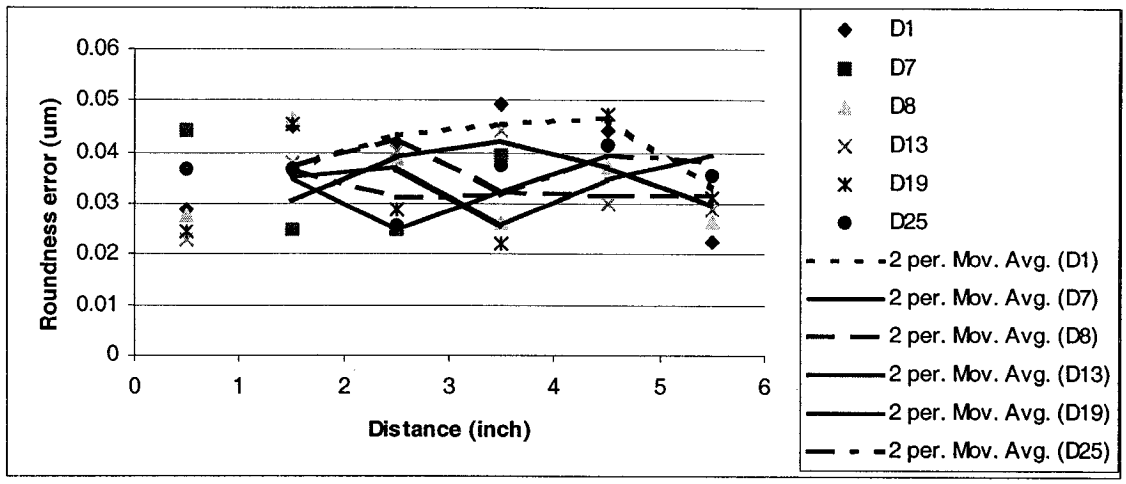


Fig. 4.27: Roundness error for D1, 7,8,13,19,25, at length equal to 76.2 mm.

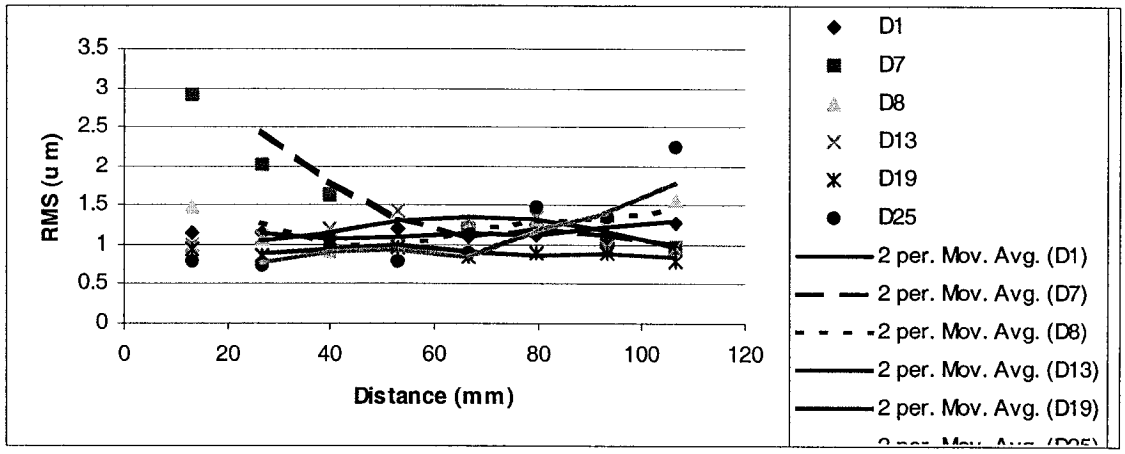


Fig. 4.28: Roughness for D1, 7,8,13,19,25, at length equal to 76.2 mm.

## 4.2.2 Effect of the whirling motion at 228.6 mm (9 in) length of cut

Table 4.4: A description of the main characteristics at a tool penetration of 228.6 mm.

| Tool penetration of 228.6 mm | Figure number | Speed (rpm) | Feed rate (mm/min) | Flow rate (G/min) |
|---|---|---|---|---|
| D2 | 4.29 | 1040 | 17 | 20 |
| | (a) | Displacement in the Y and Z coordinates | | |
| | (b) | Whirl ellipse | | |
| | (c) | Power spectral density (PSD) | | |
| First and second spectral peaks | | 17.83 Hz, 34.24 Hz | | |
| | 4.30 | Roundness characteristics | | Value ($\mu$m) |
| | (a) | Oval | | 0.038608 |
| | (b) | Oval | | 0.03683 |
| | (c) | 3-lobed out of run | | 0.03302 |
| | (d) | Random irregularities | | 0.046736 |
| | (e) | 3-lobed out of run | | 0.04572 |
| | (f) | 3-lobed out of run with irregularity | | 0.038608 |
| | (g) | Cylindricity error | | 0.239522 |
| | (h) | Straightness error | | 0.239522 |
| D9 | 3.31 | 1440 | 173 | 20 |
| | (a) | Displacement in the Y and Z coordinates | | |
| | (b) | Whirl ellipse | | |
| | (c) | Power spectral density (PSD) | | |
| First and second spectral peaks | | 24.90 Hz, 38.278 | | |
| | 4.32 | Roundness characteristics | | Value ($\mu$m) |
| | (a) | True round | | 0.027686 |
| | (b) | True round with random irregularity | | 0.043434 |
| | (c) | True round | | 0.030226 |
| | (d) | True round | | 0.025781 |
| | (e) | True round | | 0.027686 |
| | (f) | Almost true round | | 0.026924 |
| | (g) | Cylindricity error | | 0.239522 |
| | (h) | Straightness error | | 0.121158 |

Table 4.4: A description of the main characteristics at a tool penetration of 228.6 mm (continued).

| Tool penetration of 228.6 mm | Figure number | Speed (rpm) | Feed rate (mm/min) | Flow rate (G/min) |
|---|---|---|---|---|
| D14 | 4.33 | 1240 | 117 | 30 |
| | (a) | Displacement in the Y and Z coordinates | | |
| | (b) | Whirl ellipse | | |
| | (c) | Power spectral density (PSD) | | |
| First and second spectral peaks | | 21.24 Hz, 39.51 Hz | | |
| | 4.34 | Roundness characteristics | | Value ($\mu$m) |
| | (a) | 3-lobed out of roundness | | 0.049276 |
| | (b) | 3-lobed out of roundness | | 0.037084 |
| | (c) | 3-lobed out of roundness | | 0.028702 |
| | (d) | Random irregularities | | 0.035052 |
| | (e) | Almmost true round | | 0.039878 |
| | (f) | Oval | | 0.037846 |
| | (g) | Cylindricity error | | 0.152654 |
| | (h) | Straightness error | | 0.012802 |
| D20 | 4.35 | 1040 | 117 | 40 |
| | (a) | Displacement in the Y and Z coordinates | | |
| | (b) | Whirl ellipse | | |
| | (c) | Power spectral density (PSD) | | |
| First and second spectral peaks | | 17.83 Hz, 34.24 Hz | | |
| | 4.36 | Roundness characteristics | | Value ($\mu$m) |
| | (a) | Oval | | 0.032512 |
| | (b) | Oval or egg-shaped | | 0.03424 |
| | (c) | Oval with random irregularities | | 0.04826 |
| | (d) | Random irregularities | | 0.035306 |
| | (e) | Random irregularities | | 0.038862 |
| | (f) | Oval | | 0.028575 |
| | (g) | Cylindricity error | | 0.244221 |
| | (h) | Straightness error | | 0.10668 |

Table 4.4: A description of the main characteristics at a tool penetration of 228.6 mm (continued).

| Tool penetration of 228.6 mm | Figure number | Speed (rpm) | Feed rate (mm/min) | Flow rate (G/min) |
|---|---|---|---|---|
| D26 | 4.37 | 1440 | 117 | 40 |
| | (a) | Displacement in the Y and Z coordinates | | |
| | (b) | Whirl ellipse | | |
| | (c) | Power spectral density (PSD) | | |
| First and second spectral peaks | | 10.71 Hz, 24.51 Hz | | |
| | 4.38 | Roundness characteristics | | Value ($\mu$m) |
| | (a) | 2-lobed out of run with random irregularities | | 0.0508 |
| | (b) | Almost true round with random irregularity | | 0.028067 |
| | (c) | True round with random irregularities | | 0.036195 |
| | (d) | True round with random irregularities | | 0.025527 |
| | (e) | Oval | | 0.031877 |
| | (f) | Oval | | 0.026365 |
| | (g) | Cylindricity error | | 0.150368 |
| | (h) | Straightness error | | 0.154432 |

It is concluded from table 4.4 that the main roundness shapes is 3-lobed out of run for D2 and D14. For D9 it is almost true round and oval for D20 and D26.

Roughness plots are shown in Fig. 4.39(a) to (e). It is shown that the roughness is increasing in D2 and D26 while it is decreasing in D9, D14 and D20. Fig. 4.40 and 4.41 is a one-figure plot of the entire specimen at 228.6 mm of tool penetration to show the differences between them for roundness and roughness, respectively.

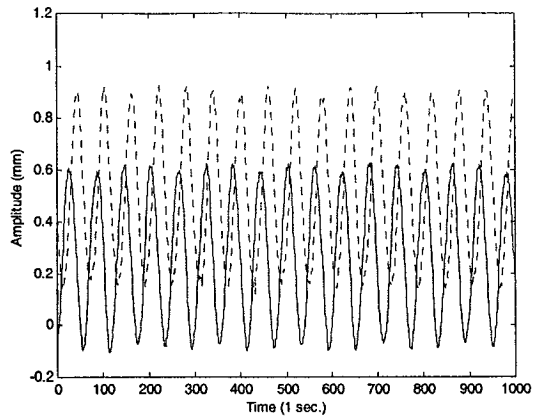


(a)

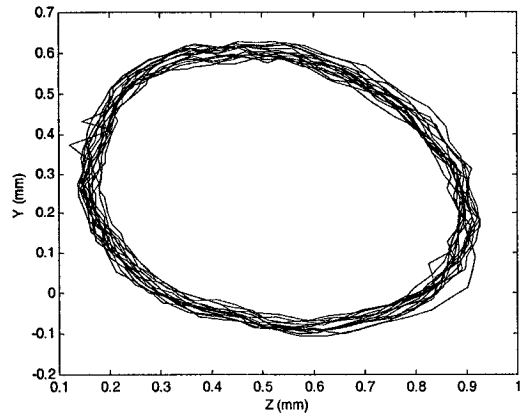


(b)

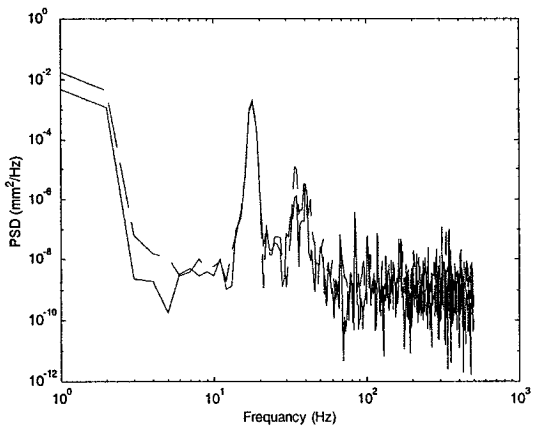


(c)

Fig. 4.29: The signal analysis of D2, (a) The two signals of master and slave sensors, (b) The whirl orbit and (c) the power spectral density of the signal.

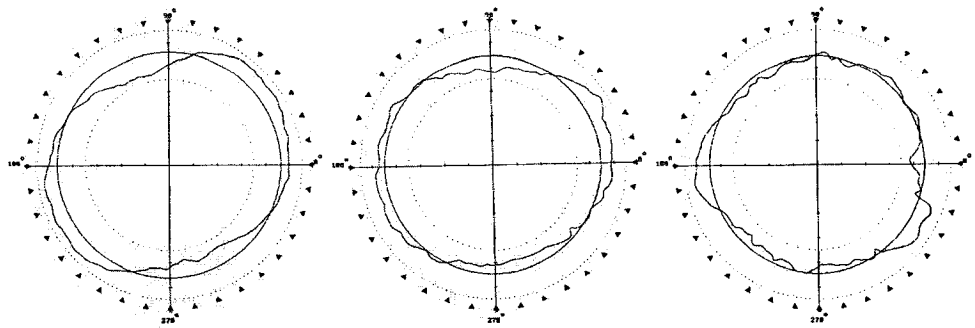

(a) (b) (c)

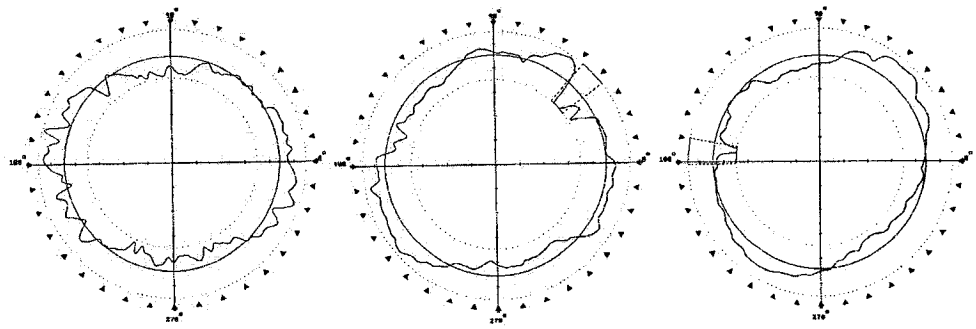

(d) (e) (f)

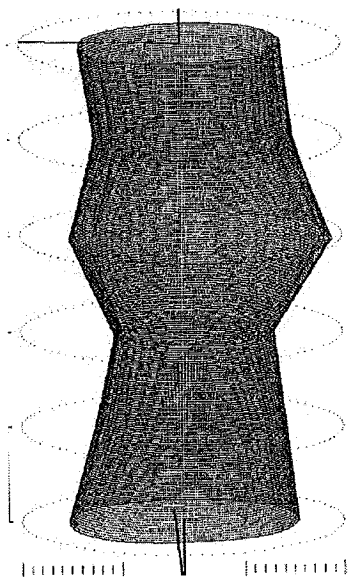

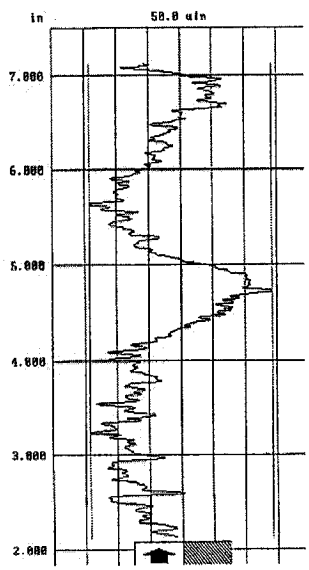


(g) (h)

Fig. 4.30: Roundness for D2 from the direction of drilling in mm (a) at 12.7, (b) at 38.1, (c) at 50.8, (d) at 88.9, (e) at 114.3, (f) at 139.7, (g) cylindricity error and (h) Straightness.

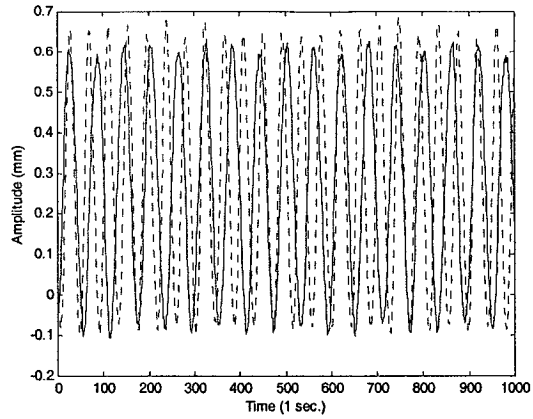


(a)

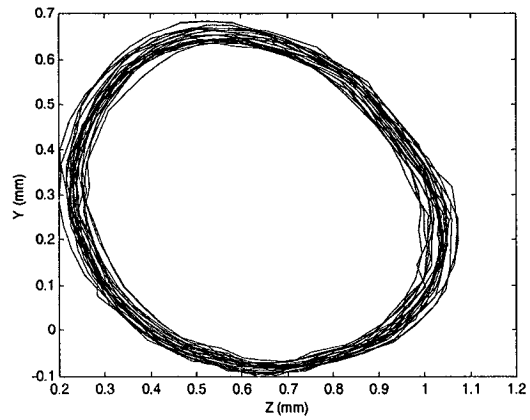


(b)

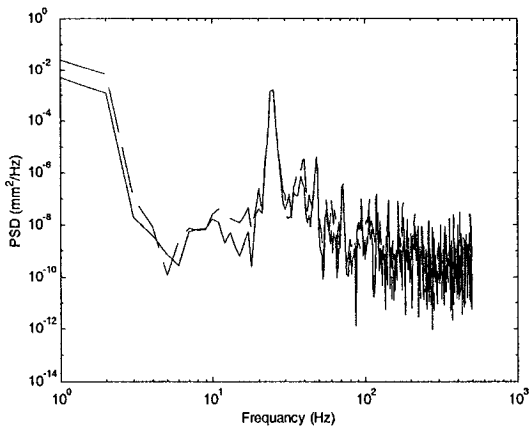


(c)

Fig. 4.31: The signal analysis of D9, (a) The two signals of master and slave sensors, (b) The whirl orbit and (c) the power spectral density of the signal.

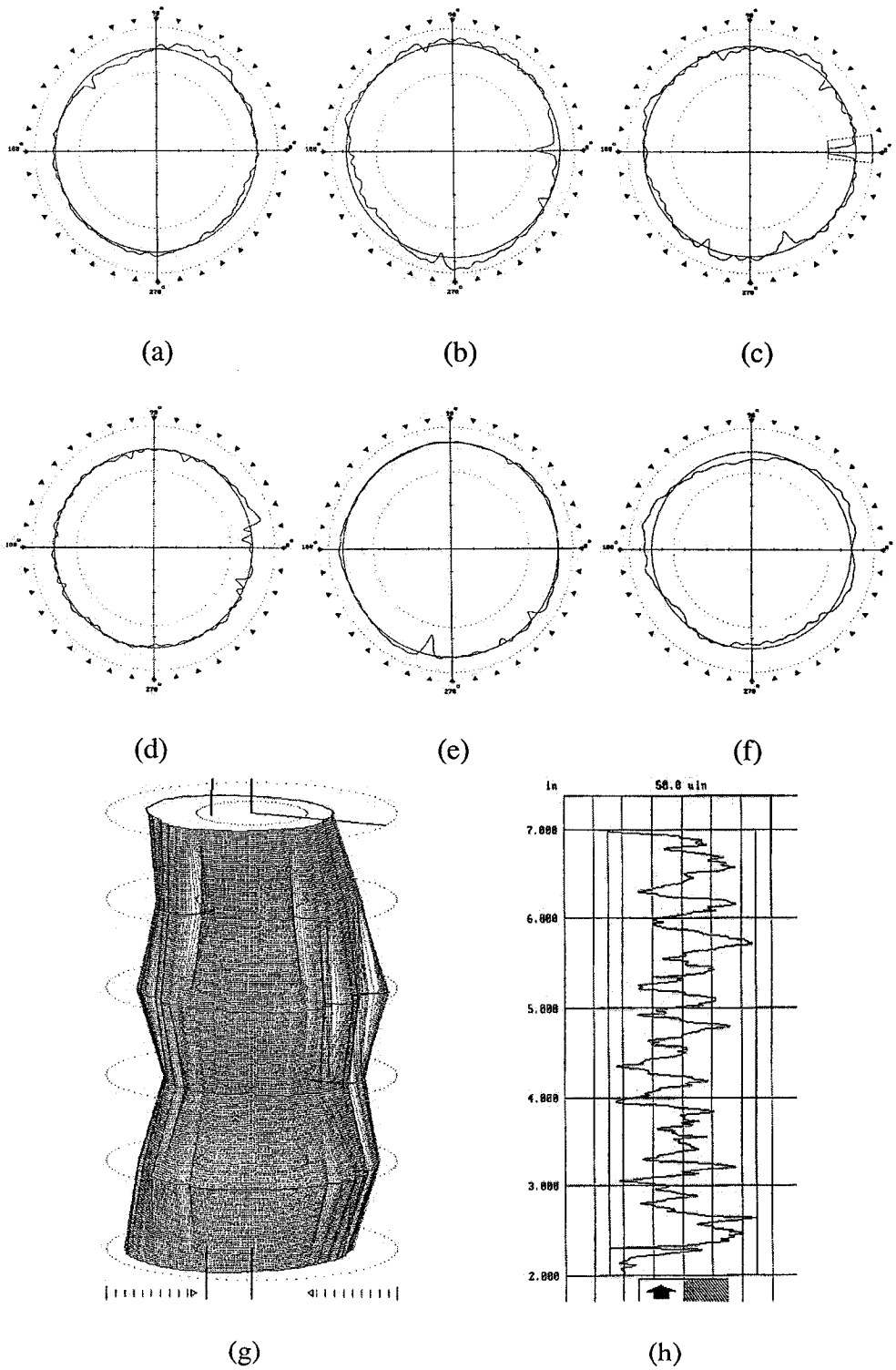


Fig. 4.32: Roundness for D9 from the direction of drilling in mm (a) at 12.7, (b) at 38.1, (c) at 50.8, (d) at 88.9, (e) at 114.3, (f) at 139.7, (g) cylindricity error and (h) Straightness.

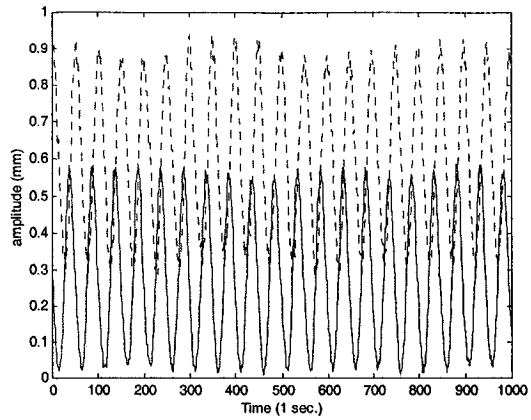


(a)

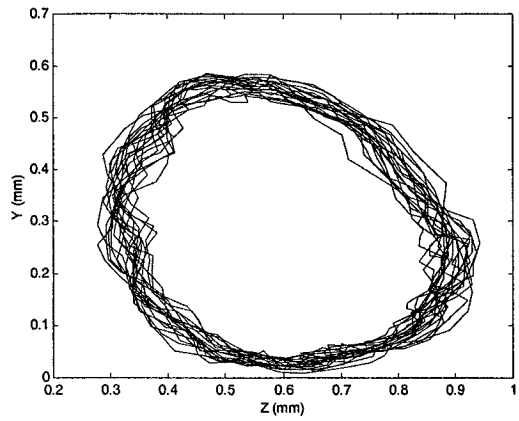


(b)

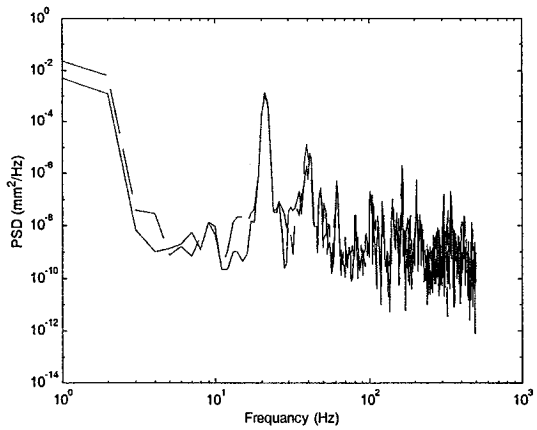


(c)

Fig. 4.33: The signal analysis of D14, (a) The two signals of master and slave sensors, (b) The whirl orbit and (c) the power spectral density of the signal.

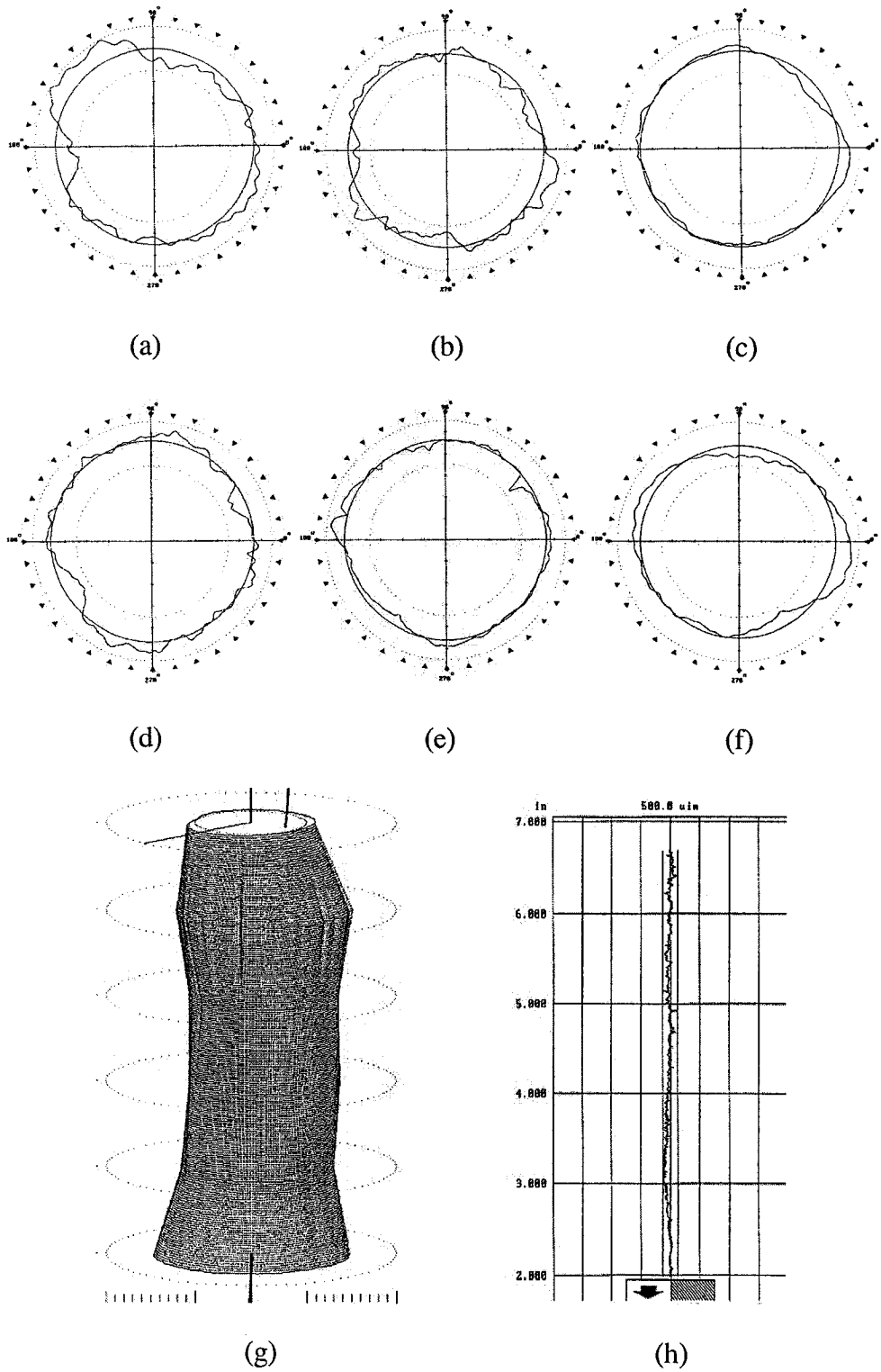


Fig. 4.34: Roundness for D14 from the direction of drilling in mm (a) at 12.7, (b) at 38.1, (c) at 50.8, (d) at 88.9, (e) at 114.3, (f) at 139.7, (g) cylindricity error and (h) Straightness.

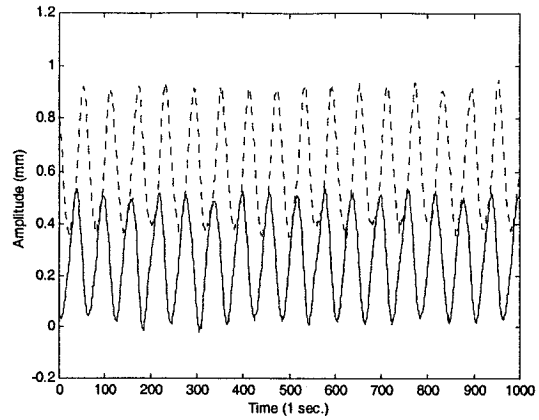


(a)

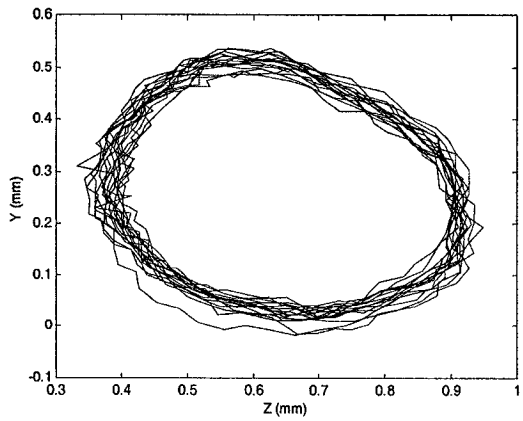


(b)

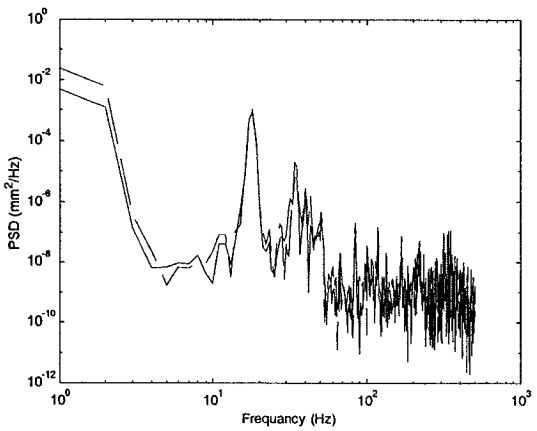


(c)

Fig. 4.35: The signal analysis of D20, (a) The two signals of master and slave sensors, (b) The whirl orbit and(c) the power spectral density of the signal.

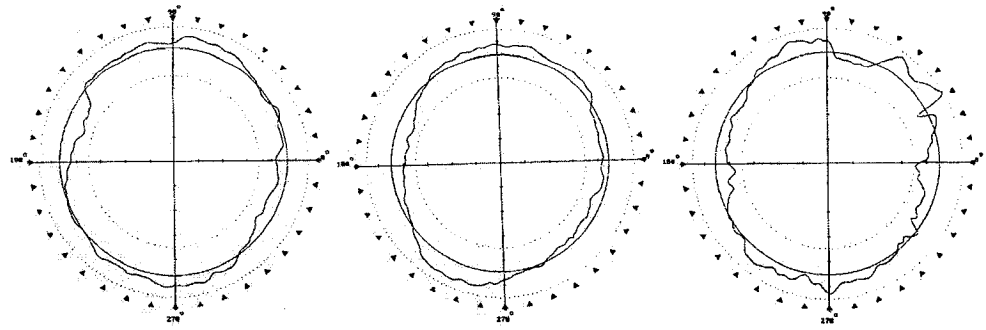

(a) (b) (c)

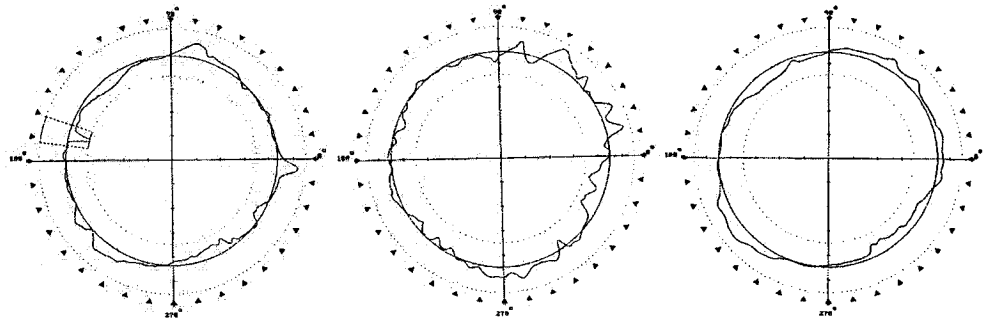

(d) (e) (f)

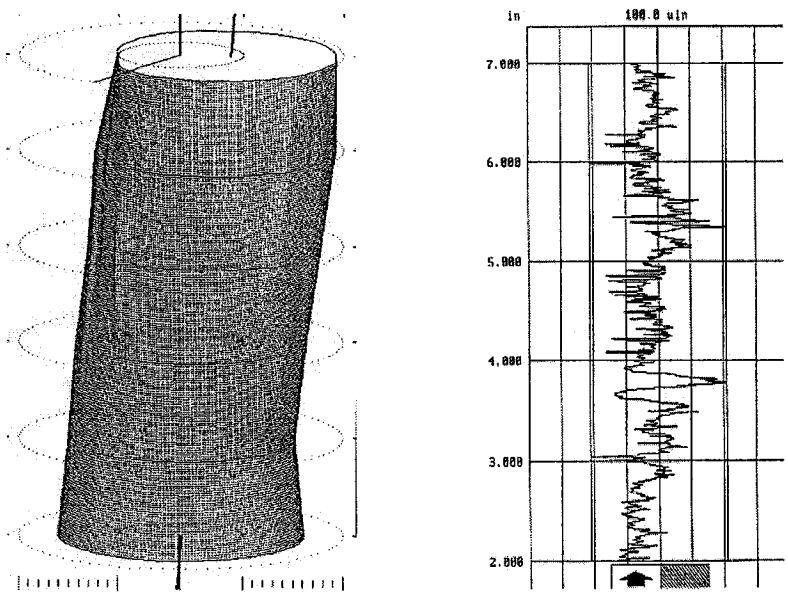


(g) (h)

Fig. 4.36: Roundness for D20 from the direction of drilling in mm (a) at 12.7, (b) at 38.1, (c) at 50.8, (d) at 88.9, (e) at 114.3, (f) at 139.7, (g) cylindricity error and (h) Straightness.

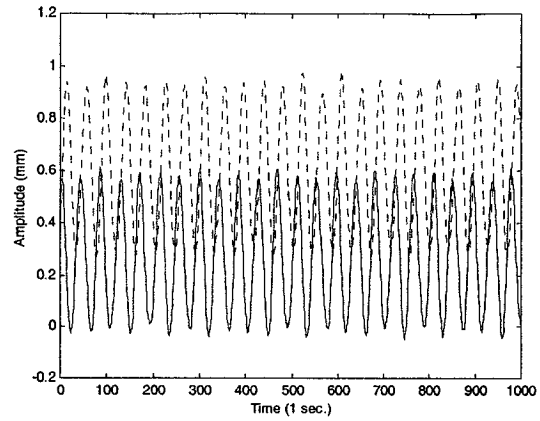


(a)

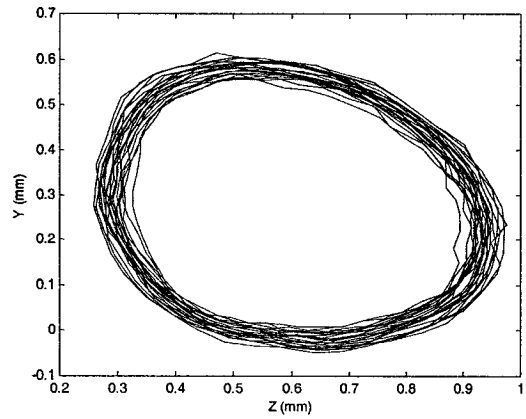


(b)

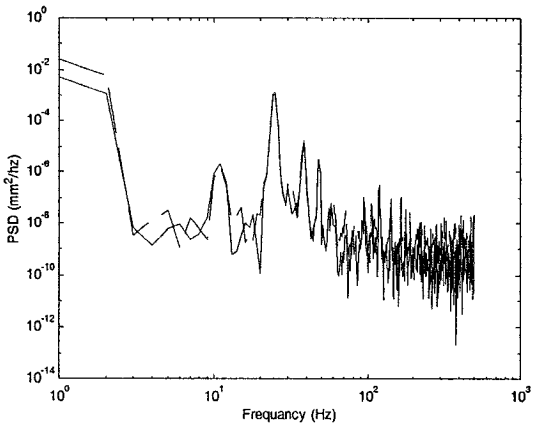


(c)

Fig. 4.37: The signal analysis of D26, (a) The two signals of master and slave sensors, (b) The whirl orbit and (c) the power spectral density of the signal.

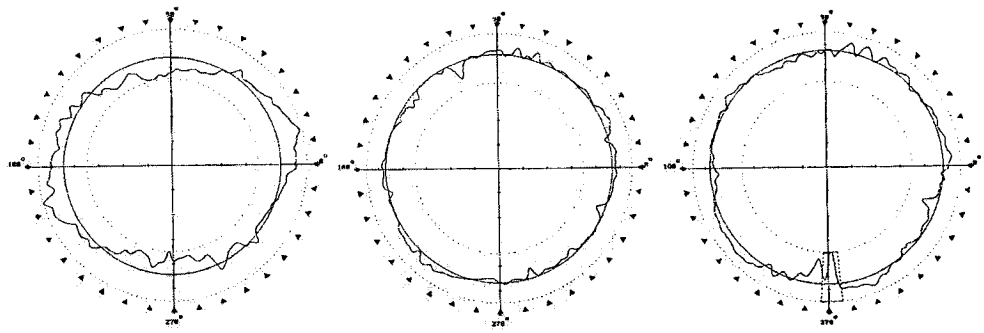

(a) (b) (c)

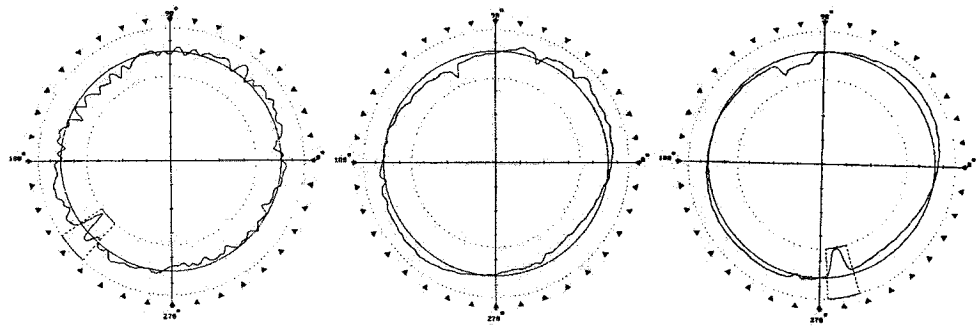

(d) (e) (f)

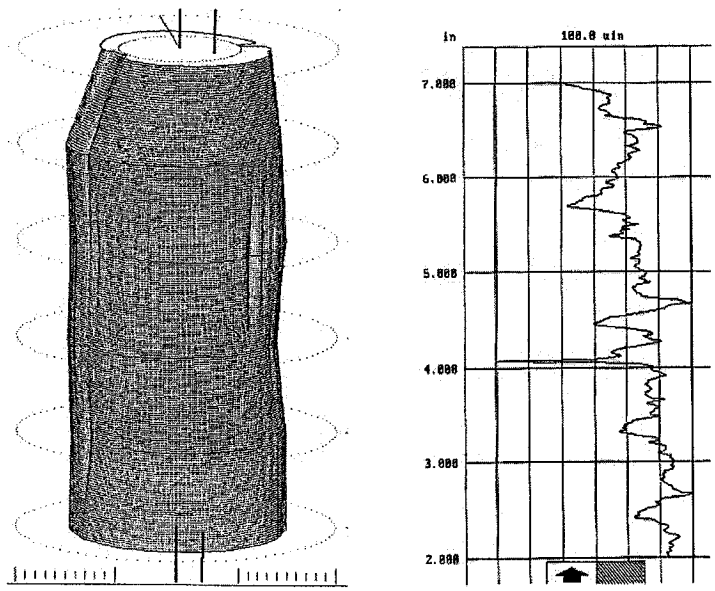


(g) (h)

Fig. 4.38: Roundness for D26 from the direction of drilling in mm (a) at 12.7, (b) at 38.1, (c) at 50.8, (d) at 88.9, (e) at 114.3, (f) at 139.7, (g) cylindricity error and (h) Straightness.

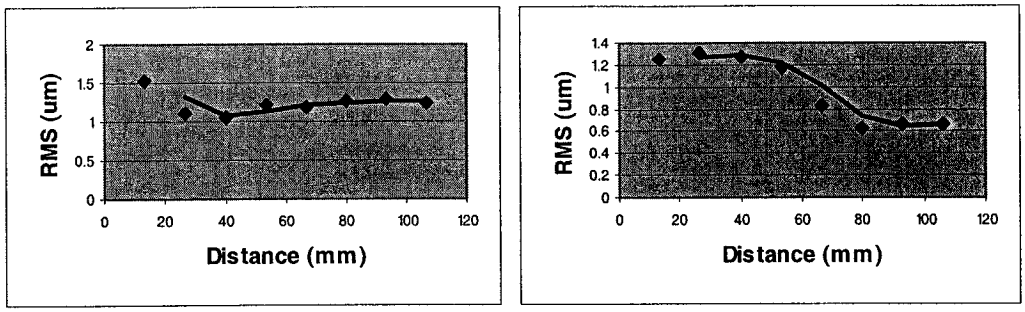


(a) (b)

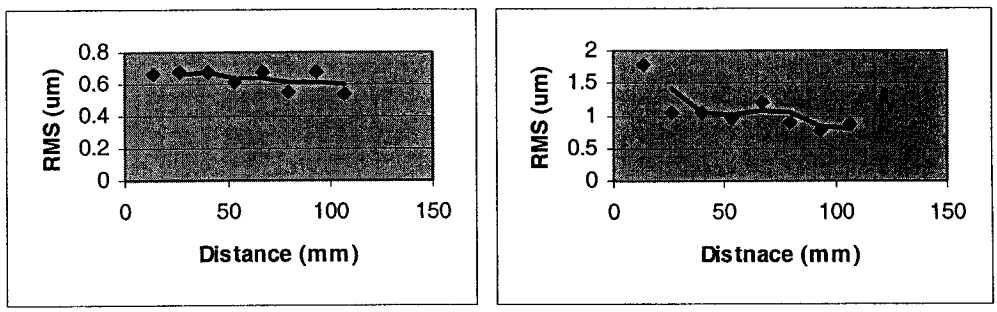


(c) (d)

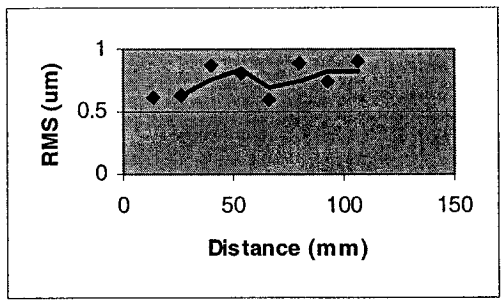


(e)

Fig. 4.39: Roughness measurements (a) D2 (b) D9, (c) D14, (d) D20, (e) and D26.

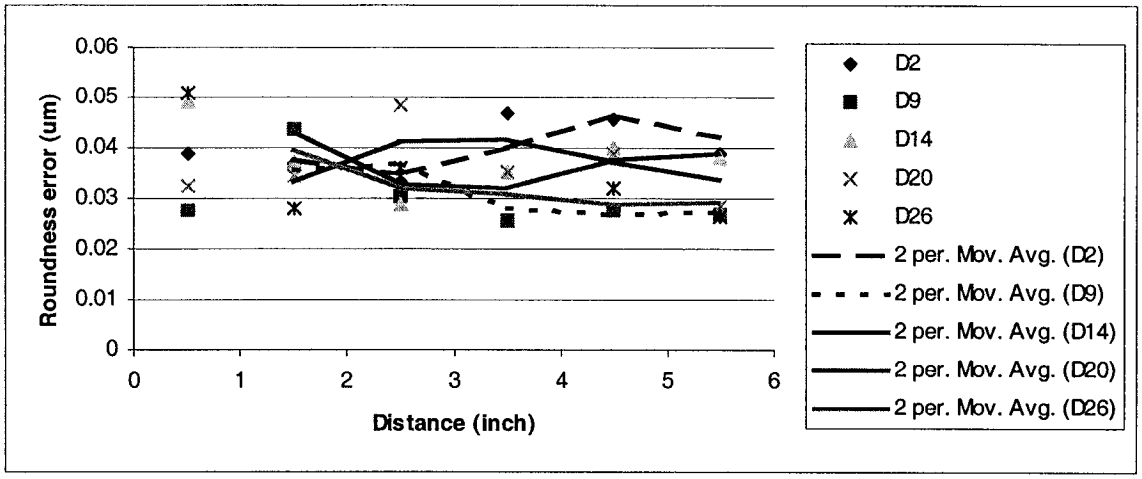


Fig. 4.40: Roundness error for D2, 9,14, 20, 26 at length equal to 228.6 mm.

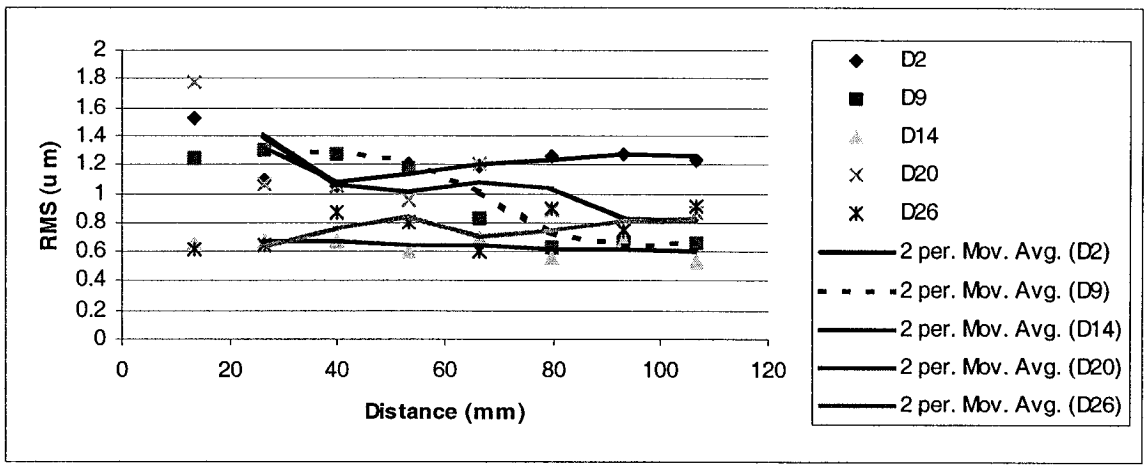


Fig. 4.41: Roughness for D2, 9,14, 20, 26 at length equal to 228.6 mm.

### 4.2.3 Effect of whirling motion at 381 mm (15 in) length of cut

Table 4.5: A description of the main characteristics at a tool penetration of 381 mm.

| Tool penetration of 381 mm | Figure number | Speed (rpm) | Feed rate (mm/min) | Flow rate (G/min) |
|---|---|---|---|---|
| D3 | 4.42 | 1040 | 173 | 20 |
| | (a) | Displacement in the Y and Z coordinates | | |
| | (b) | Whirl ellipse | | |
| | (c) | Power spectral density (PSD) | | |
| First and second spectral peaks | | 17.83 Hz, 33.70 Hz | | |
| | 4.43 | Roundness characteristics | | Value ($\mu$m) |
| | (a) | Almost true round | | 0.026924 |
| | (b) | Oval with random irregularities | | 0.04826 |
| | (c) | Oval | | 0.03302 |
| | (d) | Oval | | 0.033274 |
| | (e) | Oval | | 0.032766 |
| | (f) | Oval with random irregularities | | 0.035052 |
| | (g) | Cylindricity error | | 0.010455 |
| | (h) | Straightness error | | 0.102362 |
| D10 | 4.44 | 1040 | 71 | 30 |
| | (a) | Displacement in the Y and Z coordinates | | |
| | (b) | Whirl ellipse | | |
| | (c) | Power spectral density (PSD) | | |
| First and second spectral peaks | | 17.83 Hz, 34.24 Hz | | |
| | 4.45 | Roundness characteristics | | Value ($\mu$m) |
| | (a) | 4-loned out of run | | 0.034925 |
| | (b) | Random irregularities | | 0.045466 |
| | (c) | Random irregularities | | 0.026035 |
| | (d) | Ovality with irregularity, interrupted surface | | 0.048895 |
| | (e) | Almost tru round | | 0.02423 |
| | (f) | 2-lobed out of run | | 0.031877 |
| | (g) | Cylindricity error | | 0.219202 |
| | (h) | Straightness error | | 0.10795 |

Table 4.5: A description of the main characteristics at a tool penetration of 381 mm (continued).

| Tool penetration of 381 mm | Figure number | Speed (rpm) | Feed rate (mm/min) | Flow rate (G/min) |
|---|---|---|---|---|
| D15 | 4.46 | 1240 | 173 | 30 |
| | (a) | Displacement in the Y and Z coordinates | | |
| | (b) | Whirl ellipse | | |
| | (c) | Power spectral density (PSD) | | |
| First and second spectral peaks | | 20.90 Hz, 40.79 Hz | | |
| | 4.47 | Roundness characteristics | | Value ($\mu$m) |
| | (a) | 4-lobed out of roundness and irregularities | | 0.030734 |
| | (b) | 2-lobed out of roundness | | 0.04826 |
| | (c) | Almost true round | | 0.028321 |
| | (d) | 3-lobed out of run and irregularities | | 0.040767 |
| | (e) | 3-lobed out of run | | 0.032893 |
| | (f) | 3-lobed out of run | | 0.044323 |
| | (g) | Cylindricity error | | 0.237744 |
| | (h) | Straightness error | | 0.099695 |
| D21 | 4.48 | 1040 | 173 | 40 |
| | (a) | Displacement in the Y and Z coordinates | | |
| | (b) | Whirl ellipse | | |
| | (c) | Power spectral density (PSD) | | |
| First and second spectral peaks | | 17.27 Hz, 30.63 Hz | | |
| | 4.49 | Roundness characteristics | | Value ($\mu$m) |
| | (a) | Random irregularities | | 0.029718 |
| | (b) | 3-lobed out of run | | 0.03302 |
| | (c) | Almost True round | | 0.027813 |
| | (d) | True round | | 0.02347 |
| | (e) | Random irregularities | | 0.029845 |
| | (f) | Oval with random irregularities | | 0.049022 |
| | (g) | Cylindricity error | | 0.184277 |
| | (h) | Straightness error | | 0.119507 |

Table 4.5: A description of the main characteristics at a tool penetration of 381 mm (continued).

| Tool penetration of 381 mm | Figure number | Speed (rpm) | Feed rate (mm/min) | Flow rate (G/min) |
|---|---|---|---|---|
| D27 | 4.50 | 1440 | 173 | 40 |
| | (a) | Displacement in the Y and Z coordinates | | |
| | (b) | Whirl ellipse | | |
| | (c) | Power spectral density (PSD) | | |
| First and second spectral peaks | | 24.12 Hz, 42.11 Hz | | |
| | 4.51 | Roundness characteristics | | Value ($\mu$m) |
| | (a) | Oval with random irregularities | | 0.032258 |
| | (b) | Almost 3-lobed out of run | | 0.04064 |
| | (c) | Almost 3-lobed out of run | | 0.038359 |
| | (d) | Almost 3-lobed out of run | | 0.042672 |
| | (e) | 3-lobed out of run | | 0.023876 |
| | (f) | 3-lobed out of run | | 0.029616 |
| | (g) | Cylindricity error | | 0.180467 |
| | (h) | Straightness error | | 0.168148 |

At 381 mm the specimens are: D3, D10, D15, D21, and D27. Table 4.3 is a summary of the figures and geometrical dimensioning at 381 mm (15 in) tool penetration. The predominant characteristic of the out of roundness error is ovality with random irregularity as in D3, D10 and D27. For D15 and D27 it is 3-lobed. Fig. 4.52 shows the roughness plots for D3, 10,15,21 and 27. The roughness was increasing for D3 while decreasing in D10, 15, 21 and 27. Fig. 4.53 and 4.54 is one-figure plot of roundness and roughness for all the specimens at 381 mm.

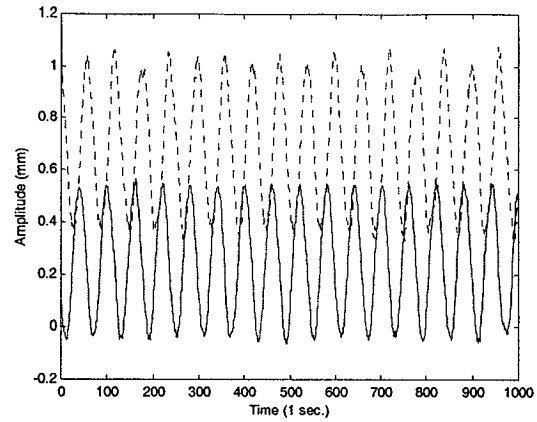


(a)

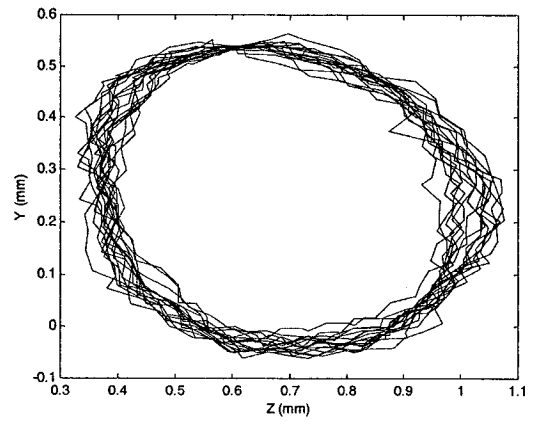


(b)

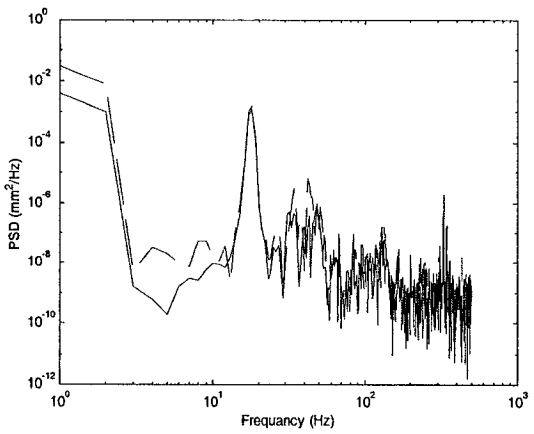


(c)

Fig. 4.42: The signal analysis of D3, (a) The two signals of master and slave sensors, (b) The whirl orbit and (c) the power spectral density of the signal.

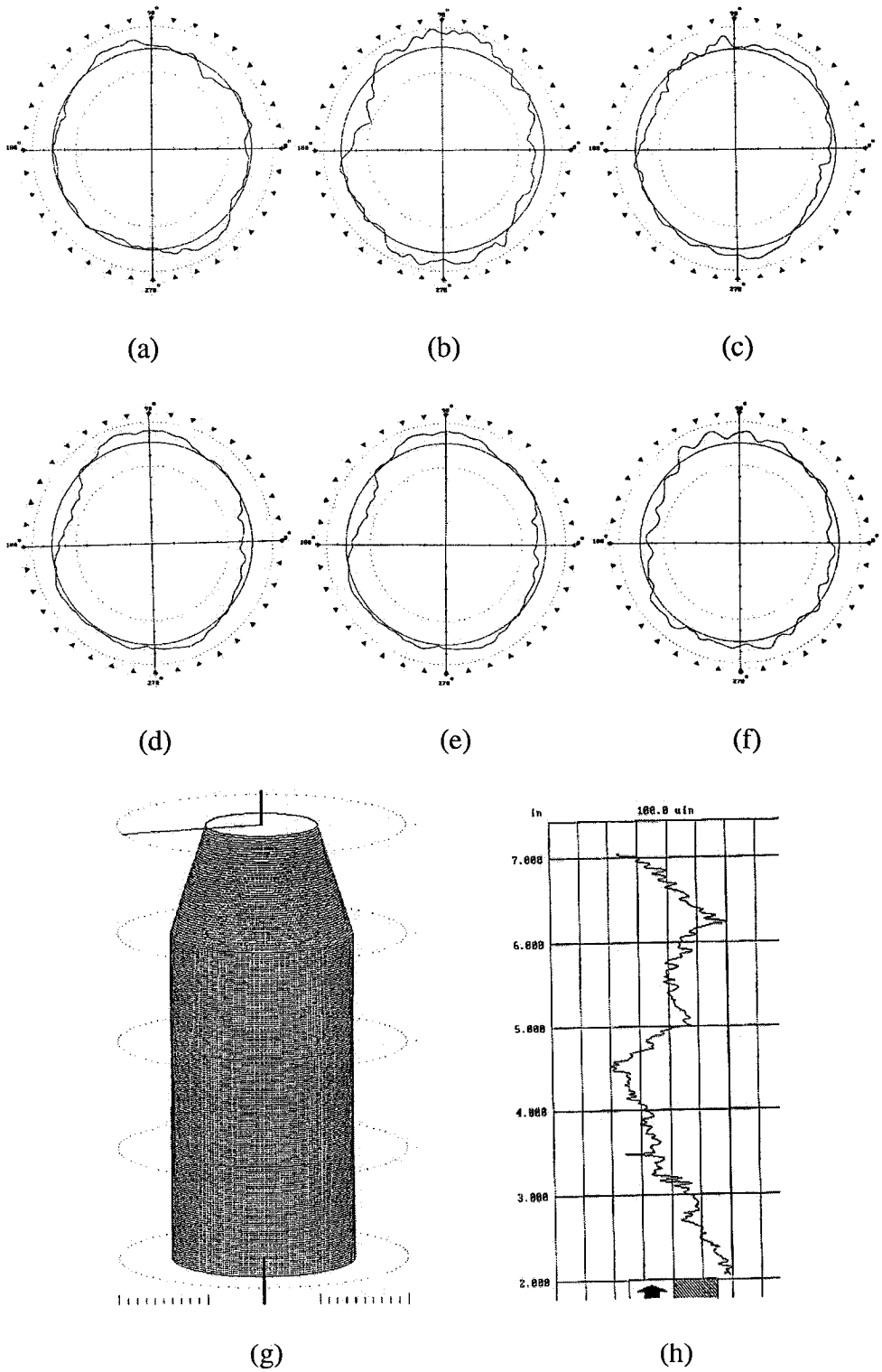


Fig. 4.43: Roundness for D3 from the direction of drilling in mm (a) at 12.7, (b) at 38.1, (c) at 50.8, (d) at 88.9, (e) at 114.3, (f) at 139.7, (g) cylindricity error and (h) Straightness.

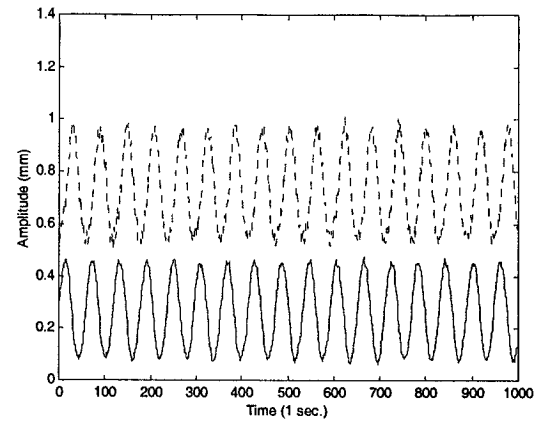


(a)

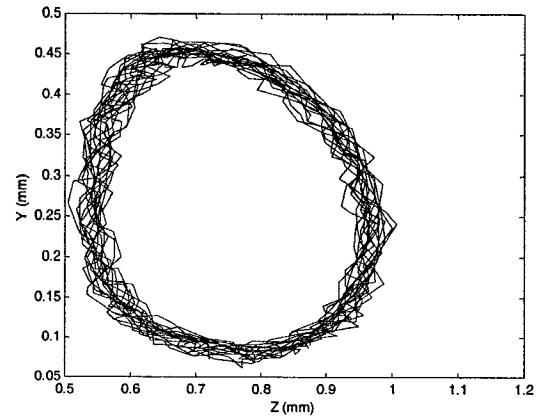


(b)

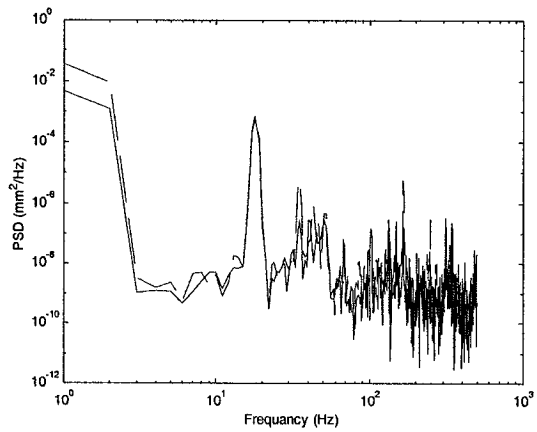


(c)

Fig. 4.44: The signal analysis of D10, (a) The two signals of master and slave sensors, (b) The whirl orbit and (c) the power spectral density of the signal.

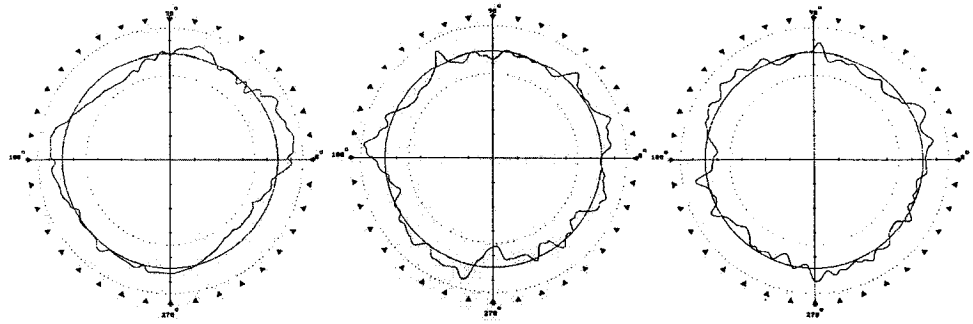

(a) (b) (c)

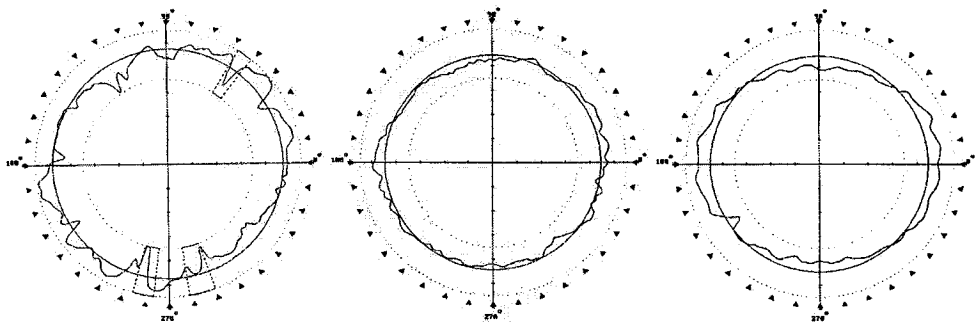

(d) (e) (f)

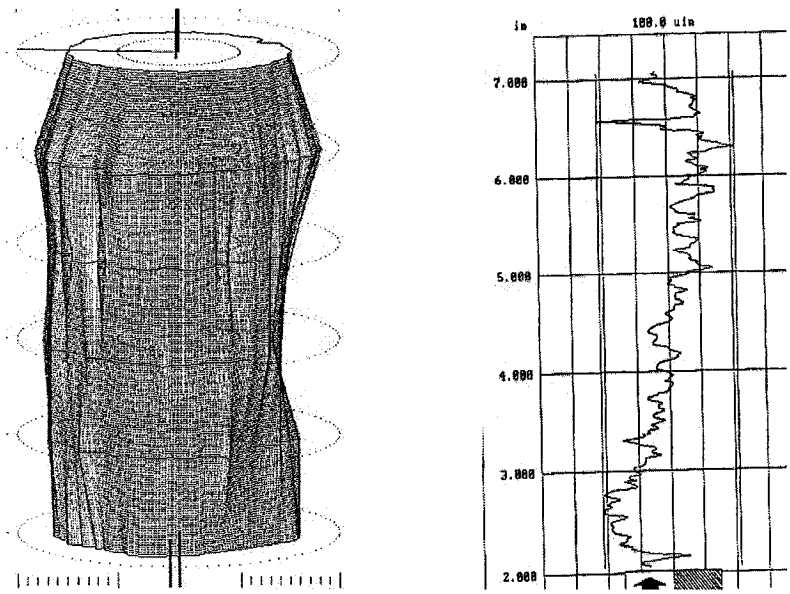


(g) (h)

Fig. 4.45: Roundness for D10 from the direction of drilling in mm (a) at 12.7, (b) at 38.1, (c) at 50.8, (d) at 88.9, (e) at 114.3, (f) at 139.7, (g) cylindricity error and (h) Straightness.

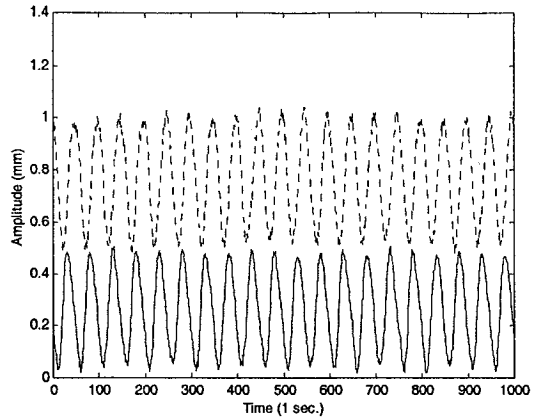


(a)

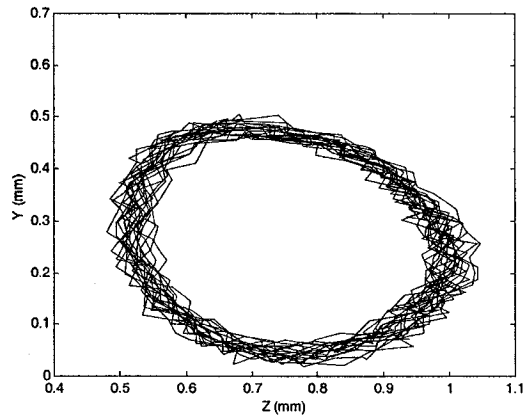


(b)

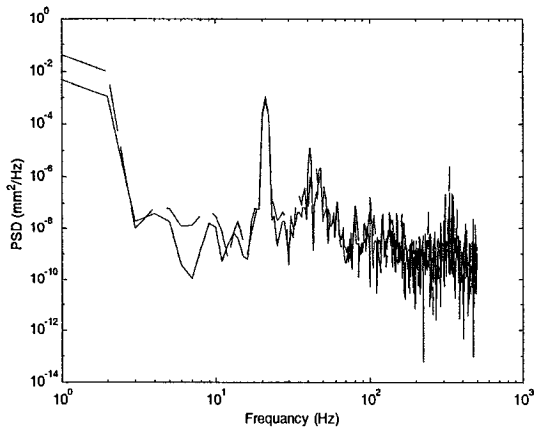


(c)

Fig. 4.46: The signal analysis of D15, (a) The two signals of master and slave sensors, (b) The whirl orbit and (c) the power spectral density of the signal.

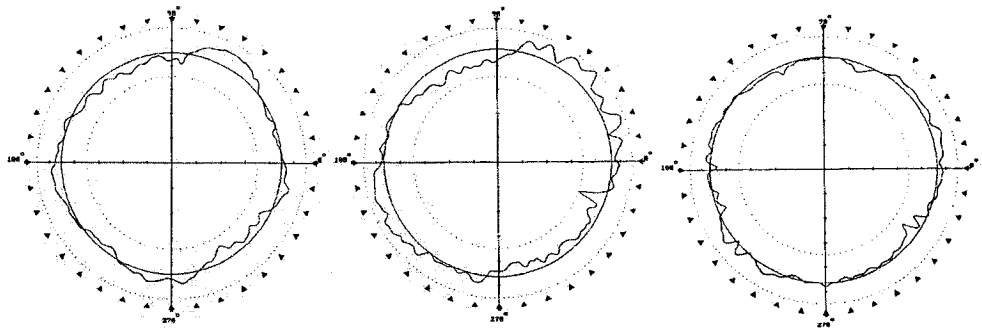

(a) (b) (c)

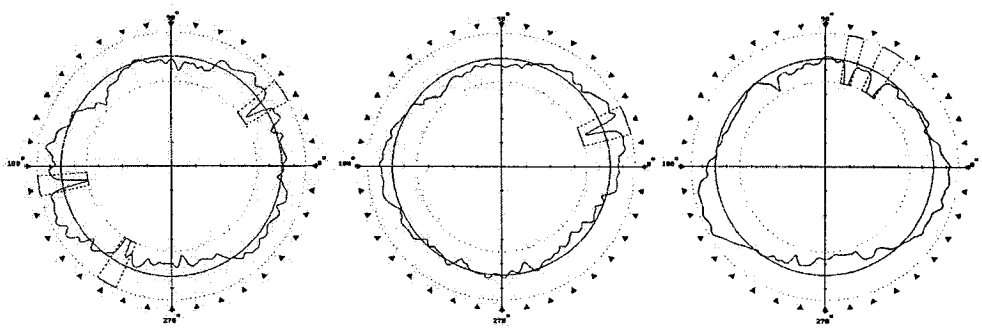

(d) (e) (f)

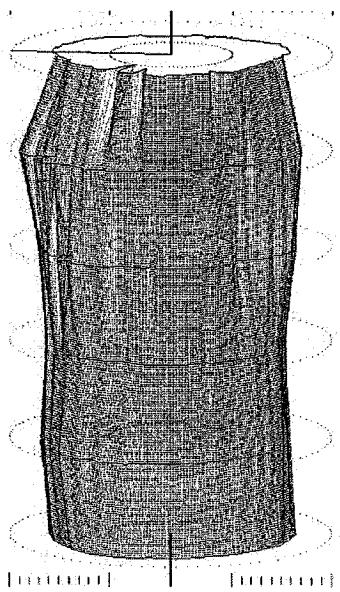

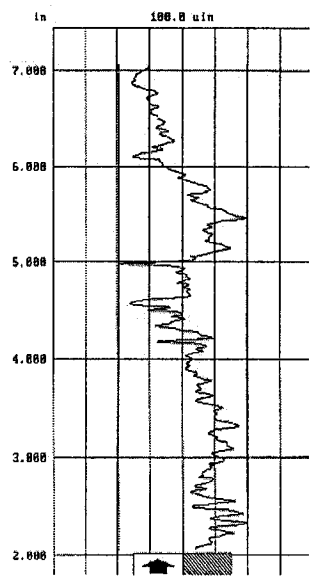


(g) (h)

Fig. 4.47: Roundness for D15 from the direction of drilling in mm (a) at 12.7, (b) at 38.1, (c) at 50.8, (d) at 88.9, (e) at 114.3, (f) at 139.7, (g) cylindricity error and (h) Straightness.

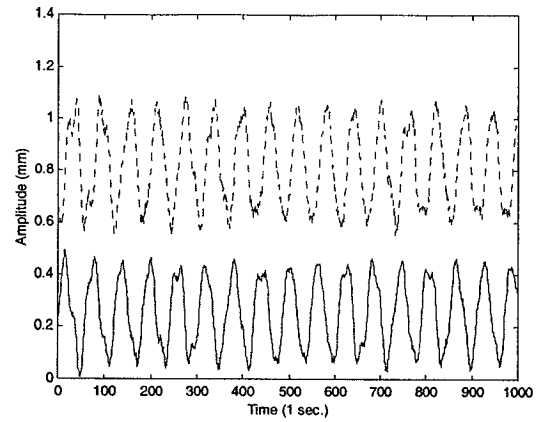


(a)

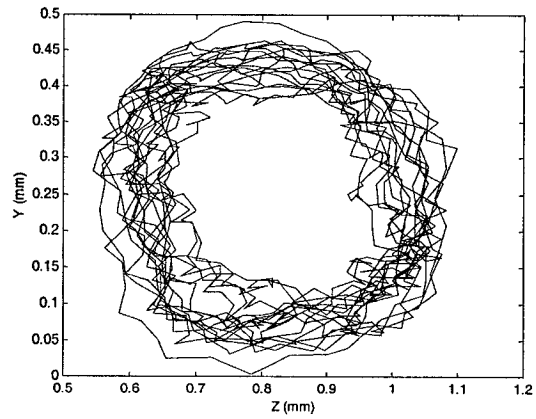


(b)

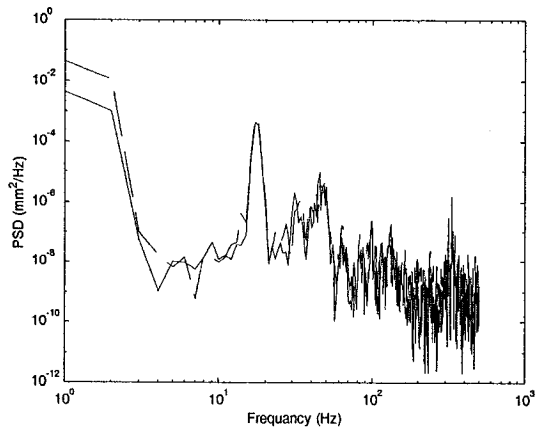


(c)

Fig. 4.48: The signal analysis of D21, (a) The two signals of master and slave sensors, (b) The whirl orbit and (c) the power spectral density of the signal.

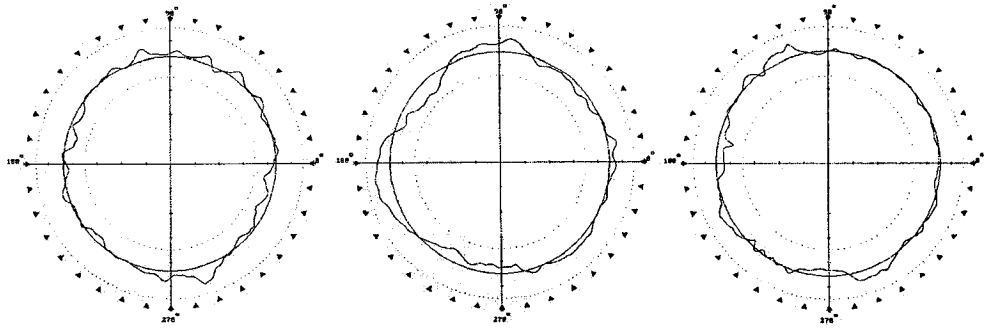

(a) (b) (c)

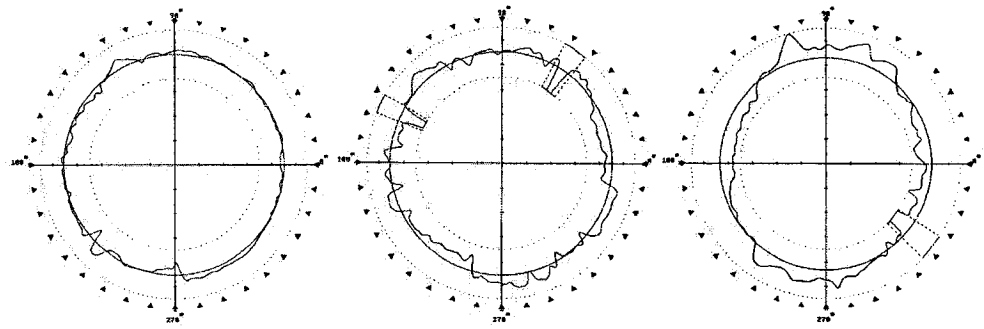

(d) (e) (f)

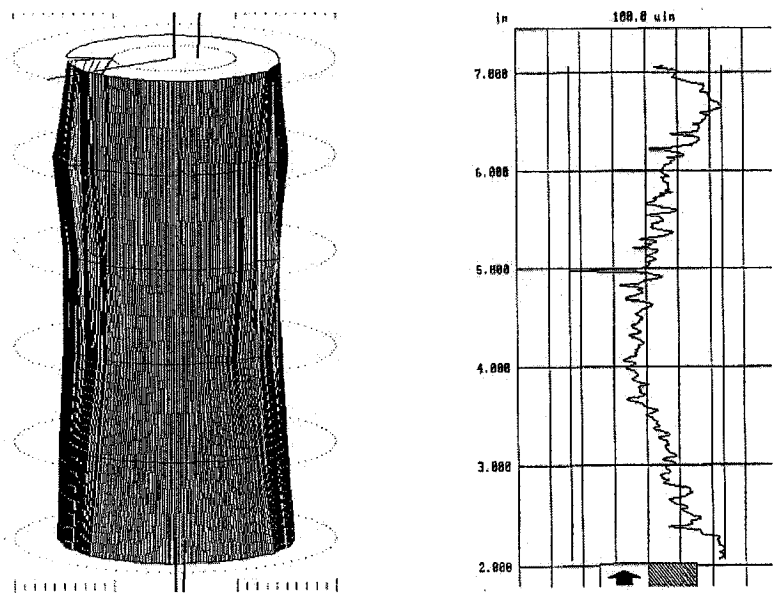


(g) (h)

Fig. 4.49: Roundness for D21 from the direction of drilling in mm (a) at 12.7, (b) at 38.1, (c) at 50.8, (d) at 88.9, (e) at 114.3, (f) at 139.7, (g) cylindricity error and (h) Straightness.

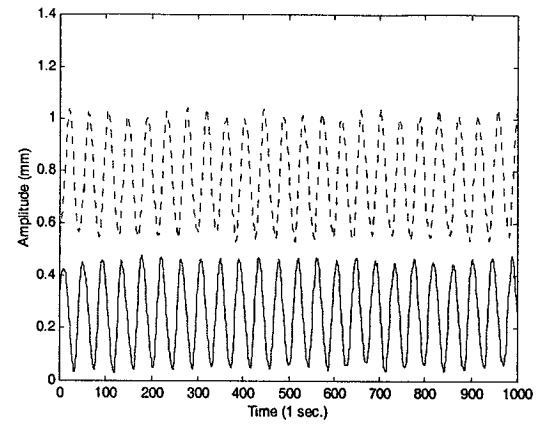


(a)

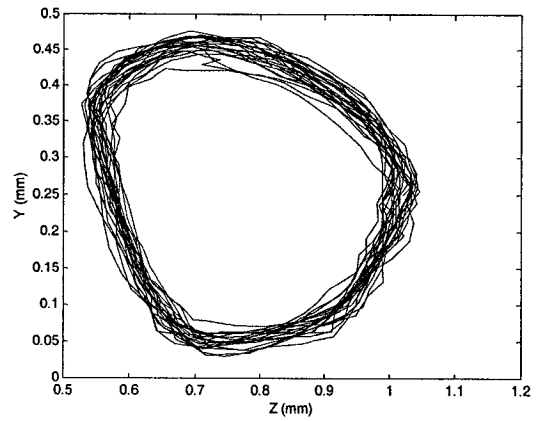


(b)

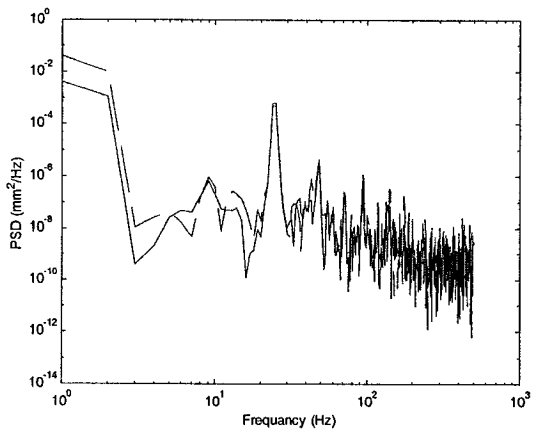


(c)

Fig. 4.50: The signal analysis of D27, (a) The two signals of master and slave sensors, (b) The whirl orbit and (c) the power spectral density of the signal.

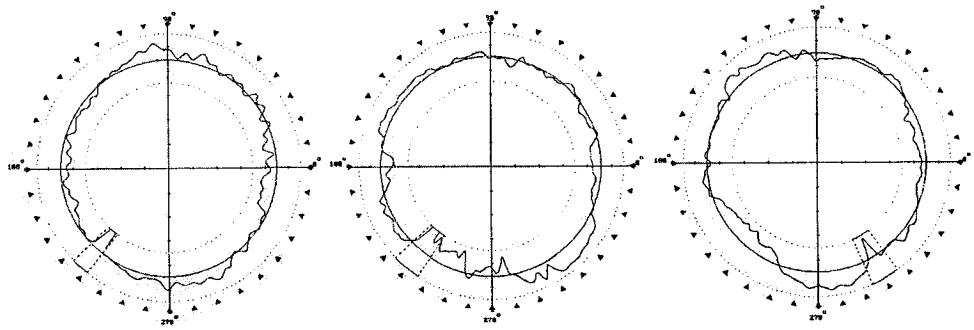

(a) (b) (c)

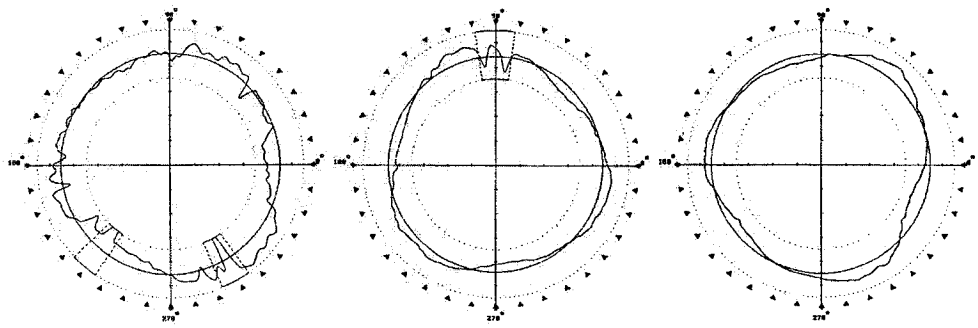

(d) (e) (f)

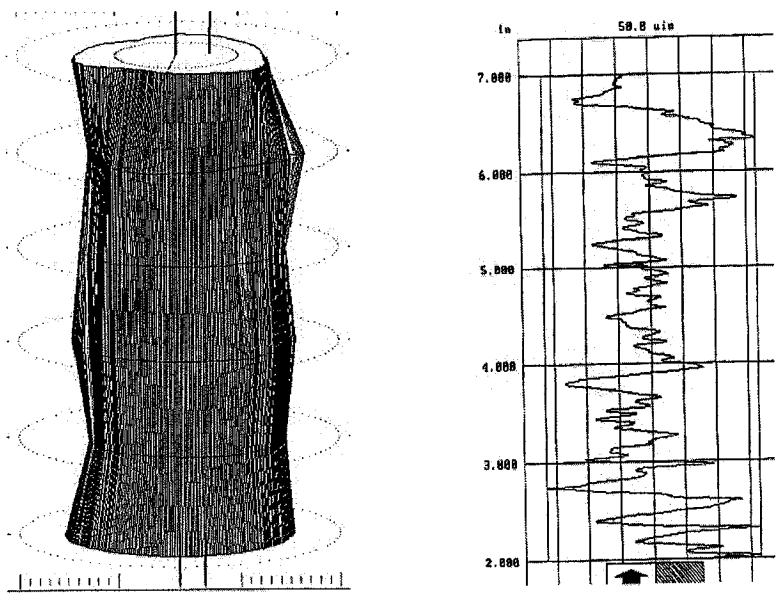


(g) (h)

Fig. 4.51: Roundness for D27 from the direction of drilling in mm (a) at 12.7, (b) at 38.1, (c) at 50.8, (d) at 88.9, (e) at 114.3, (f) at 139.7, (g) cylindricity error and (h) Straightness.

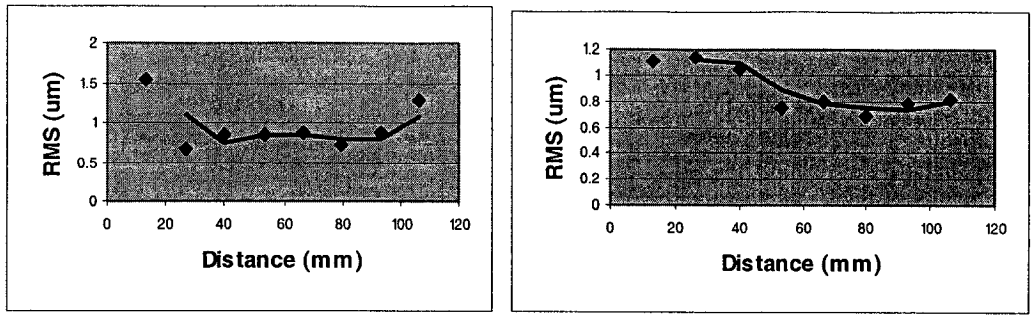


(a)




(b)

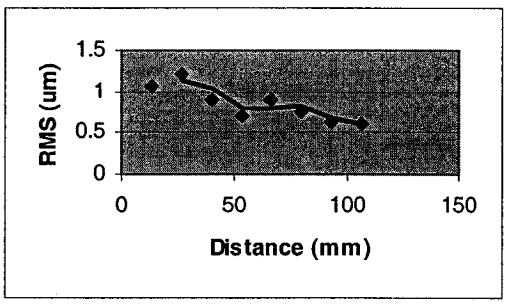


(c)

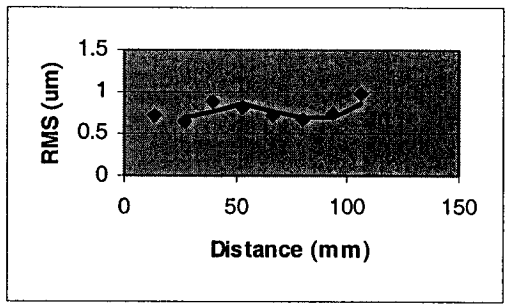


(d)

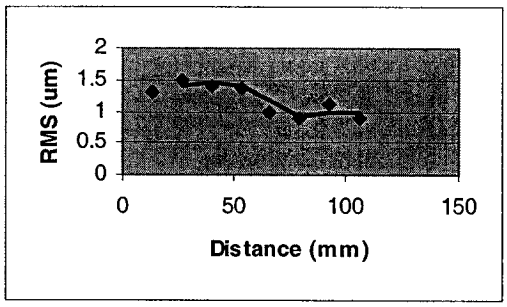


(e)

Fig. 4.52: Roughness measurements (a) D3 (b) D10, (c) D15, (d) D21 and (e) D27.

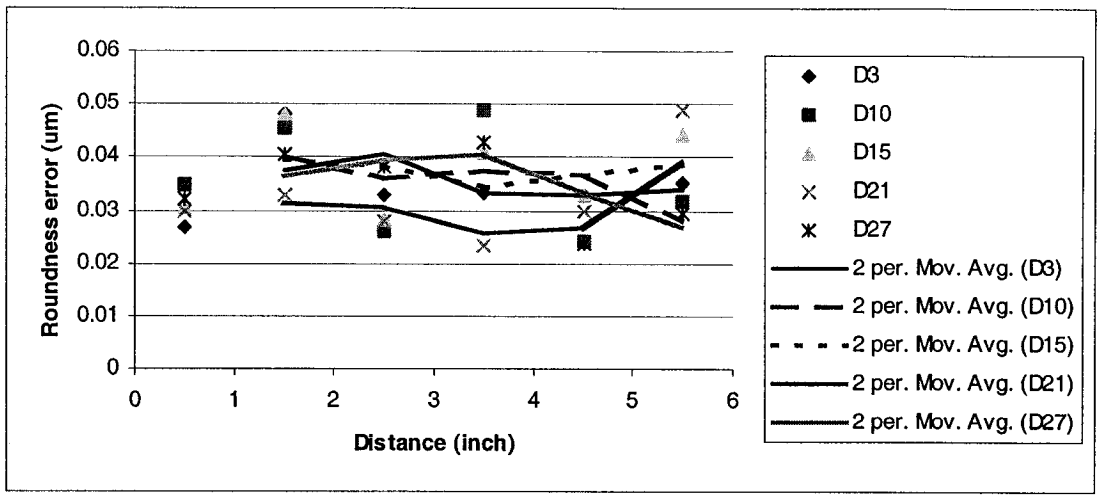


Fig. 4.53: Roundness error for D3, 10, 15, 21, 27 at length equal to 381 mm.

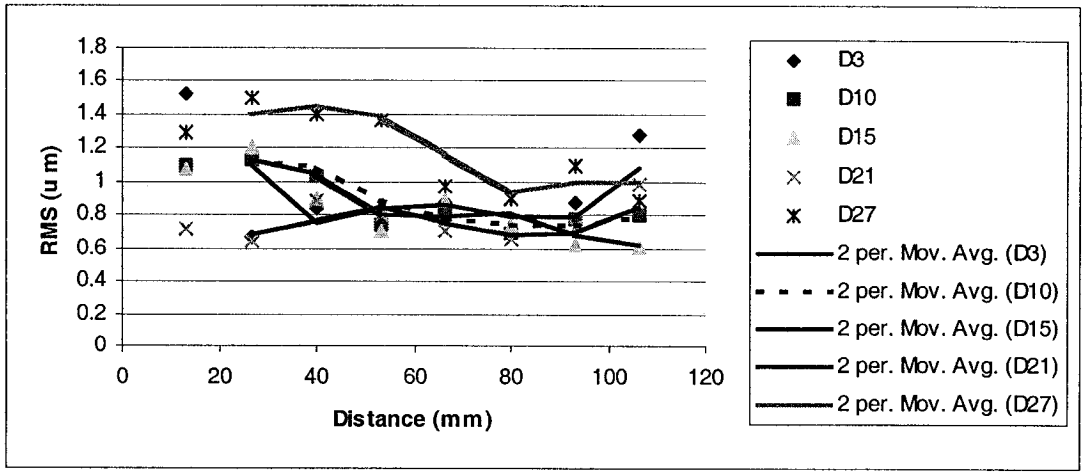


Fig. 4.54: Roughness for D3, 10, 15, 21, 27 at length equal to 381 mm.

## 4.2.4 Effect of whirling motion at 533.4 mm (21 in) length of cut

Table 4.6: A description of the main characteristics at a tool penetration of 533.4 mm.

| Tool penetration of 533.4 mm | Figure number | Speed (rpm) | Feed rate (mm/min) | Flow rate (G/min) |
|---|---|---|---|---|
| D4 | 4.55 | 1240 | 71 | 20 |
| | (a) | Displacement in the Y and Z coordinates | | |
| | (b) | Whirl ellipse | | |
| | (c) | Power spectral density (PSD) | | |
| First and second spectral peaks | | 21.24 Hz, 41.44 Hz | | |
| | 4.56 | Roundness characteristics | | Value ($\mu$m) |
| | (a) | 4-lobed out of run | | 0.046482 |
| | (b) | 3-lobed out of run | | 0.033147 |
| | (c) | Almost true round | | 0.022707 |
| | (d) | Almost true round with random irregularities | | 0.021133 |
| | (e) | Almost true round with random irregularities | | 0.037973 |
| | (f) | Almost true round | | 0.021488 |
| | (g) | Cylindricity error | | 0.174752 |
| | (h) | Straightness error | | 0.15494 |
| D11 | 4.57 | 1040 | 117 | 30 |
| | (a) | Displacement in the Y and Z coordinates | | |
| | (b) | Whirl ellipse | | |
| | (c) | Power spectral density (PSD) | | |
| First and second spectral peaks | | 17.83 Hz, 33.70 Hz | | |
| | 4.58 | Roundness characteristics | | Value ($\mu$m) |
| | (a) | 3-lobed out of run | | 0.028702 |
| | (b) | 2-lobed out of run with random irregularities | | 0.038354 |
| | (c) | Random irregularities | | 0.048006 |
| | (d) | 2-lobed out of run | | 0.03348 |
| | (e) | 4-lobed out of run with random irregularities | | 0.046736 |
| | (f) | Almost true round | | 0.029413 |
| | (g) | Cylindricity error | | 0.224536 |
| | (h) | Straightness error | | 0.14097 |

Table 4.6: A description of the main characteristics at a tool penetration of 533.4 mm (continued).

| Tool penetration of 533.4 mm | Figure number | Speed (rpm) | Feed rate (mm/min) | Flow rate (G/min) |
|---|---|---|---|---|
| D16 | 4.59 | 1440 | 71 | 30 |
| | (a) | Displacement in the Y and Z coordinates | | |
| | (b) | Whirl ellipse | | |
| | (c) | Power spectral density (PSD) | | |
| First and second spectral peaks | | 24.51 Hz, 47.83 Hz | | |
| | 4.60 | Roundness characteristics | | Value ($\mu$m) |
| | (a) | 7-lobed out of run | | 0.032512 |
| | (b) | Random irregularities | | 0.029337 |
| | (c) | 2-lobed out of run | | 0.038608 |
| | (d) | 3-lobed out of run with random irregularities | | 0.037846 |
| | (e) | 3-lobed out of run | | 0.040843 |
| | (f) | 4-lobed out of run | | 0.031039 |
| | (g) | Cylindricity error | | 0.136398 |
| | (h) | Straightness error | | 0.099695 |
| D22 | 4.61 | 1240 | 71 | 40 |
| | (a) | Displacement in the Y and Z coordinates | | |
| | (b) | Whirl ellipse | | |
| | (c) | Power spectral density (PSD) | | |
| First and second spectral peaks | | 21.24 Hz, 40.79 Hz | | |
| | 4.49 | Roundness characteristics | | Value ($\mu$m) |
| | (a) | 7-lobed out of run | | 0.03363 |
| | (b) | 7-lobed out of run | | 0.038252 |
| | (c) | 4-lobed out of run | | 0.04892 |
| | (d) | 3-lobed out of run | | 0.038913 |
| | (e) | 3-lobed out of run | | 0.042621 |
| | (f) | 3-lobed out of run | | 0.047447 |
| | (g) | Cylindricity error | | 0.211328 |
| | (h) | Straightness error | | 0.157226 |

The main characteristics of roundness are almost true round for D4, 2 to 3- lobed for D11 and D16. The 3-lobed characterizes D22.

The roughness was decreasing for D4, 11 and 22, while it was increasing for D16. One-figure plot for roundness and roughness are shown in Fig. 4.64 and Fig. 4.65. Roundness error was decreasing for D11 and D16 and increasing for D4 and D22.

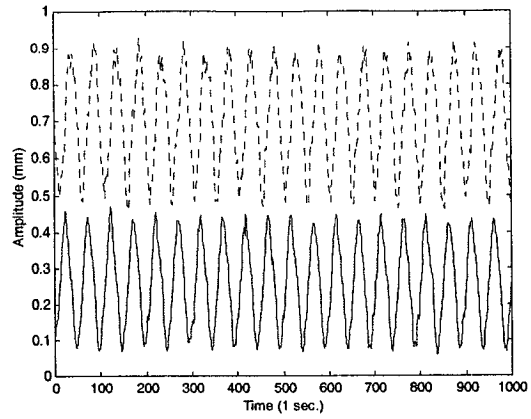


(a)

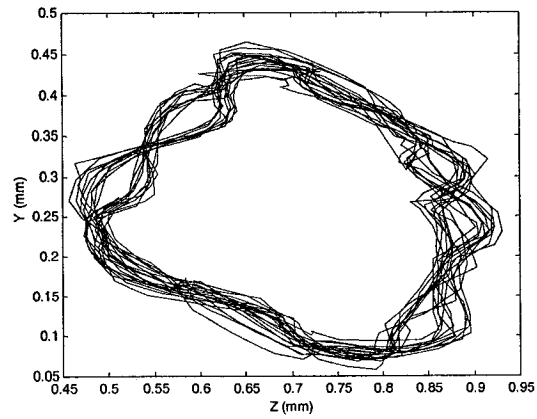


(b)

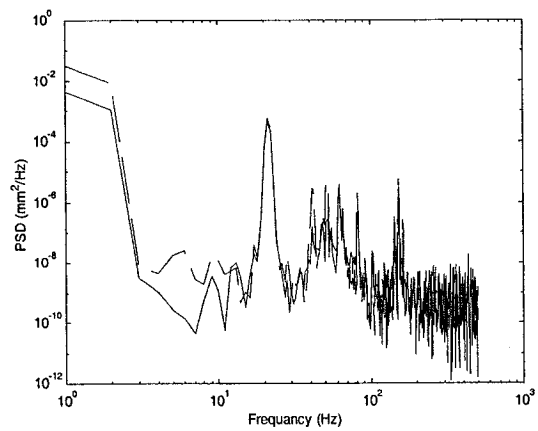


(c)

Fig. 4.55: The signal analysis of D4, (a) The two signals of master and slave sensors, (b) The whirl orbit and (c) the power spectral density of the signal.

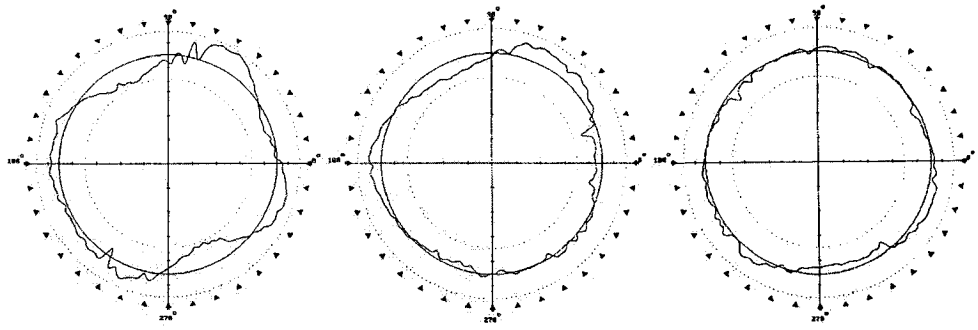

(a) (b) (c)

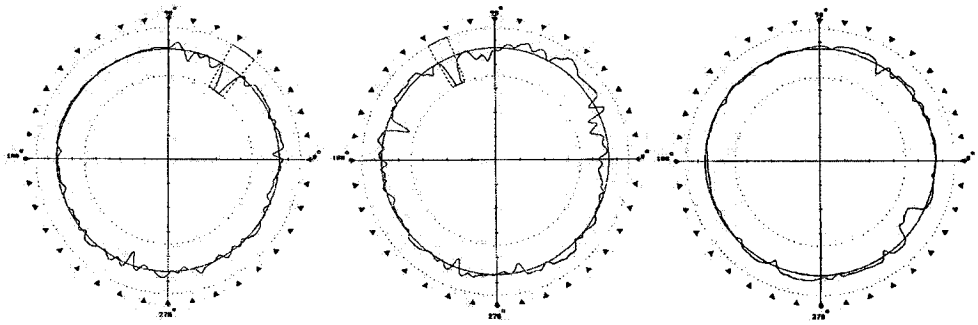

(d) (e) (f)

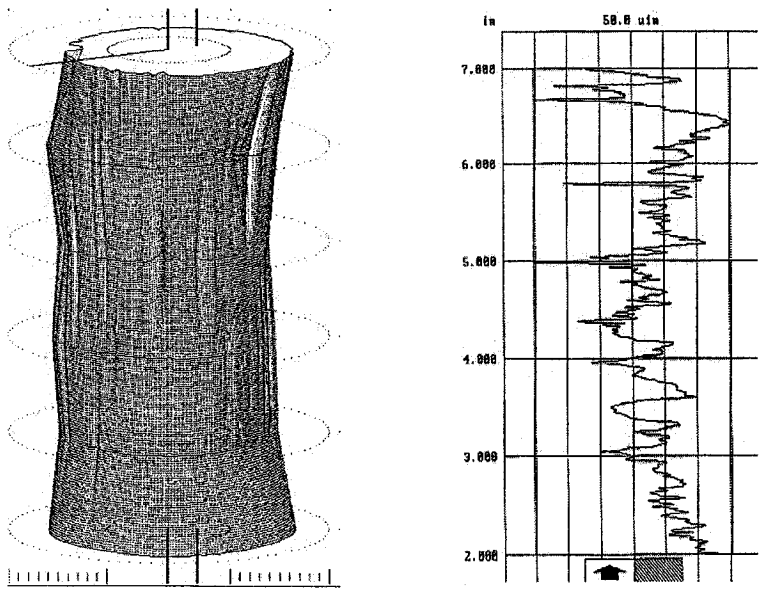


(g) (h)

Fig. 4.56: Roundness for D4 from the direction of drilling in mm (a) at 12.7, (b) at 38.1, (c) at 50.8, (d) at 88.9, (e) at 114.3, (f) at 139.7, (g) cylindricity error and (h) Straightness.

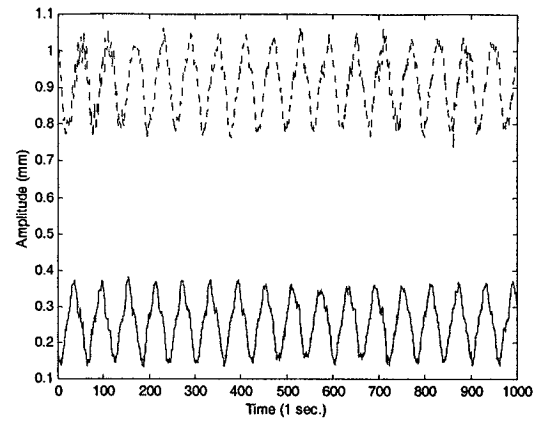


(a)

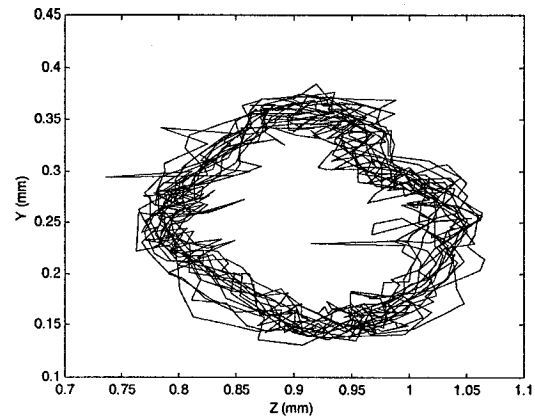


(b)

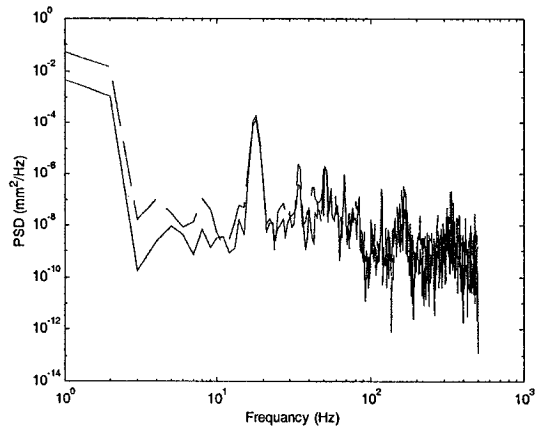


(c)

Fig. 4.57: The signal analysis of D11, (a) The two signals of master and slave sensors, (b) The whirl orbit and (c) the power spectral density of the signal.

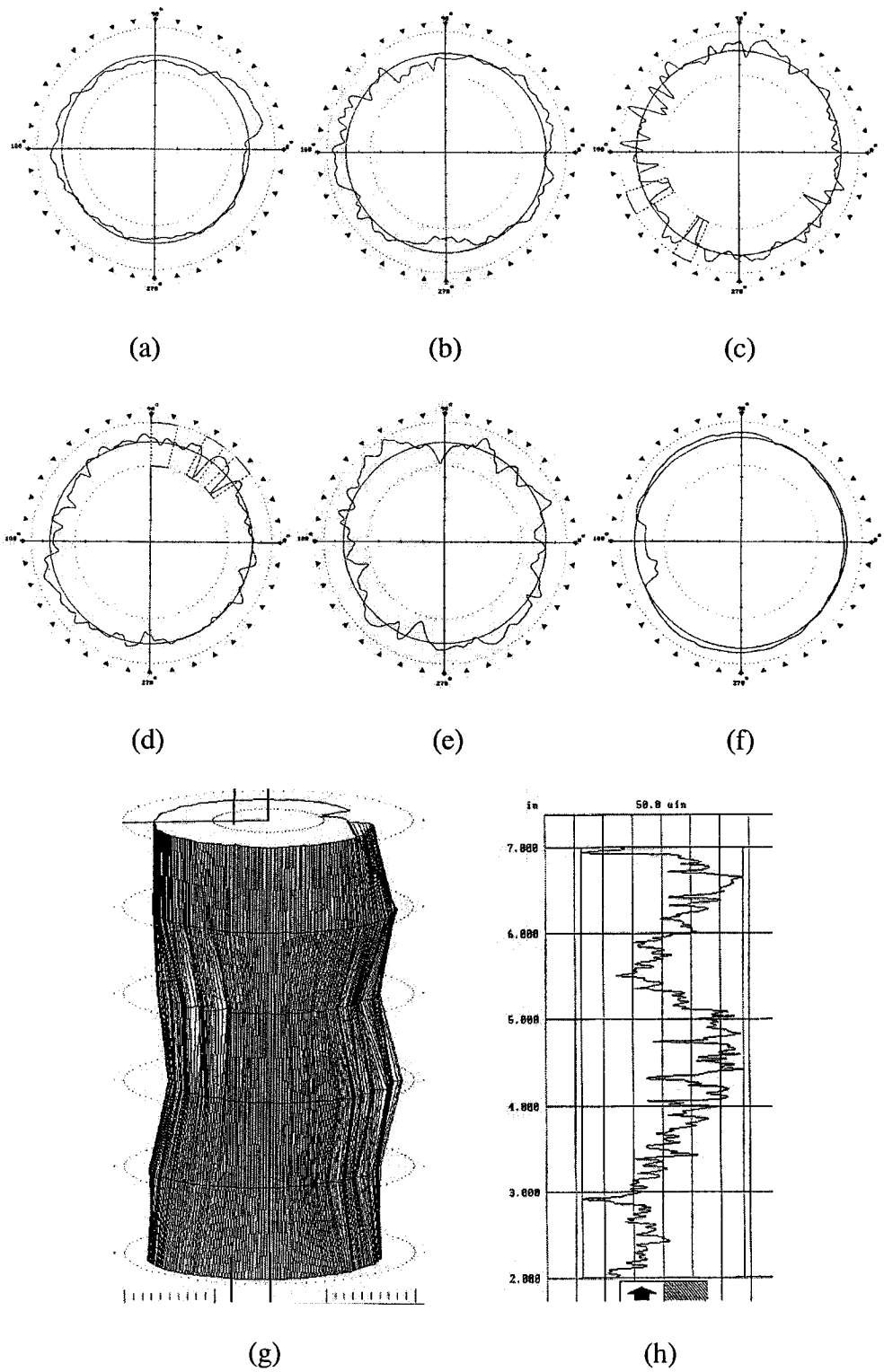


Fig. 4.58: Roundness for D11 from the direction of drilling in mm (a) at 12.7, (b) at 38.1, (c) at 50.8, (d) at 88.9, (e) at 114.3, (f) at 139.7, (g) cylindricity error and (h) Straightness.

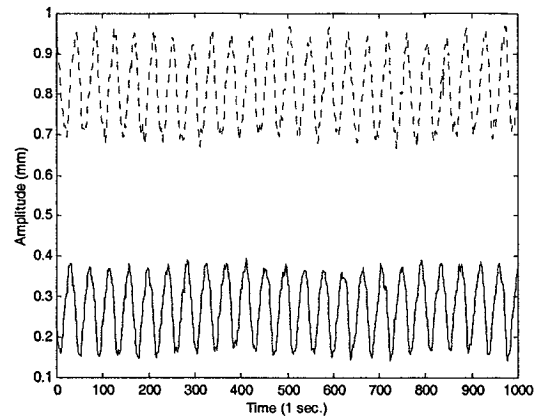


(a)

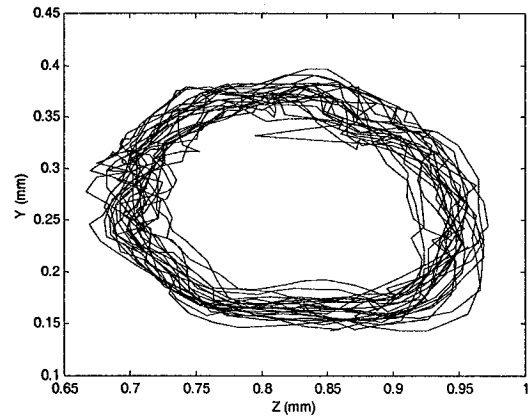


(b)

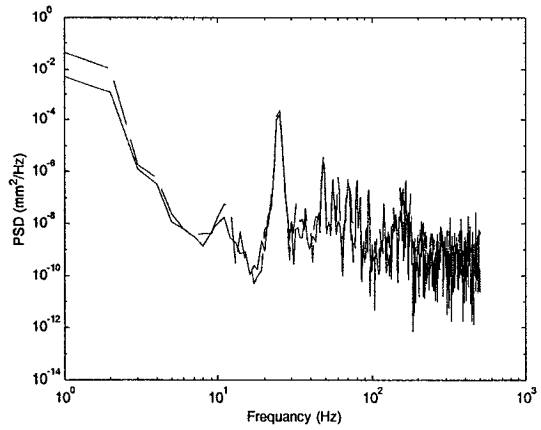


(c)

Fig. 4.59: The signal analysis of D16, (a) The two signals of master and slave sensors, (b) The whirl orbit and (c) the power spectral density of the signal.

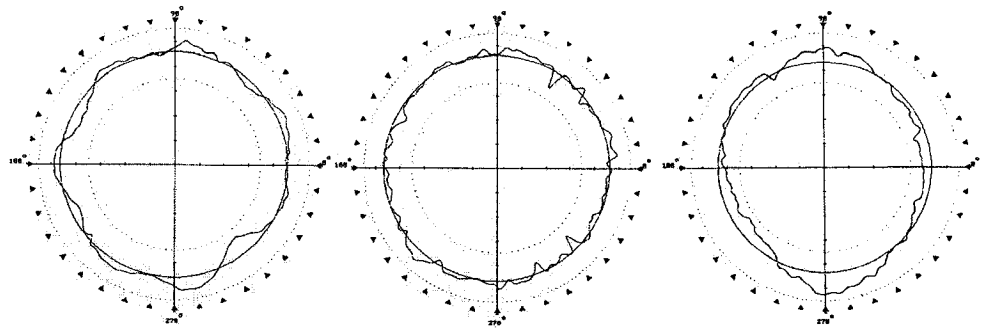

(a) (b) (c)

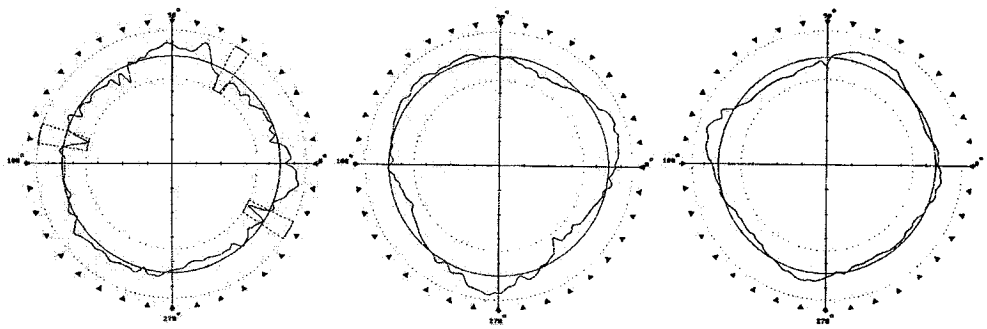

(d) (e) (f)

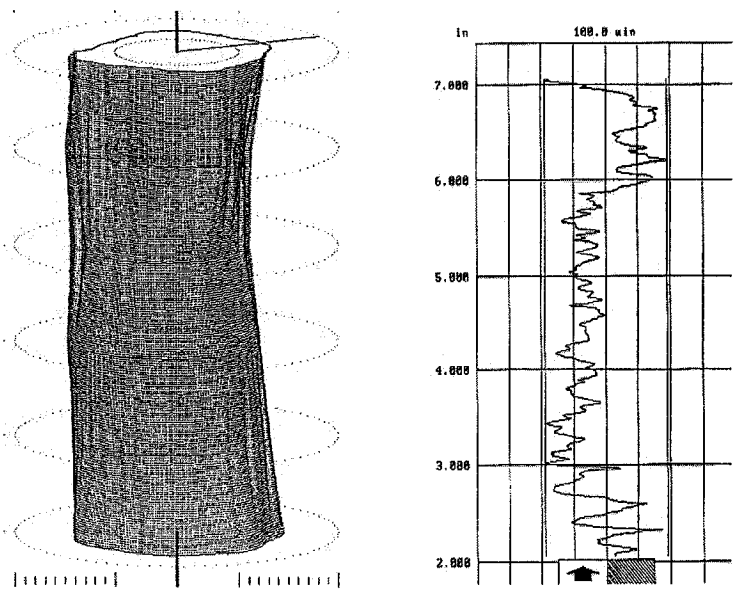


(g) (h)

Fig. 4.60: Roundness for D16 from the direction of drilling in mm (a) at 12.7, (b) at 38.1, (c) at 50.8, (d) at 88.9, (e) at 114.3, (f) at 139.7, (g) cylindricity error and (h) Straightness.

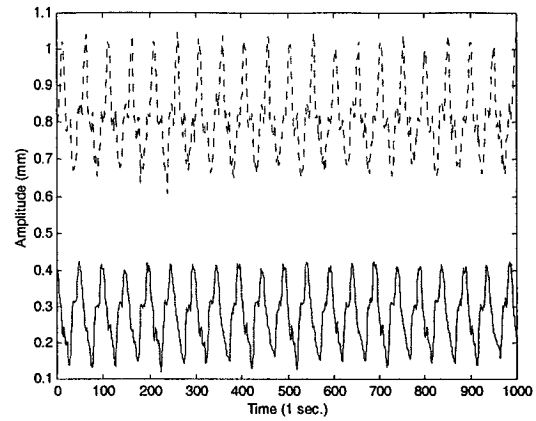


(a)

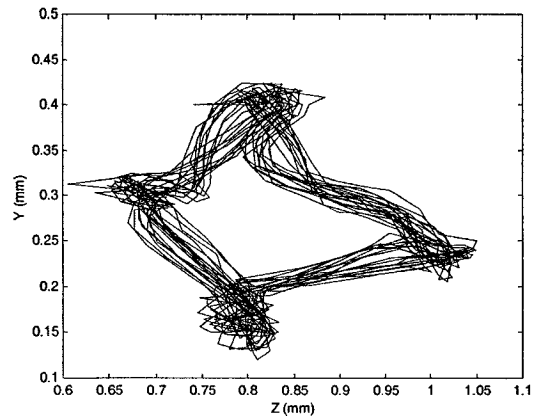


(b)

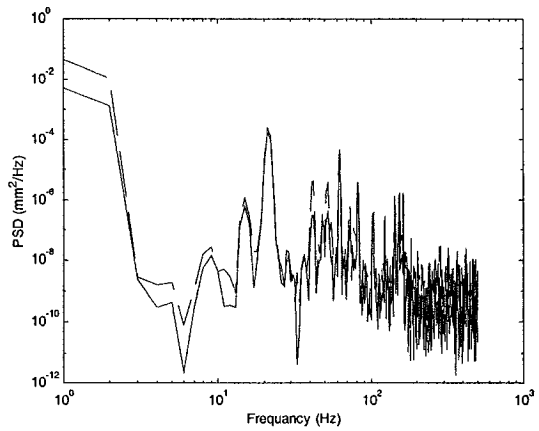


(c)

Fig. 4.61: The signal analysis of D22, (a) The two signals of master and slave sensors, (b) The whirl orbit and (c) the power spectral density of the signal.

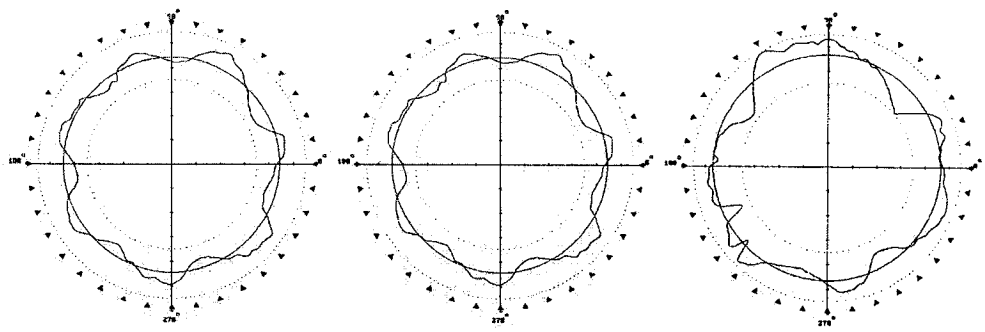

(a) (b) (c)

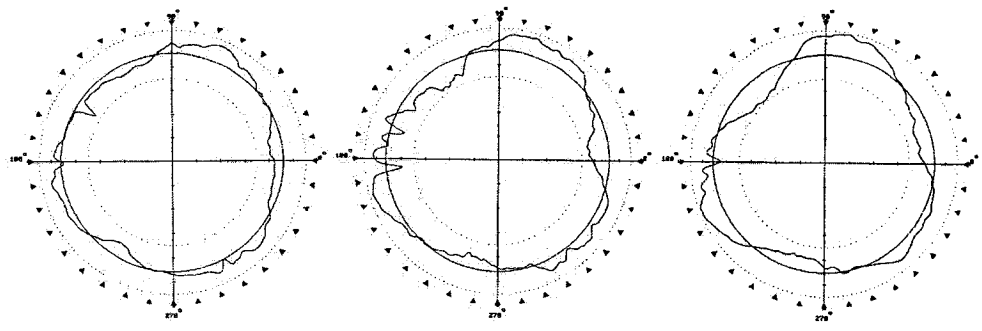

(d) (e) (f)

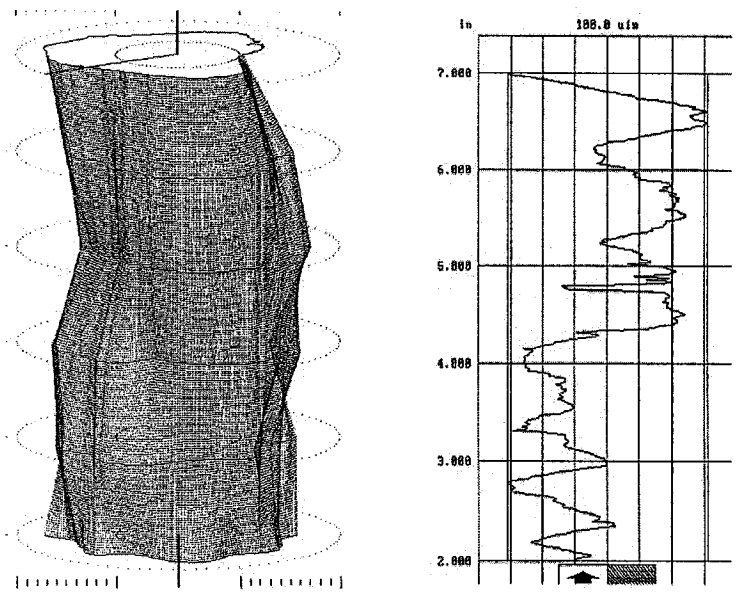


(g) (h)

Fig. 4.62: Roundness for D22 from the direction of drilling in mm (a) at 12.7, (b) at 38.1, (c) at 50.8, (d) at 88.9, (e) at 114.3, (f) at 139.7, (g) cylindricity error and (h) Straightness.

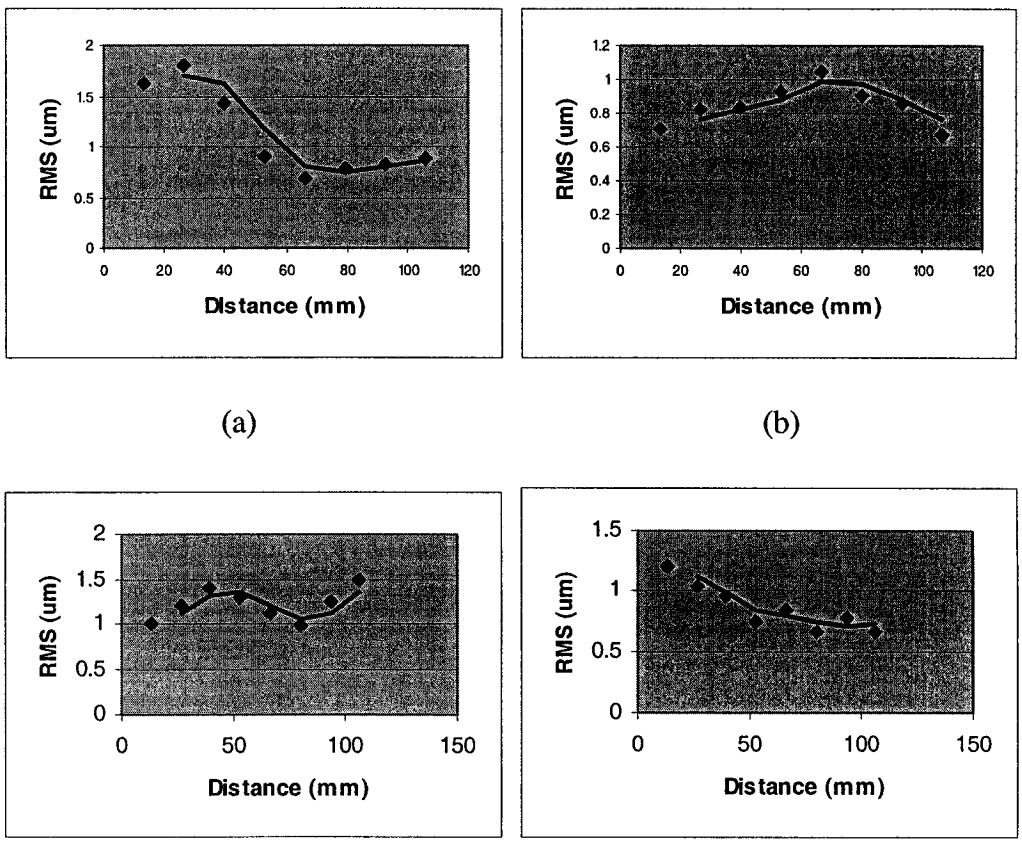


Fig. 4.63: Roughness measurements (a) D4 (b) D11 (c) D16 and (d) D22.

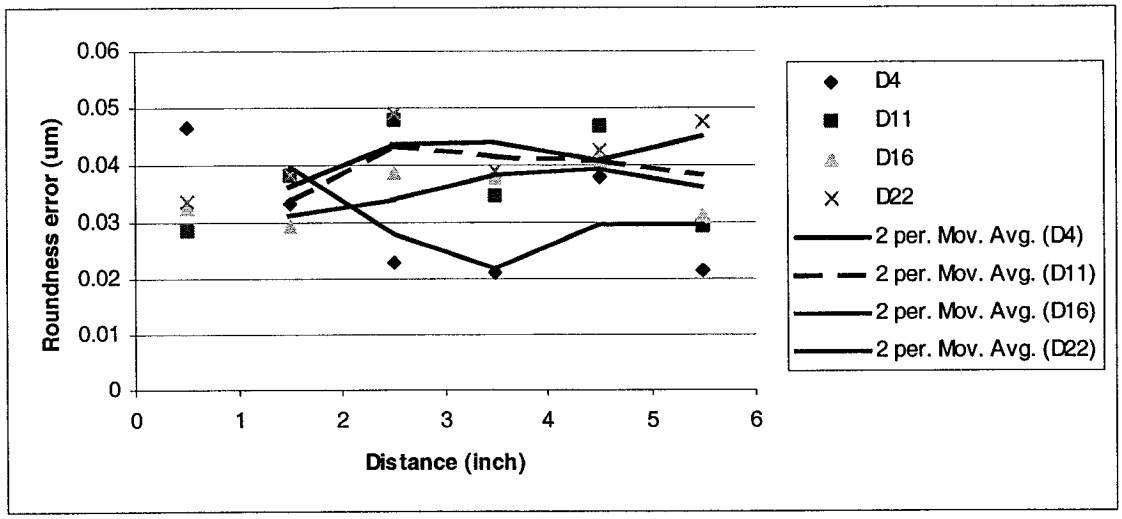


Fig. 4.64: Roundness error for D4, 11,16, 22 at length equal to 533.4 mm.

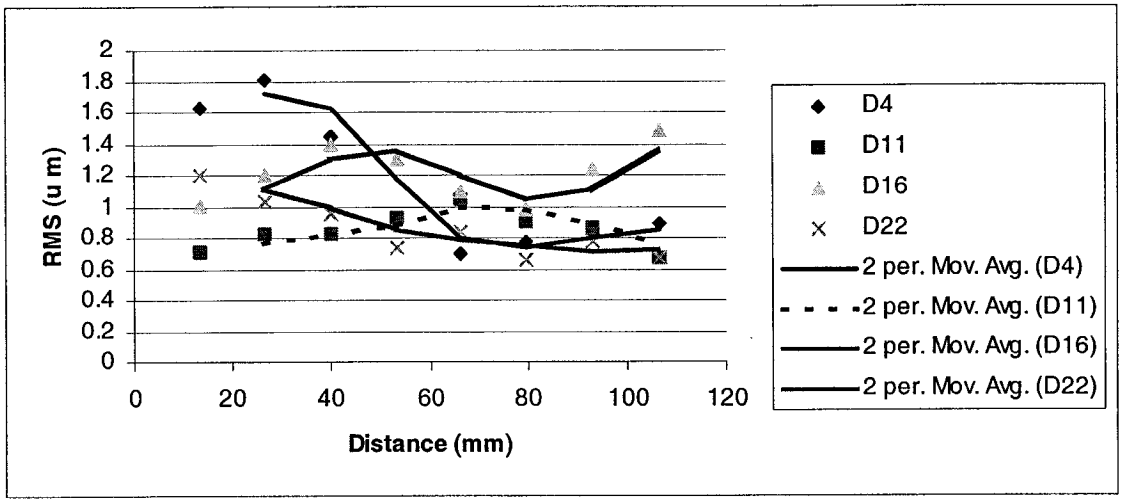


Fig. 4.65: Roughness for D4, 11, 16, 22 at length equal to 533.4 mm.

### 4.2.5 Effect of the whirling motion at 685.8 mm (27 in) length of cut

Table 4.7: A description of the main characteristics at a tool penetration of 685.8 mm.

| Tool penetration of 685.8 mm | Figure number | Speed (rpm) | Feed rate (mm/min) | Flow rate (G/min) |
|---|---|---|---|---|
| D5 | 4.66 | 1240 | 117 | 20 |
| | (a) | Displacement in the Y and Z coordinates | | |
| | (b) | Whirl ellipse | | |
| | (c) | Power spectral density (PSD) | | |
| First and second spectral peaks | | 20.90 Hz, 31.62 Hz | | |
| | 4.67 | Roundness characteristics | | Value ($\mu$m) |
| | (a) | Almost egg-shaped with random irregularities | | 0.044704 |
| | (b) | True round with random irregularities | | 0.027178 |
| | (c) | Random irregularities with interrupted surface | | 0.033528 |
| | (d) | True round | | 0.030094 |
| | (e) | 3-lobed out of run with random irregularities | | 0.041148 |
| | (f) | 3-lobed out of run | | 0.034696 |
| | (g) | Cylindricity error | | 0.25019 |
| | (h) | Straightness error | | 0.150876 |
| D12 | 4.68 | 1040 | 173 | 30 |
| | (a) | Displacement in the Y and Z coordinates | | |
| | (b) | Whirl ellipse | | |
| | (c) | Power spectral density (PSD) | | |
| First and second spectral peaks | | 17.54 Hz, 49.37 Hz | | |
| | 4.69 | Roundness characteristics | | Value ($\mu$m) |
| | (a) | 2-lobed with random irregularities | | 0.040259 |
| | (b) | 2-lobed out of run | | 0.031242 |
| | (c) | 2-lobed out of run | | 0.023266 |
| | (d) | 3-lobed out of run | | 0.027686 |
| | (e) | 2-lobed out of run | | 0.037719 |
| | (f) | 3-lobed out of run | | 0.035763 |
| | (g) | Cylindricity error | | 0.224536 |
| | (h) | Straightness error | | 0.14097 |

Table 4.7: A description of the main characteristics at a tool penetration of 27 inches (continued).

| Tool penetration of 685.8 mm | Figure number | Speed (rpm) | Feed rate (mm/min) | Flow rate (G/min) |
|---|---|---|---|---|
| D17 | 4.70 | 1440 | 117 | 30 |
| | (a) | Displacement in the Y and Z coordinates | | |
| | (b) | Whirl ellipse | | |
| | (c) | Power spectral density (PSD) | | |
| First and second spectral peaks | | 11.60 Hz, 24. 12 Hz | | |
| | 4.71 | Roundness characteristics | | Value ($\mu$m) |
| | (a) | 3-lobed out of run | | 0.03048 |
| | (b) | 4-lobed out of run with random irregularities | | 0.044704 |
| | (c) | 2-lobed out of run with random irregularities | | 0.045466 |
| | (d) | 2-lobed out of run | | 0.036322 |
| | (e) | 2-lobed out of run with random irregularities | | 0.038608 |
| | (f) | 3-lobed out of run | | 0.041453 |
| | (g) | Cylindricity error | | 0.25222 |
| | (h) | Straightness error | | 0.093839 |
| D23 | 4.72 | 1240 | 117 | 40 |
| | (a) | Displacement in the Y and Z coordinates | | |
| | (b) | Whirl ellipse | | |
| | (c) | Power spectral density (PSD) | | |
| First and second spectral peaks | | 20.90 Hz, 41.44 Hz | | |
| | 4.73 | Roundness characteristics | | Value ($\mu$m) |
| | (a) | 3-lobed out of run | | 0.03495 |
| | (b) | 3-lobed out of run | | 0.033172 |
| | (c) | 3-lobed out of run | | 0.039218 |
| | (d) | 3-lobed out of run | | 0.038252 |
| | (e) | 3-lobed out of run | | 0.03871 |
| | (f) | 3-lobed out of run | | 0.026848 |
| | (g) | Cylindricity error | | 0.211328 |
| | (h) | Straightness error | | 0.157226 |

The main characteristic for D5 and D23 is 3-lobed while for D12 and D17 is 2 to 3-lobed. Fig. 4.74 is a plot of roughness for D4, 11,16 and 22. For D4 and D22 the roughness was increasing while it was decreasing for D11 and D16. Fig. 4.75 and 4.76 is a one-figure plot of roundness and roughness to compare between them. Roundness was decreasing for D17 and increasing doe D5, 12 and 22.

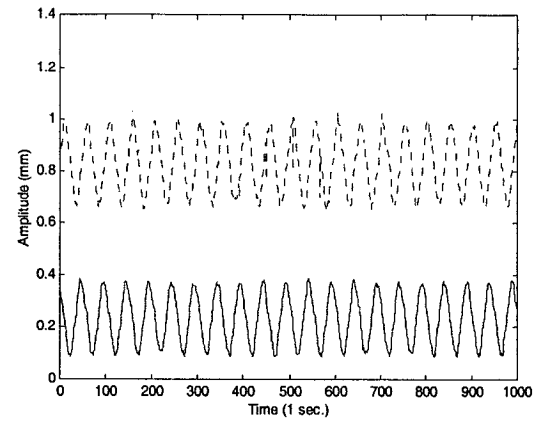


(a)

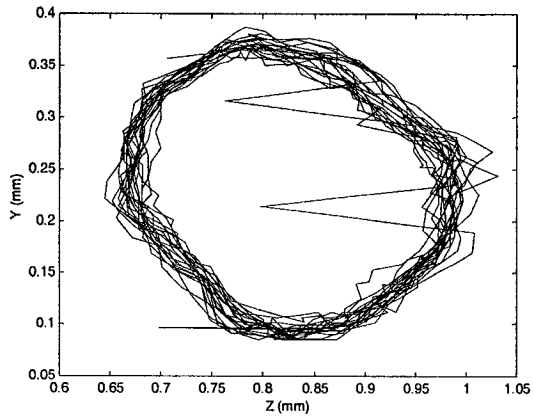


(b)

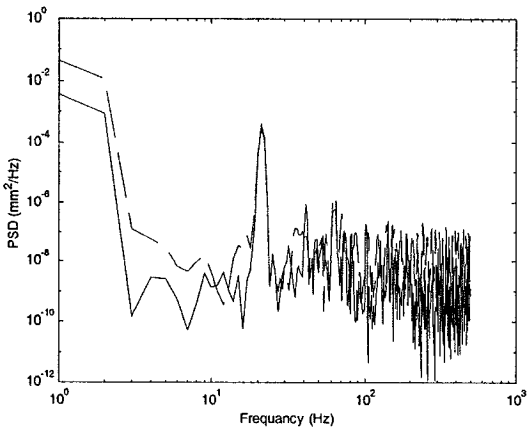


(c)

Fig. 4.66: The signal analysis of D5, (a) The two signals of master and slave sensors, (b) The whirl orbit and (c) the power spectral density of the signal.

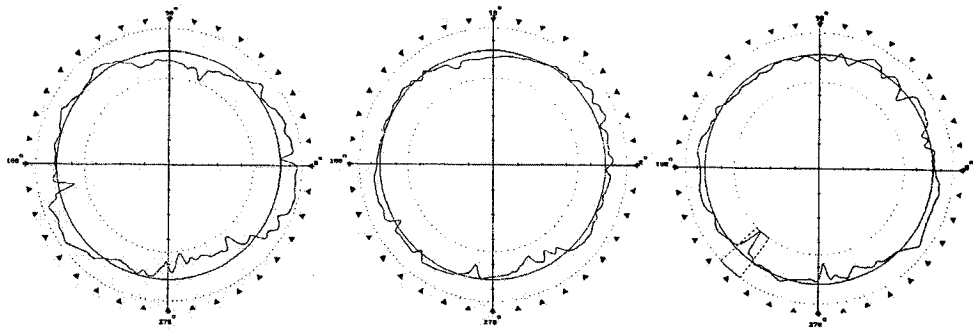

(a) (b) (c)

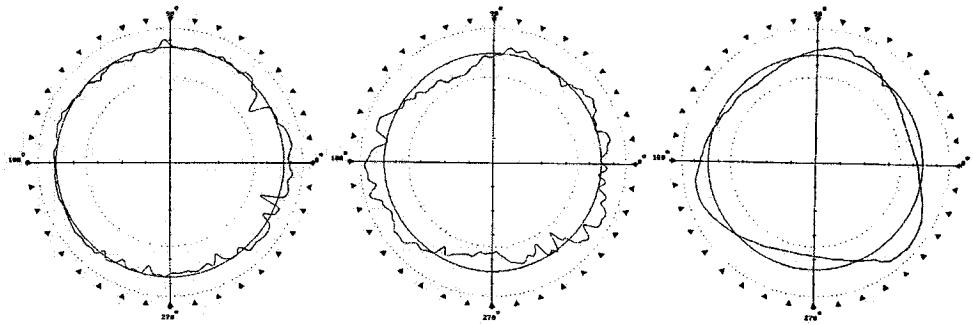

(d) (e) (f)

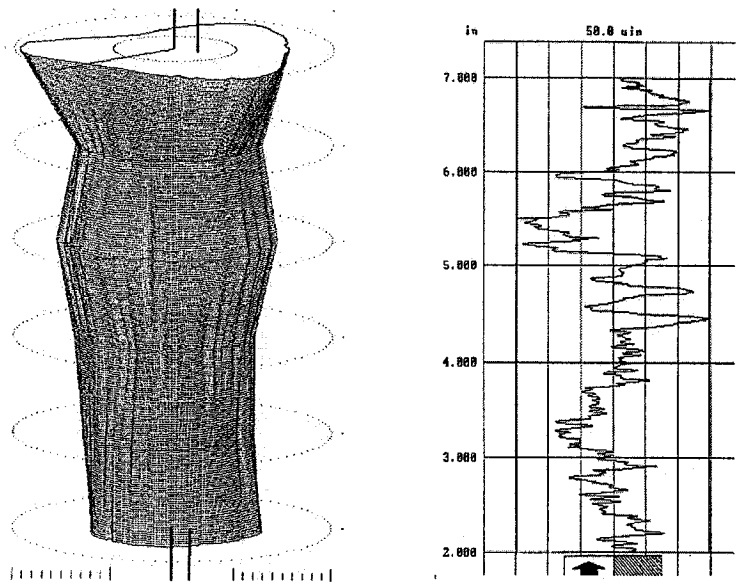


(g) (h)

Fig. 4.67: Roundness for D5 from the direction of drilling in mm (a) at 12.7, (b) at 38.1, (c) at 50.8, (d) at 88.9, (e) at 114.3, (f) at 139.7, (g) cylindricity error and (h) Straightness.

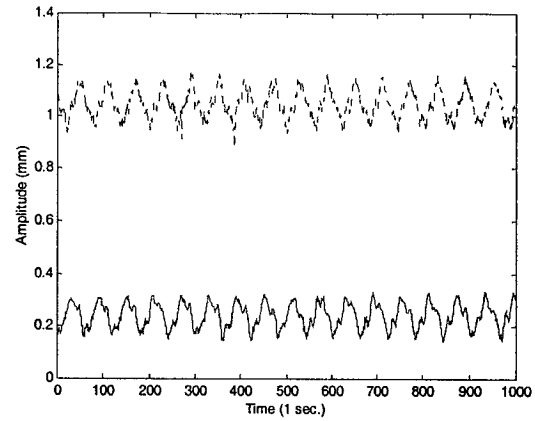


(a)

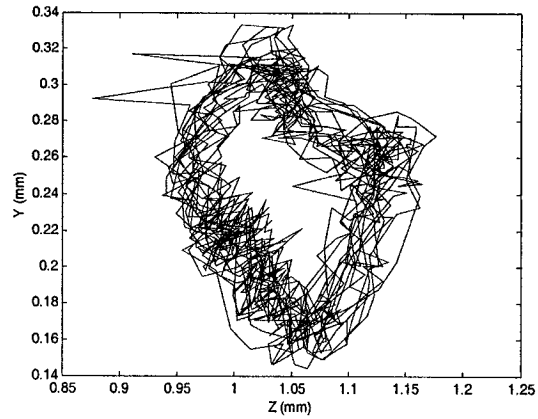


(b)

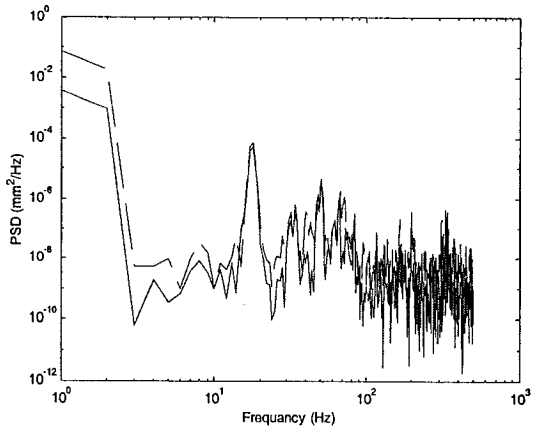


(c)

Fig. 4.68: The signal analysis of D12, (a) The two signals of master and slave sensors, (b) The whirl orbit and (c) the power spectral density of the signal.

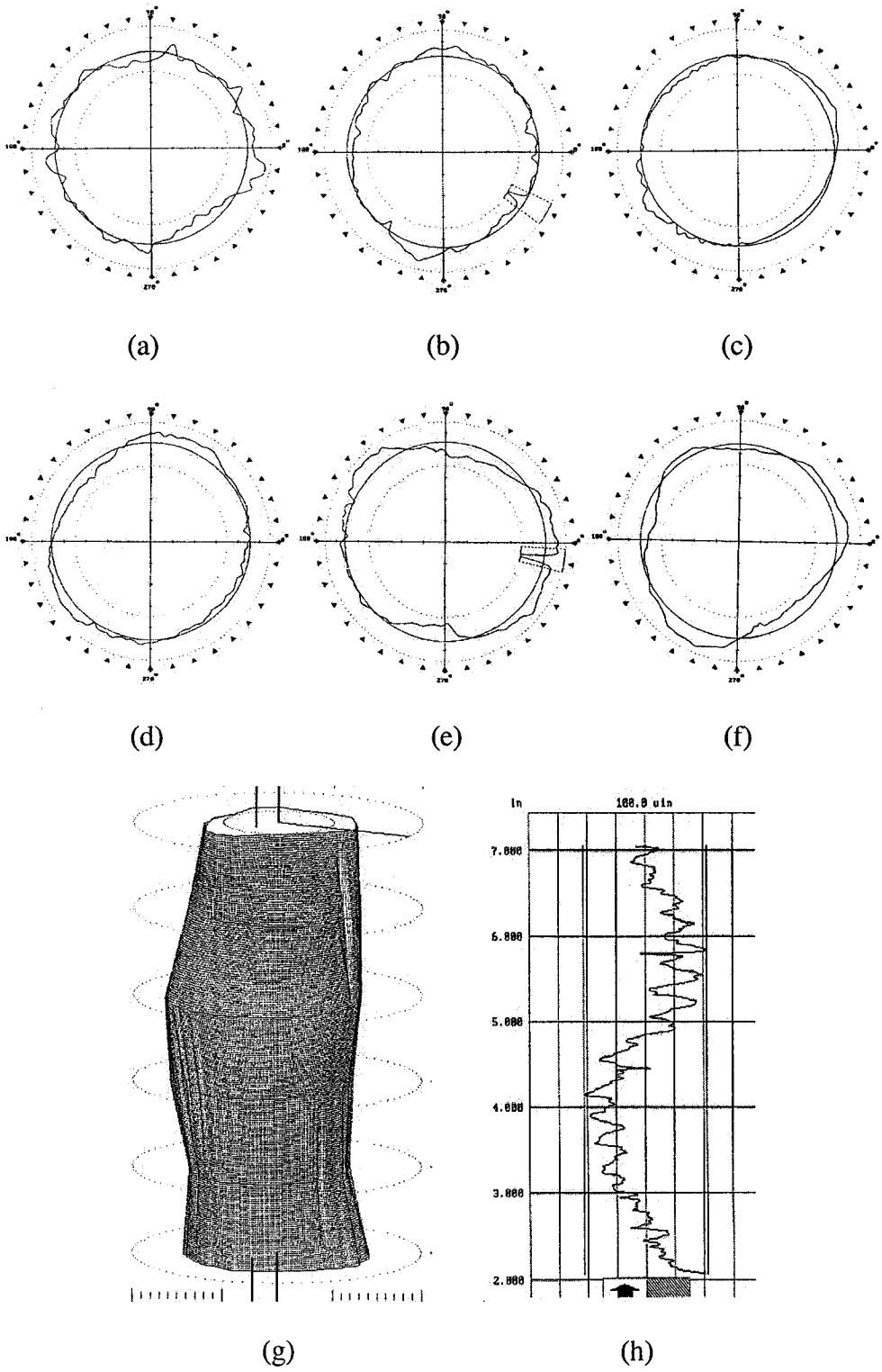


Fig. 4.69: Roundness for D12 from the direction of drilling in mm (a) at 12.7, (b) at 38.1, (c) at 50.8, (d) at 88.9, (e) at 114.3, (f) at 139.7, (g) cylindricity error and (h) Straightness.

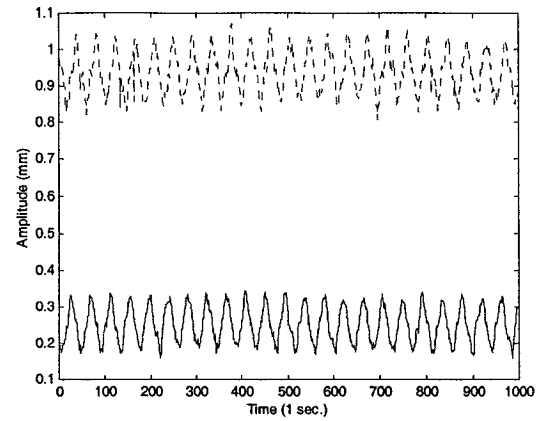


(a)

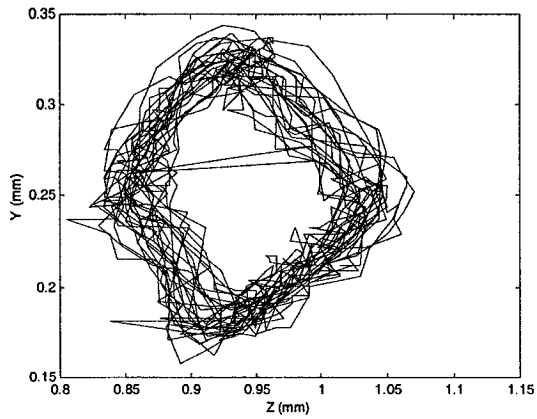


(b)

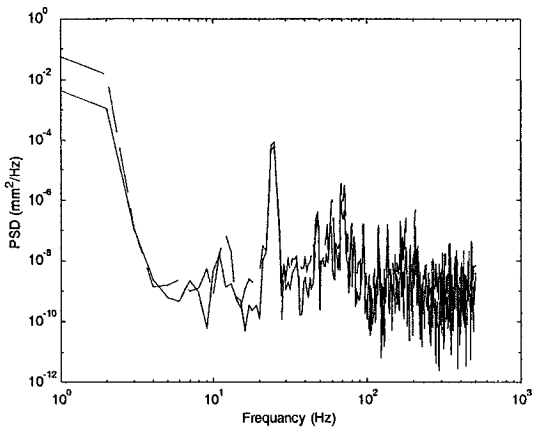


(c)

Fig. 4.70: The signal analysis of D17, (a) The two signals of master and slave sensors, (b) The whirl orbit and (c) the power spectral density of the signal.

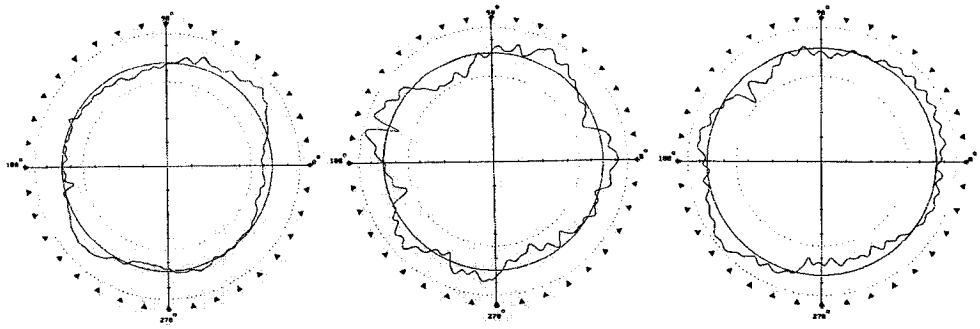

(a) (b) (c)

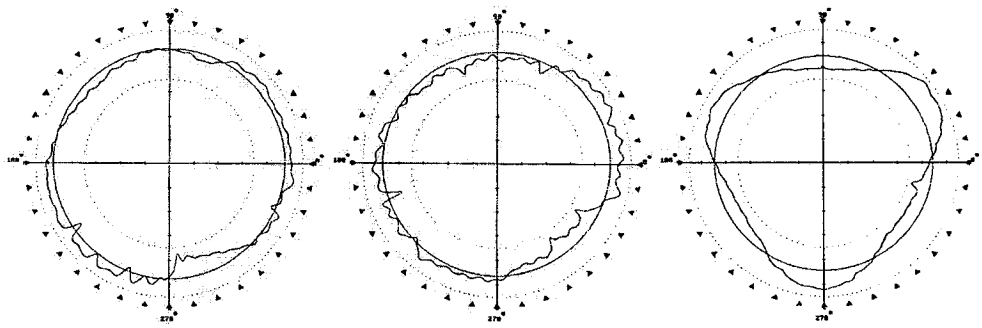

(d) (e) (f)

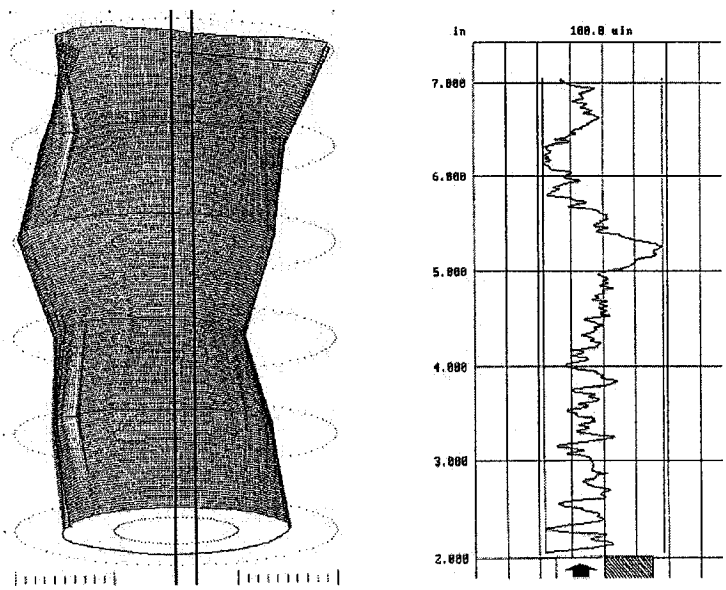


(g) (h)

Fig. 4.71: Roundness for D17 from the direction of drilling in mm (a) at 12.7, (b) at 38.1, (c) at 50.8, (d) at 88.9, (e) at 114.3, (f) at 139.7, (g) cylindricity error and (h) Straightness.

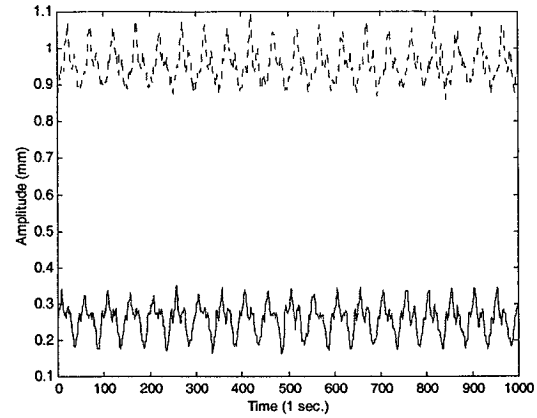


(a)

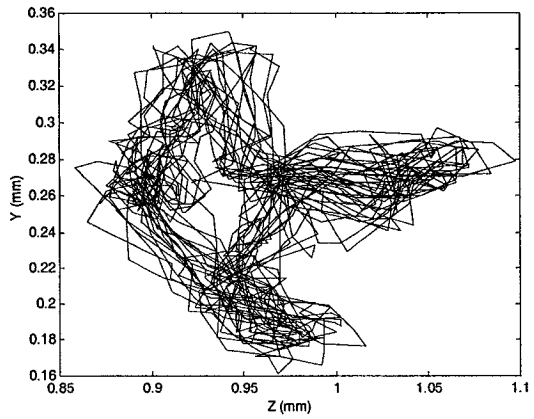


(b)

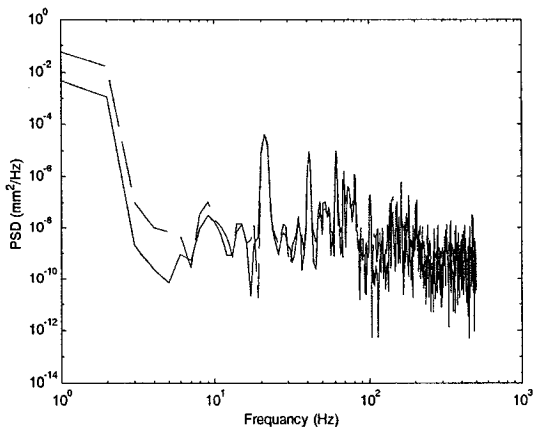


(c)

Fig. 4.72: The signal analysis of D23, (a) The two signals of master and slave sensors, (b) The whirl orbit and (c) the power spectral density of the signal.

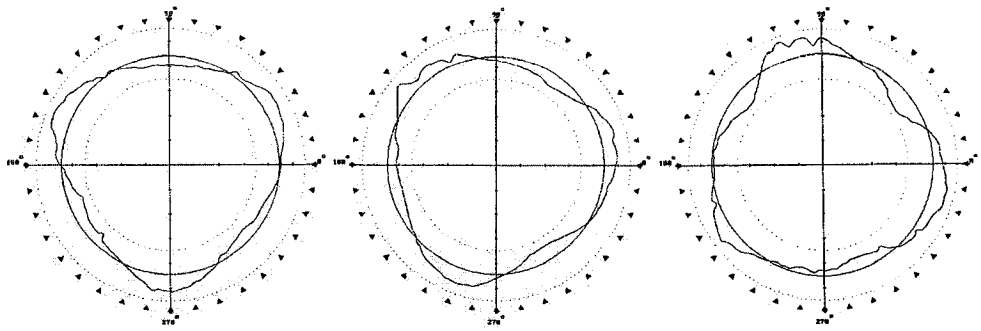

(a) (b) (c)

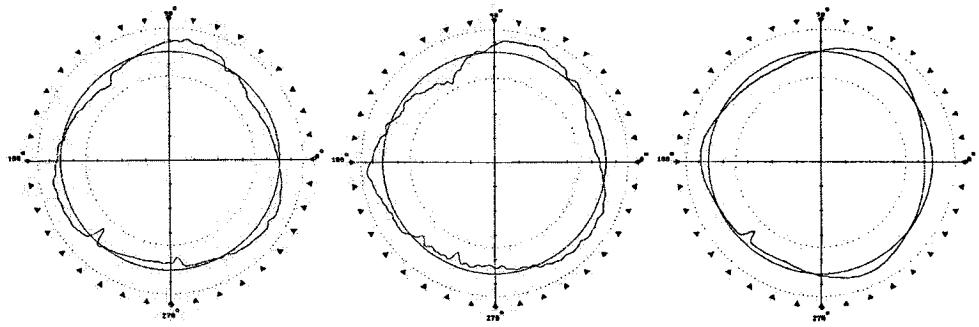

(a) (b) (c)

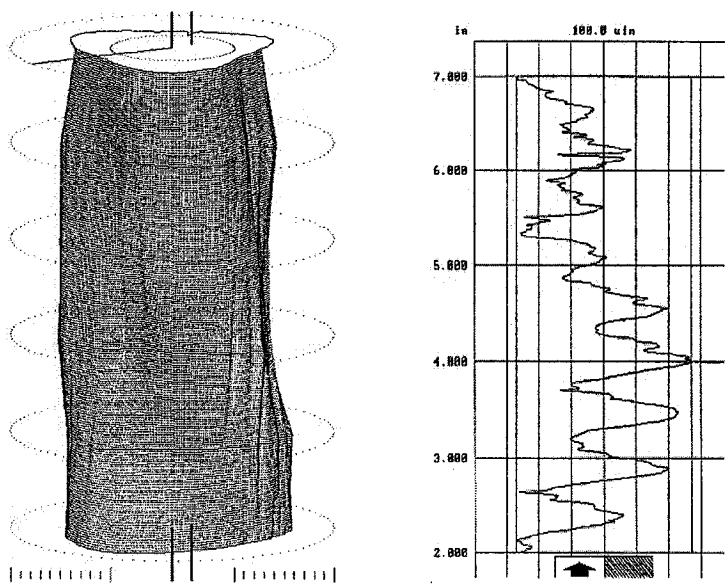


(g) (h)

Fig. 4.73: Roundness for D23 from the direction of drilling in mm (a) at 12.7, (b) at 38.1, (c) at 50.8, (d) at 88.9, (e) at 114.3, (f) at 139.7, (g) cylindricity error and (h) Straightness.

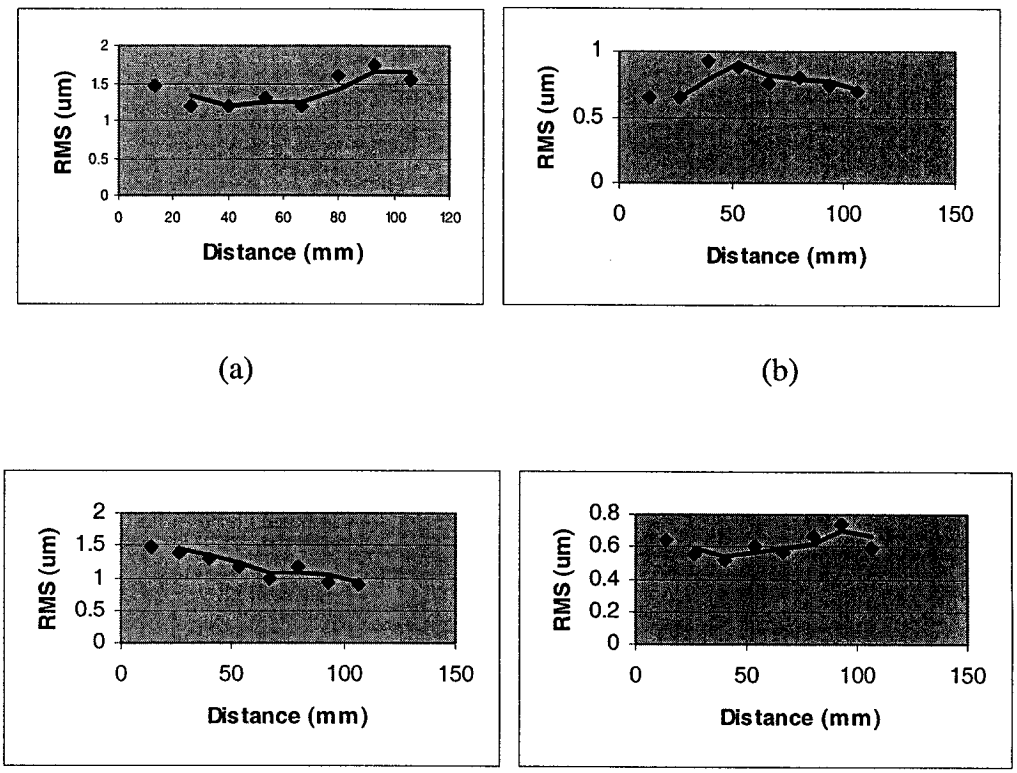


Fig. 4.74: Roughness measurements (a) D4 (b) D11, (c) D16 and (d) D22.

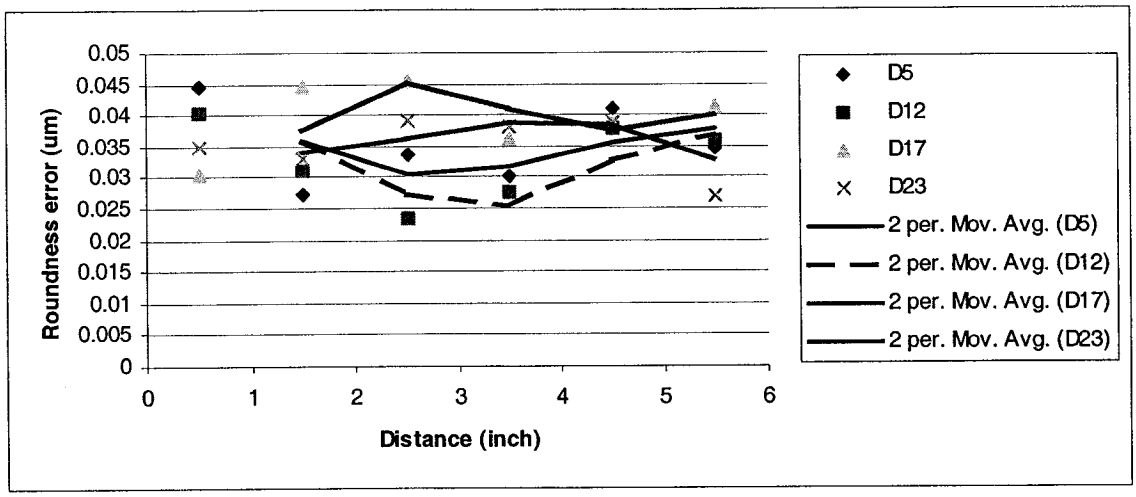


Fig. 4.75: Roundness error for D5, 12, 17, 23 at length equal to 685.8 mm.

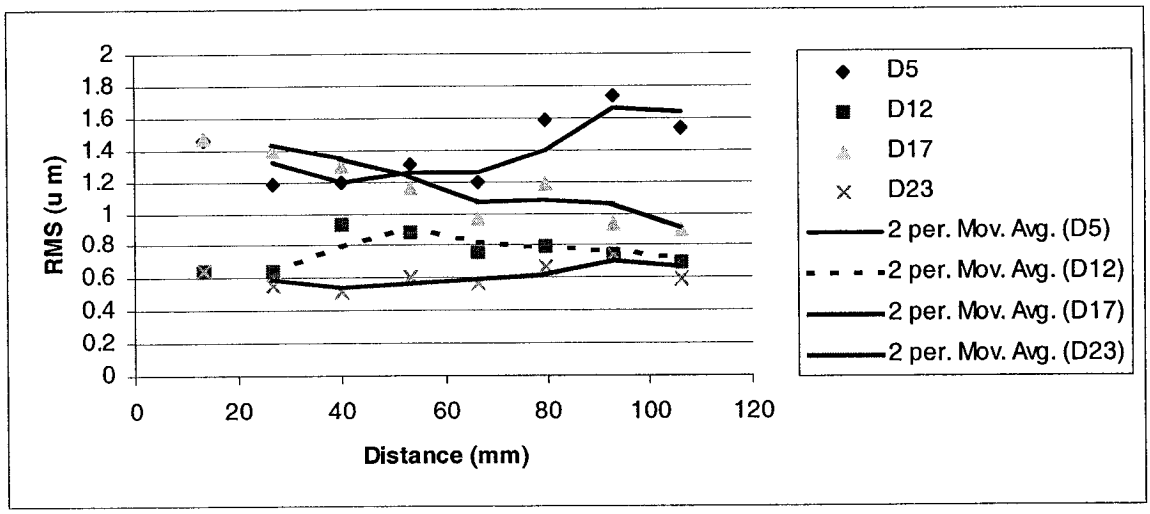


Fig. 4.76: Roughness for D5, 12, 17, 23 at length equal to 685.8 mm.

### 4.2.6 Effect of whirling motion at 838.2 mm (33 in) length of cut

Table 4.8: A description of the main characteristics at a tool penetration of 838.2 mm.

| Tool penetration of 838.2 mm | Figure number | Speed (rpm) | Feed rate (mm/min) | Flow rate (G/min) |
|---|---|---|---|---|
| D6 | 4.77 | 1240 | 173 | 20 |
| | (a) | Displacement in the Y and Z coordinates | | |
| | (b) | Whirl ellipse | | |
| | (c) | Power spectral density (PSD) | | |
| First and second spectral peaks | | 20.90 Hz, 40.79 Hz | | |
| | 4.78 | Roundness characteristics | | Value ($\mu$m) |
| | (a) | 3-lobed out of run | | 0.02855 |
| | (b) | 3-lobed out of run | | 0.03048 |
| | (c) | Almost true round | | 0.037592 |
| | (d) | Almost true round | | 0.026924 |
| | (e) | 2-lobed out of run with random irregularities | | 0.040894 |
| | (f) | 3-lobed out of run | | 0.030094 |
| | (g) | Cylindricity error | | 0.005876 |
| | (h) | Straightness error | | 0.00876 |
| D18 | 4.79 | 1440 | 173 | 30 |
| | (a) | Displacement in the Y and Z coordinates | | |
| | (b) | Whirl ellipse | | |
| | (c) | Power spectral density (PSD) | | |
| First and second spectral peaks | | 24.51 Hz, 33.7015 | | |
| | 4.80 | Roundness characteristics | | Value ($\mu$m) |
| | (a) | 3-lobed out of run | | 0.02855 |
| | (b) | 3-lobed out of run | | 0.03048 |
| | (c) | 2-lobed out of run with random irregularities | | 0.037592 |
| | (d) | 2-lobed out of run with random irregularities | | 0.026924 |
| | (e) | 2-lobed out of run with random irregularities | | 0.040894 |
| | (f) | 2-lobed out of run with random irregularities | | 0.030094 |
| | (g) | Cylindricity error | | 0.189611 |
| | (h) | Straightness error | | 0.127635 |

Table 4.8: A description of the main characteristics at a tool penetration of 838.2 mm (continued).

| Tool penetration of 838.2 mm | Figure number | Speed (rpm) | Feed rate (mm/min) | Flow rate (G/min) |
|---|---|---|---|---|
| D24 | 4.81 | 1240 | 173 | 40 |
| | (a) | Displacement in the Y and Z coordinates | | |
| | (b) | Whirl ellipse | | |
| | (c) | Power spectral density (PSD) | | |
| First and second spectral peaks | | 20.57 Hz, 40.15 Hz | | |
| | 4.82 | Roundness characteristics | | Value ($\mu$m) |
| | (a) | 3-lobed out of run | | 0.030327 |
| | (b) | 3-lobed out of run | | 0.037439 |
| | (c) | Random irregularities | | 0.028448 |
| | (d) | 2-lobed out of run | | 0.028956 |
| | (e) | 2-lobed out of run | | 0.042926 |
| | (f) | 3-lobed out of run | | 0.044069 |
| | (g) | Cylindricity error | | 0.001345 |
| | (h) | Straightness error | | 0.082347 |

The main roundness characteristic for D6, D18 and D24 is 2 to 3 lobed. and capture the unwanted data by detection of the holes [61]. Another possible method is by manual means where the user selects the area for analysis.

Fig. 4.83 is roughness plot for D6, 18 and 24. The roughness was increasing in D6 and D24 and decreasing in D18. Fig. 4.84 and 4.85 are a one-figure plot for roundness and roughness for all the specimens. Roundness was increasing for D6 and D24 and decreasing for D18. Fig. 4.86 and 4.87 are the first five natural frequencies for D1, 2, 3, 4, 5 and D7, 9, 11, 12 and 18 respectively. Fig. 488 is the whirl amplitude plot vs. the tool

penetration at 76.2 mm, 228.6 mm, 381 mm, 533.4 mm, 685.8 mm and 838.2 mm (3, 9, 15, 21, 27 and 33 in) length of cut or tool penetration. It is obvious from the figure that the whirl amplitude was decreasing relatively while the penetration going deeper.

Fig. 4.89 shows that the whirl amplitude is decreasing while the tool penetration increasing, due to the fact that the boring bar is more constrained when it goes deeper. However, the lobes of the surface are clearer as the tool penetration increases with almost no random irregularities compared with the ones at lower tool penetration.

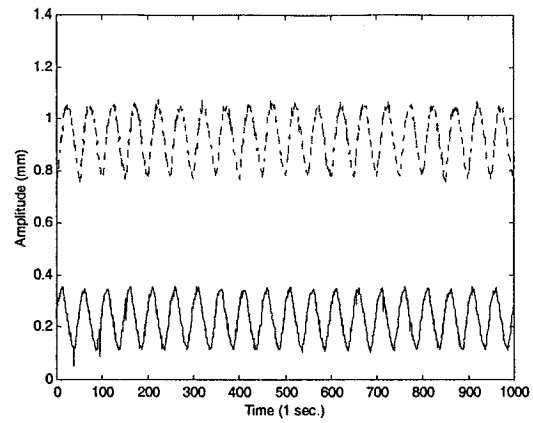


(a)

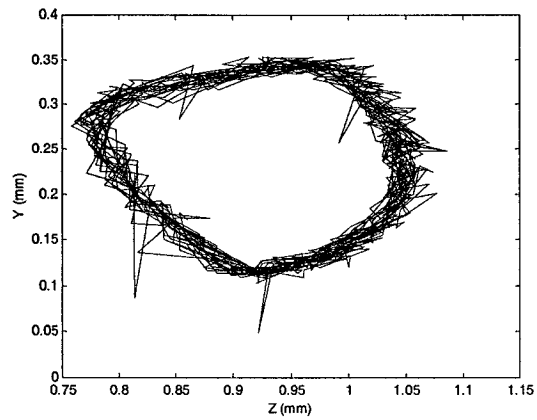


(b)

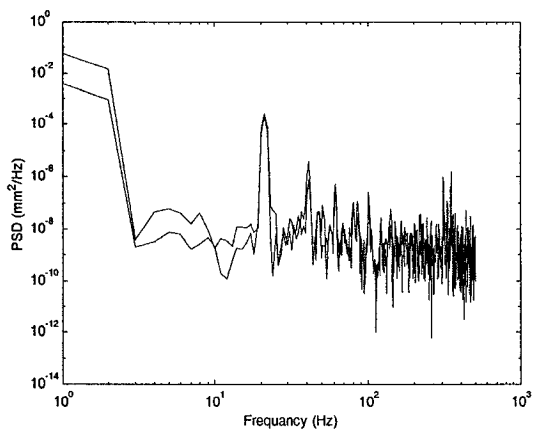


(c)

Fig.4.77: The signal analysis of D6, (a) The two signals of master and slave sensors, (b) The whirl orbit and (c) the power spectral density of the signal.

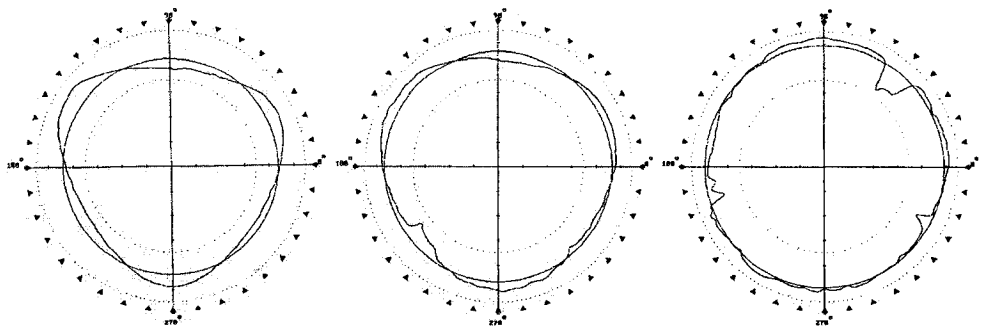

(a) (b) (c)

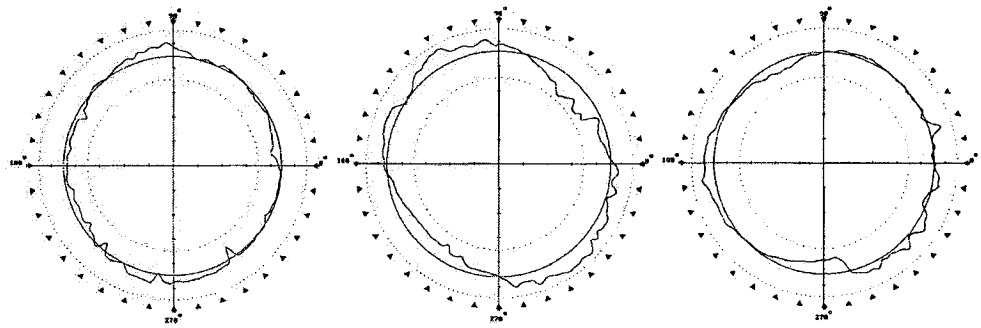

(a) (b) (c)

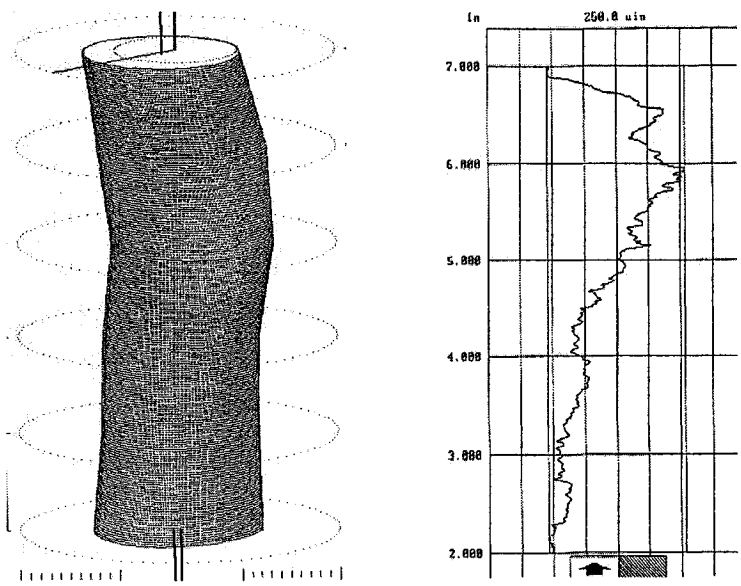


(g) (h)

Fig.4.78: Roundness for D6 from the direction of drilling in mm (a) at 12.7, (b) at 38.1, (c) at 50.8, (d) at 88.9, (e) at 114.3, (f) at 139.7, (g) cylindricity error and (h) Straightness.

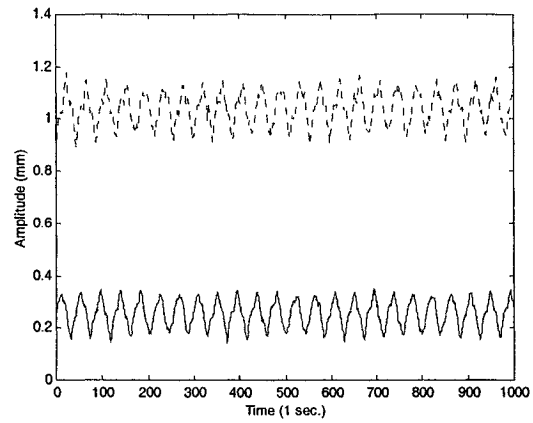


(a)

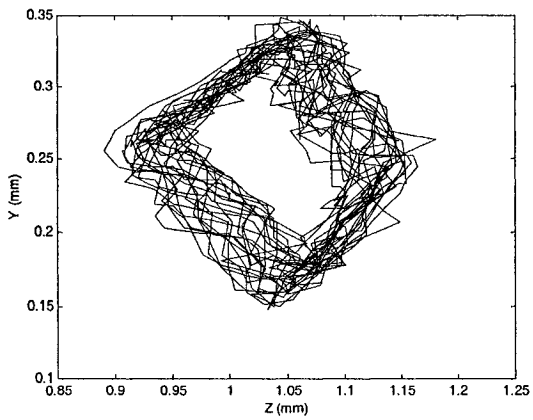


(b)

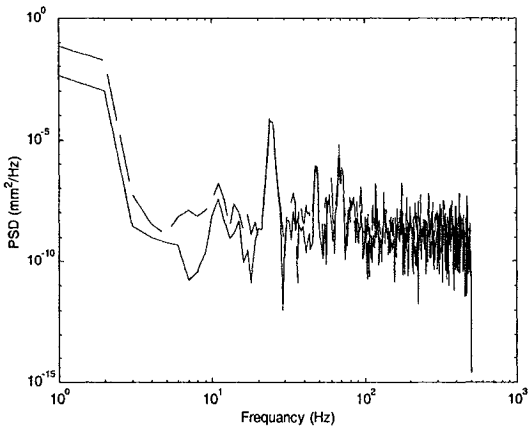


(c)

Fig.4.79: The signal analysis of D18, (a) The two signals of master and slave sensors, (b) The whirl orbit and (c) the power spectral density of the signal.

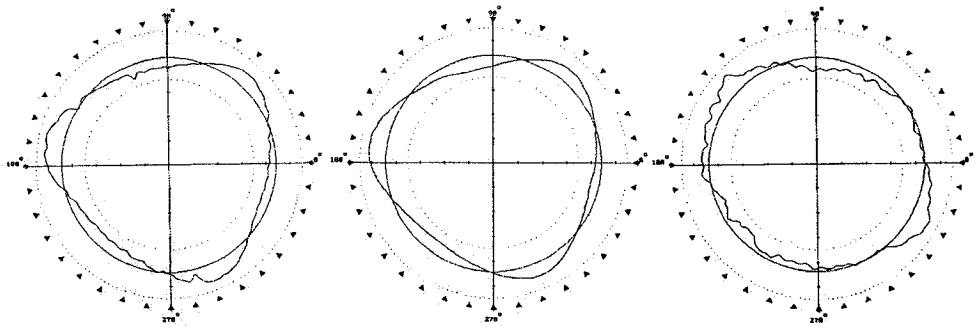

(a) (b) (c)

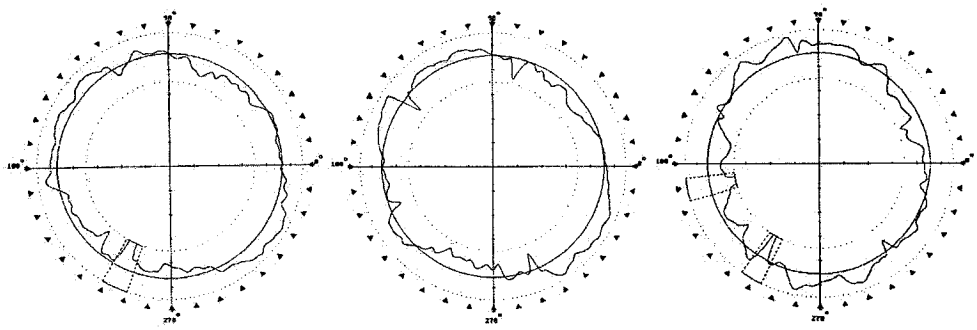

(a) (b) (c)

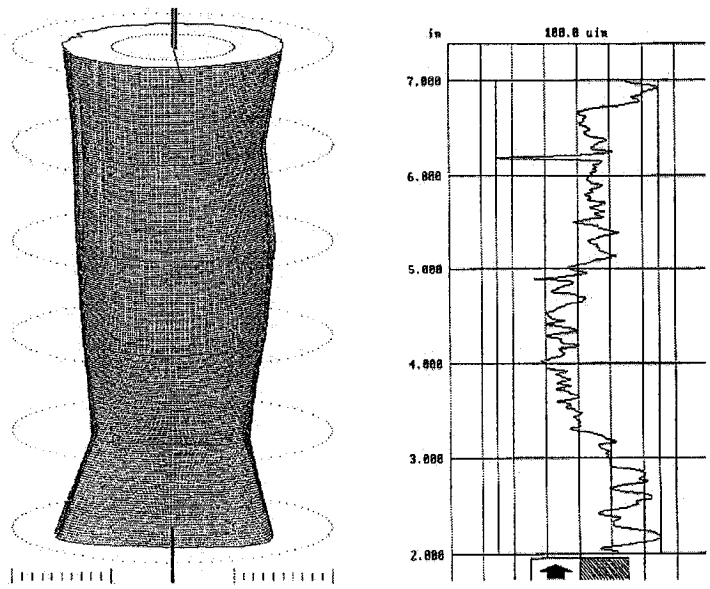


(g) (h)

Fig. 4.80: Roundness for D18 from the direction of drilling in mm (a) at 12.7, (b) at 38.1, (c) at 50.8, (d) at 88.9, (e) at 114.3, (f) at 139.7, (g) cylindricity error and (h) Straightness.

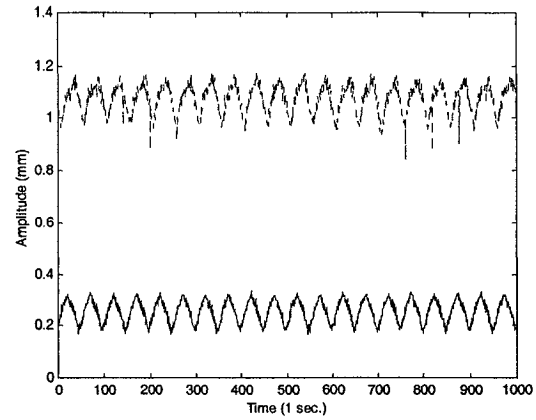


(a)

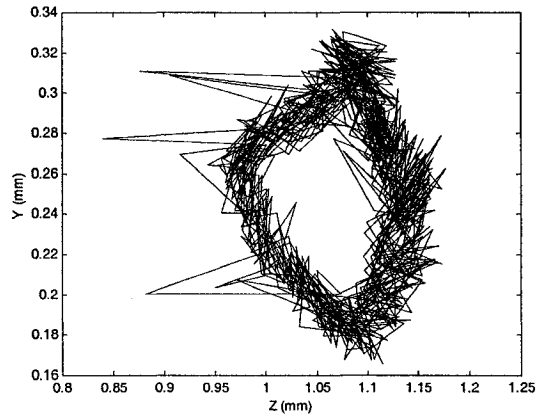


(b)

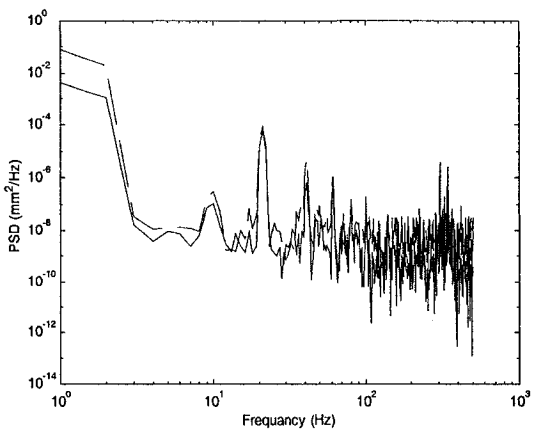


(c)

Fig. 4.81: The signal analysis of D24, (a) The two signals of master and slave sensors, (b) The whirl orbit and (c) the power spectral density of the signal.

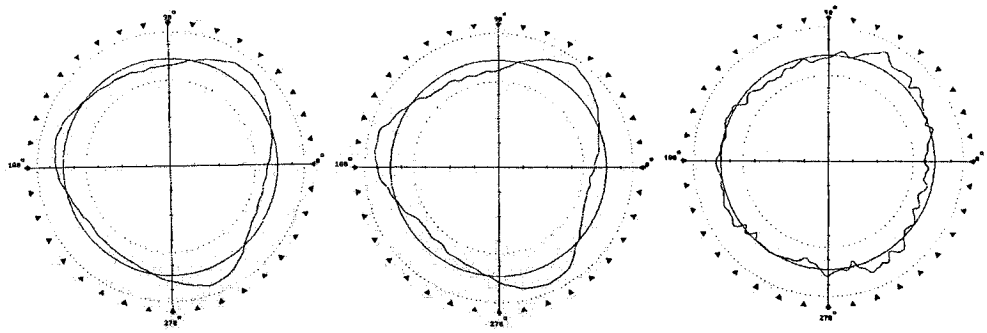

(a) (b) (c)

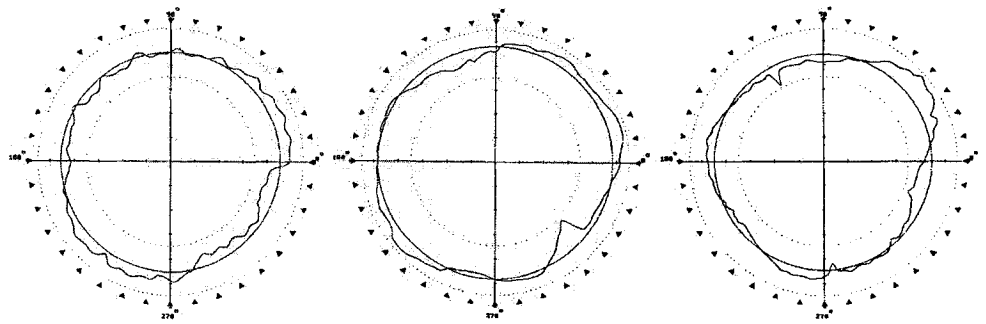

(a) (b) (c)

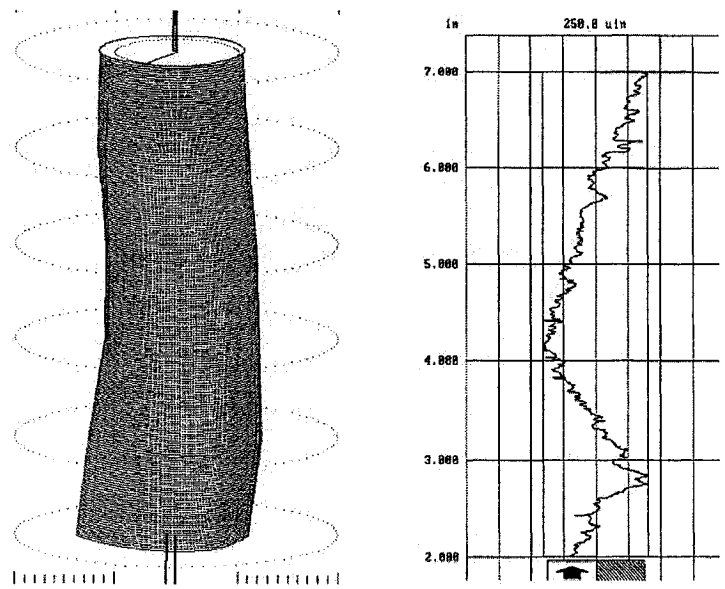


(g) (h)

Fig. 4.82: Roundness for D24 from the direction of drilling in mm (a) at 12.7, (b) at 38.1, (c) at 50.8, (d) at 88.9, (e) at 114.3, (f) at 139.7, (g) cylindricity error and (h) Straightness.

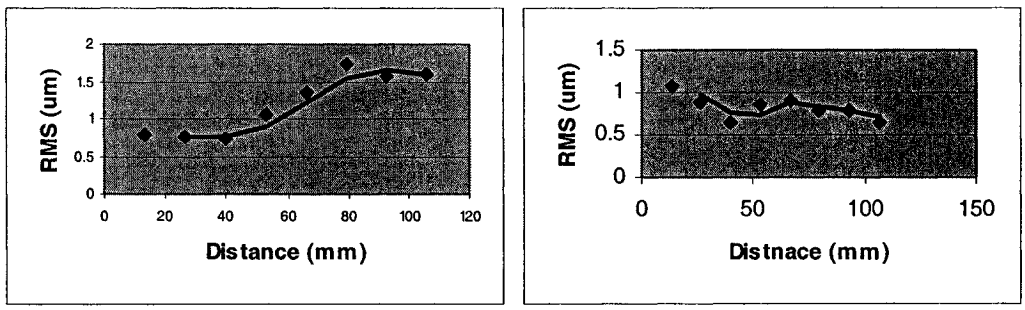


(c) (d)

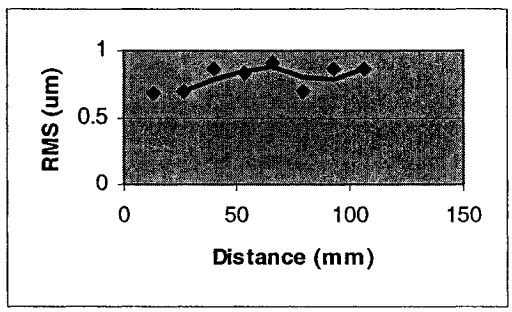


(d)

Fig. 4.83: Roughness measurements (a) D6, (b) 18 and (c) 24.

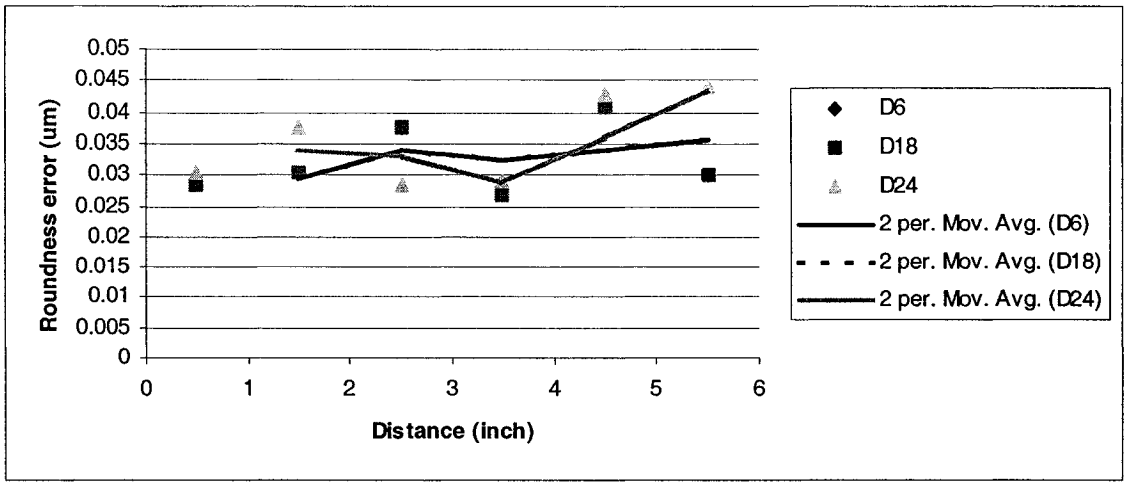


Fig. 4.84: Roundness error for D6, 18, 24 at length equal to 838.2 mm.

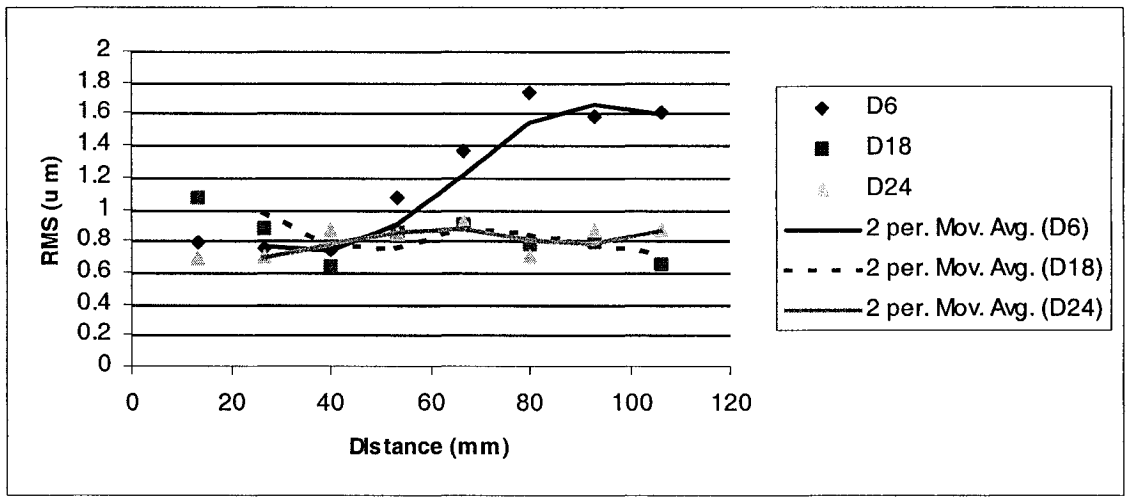


Fig. 4.85: Roughness for D6, 18, 24 at length equal to 838.2 mm.

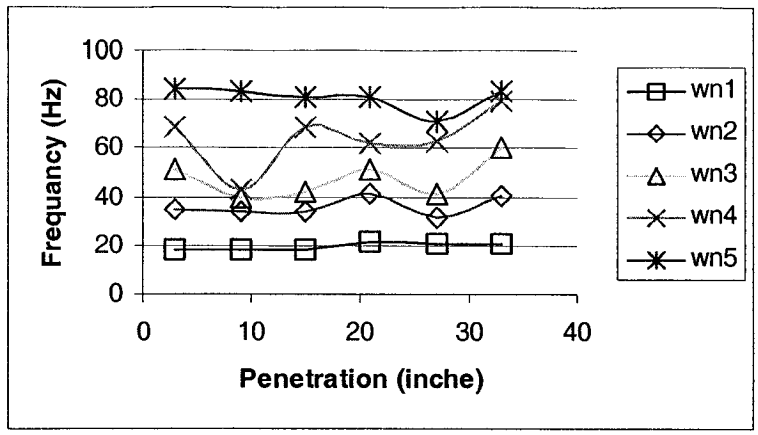


Fig. 4.86: Natural Frequency variation for D1, 2, 3, 4, 5, 6.

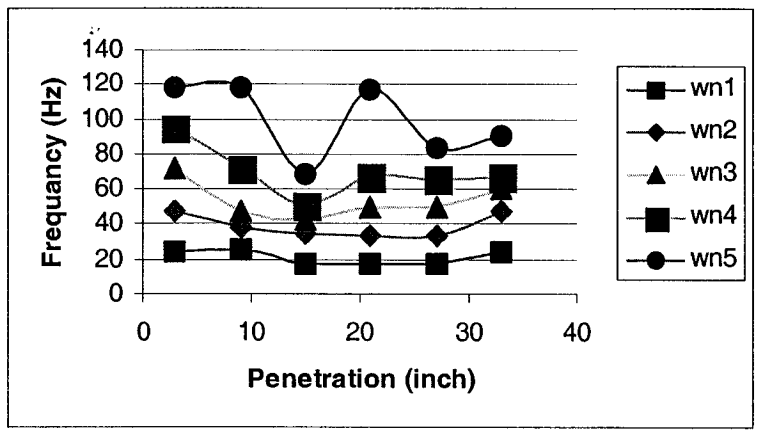


Fig. 4.87: Natural Frequency variation for D7, 9, 11, 12, 18.

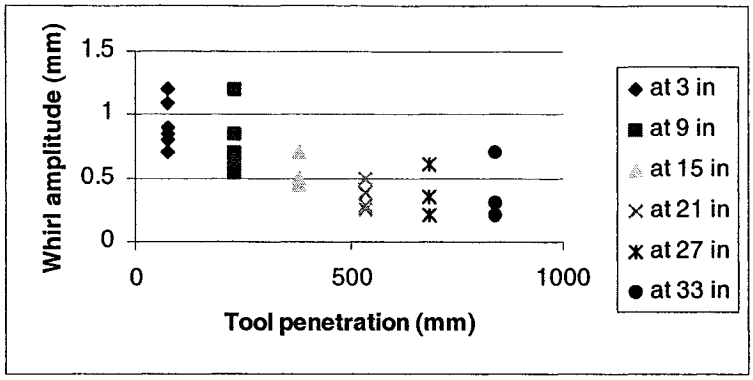


Fig. 4.89: Whirl amplitude vs. Length of cut (tool penetration).

In this chapter, the effect of whirling vibration of the boring bar on the outcome surface irregularities and geometrical dimensioning and tolerancing in BTA deep hole boring process were carried out under different cutting conditions. Chapter 5 will present the fuzzy models of the outcome surface irregularities, i.e. cylindricity, straightness and the surfaces roughness, RMS.

# CHAPTER 5

# FUZZY SETS AND FUZZY SYSTEMS

From the previous chapter, it is seen that modeling and prediction of surface integrity of a workpiece in machining operation plays an important role in the manufacturing industry. Also, it is necessary to do the drilling at optimum cutting parameters so as to minimize the range of size variation and surface roughness. In this chapter fuzzy logic principles will be applied to select the best cutting conditions in deep hole boring. Before applying the fuzzy logic to the present problem, an introduction to fuzzy sets and fuzzy systems will be given. The basic principle of fuzzy systems, fuzzy connectives and fuzzy implication will be discussed briefly. A method is proposed to accurately establish the relationship between the different cutting parameters and the resulting surface irregularities using subtractive clustering based fuzzy system modeling technique with adaptive neuro-fuzzy inference system (ANFIS). Consequently, the proposed model will successfully be used to predict surface irregularities using different cutting parameters involved in the study.

## 5.1 Introduction

While classical sets have crisp values, fuzzy sets contain elements with partial degree of memberships.

Classical sets wholly include or exclude any given element. The membership function $\mu_A(x)$ of a classical set A, as a subset of the universe X is defined as:

$$\mu_A(x) = \begin{cases} 1, & if\ x \in A \\ 0, & if\ x \notin A \end{cases}$$

This means that any element x is either a member of set A (with $\mu_A(x) = 1$) or not a member (with $\mu_A(x) = 0$).

Fuzzy sets were introduced by Zadeh [154] in 1965. A fuzzy set has graded membership in the real interval: $\mu_A(x) \in [0,1]$. It allows each element of X to belong to the set with a degree (degree of belongingness), characterized by a real number in the closed interval [0, 1]. This degree of belongingness corresponds to the degree to which that individual element is similar or compatible with the concept represented by the fuzzy subset. Hence, the full membership and full non-membership in the fuzzy set can still be indicated by the values of 1 and 0, respectively.

The basic properties of the fuzzy set are as shown in Fig. 5.1 where the height of a fuzzy set A is the largest membership grade or value obtained by any element in the set. The support of a fuzzy set A within a universal set X is the crisp set that contains all elements of X that have nonzero membership in A.

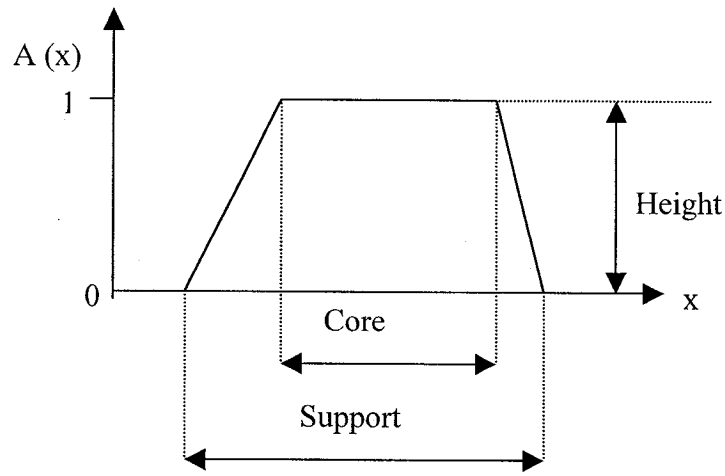


Fig. 5.1: The support, core and height of a fuzzy set

## 5.2 Implication Function

The most widely studied and known type of fuzzy statements involving several variables is the IF-THEN rule with fuzzy predicates. It can be written also in the form of "*If x is A Then y is B*" where A is the antecedent or the premise part and B is the consequence part. According to Zadeh [154], a conditional statement "*If x is A Then y is B*", describes relation between two fuzzy variables x and y. Hence, he suggests that a fuzzy relation should represent the conditional statement from the universe of the antecedent to the universe of the consequence or a way to map the input space with the output space. This elementary fuzzy conditional statement can be defined at fuzzy membership level by:

$$\mu_{A\to B} = I(\mu_A(x), \mu_B(y))$$

where I is a fuzzy implication function. I is a function of the form:

$$I : [0,1] \times [0,1] \rightarrow [0,1]$$

Dubois and Prade [156] made a summary of the different types of fuzzy implications.

## 5.3 Fuzzy Models

There are two basic fuzzy models, named after Mamdani and Sugeno. The difference between these fuzzy models lies in the consequents of their fuzzy rules. The THEN part in Mamdani model is a fuzzy membership function, while that in Sugeno model is a polynomial function of the input variables, which contains the regression parameters.

### 5.3.1 Mamdani fuzzy model

The first proposed model using Mamdani fuzzy model was introduced by Mamdani and Assillian [114] to control a steam engine and boiler combination by a set of linguistic variable rules obtained from experienced operator. The basic idea of this model is to integrate the experience of a human operator in the design of a controller for a process whose input-output relationship is described by a collection of fuzzy control rules involving linguistic variables rather than a complicated dynamic model, which will make the system easy to deal with. The typical architecture of Mamdani fuzzy model is a shown in the Fig. 5.2.

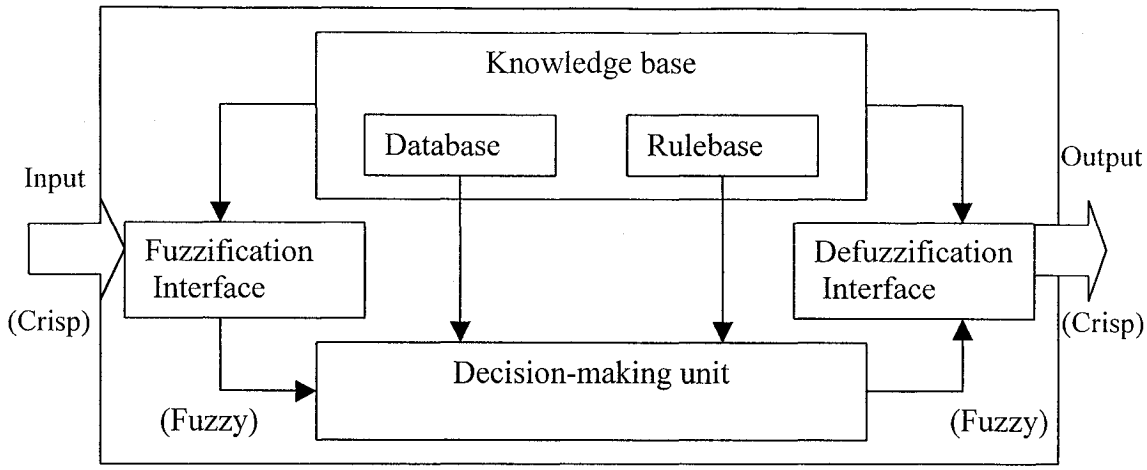


Fig. 5.2: The typical architecture of Mamdani fuzzy model.

The fuzzification involves measuring the values of input variables and then performing a scale mapping which transfers the range of values of input into corresponding universe of discourse. Finally the function of fuzzification converts input data into suitable linguistic values that may be labels or linguistic variables of fuzzy sets.

The knowledge base consists of a data base and a linguistic fuzzy control rule base. The data base provides important information, which are used to define linguistic control rules to manipulate the fuzzy data. The rule base characterizes the control targets and control guiding principle. Fuzzy control rules are characterized by a collection of fuzzy IF-THEN rules. In the inference engine, the processing unit determines the corresponding output value from the measured input according to the knowledge base. The final step is the defuzzification, which is the opposite of fuzzification, to obtain nonfuzzy or crisp value.

## 5.3.2 Sugeno Fuzzy Model

The introduction of Sugeno model [70] was in 1985. The type of Sugeno rule has the form of:

$$\text{IF x } \textit{is} \text{ A AND y is B THEN } F = f(x, y)$$

which shows that the rules have fuzzy antecedents or premise parameters, same as Mamdani, and the consequent of these rules are functions of the inputs rather than fuzzy sets. The consequence function is most of the time of first order. When the consequent is a first-order polynomial, the resulting fuzzy system is called a first-order Sugeno model, when the consequent is a second-order polynomial the resulting fuzzy system is called a second-order Sugeno model and so on. In practical case the simplest case of Sugeno rules is that when the consequent part are constants, all output membership functions are fuzzy numbers. When the consequent is a constant, the model is a constant consequent Sugeno fuzzy model.

For example, consider the following set of Sugeno fuzzy rules that describe the behavior of a fuzzy system:

$$R_1: \text{ IF } x_1 \text{ is } A_1 \text{ AND } x_2 \text{ is } B_1 \text{ THEN } \omega_1 = a_1 x_1 + b_1 x_2$$

$$R_2: \text{ IF } x_1 \text{ is } A_2 \text{ AND } x_2 \text{ is } B_2 \text{ THEN } \omega_2 = a_2 x_1 + b_2 x_2$$

Using fuzzy approach with the fuzzy inputs $x_{10}$ *and* $x_{20}$ the conclusions $\omega_1^*$ *and* $\omega_2^*$ are obtained as shown in Fig. 5.3. The firing strength of the rules, denoted by $\alpha_1$ , $\alpha_2$ , are computed by:

$$\alpha_1 = T(A_1(x_{10}), B_1(x_{20})),$$

$$\alpha_2 = T(A_2(x_{10}), B_1(x_{20}))$$

$T_{min}$ is used as a conjunction operator in Fig. 5.3. Each rule conclusion is obtained by:

$$\omega_1^* = a_1 x_{10} + b_1 x_{20}$$

$$\omega_2^* = a_2 x_{10} + b_2 x_{20}$$

The rule results are aggregated as weighted sums of the control actions corresponding to each rule. The overall system conclusion is obtained by:

$$\omega^* = \frac{\alpha_1 * \omega_1^* + \alpha_2 * \omega_2^*}{\alpha_1 + \alpha_2}$$

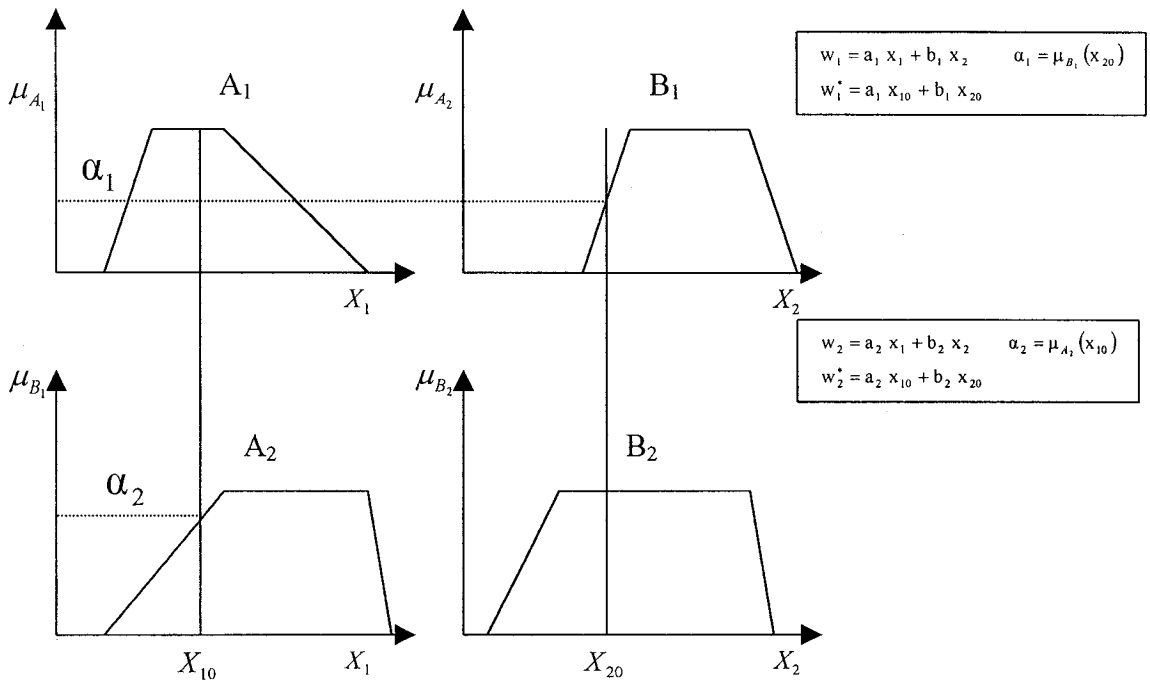


Fig. 5.3: Fuzzy inference with two antecedent using Sugeno approach.

## 5.4 Fuzzy Logic Modeling using subtractive clustering

The subtractive clustering is first proposed by Chiu [151]. In this clustering technique, all data points are considered to be candidates for cluster center despite the dimension of the problem under study. There is a density measure for each data point $x_i$, which is equal to

$$B_i = \sum_{j}^{N} \exp\left( - \frac{\gamma \left\| x_i - x_j \right\|^2}{r_a^2} \right) \tag{5.1}$$

where, $x_i$ is a collection of $N$ data points $\{x_1,\cdots,x_n\}$, $\gamma$ is a positive constant and $r_a$ is a radius of neighbourhood. The data point with the highest $B$ (density measure or potential) is selected as the first cluster center. The potential of any data point in the combined input-output space is a function of its distances to all data points including the point itself. If we have large number of points, the potential values will be higher.

For the next cluster center, revising the density measure reduces the effect of the previous center and the data points near this center. This is done by subtraction as shown below:

$$B_i = B_i - B_s^* \exp\left(-\frac{\gamma\|x_i - c_s\|^2}{r_b^2}\right), \quad r_b = \eta \times r_a \tag{5.2}$$

$B_s^*$ is the potential of the $s'th$ cluster center and $c_s$ is the $s'th$ cluster center, $r_b$ is a constant that defines the required subtractive range and $\eta$ is a positive constant called the squash factor. After subtraction, the second cluster center is selected based on its new potential depending upon the upper acceptance threshold $\bar{\in}$ called accept ratio, lower rejection threshold $\underline{\in}$ called reject ratio and the relative distance criterion. The minimum of the distances between the points and all other previously found cluster centers is the criterion for the acceptance of the data point.

$$\frac{L_{\min}}{r_a} + \frac{B_s^*}{B_1} \geq 1$$

where $L_{\min}$ is the minimum of the distances between $c_s$ and all previously found cluster centers. Doing this will avoid the emerging of new clusters close to the existing ones. Once all clusters are found through the subtraction process, the membership functions of all data points are assigned exponentially as proposed by Chiu [151] with respect to all cluster centers as follow:

$$\mu_{ij} = \exp\left(-\sigma \left\| x_i - c_s \right\|^2\right)$$

where,

$$\sigma = \frac{\gamma}{r_a^2}$$

and

$\left\| x_i - c_s \right\|$ is the distance measure between the $i'th$ data point and the $s'th$ centers.

The closeness of the predicted model to the actual system is a factor of the selection of the clustering parameters such as cluster radius, squash factor, accept ratio and reject ratio. Since each of these parameters has specific influence on the clustering performance and therefore the predicted model. Table 5.1 below presents the effect of each clustering parameters on the clustering process. This is due to the fact that these parameters have individual and combined effects, the need for obtaining the optimum clustering parameters combination is highly needed.

Table 5.1: the effect of clustering parameters on the clustering process.

| Clustering parameter | Effect on the clustering performance (or the predicted model) |
|---|---|
| $r_a$ | Is the radius of influence of a cluster center in the data space. Generally, a large value of $r_a$ results in fewer clusters that leads to a coarse model. A small value of $r_a$ can produce large number of rules resulting in an over-defined system. |
| $r_b$ | Is a value of the zone of penalty for enhancing the emergence of new clusters outside the zone of $r_b$ or the zone of penalty for being affected by the cluster center. |
| Squash factor ($\eta$) | Higher values help in identifying new clusters farther away from the previous ones. |
| accept and reject Ratios ($\overline{\varepsilon}$, $\underline{\varepsilon}$) | Have influence on selecting the cluster centers and therefore the rule base. |

Higher order system identification is proposed by Demirli and Muthukumaran [74], in order to find the best combination of clustering parameters which will result in better model with fewer rules and minimum least square error. The fuzzy system identification involves producing clusters using the data set available for the given values of clustering parameters, i.e. $r_a, \eta, \overline{\varepsilon}, \underline{\varepsilon}$ and the regression coefficients by the least square estimation.

The least square estimation ensures the overall optimization of the regression parameters for a given set of clusters. Therefore, the optimization of the system identification relies mainly on obtaining the optimum clustering parameters. The fact that the clustering parameters are highly interactive in nature and depend on the system behaviour and the data available should not be ignored to identify the system. Therefore, an enumerative

search is carried out on the clustering parameters and the predicted models are compared based on the modeling least square error as:

$$LSE = \sum_{i=1}^{N} \left(C_i - C_i^*\right)^2$$

where,

$C_i$ : is the actual training data output.

$C^*_i$ : is the predicted output from the identified model

$N$ : Total number of data.

From each enumerative search, for each model a number of rules versus the LSE will be obtained.

## 5.5 Fuzzy modeling of surface irregularities

Table A2 in appendix A shows the input-output data for cylindricity, straightness and roughness errors. The enumerative search is carried out for the three surface irregularities mentioned above using three inputs only (speed, feed rate and flow rate). The second enumerative search was done using four inputs (speed, feed rate, flow rate and depth of cut or tool penetration) to study the effect of the fourth variable on the outcome surface irregularities. The first order Sugeno fuzzy model is used to construct the fuzzy rules. For example:

*IF speed is* $A_1^1$ *AND feed is* $A_2^1$ *AND flow rate is* $A_3^1$ *AND length of cut is* $A_4^1$ *THEN*

$y = f$ *(speed, feed, flow rate, length of cut)*

where y is the outcome surface irregularities or any kind of surface geometrical dimensioning and tolerancing and $A_1^1$ is the membership function associated with the input. The IF part is the premise parameter and the THEN part contains the consequent parameters.

The identified first order Sugeno fuzzy model in our study is as follows:

**$R_1$:** *IF speed is* $(A_1^1)$ *AND feed is* $(A_2^1)$ *AND flow rate is* $(A_3^1)$ *AND length of cut is* $(A_4^1)$ *THEN* $y_1 = a_{10} + a_{11} * speed + a_{12} * feed + a_{13} * flow\ rate + a_{14} * length\ of\ cut$

⋮

⋮

**$R_K$:** *If speed is* $(A_1^K)$ *AND feed is* $(A_2^K)$ *AND flow rate is* $(A_3^K)$ *AND length of cut is* $(A_4^K)$ *then* $y_K = a_{K0} + a_{K1} * speed + a_{K2} * feed + a_{K3} * flow\ rate + a_{K4} * length\ of\ cut$

where the four inputs, speed, feed, flow rate and length of cut, are the cutting variables while the output variable $y_i$, $i = 1, 2, \cdots, k$ are the outcome surface irregularity (roughness, cylindricity, straightness...etc.) and $a_{k0}$, $a_{k1}$, $a_{k2}$, $a_{k3}$ and $a_{k4}$ (for

$i = 1, 2, \cdots, k$) are regression parameters which are identified using LSE algorithm. These resulting models will be tuned using ANFIS in the next section to establish the final model.

For each model a curve between the number of rules versus the LSE is obtained. Fig. 5.4 is an example of the enumerative search for cylindricity with three inputs, where the LSE decreases with increasing number of rules. The optimum clustering parameters were chosen so that the model will have fewer rules with minimum LSE.

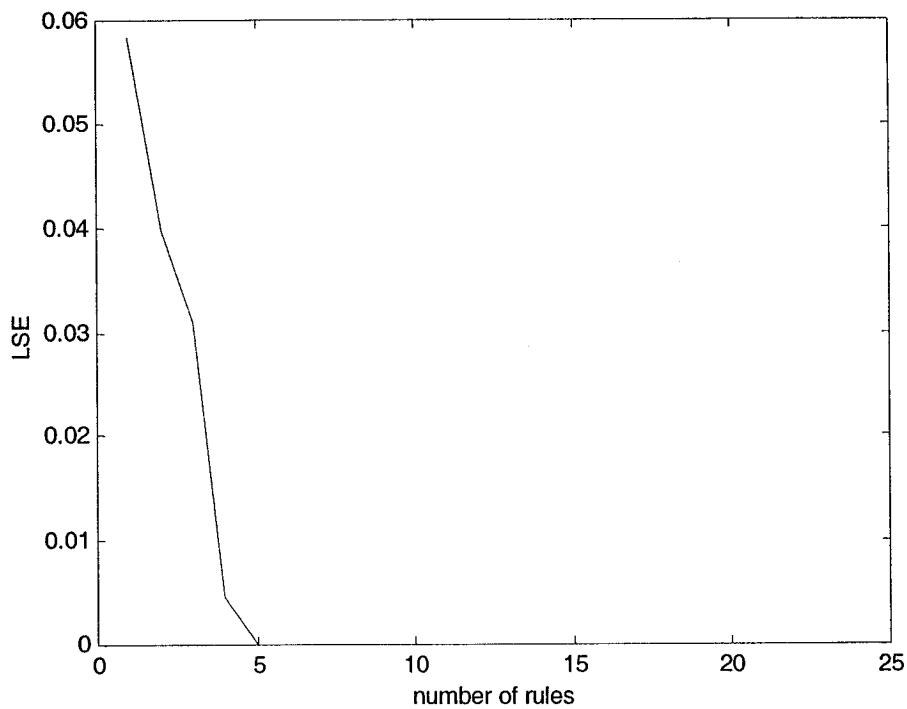


Fig. 5.4: The number of rules vs. LSE as a result of enumerative search for cylindricity with three inputs (feed, speed and flow rate).

Table 5.2 below shows the values of the optimum clustering parameters, LSE and the number of rules for each model.

Table 5.2: the optimum clustering parameters as a result of enumerative search.

| Irregularity type | Three input model (First order Sugeno model) | Four input model (First order Sugeno model) |
|---|---|---|
| Cylindricity error | $r_a = 0.65$<br>$\eta = 1.9$<br>$\overline{\varepsilon} = 0.4$<br>$\underline{\varepsilon} = 0.5$<br>LSE = 3.597e-4<br>number of rules = 7 | $r_a = 0.5$<br>$\eta = 1.8$<br>$\overline{\varepsilon} = 0.9$<br>$\underline{\varepsilon} = 0.9$<br>LSE = 3.006e-2<br>number of rules = 9 |
| Straightness error | $r_a = 0.55$<br>$\eta = 2$<br>$\overline{\varepsilon} = 0.7$<br>$\underline{\varepsilon} = 0.7$<br>LSE = 3.55e-4<br>number of rules = 7 | $r_a = 0.65$<br>$\eta = 1.8$<br>$\overline{\varepsilon} = 0.9$<br>$\underline{\varepsilon} = 0.8$<br>LSE = 6.59e-2<br>number of rules = 5 |
| Roughness error | $r_a = 0.8$<br>$\eta = 1.7$<br>$\overline{\varepsilon} = 0.5$<br>$\underline{\varepsilon} = 0.3$<br>LSE = 7.854e-2<br>number of rules = 6 | $r_a = 0.7$<br>$\eta = 1.2$<br>$\overline{\varepsilon} = 0.9$<br>$\underline{\varepsilon} = 0.9$<br>LSE = 7.43e-2<br>number of rules = 5 |

## 5.6 Adaptive Neural-based fuzzy inference system

ANFIS can modify the parameters of the membership functions of the fuzzy model. It contains a hybrid-learning rule, which combines gradient descent and the LSE for fast identification of the parameters. In the forward pass of the hybrid-learning algorithm, the consequent parameters are identified by LSE. In the backward pass, the error signals propagate backward and the premise parameters are updated by gradient descent. By updating the membership functions, we are actually tuning the fuzzy model for a better model performance. The rule base of the model built by subtractive clustering and ANFIS for all the models are shown in the following sections.

Adaptive network-based fuzzy inference system (ANFIS) [151] combines the structure of fuzzy logic controllers with the learning aspects from neural networks. If human expertise is not available, we can still set up intuitively reasonable initial membership functions and start the learning process to generate a set of fuzzy if-then rules to approximate a desired data set. ANFIS uses a high efficient training method that combines gradient descent method and least squares optimization to improve training speed compared to standard back propagation. ANFIS implements a first order Sugeno fuzzy system. ANFIS structure will be shown in the next section for the first two models.

As seen in Fig. 5.5, Layer 1 consists of membership functions described as Gaussian membership function. Layer 2 implements the fuzzy "AND" operator, while layer 3 acts to scale or normalize the firing strength. The output of the fourth layer is a linear

combination of the inputs multiplied by the normalized firing strength. Layer 5 is a simple summation of the outputs of layer 4. Layer 1 contains premise modifiable parameters, and layer 4 contains consequent parameters.

The consequent parameters are identified by a least squares estimator in the forward pass and this is the half epoch. In the backward pass, the consequent parameters are held fixed, and the premise parameters are modified using gradient descent, which is the second half epoch. Going forward and backward on the neural network is a complete one epoch.
After tuning the system rules using ANFIS, the optimized machining process parameters are determined by using the surface plot of the machining parameters vs. the surface irregularity (roughness, cylindricity and straightness) individually.

## 5.7 Fuzzy modeling of surface irregularities

In this section we present six models of surface irregularities. The first and second models will be for cylindricity. The third and fourth models will be for straightness, the fifth and sixth models will be for roughness. The first, third, and fifth models will be with three inputs only (speed, feed rate, and flow rate) for cylindricity, straightness, and roughness respectively. The second, fourth, and sixth models will be using four inputs, where the tool penetration or length of cut is added as a fourth input for cylindricity, straightness and roughness, respectively.

### 5.7.1 First fuzzy model of cylindricity error with three inputs using first Sugeno model with ANFIS

In this model, the cutting parameters, speed, feed rate, and flow rate are the inputs to the model. The output is the cylindricity error.

Table 5.3 summarizes the rules ($\sigma's$, $c's$, $a_{k0}$, $\cdots$, $a_{k3}$) where $c's$ corresponds to the centres, and $a_{k0}$, $\cdots$, $a_{k3}$ are the coefficients of the consequent part of each rule. A plot of the surface response model is shown in Fig. 5.7(a) with a fixed flow rate of 40 G/min, (b) a fixed speed of 1400 rev/min and (c) a fixed feed of 130 mm/min. The error curves are shown in Fig. 5.7(d). Fig. 5.5 explains the process of modeling with the designed ANFIS structure to fit the modeling data. The initial and final membership functions are shown in Fig. 5.6, where the tuned membership functions are shown.

In Fig 5.7 (d) the training and checking error drops quickly between 0.5 – 250 epochs. After 250 epochs there is no difference between the training and checking data, which means that the model is able to reproduce the actual behavior of the system. The training process could be stopped at 250 epochs. More than 250 epochs is shown to assure that the model error is at minimum. This is due to the fact that this model with three inputs was not "so complex". or the initial model without tuning with ANFIS was close as much as possible to the actual model.

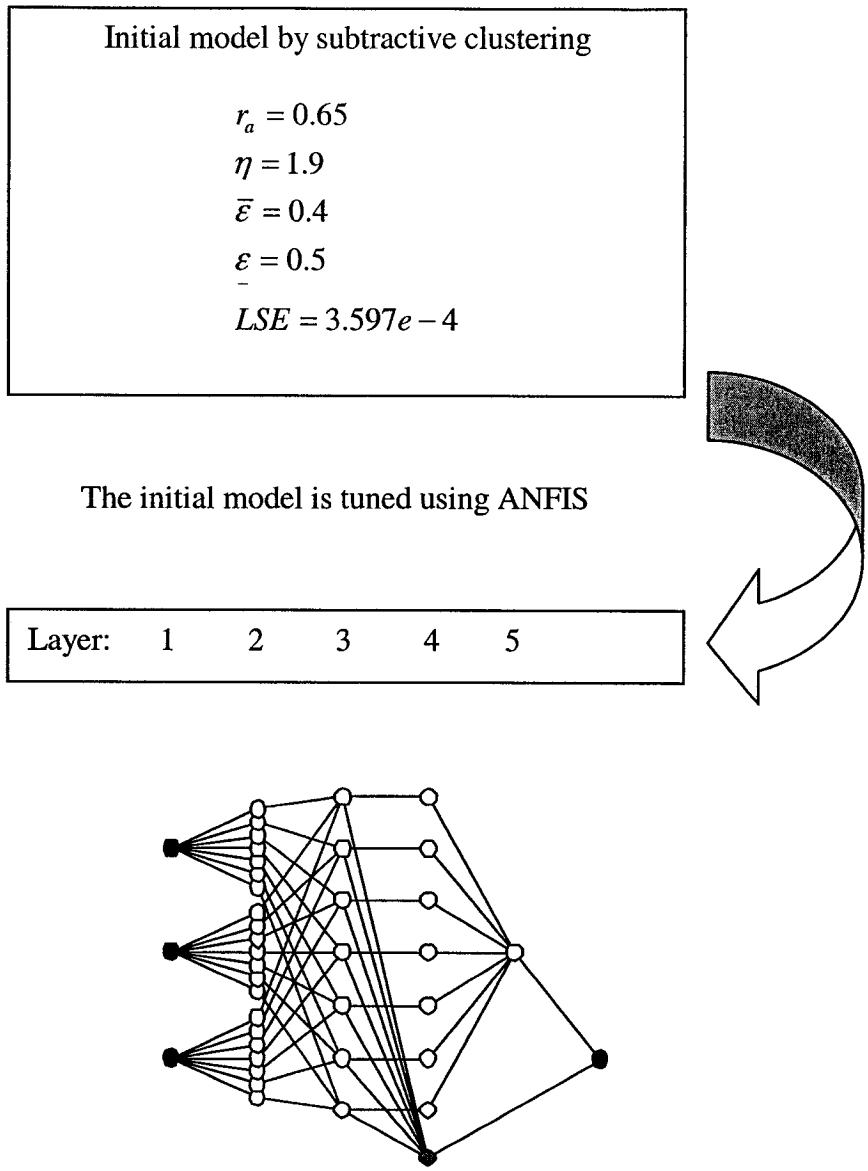


Fig. 5.5: The process of modeling the data for cylindricity with three inputs (feed, speed and flow rate) with the ANFIS structure.

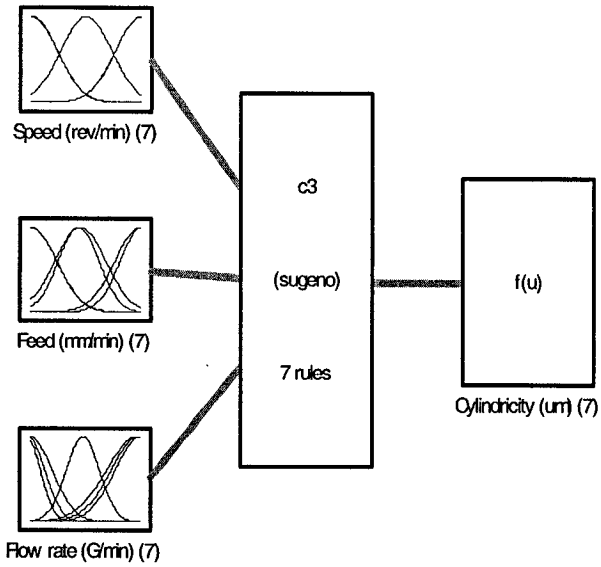


Fig. 5.5: The process of modeling the data for cylindricity with three inputs (feed, speed and flow rate), the final model after ANFIS (continued).

From the surface plot the best parametric combination for cylindricity considering three inputs only are speed =1406 (rev/min), feed rate = 126.3 (mm/min) and flow rate = 40 (G/min) with cylindricity error = 0.149 $\mu$m.

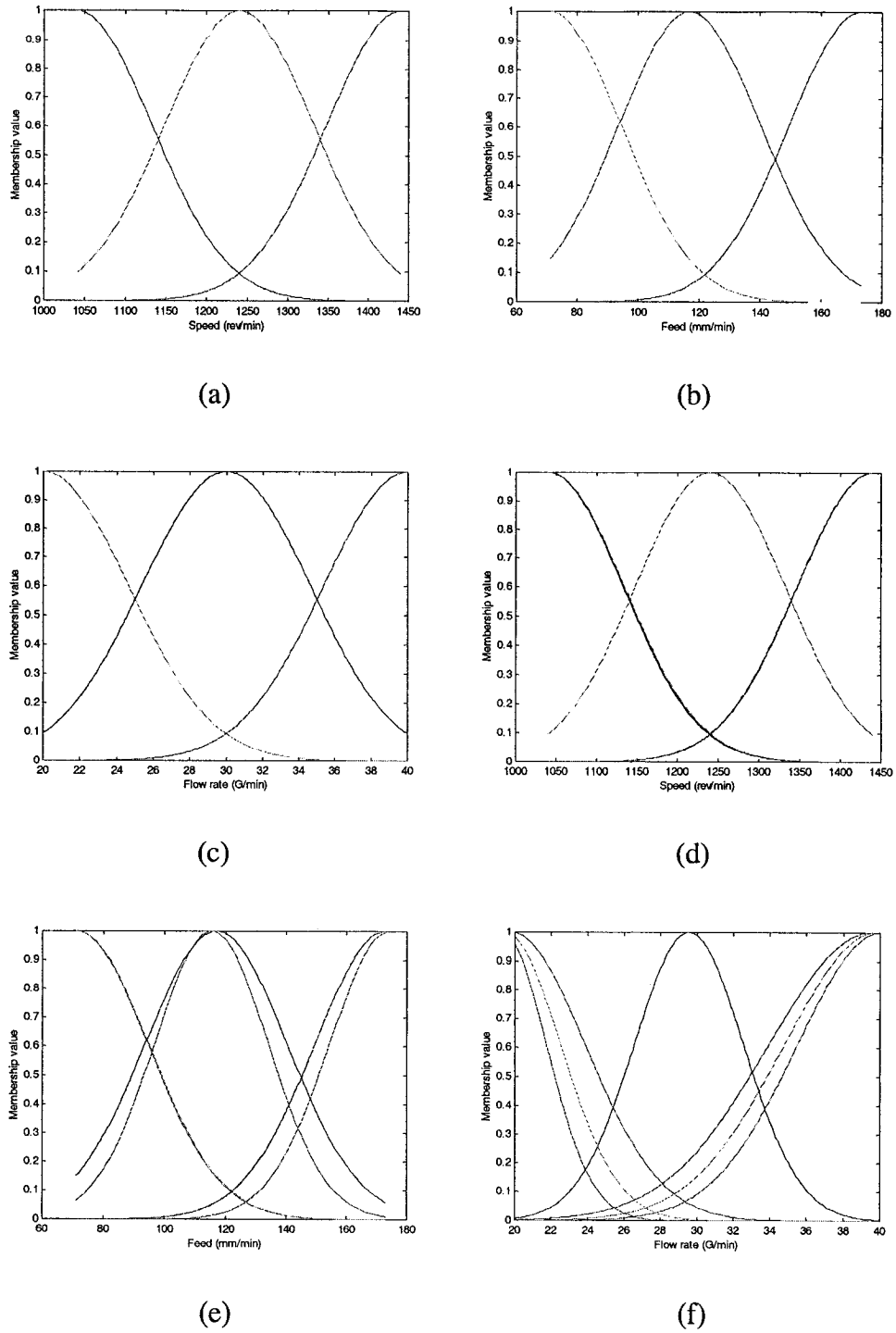


Fig. 5.6: (a) to (c) initial MF's and (d) to (f) final MF's for cylindricity with 3 inputs.

Table 5.3: 7 rules for cylindricity fuzzy model, 3 inputs were taken into consideration.

| $R_i$ | $\sigma_1^t, c_1^t$ | $\sigma_2^t, c_2^t$ | $\sigma_3^t, c_3^t$ | $a_{i3}$ | $a_{i2}$ | $a_{i1}$ | $a_{i0}$ |
|---|---|---|---|---|---|---|---|
| 1 | 91.85,1039.96 | 23.53,116.99 | 3.03,29.56 | -0.000348 | -0.000341 | 0.0204147 | 0.014300 |
| 2 | 92.43,1439.76 | 18.88,115.39 | 4.10,19.78 | -0.000401 | 0.001363 | 0.003202 | 0.5932354 |
| 3 | 91.91,1440.00 | 23.45,172.99 | 4.56,40.03 | 1.01e-005 | 0.000773 | -0.000836 | 0.065553 |
| 4 | 91.97,1239.98 | 23.45,71.00 | 5.03,39.79 | 6.15e-005 | -0.000384 | 0.010175 | -0.244704 |
| 5 | 92.71,1039.74 | 19.93,174.33 | 2.46,19.28 | -0.021304 | 0.128670 | -0.004691 | -7.2e-005 |
| 6 | 93.08,1040.53 | 23.63,71.09 | 3.09,19.44 | -0.000172 | 0.017628 | -0.043394 | 0.0002734 |
| 7 | 92.25,1040.15 | 23.50,172.97 | 5.61,39.509 | 0.0005539 | -0.001182 | 0.001277 | -0.238504 |

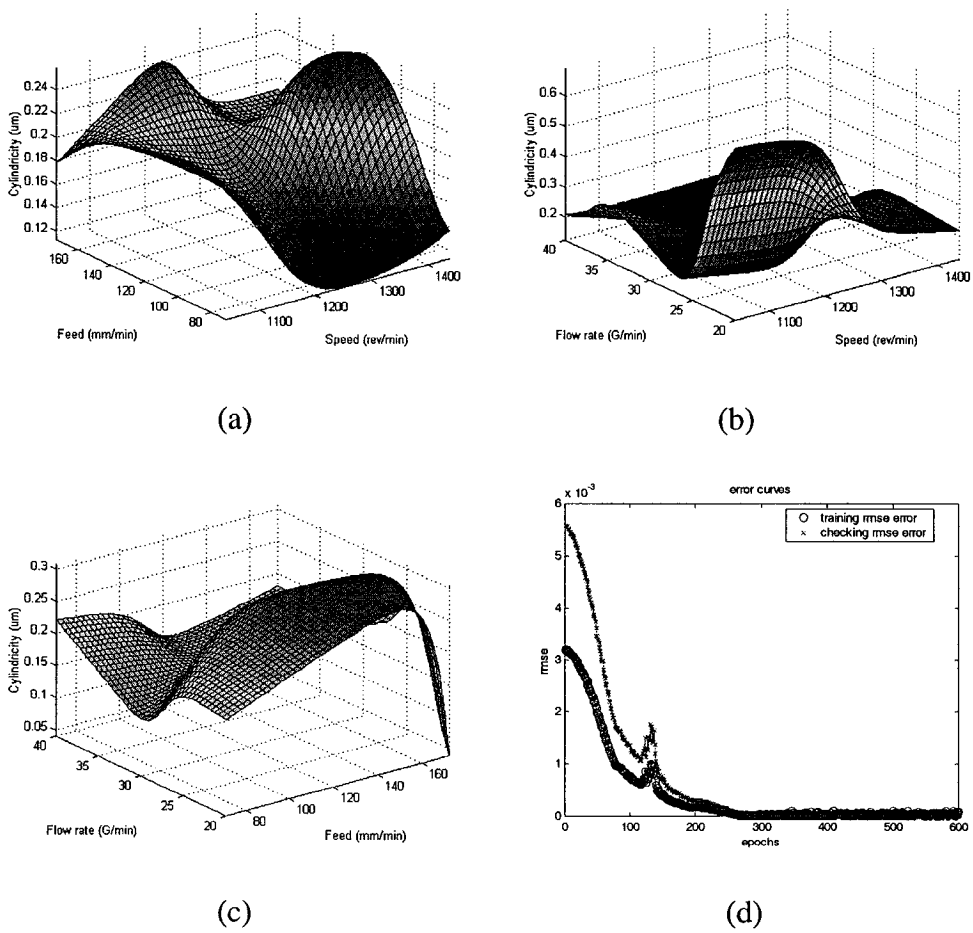


Fig. 5.7: (a) to (c) Surface plot for cylindricity with 3 inputs (d) Error plot of the fuzzy model.

### 5.7.2 Second model of cylindricity error with four inputs using first order Sugeno Model with ANFIS

In this model, the cutting parameters, speed, feed rate, flow rate and tool penetration are the inputs to the model. The output is the cylindricity error.

In this model for cylindricity error, the length of cut or tool penetration is considered as a fourth input to the process to study the effect of the tool penetration on the outcome surface irregularities, and also to find out the best combination of the cutting parameters at different locations of tool penetration.

Fig. 5.8: Shows the complete process from initial model by clustering and the ANFIS structure towards the final model.

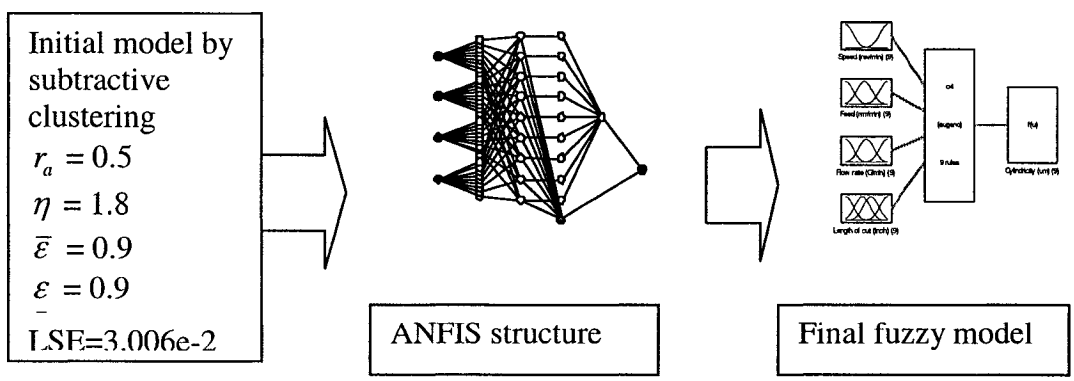


Fig. 5.8: The process of modeling the data for cylindricity with four inputs (feed, speed, flow rate and length of cut).

In Fig. 5.9, the initial membership functions are shown. The final membership functions are shown in Fig. 5.10(a), (b), (c) and (d). The error plot of training and checking data is shown in Fig. 5.11. From Fig. 5.11 It is shown that the second model of cylindricity with 4 inputs is more complex than the first one with 3 inputs. In Fig. 5.11 there are two main regions. From 0.5-3125 epochs there is a difference between the training and checking data, which means that the model is not yet able to produce the actual behavior of the system. This means that the model needs to be trained more. Increasing the epochs more than 3125 up to 3500 epochs assures that the difference between the training and checking data is at minimum and the model can produce the actual behavior of the system.

Table 5.4 summarizes the rules in terms of $(\sigma's, c's, a_{k0}, \cdots, a_{k3})$. The surface plot for the fuzzy model is shown in Fig. 5.11. Table 5.5 shows the values of the fixed cutting parameters corresponding to each figure. From these surface responses, the best parameters were obtained at different lengths of cut or tool penetration. Table. 5.6 summarizes the best combination of parameters at different tool penetration.

The first row of Table 5.6 shows that at a penetration of 76.2 mm (3 inch) the best cutting parameters are 1440 rev/min, 71 mm/min and 31.82 G/min. The second row shows that at a penetration of 152.4 mm (6 in) the best cutting parameters are 1319 rev/min, 86.69 mm/min and 25.58 G/min. Studying the table closely reveals that at each tool penetration the cutting parameters are different in order to get a minimum cylindricity error.

It is obvious from the last model for cylindricity that the cutting parameters should vary while drilling along the workpiece. This is due to the fact that at different length of cut or tool penetration the whirling motion is different either in amplitude or shape. The harmonics associated with the signal are different too. As a result of this the type of surface irregularities will be different. Changing the cutting parameters while drilling in deep hole boring operation is highly needed in order to get better cylindricity and surface finish.

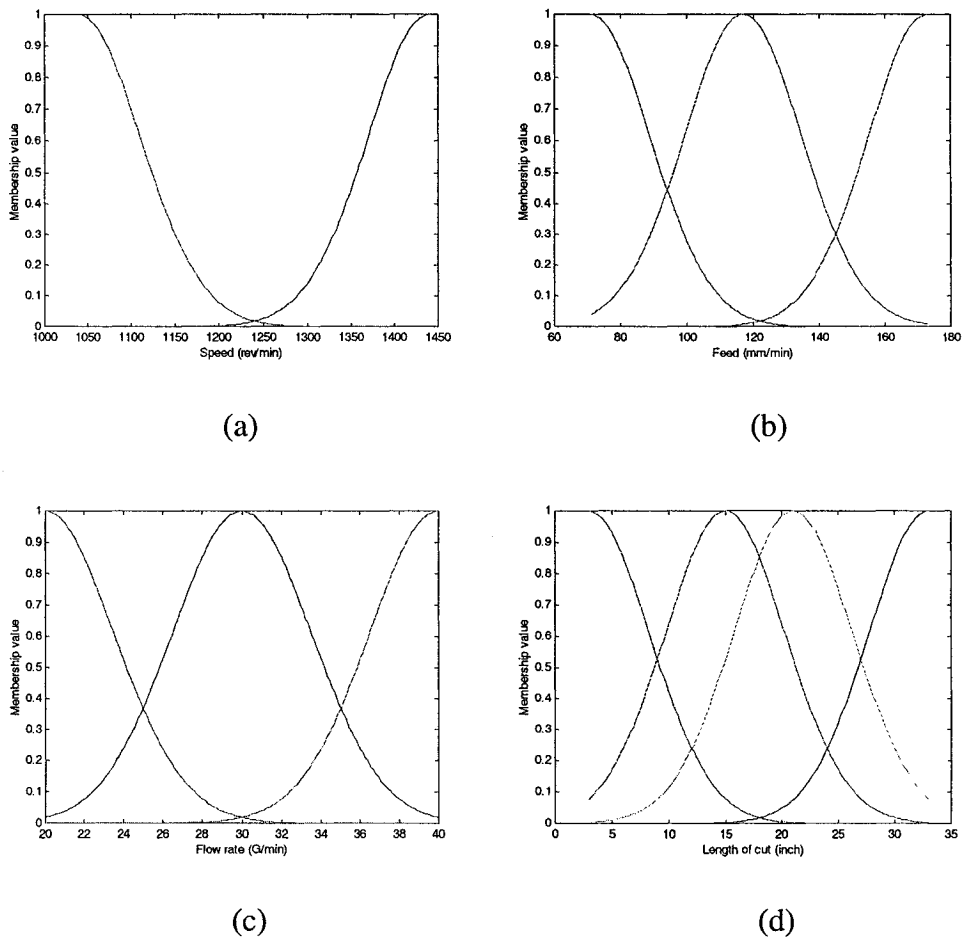


Fig. 5.9: (a) to (b) Initial Membership functions for cylindricity using higher order subtractive clustering for cylindricity with 4 inputs.

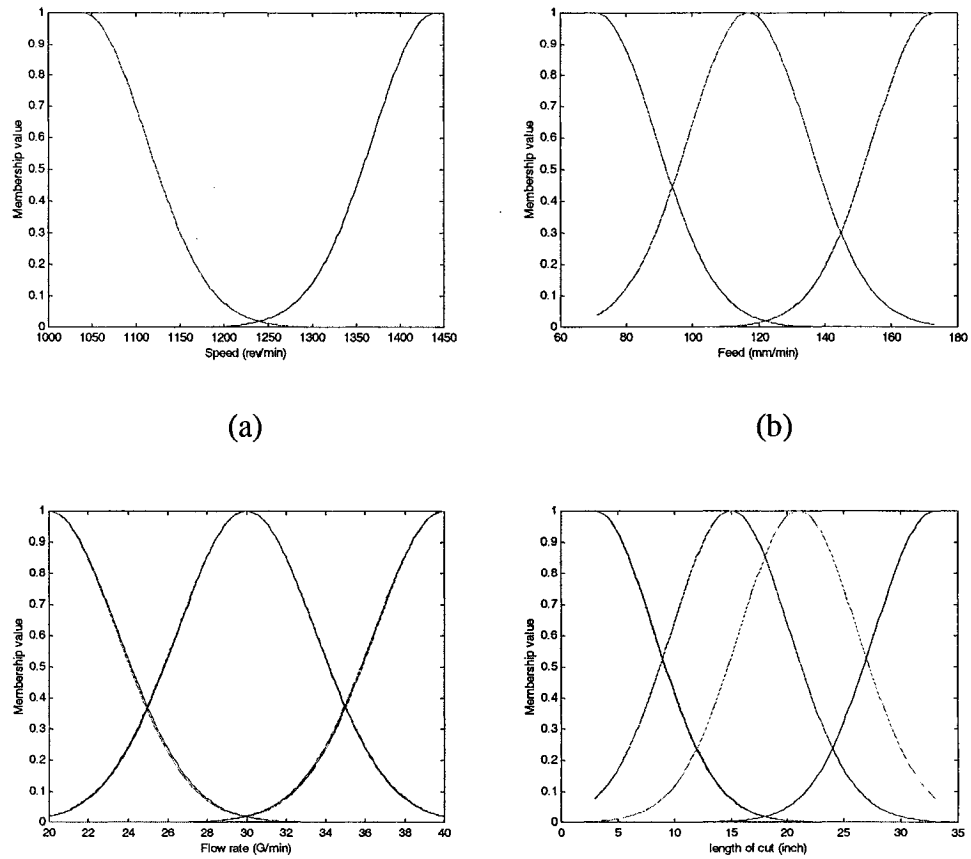


Fig. 5.10: (a) to (d) Final Membership functions after training using ANFIS.

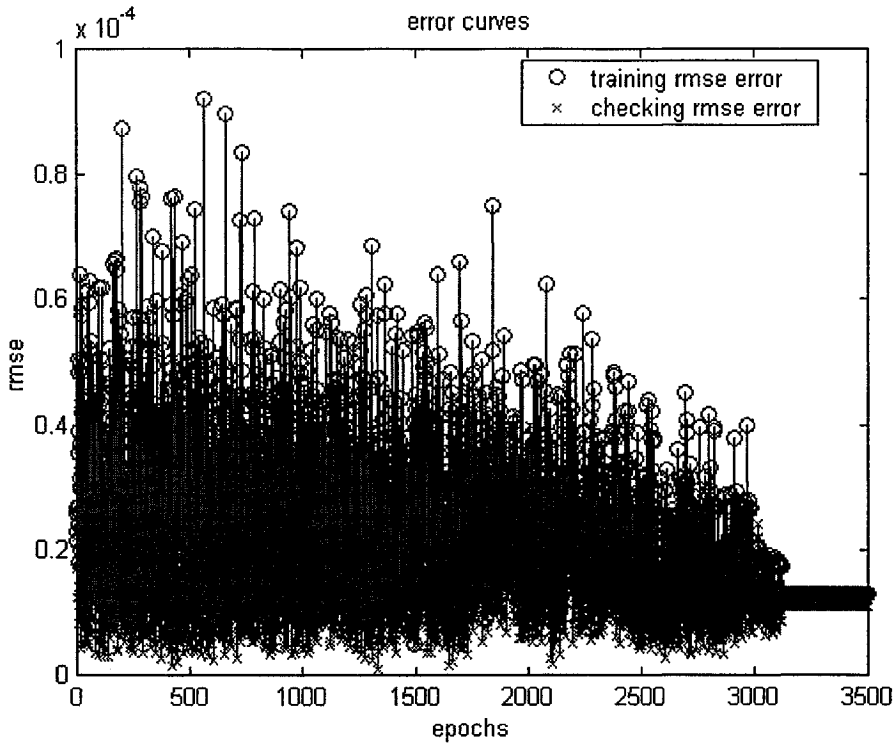


Fig 5.11:Error curves for training and checking data and rules, cylindricity 4 inputs.

Table 5.4: 9 rules for cylindricity fuzzy model, 4 inputs were taken into consideration.

| $R_i$ | $\sigma_1^t, c_1^t$ | $\sigma_2^t, c_2^t$ | $\sigma_3^t, c_3^t$ | $\sigma_4^t, c_4^t$ | $a_{i4}$ | $a_{i3}$ | $a_{i2}$ | $a_{i1}$ | $a_{i0}$ |
|---|---|---|---|---|---|---|---|---|---|
| 1 | 70.71, 1040.00 | 18.03, 117.00 | 3.54, 29.994 | 5.30, 21.00 | -7.26e-005 - | 3.92E-05 | 0.0072 | 0.004067 | 0.003036 |
| 2 | 70.71, 1439.99 | 18.03, 116.99 | 3.53, 19.99 | 5.30, 3.00 | 0.000187 | -8.15E-05 | -0.01318 | -0.0075 | 0.001361 |
| 3 | 70.71, 1439.99 | 18.03, 172.99 | 3.53, 39.99 | 5.30, 15.00 | 0.000251 | 0.0017452 | -0.0079 | -0.01114 | 5.35E-05 |
| 4 | 70.70, 1039.99 | 18.01, 173.00 | 3.489, 19.98 | 5.29, 15.00 | 0.0033094 | -0.019716 | 0.0034684 | -0.0059761 | -0.000147 |
| 5 | 70.71, 1039.99 | 18.03, 70.99 | 3.53, 39.99 | 5.30, 2.99 | 0.0001035 | 0.004004 | -0.00546 | 0.008857 | -2.10E-05 |
| 6 | 70.71, 1439.99 | 18.03, 71.00 | 3.57, 29.98 | 5.30, 20.99 | -0.000134 | 0.002401 | 0.001852 | 0.00494 | 0.0001261 |
| 7 | 70.70, 1039.99 | 18.03, 71.00 | 3.53, 20.00 | 5.26, 2.99 | 0.000373 | -0.004049 | 0.00414 | 0.006977 | -1.47E-05 |
| 8 | 70.71, 1439.99 | 18.03, 173.00 | 3.53, 29.99 | 5.30, 33.00 | 5.16E-05 | 0.001251 | -0.00031 | -0.0027849 | 1.15E-05 |
| 9 | 70.71, 1040.00 | 18.03, 172.99 | 3.57, 39.98 | 5.30, 14.99 | -0.001984 | 0.0168376 | -0.01191 | -0.01257 | -9.51E-05 |

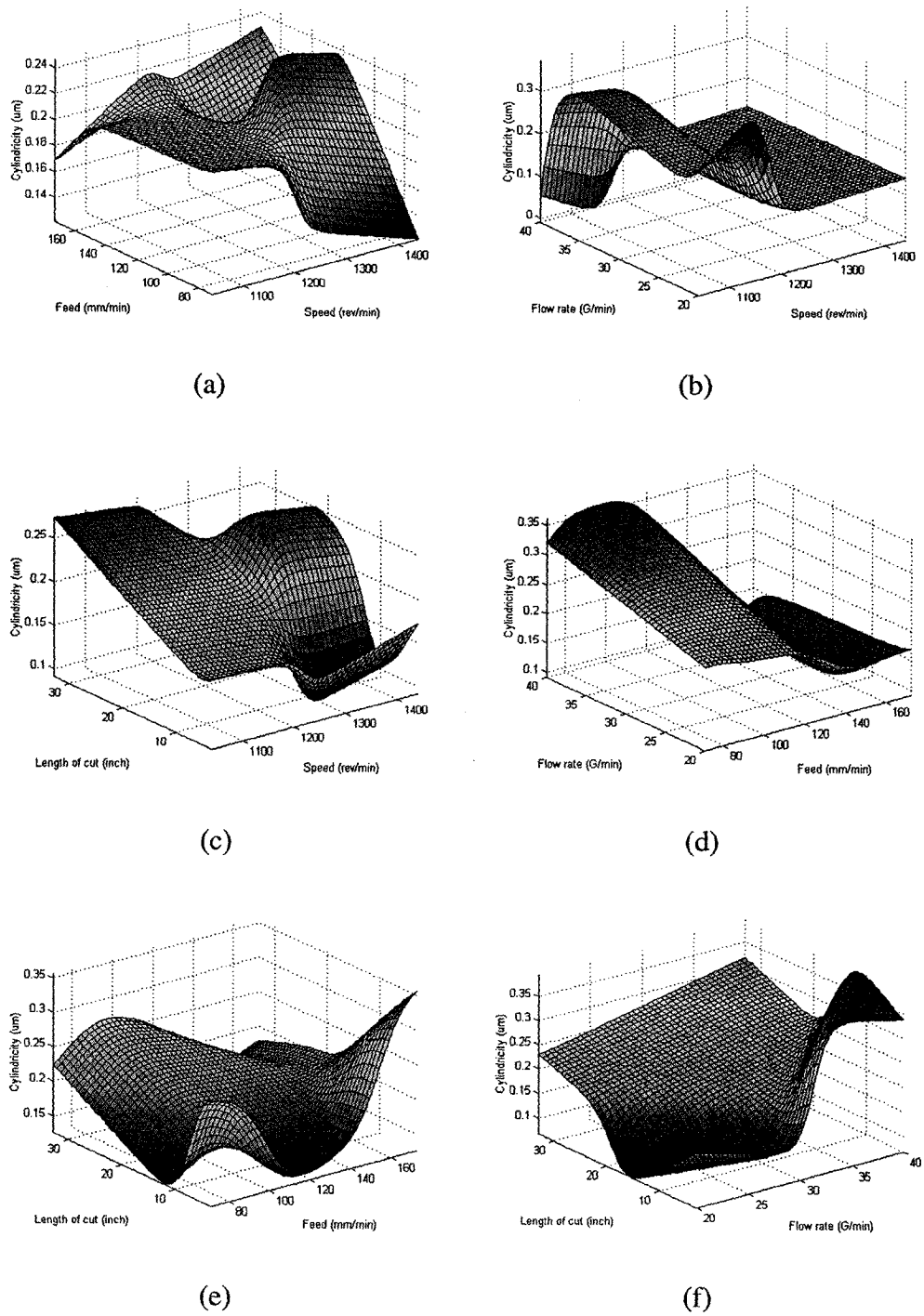


Fig. 5.12: (a) to (f) Surface plot for cylindricity error with 4 inputs.

Table 5.5: The values of the fixed cutting parameters for Fig. 5.12 (----- indicates full scale data).

| Fig. 5.12 | Speed (rev/min) | Feed rate (mm/min) | Flow rate (G/min) | Tool penetration (inch) | Tool penetration (mm) |
|---|---|---|---|---|---|
| (a) | ----- | ----- | 30 | 3 | 76 |
| (b) | ----- | 100 | ----- | 6 | 156 |
| (c) | ----- | 71 | 25 | ----- | ----- |
| (d) | 1440 | ----- | ----- | 9 | 229 |
| (e) | 1276 | ----- | 40 | ----- | ----- |
| (f) | 1365 | 130 | ----- | ----- | ----- |

Table 5.6: The best cutting parameters at different lengths of cut and the cylindricity associated with it resulted from fuzzy model.

| Speed (rev/min) | Feed (mm/min) | Flow rate (G/min) | Length of cut mm (inch) | Cylindricity (μm) |
|---|---|---|---|---|
| 1440 | 71 | 31.82 | 76.2 (3) | 0.0527 |
| 1422 | 75.71 | 32.42 | 76.2 (3) | 0.067 |
| 1319 | 86.69 | 27.58 | 152.4 (6) | 0.0905 |
| 1398 | 91.4 | 24.55 | 228.6(9) | 0.0886 |
| 1440 | 71 | 23.94 | 228.6 (9) | 0.0668 |
| 1301 | 119.6 | 25.76 | 304.8 (12) | 0.0665 |
| 1301 | 119.6 | 23.33 | 381 (15) | 0.0466 |
| 1276 | 119.6 | 40 | 381 (15) | 0.00273 |
| 1234 | 119.6 | 38.48 | 457.2 (18) | 0.0321 |
| 1282 | 124.4 | 38.18 | 533.4 (21) | 0.0274 |
| 1282 | 124.4 | 38.79 | 533.4 (21) | 0.00323 |
| 1282 | 124.4 | 38.53 | 533.4 (21) | 0.0129 |
| 1282 | 124.4 | 38.53 | 609.6 (24) | 0.0279 |
| 1282 | 124.4 | 38.87 | 609.6 (24) | 0.00825 |
| 1324 | 124.4 | 38.87 | 609.6 (24) | 0.00654 |
| 1324 | 125.7 | 38.87 | 609.6 (24) | 0.000998 |
| 1295 | 124.2 | 38.87 | 609.6 (24) | 0.00529 |
| 1365 | 128.7 | 39.12 | 685.8 (27) | 0.0039 |
| 1312 | 130.1 | 40 | 762 (30) | 0.0146 |
| 1283 | 133.1 | 40 | 762 (30) | 0.00331 |
| 1226 | 131.6 | 40 | 762 (33) | 0.0785 |

### 5.7.3 First model for straightness with 3 inputs

In this model, the cutting parameters, speed, feed rate, and flow rate are the inputs to the model. The output is the straightness error.

The initial and final membership functions are shown in Fig. 5.13. Table 5.7 summarizes the rules in terms of ($\sigma's$ , $c's$ , $a_{k0}$ ,$\cdots$, $a_{k3}$). Fig. 14(a), (b) and (c) is a plot of the surface response. The training and checking data root mean square error is shown in Fig. 5.14(d). Fig. 5.14(d) shows that at the beginning of training, for 0.5-40 epochs, there is a big gap between the training and the checking data. This means that the model up to 40 epochs is not able to reproduce the actual behavior of the system. At 45 epochs the difference between the training and checking data are at minimum. The training could stop at 45 epochs. To ensure that there will be no variation between the training and the checking data the training process stopped at 200 epochs.

Table 5.8 shows the values of the fixed cutting parameters corresponding to Fig. 5.14. From the surface response plot, the best combination of cutting parameters is shown in Table 5.9. In Table 5.9, different optimum combinations of cutting parameters were identified to obtain minimum straightness. The minimum straightness is of 0.000171 $\mu$m at speed of 1240 rev/min, feed of 122 mm/min and a flow rate of 30.36 G/min.

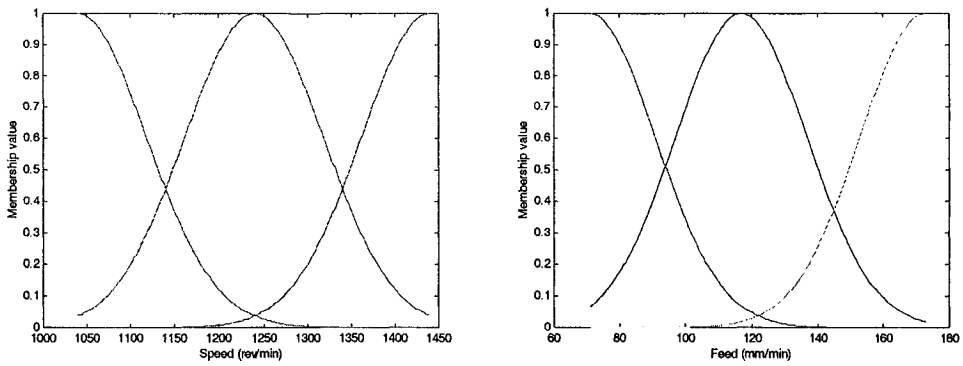


(a) (b)

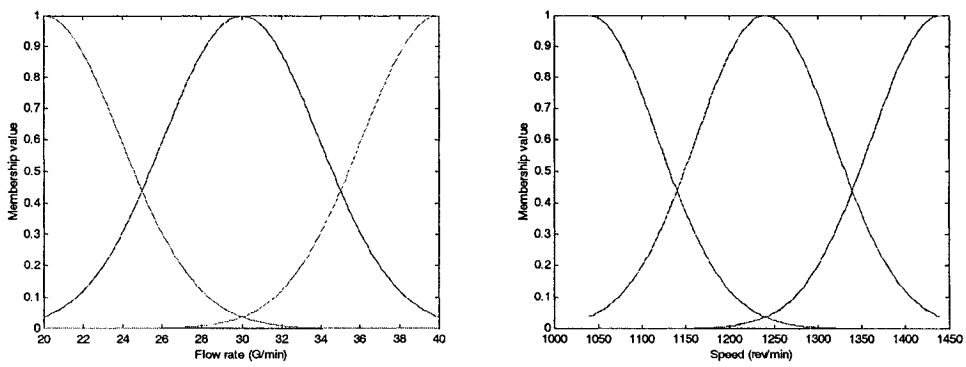


(a) (b)

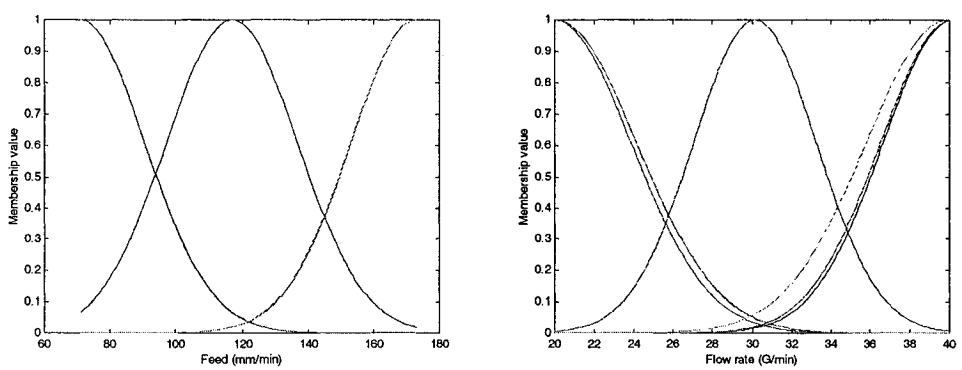


(a) (b)

Fig. 5.13: (a) to (c) initial MF's and (d) to (f) final MF's for straightness with 3 inputs.

Table 5.7: 7 rules fuzzy straightness model with 3 inputs.

| $R_i$ | $\sigma_1^t, c_1^t$ | $\sigma_2^t, c_{y2}^t$ | $\sigma_3^t, c_3^t$ | $a_{i3}$ | $a_{i2}$ | $a_{i1}$ | $a_{i0}$ |
|---|---|---|---|---|---|---|---|
| 1 | 77.77, 1240.00 | 19.85, 117.00 | 3.49, 40.14 | -0.000100 | -0.000699 | 0.015259 | -0.265986 |
| 2 | 77.78, 1240.00 | 19.74, 70.96 | 4.07, 20.07 | 0.0001500 | -9.774e-005 | -0.0062729 | 0.1013338 |
| 3 | 77.80, 1439.99 | 19.91, 172.97 | 3.88, 19.99 | 0.0004018 | 0.0002216 | -0.0206872 | -0.0769960 |
| 4 | 77.76, 1039.99 | 19.98, 172.94 | 4.09, 20.08 | 0.00025654 | -0.0027075 | 0.0074639 | 0.1546891 |
| 5 | 77.78, 1040.00 | 19.80, 70.98 | 3.59, 40.11 | -1.979e-005 | -0.0012913 | 0.0025522 | 0.1483465 |
| 6 | 77.77, 1440.00 | 19.84, 172.99 | 4.12, 39.90 | 0.0004711 | -0.0010789 | -0.0095548 | 0.05856177 |
| 7 | 77.78, 1440.00 | 19.83, 70.99 | 3.11, 30.15 | 0.0001285 | -6.434e-005 | -0.001907 | -0.0270875 |

Table 5.8: The values of the fixed cutting parameters for Fig. 5.14 (----- indicates full scale data).

| Fig. 5.14 | Speed (rev/min) | Feed rate (mm/min) | Flow rate (G/min) |
|---|---|---|---|
| (a) | ----- | ----- | 20 |
| (b) | ----- | 122 | ----- |
| (c) | 1300 | ----- | ----- |

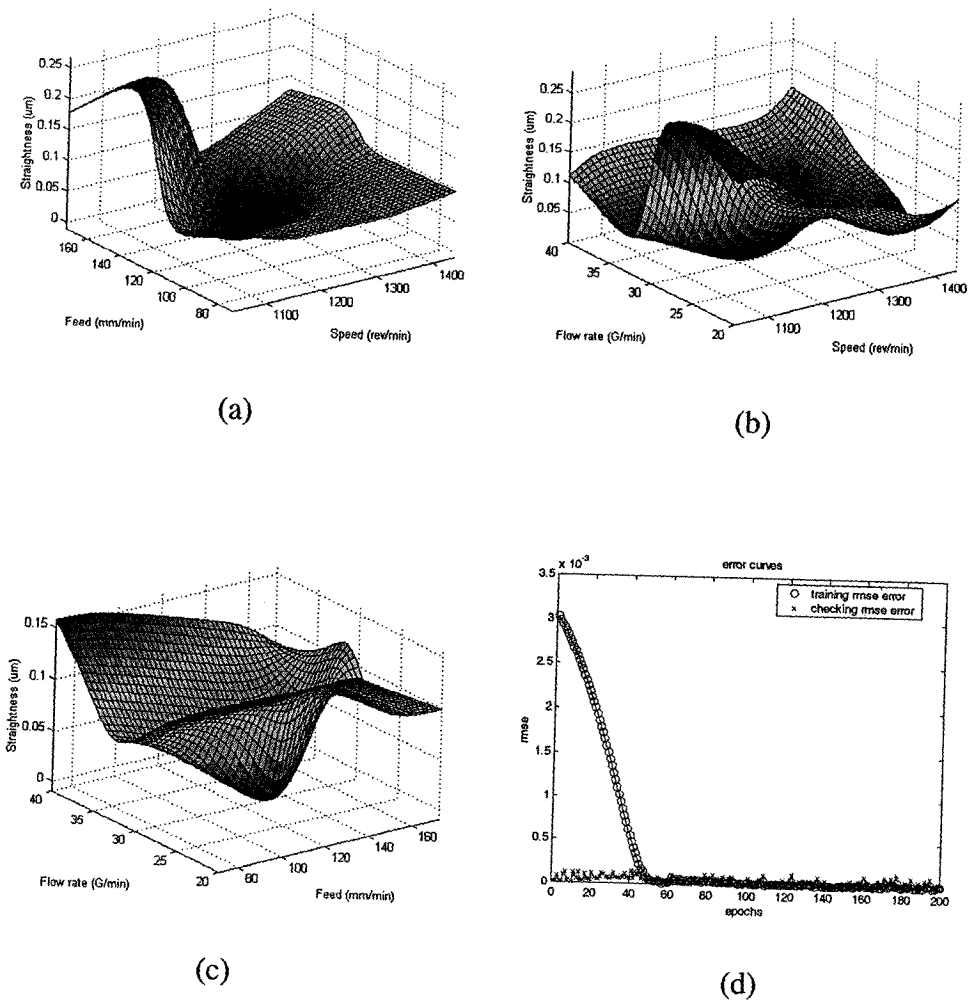


Fig. 5.14: (a) to (c) Surface plot for straightness with 3 inputs and (d) Error plot of the fuzzy model.

Table 5.9: The best cutting parameters and the straightness associated with it resulting from the fuzzy model.

| Speed (rev/min) | Feed (mm/min) | Flow rate (G/min) | Straightness ($\mu$m) |
|---|---|---|---|
| 1240 | 122 | 30 | 0.00128 |
| 1240 | 122 | 30.6 | 0.0007 |
| 1240 | 122 | 30.36 | 0.000171 |
| 1440 | 173 | 28.19 | 0.00215 |
| 1257 | 173 | 28.9 | 0.00433 |
| 1257 | 138.6 | 28.19 | 0.00588 |
| 1257 | 138.6 | 28.43 | 0.00208 |
| 1257 | 138.6 | 31.08 | 0.000853 |
| 1218 | 138.6 | 31.08 | 0.000142 |

### 5.7.4 Second model for straightness with 4 inputs

In this model, the cutting parameters, speed, feed rate, flow rate and tool panetration are the inputs to the model. The output is the straightness error.

In Fig. 5.15, the initial membership functions are shown. The final membership functions are shown in Fig. 5.16 (a), (b), (c) and (d). The error plot of training and checking data is shown in Fig. 5.16 (e). Fig. 5.16 (e) shows that the second model of cylindricity with 4 inputs is more complex and 100 epochs are needed to train the data compared to the first one with 3 inputs, where the training process ends at 45 epochs. There are three main regions in Fig. 5.16 (e). The first region is between 0.5-70 epochs where there is a difference between the training and checking data without a reduction in the error. The second region is between 70-92 epochs, where we see a drop in the error, with almost a minimum difference between the training and checking data. The third is between 100-

200 epochs where there is no difference between the training and checking data and the error is at minimum. This means that the model, after 100 epochs is able to produce the actual behavior of the system.

Table 5.10 summarizes the rules in terms of their parameters ($\sigma's$, $c's$, $a_{k0}$, $\cdots$, $a_{k3}$). Table 5.17 shows the values of the fixed cutting parameters corresponding to Fig. 5.17. The surface plot for the fuzzy model is shown in Fig. 5.11. From these surface responses, the best parameters were obtained at different length of cut or tool penetration. Table. 5.12 summarize the best combination of parameters at different tool penetration.

The first row of Table 5.12 shows that at a penetration of 76.2 mm (3 in) the best cutting parameters are 1337 rev/min, 75.71 mm/min and 31.44 G/min. At 152.4 mm (6 in), the best cutting parameters are 1440 rev/min, 173 mm/min and 39.7 G/min. Studying the table up to the end, it is noticed that at each tool penetration the cutting parameters are different in order to get a minimum straightness error.

As in cylindricity model with four inputs it is obvious that the cutting parameters should vary while drilling toward the end of the workpiece to make a deep hole with minimum straightness error.

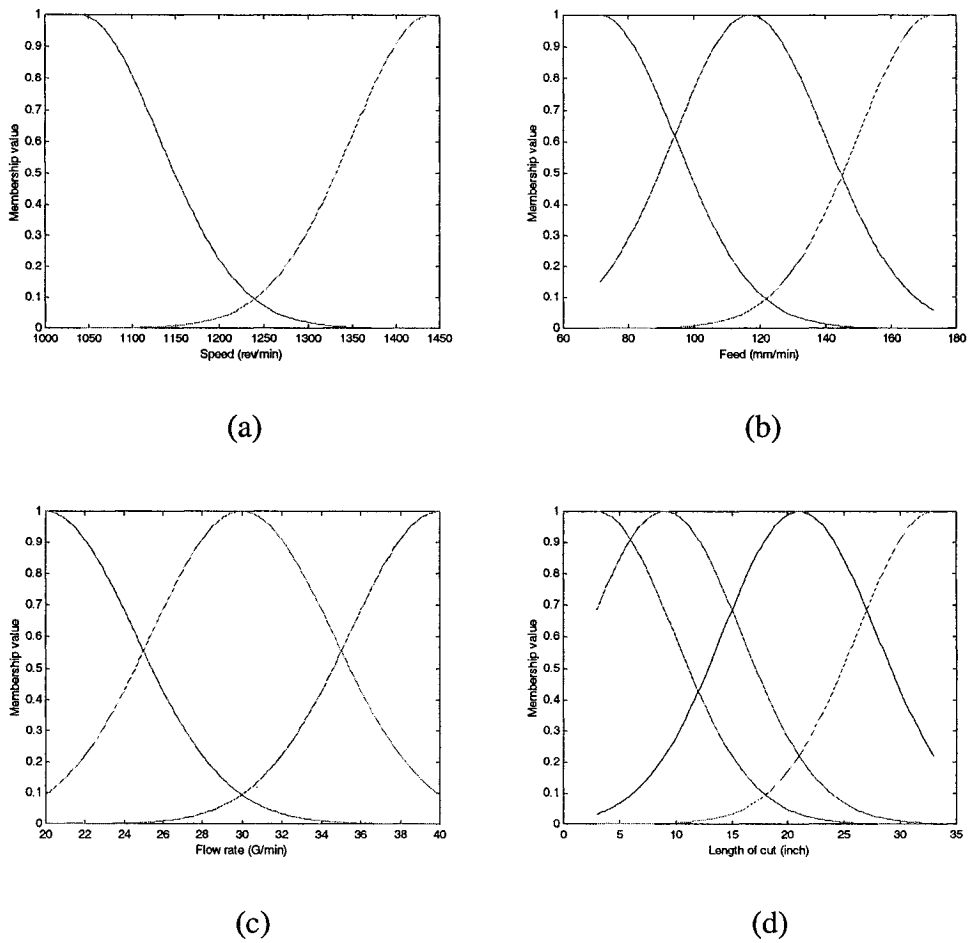


Fig. 5.15: Initial membership functions for straightness with 4 inputs.

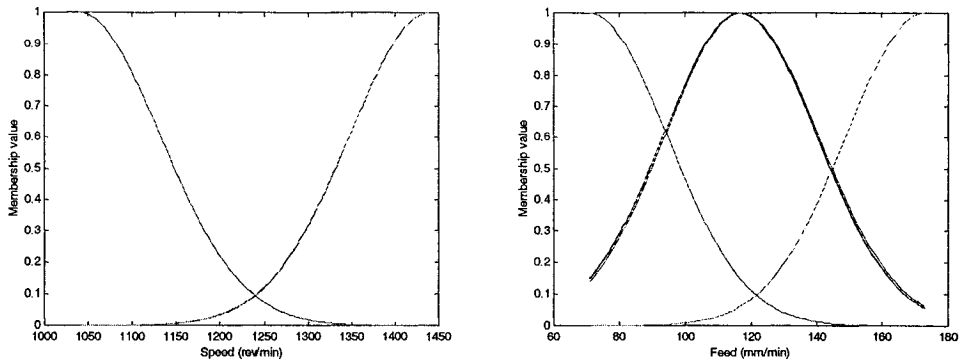


(a)




(b)

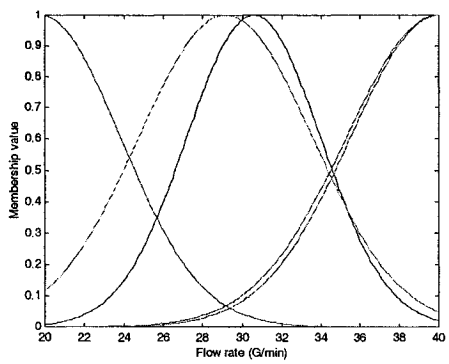


(c)

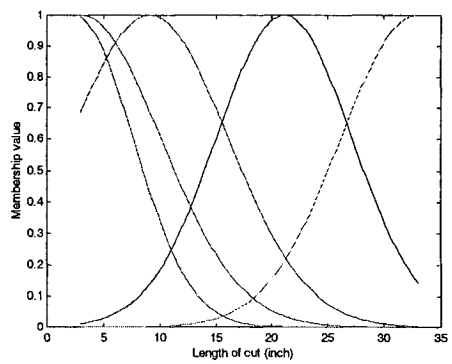


(d)

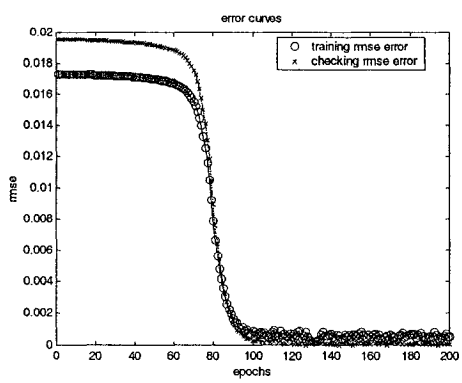


(e)

Fig. 5.16: (a) to (d) Final membership functions for straightness with 4 inputs and (e) Error plot of the fuzzy model.

Table 5.10: 5 rules for straightness fuzzy model with 4 inputs were taken into consideration.

| $R_i$ | $\sigma_1^1, c_1^1$ | $\sigma_2^1, c_{i2}^1$ | $\sigma_3^1, c_3^1$ | $\sigma_4^1, c_{i4}^1$ | $a_{i4}$ | $a_{i3}$ | $a_{i2}$ | $a_{i1}$ | $a_{i0}$ |
|---|---|---|---|---|---|---|---|---|---|
| 1 | 91.94, 1040.00 | 23.24, 116.71 | 3.57, 30.84 | 5.86, 21.33 | -0.00190 | 2.49e-005 | 0.001192 | 0.005581 | 1.96128 |
| 2 | 92.14, 1439.97 | 23.17, 117.13 | 3.53, 19.57 | 5.09, 2.50 | -0.01438 | -0.001205 | 1.0307 | 0.011388 | 0.321350 |
| 3 | 91.91, 1440.00 | 23.55, 117.04 | 4.75, 39.92 | 6.73, 8.98 | 0.000469 | -0.001435 | 0.0375223 | 0.020503 | -2.03898 |
| 4 | 92.19, 1439.91 | 23.60, 172.92 | 4.35, 29.40 | 7.28, 32.68 | -0.00134 | 0.00023638 | -0.0314386 | 0.003956 | 2.8404 |
| 5 | 91.93, 1040.00 | 23.44, 70.99 | 4.72, 39.93 | 7.03, 3.04 | -0.00208 | -0.0030007 | 0.0240783 | 0.017892 | 1.50283 |

Table 5.11: The values of the fixed cutting parameters for Fig. 5.17 (----- indicates full scale data).

| Fig. 5.17 | Speed (rev/min) | Feed rate (mm/min) | Flow rate (G/min) | tool penetration (inch) | Tool penetration (mm) |
|---|---|---|---|---|---|
| (a) | ----- | ----- | 20 | 5 | 127 |
| (b) | ----- | 120 | ----- | 15 | 381 |
| (c) | ----- | 90 | 24 | ----- | ----- |
| (d) | 1200 | ----- | | 25 | 635 |
| (e) | 1330 | ----- | 35 | ----- | ----- |
| (f) | 1000 | 150 | ----- | ----- | ----- |

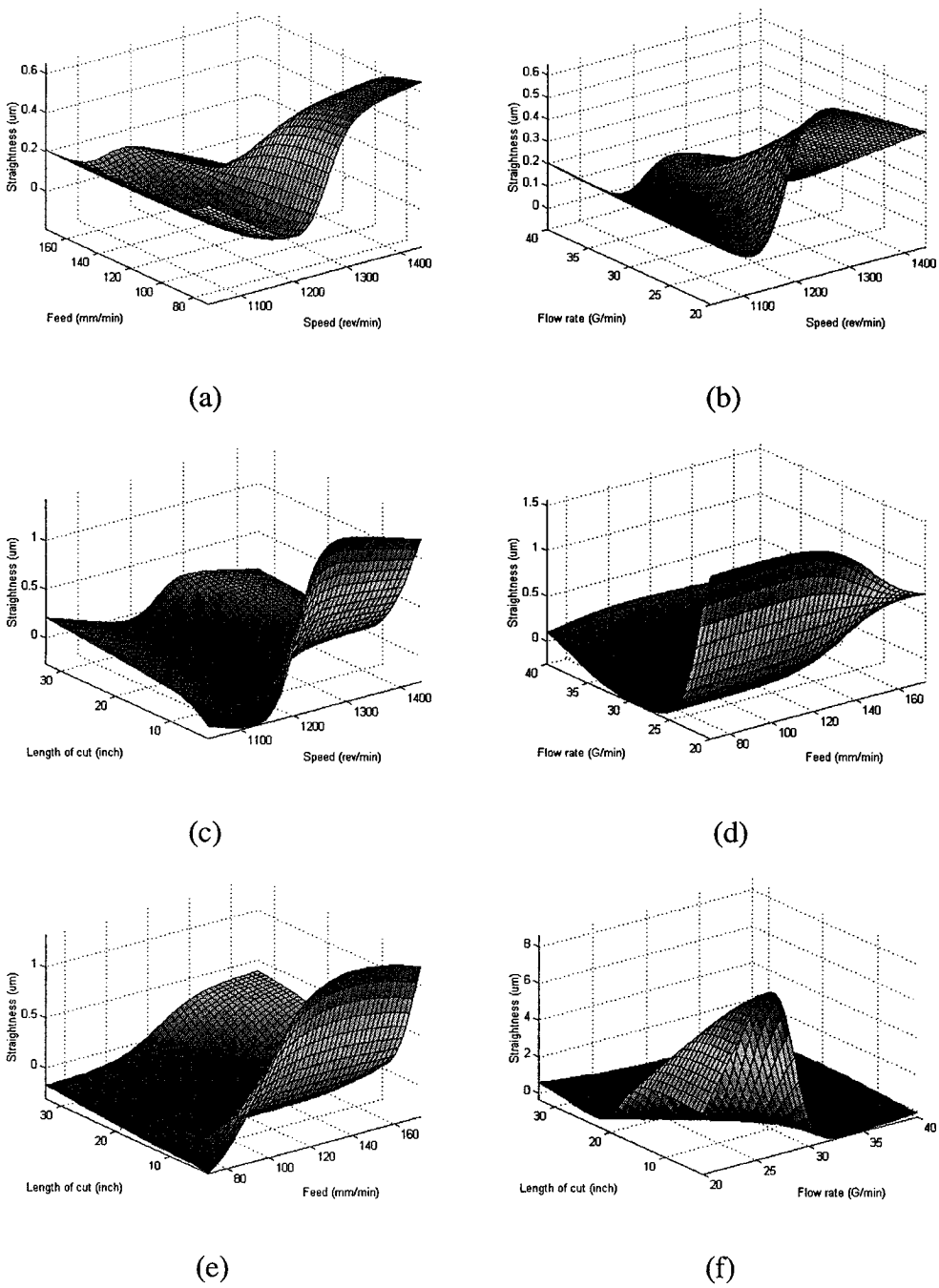


Fig. 5.17: Surface plot for straightness with 4 inputs.

Table 5.12: The best cutting parameters at different lengths of cut and the straightness associated with it resulted from fuzzy model.

| Speed (rev/min) | Feed (mm/min) | Flow rate (G/min) | Length of cut mm (inch) | Cylindricity (μm) |
|---|---|---|---|---|
| 1337 | 75.71 | 31.44 | 76.2 (3) | 0.00238 |
| 1440 | 131 | 39.7 | 76.2 (3) | 0.0000655 |
| 1440 | 173 | 39.7 | 152.4 (6) | 0.000833 |
| 1440 | 167.6 | 30.91 | 152.4 (6) | 0.00234 |
| 1348 | 110.4 | 31.2 | 152.4 (6) | 0.00002 |
| 1235 | 155.3 | 40 | 228.6 (9) | 0.00006 |
| 1235 | 155.3 | 29.87 | 228.6 (9) | 0.0333 |
| 1083 | 122.7 | 27.47 | 304.8 (12) | 0.00473 |
| 1186 | 163.5 | 40 | 304.8 (12) | 0.000693 |
| 1240 | 137.6 | 37.33 | 381 (15) | 0.00303 |
| 1321 | 166.2 | 36.27 | 381 (15) | 0.00999 |
| 1321 | 173 | 36.27 | 381 (15) | 0.00551 |
| 1321 | 173 | 35.47 | 381 (15) | 0.000835 |
| 1440 | 156.7 | 31.73 | 457.2 (18) | 0.00289 |
| 1283 | 141.7 | 31.47 | 533.4 (21) | 0.00687 |
| 1283 | 141.7 | 34.67 | 533.4 (21) | 0.0038 |
| 1408 | 152.6 | 34.67 | 609.6 (24) | 0.00115 |
| 1364 | 151.2 | 37.33 | 685.8 (27) | 0.000462 |
| 1364 | 151.2 | 37.07 | 685.8 (27) | 0.00368 |
| 1332 | 173 | 38.13 | 762 (30) | 0.007 |
| 1332 | 147.2 | 40 | 762 (30) | 0.00202 |
| 1348 | 130.8 | 39.73 | 838.2 (33) | 0.00238 |
| 1343 | 132.2 | 39.73 | 838.2 (33) | 0.000915 |

### 5.7.5 First fuzzy model for surface roughness (RMS) with 3 inputs

In this model, the cutting parameters, speed, feed rate, and flow rate are the inputs to the model. The output is the surface roughness.

The initial and final membership functions are shown in Fig. 5.18. Table 5.13 summarizes the rules in terms of their parameters ($\sigma's$, $c's$, $a_{k0}$, $\cdots$, $a_{k3}$).

Fig. 5.19 (a), (b) and (c) gives the plot of the surface response. The training and checking data root mean square error is shown in Fig. 5.19 (d). Fig. 5.19 (d) shows that from the beginning to the end of training the difference between the training and checking data is at minimum. There are four main regions in Fig. 5.19 (d). The first region is between 0.5-24 epochs where there is a reduction in the error from 0.055 to 0.025. The second region between 24-125 epochs, where we see a drop in the error again from 0.025 to 0.005. The third is between 125-150 where there is a drop in the error again form 0.005 to 0.00125. The fourth region is between 150 to 250 epochs where the error drops from 0.00125 to 0.

Table 5.14 shows the values of the fix cutting parameters corresponding to Fig. 5.19. From the surface response plot, the best combination of cutting parameters is identified shown in Table 5.15.

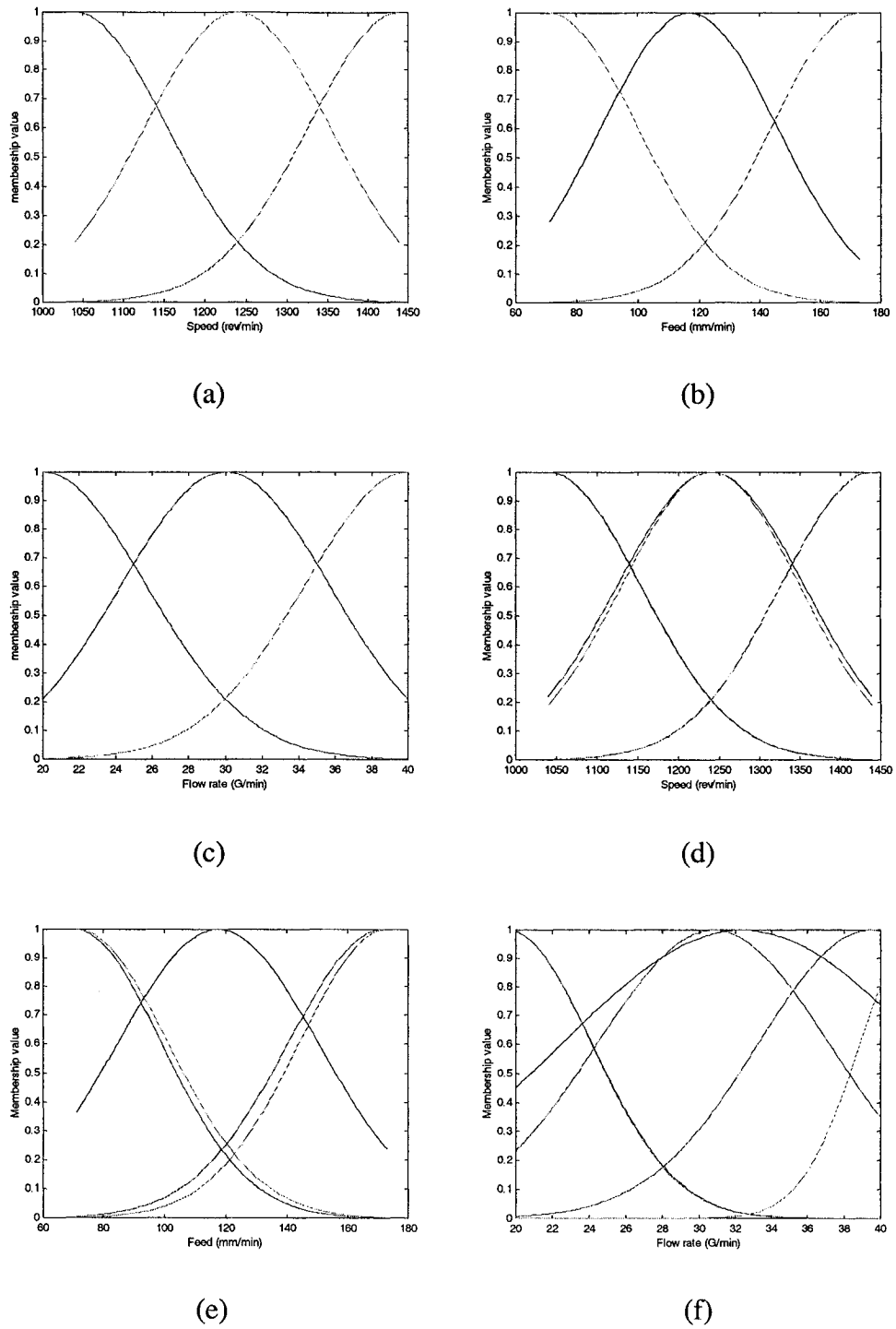


Fig. 5.18: (a) to (c) initial MF's and (d) to (f) final MF's for roughness with 3 inputs.

Table 5.13: 6 rules for straightness fuzzy model, 3 inputs were taken into consideration.

| $R_i$ | $\sigma_1^t, c_1^t$ | $\sigma_2^t, c_2^t$ | $\sigma_3^t, c_3^t$ | $a_{i3}$ | $a_{i2}$ | $a_{i1}$ | $a_{i0}$ |
|---|---|---|---|---|---|---|---|
| 1 | 112.89, 1039.86 | 32.65, 117.52 | 9.80, 32.36 | -2.051937 | 0.0195411 | -0.00018873 | 0.0023868 |
| 2 | 112.93, 1440.11 | 28.24, 70.61 | 6.33, 30.80 | 2.91162 | -0.0067761 | 0.0037994 | -0.0012364 |
| 3 | 115.20, 1240.16 | 31.02, 171.74 | 6.13, 39.44 | -12.68772 | 0.0081856 | 0.0631168 | 0.0017990 |
| 4 | 113.08, 1440.01 | 28.75, 173.03 | 4.52, 19.57 | 3.905137 | -0.0472015 | -0.00068684 | -0.0012947 |
| 5 | 113.07, 1039.98 | 28.18, 70.70 | 4.57, 19.55 | 4.51699 | -0.1201698 | 0.01487052 | -0.0019354 |
| 6 | 109.80, 1240.07 | 29.53, 71.47 | 3.22, 42.12 | 0.01294644 | -0.092037 | 0.0430529 | 0.0010766 |

Table 5.14: The values of the fixed cutting parameters for Fig. 5.19 (----- indicates full scale data).

| Fig. 5.19 | Speed (rev/min) | Feed rate (mm/min) | Flow rate (G/min) |
|---|---|---|---|
| (a) | ----- | ----- | 23 |
| (b) | ----- | 140 | ----- |
| (c) | 1100 | ----- | ----- |

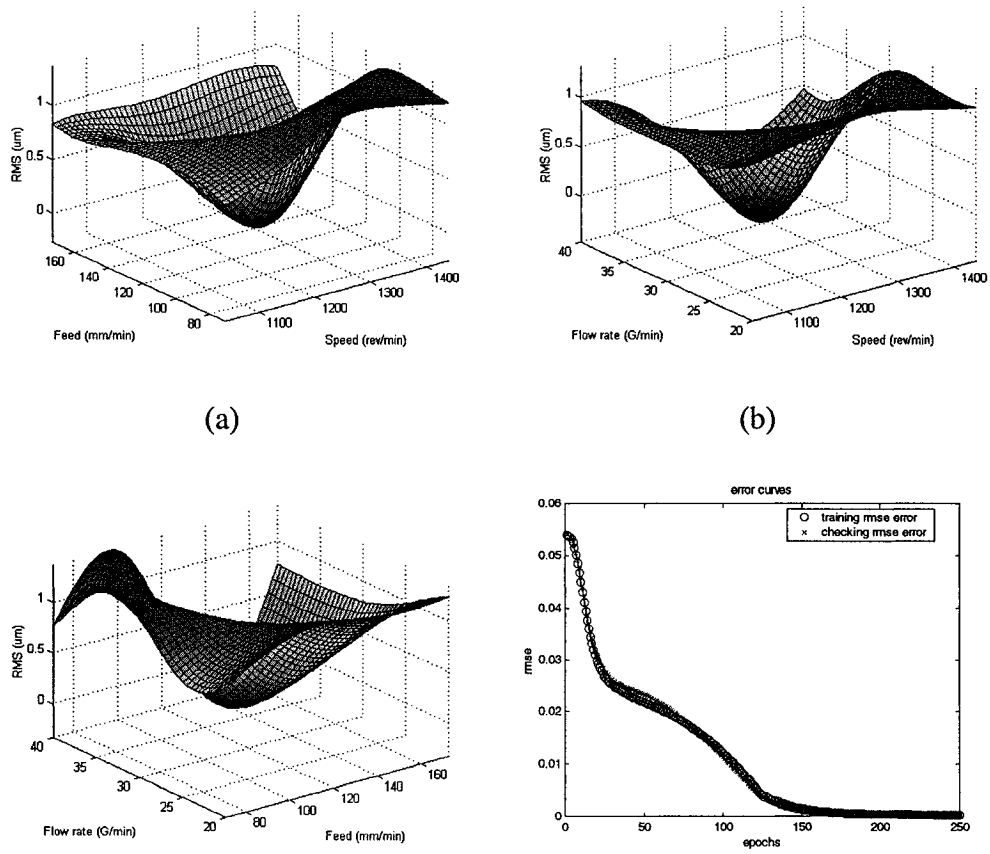


Fig. 5.19: (a) to (c) Surface plot for roughness (RMS) with 3 inputs and (d) Error plot of the fuzzy model.

Table 5.15: The best cutting parameters and the RMS associated with it resulted from fuzzy model.

| Speed (rev/min) | Feed (mm/min) | Flow rate (G/min) | Cylindricity (μm) |
|---|---|---|---|
| 1245 | 121.4 | 32.77 | 0.00262 |

### 5.7.6 Second fuzzy model for surface roughness (RMS) with 4 inputs

In this model, the cutting parameters, speed, feed rate, flow rate, and the tool penetration are the inputs to the model. The output is the surface roughness.

In Fig. 5.20, the initial membership functions are shown. The final membership functions are shown in Fig. 5.21 (a), (b), (c) and (d). The error plot of training and checking data is shown in Fig. 5.21 (e). Fig. 5.21 (e) has 5 regions. The first region is between 0.5-40 epochs where there is a difference between the training and the checking data, which means more training, is needed. The second region between 40-75 epochs where the error of the training data is of 0.019 while it is of 0.03 for the checking data, which creates a gap up to 240 epochs in the third region. The fourth region is between 240-344 epochs where there is a difference between the training and the checking data and a drop in the error for both of them. In the fifth region the training and checking data meet with a minimal difference and minimum RMSE.

Table 5.16 summarizes the rules in terms of their parameters $(\sigma's, c's, a_{k0}, \cdots, a_{k3})$. Table 5.17 shows the values of the fixed cutting parameters corresponding to Fig. 3.22. The surface plot for the fuzzy model is shown in Fig. 5.11. From these surface responses, the best parameters were obtained at different length of cut or tool penetration. Table. 5.18 summarizes the best combination of parameters at different tool penetration.

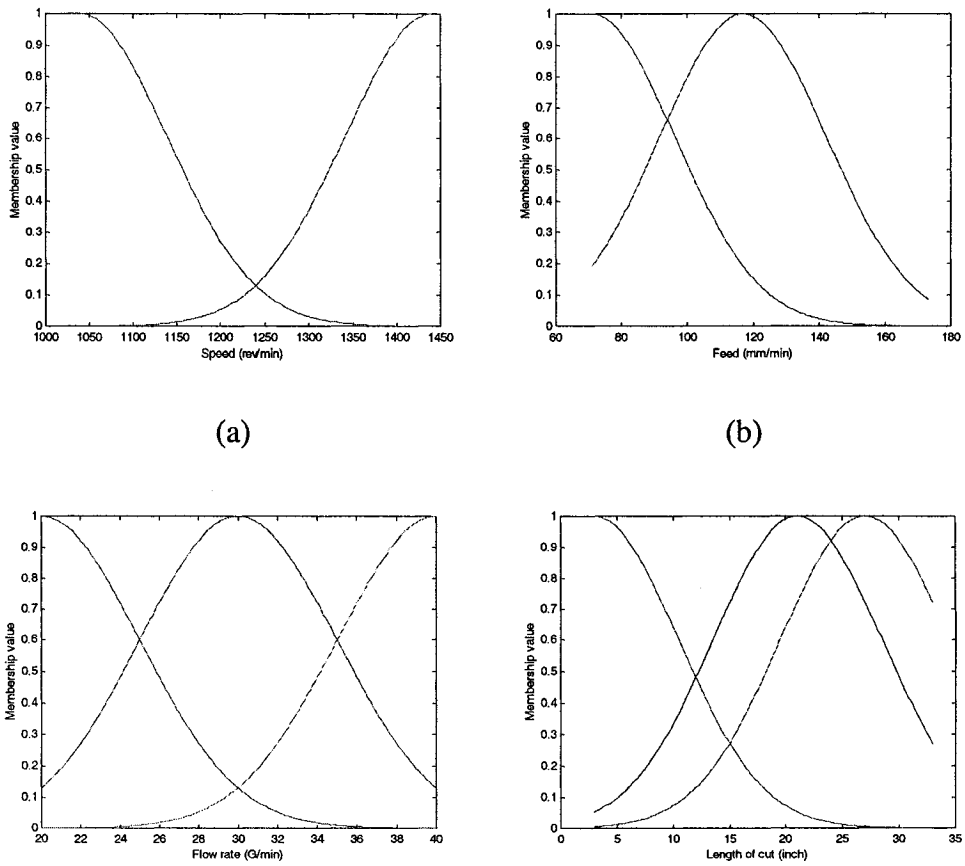


Fig. 5.20: (a) to (b) Initial Membership functions for RMS using higher order subtractive clustering (5 rules).

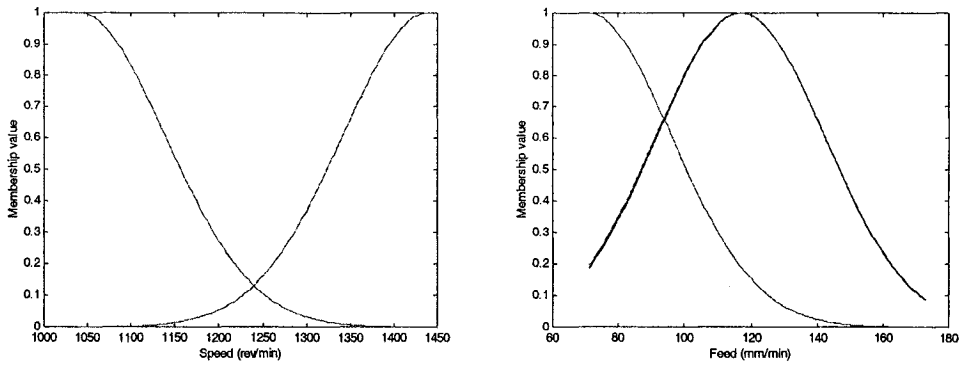


(a)




(b)

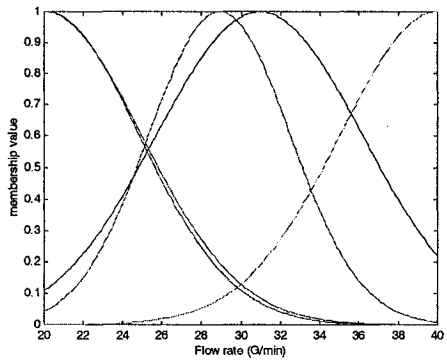


(c)

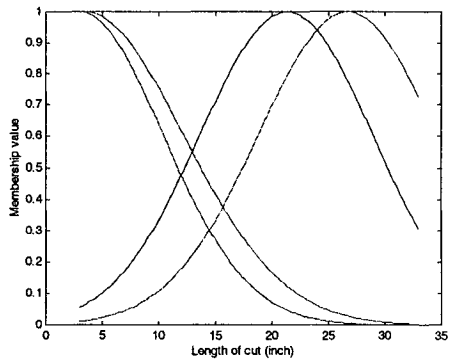


(d)

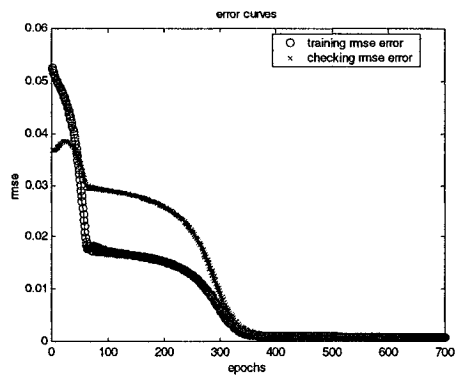


(e)

Fig. 5.21: (a) to (d) Final Membership functions for RMS using ANFIS with (5 rules), (e) Error plot of training and checking data.

Table 5.16: Summary of the result of the rules, sigma's, center's and the regression coefficients.

| $R_i$ | $\sigma_1^t, c_1^t$ | $\sigma_2^t, c_{,2}^t$ | $\sigma_3^t, c_3^t$ | $\sigma_4^t, c_{,4}^t$ | $a_{i4}$ | $a_{i3}$ | $a_{i2}$ | $a_{i1}$ | $a_{i0}$ |
|---|---|---|---|---|---|---|---|---|---|
| 1 | 98.97, 1039.99 | 25.23, 116.99 | 5.26, 30.89 | 7.62, 21.28 | 5.54764 | 0.00455018 | -0.0021421 | -0.0020730 | -0.0042403 |
| 2 | 99.01, 1439.98 | 25.39, 116.90 | 4.67, 20.14 | 8.61, 3.45 | 21.2806 | 0.0039656 | -0.3213615 | -0.0026505 | -0.0093175 |
| 3 | 98.98, 1440.00 | 25.10, 117.10 | 3.58, 28.95 | 7.83, 26.70 | 27.1854 | 0.1850841 | 0.384848 | -0.026296 | -0.0274257 |
| 4 | 98.99, 1040.00 | 25.24, 70.99 | 4.94, 40.00 | 7.41, 2.99 | 0.761431 | -0.0083027 | -0.0434901 | 0.0047797 | 0.00153260 |
| 5 | 98.99 1039.99 | 25.23, 70.99 | 4.94, 20.00 | 7.40, 2.9 | -1.55151 | -0.0893929 | -0.0331730 | 0.01446557 | 0.00246462 |

Table 5.17: The fixed cutting parameters in Fig. 5.22 (----- indicates full scale data).

| Fig. 5.22 | Speed (rev/min) | Feed rate (mm/min) | Flow rate (G/min) | tool penetration (inch) | Tool penetration (mm) |
|---|---|---|---|---|---|
| (a) | ----- | ----- | 30 | 7 | 177.8 |
| (b) | ----- | 90 | ----- | 20 | 508 |
| (c) | ----- | 89 | 35 | ----- | ----- |
| (d) | 1200 | ----- | ----- | 27 | 685.8 |
| (e) | 1300 | ----- | 40 | ----- | ----- |
| (f) | 1440 | 135 | ----- | ----- | ----- |

From the three models for cylindricity, straightness and roughness with four inputs, the conclusion is that the cutting parameters should vary while drilling toward the end of the workpiece to make a deep hole in order to obtain minimum surface irregularities.

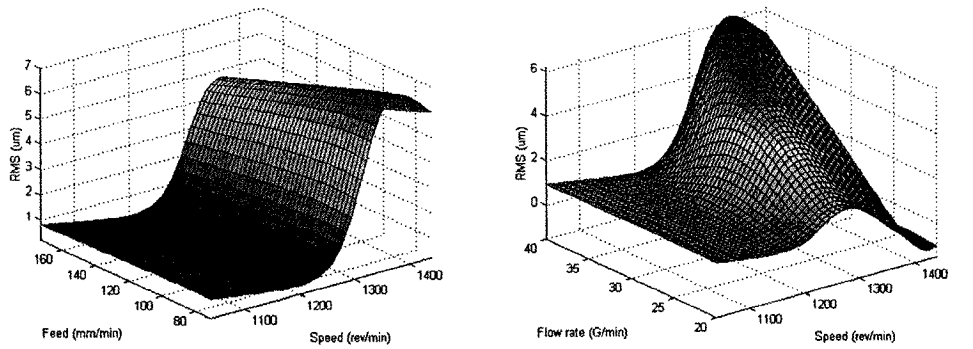


(a) (b)

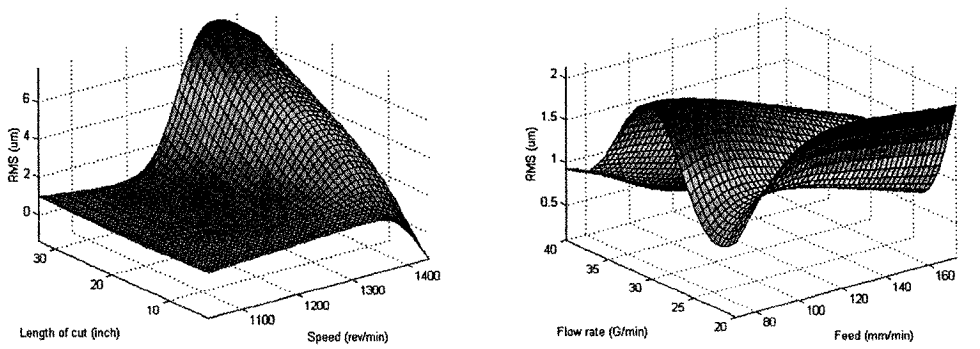


(a) (b)

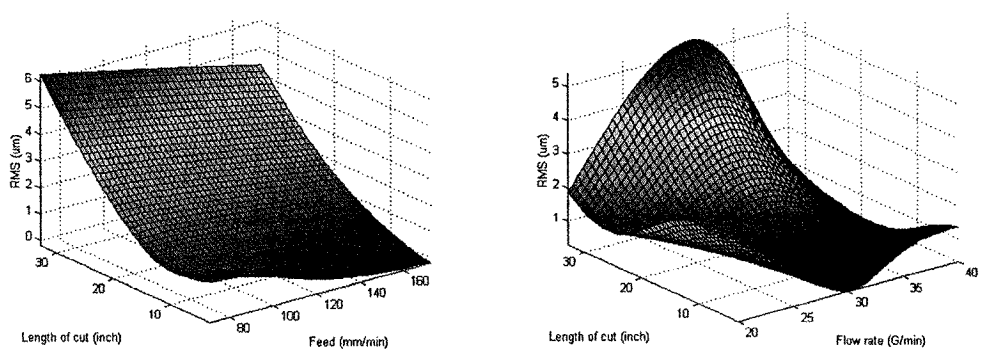


(a) (b)

Fig. 5.22: Roughness (RMS) with 4 inputs.

Table 5.18: The best cutting parameters at different lengths of cut and the RMS associated with it resulted from fuzzy model.

| Speed (rev/min) | Feed (mm/min) | Flow rate (G/min) | Length of cut (Tool penetration) mm (inch) | RMS (μm) |
|---|---|---|---|---|
| 1258 | 120.7 | 30.5 | 76.2 (3) | 0.0178 |
| 1370 | 145 | 25 | 152.4 (6) | 0.0183 |
| 1313 | 124.6 | 30 | 228.6 (9) | 0.0121 |
| 1358 | 110.2 | 29.49 | 304.8 (12) | 0.046 |
| 1358 | 145.5 | 29.49 | 381 (15) | 0.0235 |
| 1230 | 173 | 40 | 457.2 (18) | 0.0853 |
| 1219 | 169.1 | 40 | 533.4 (21) | 0.144 |
| 1173 | 141.6 | 35.38 | 609.6 (24) | 0.481 |
| 1225 | 166.5 | 39.74 | 685.8 (27) | 0.331 |
| 1219 | 171.7 | 39.74 | 762 (30) | 0.394 |
| 1184 | 161.2 | 39.74 | 838.2 (33) | 0.379 |

In this chapter, fuzzy models for cylindricity, straightness and roughness were formulated. The best combinations of the cutting parameters were concluded form the surface plot of the surface response. Chapter 6 will investigate the active suppression of the whirling motion in two directions by means of two electrodynamic shakers.

# CHAPTER 6

# ACTIVE SUPPRESSION OF THE WHIRLING MOTION IN BTA DEEP HOLE BORING PROCESS

In the previous chapter an off line modeling of the machining parameters in deep hole boring process was carried out to reduce the outcome surface irregularities by obtaining the best combinations of the cutting parameters using fuzzy logic modeling with subtractive clustering technique and ANFIS. In this chapter an active suppression of the whirling motion will be carried out. A continuation of the model seen in chapter 2 including the control forces is presented in this chapter. The electrodynamic forces are added to the model in order to predict the action of suppression of the whirling motion due to these forces. Then, experiments are conducted using two electrodynamic exciters directly on the boring bar in deep hole boring process to validate the model.

## 6.1 The cutting model with electrodynamic forces

In chapter 2, The electrodynamic control forces were not included in the model in order of the boring bar-workpiece system. In this section these two electrodynamic control forces will be included to see the effect of these suppressing forces on the system.

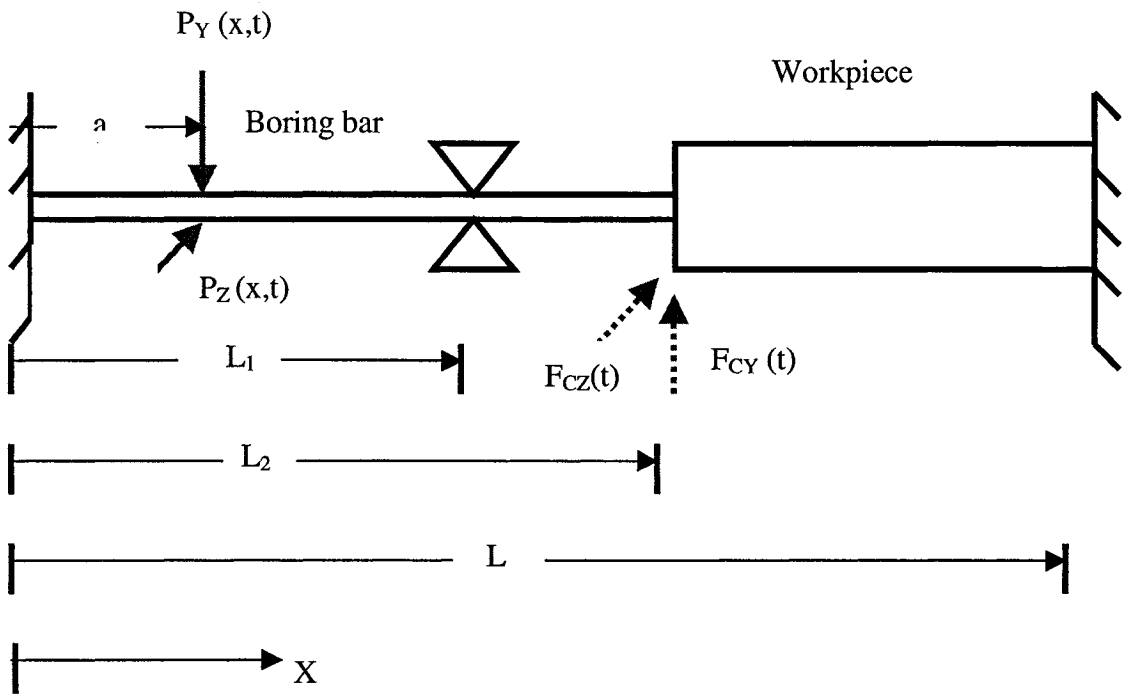


Fig. 6.1: Electrodynamic forces $P_Y(x,t)$ and $P_Z(x,t)$ acting on the boring bar-workpiece system.

A complete overview of the solution is presented in chapter 2. The equations of motion in the Y and Z directions are:

$$\ddot{\eta}_{yi}(t)+2\varsigma\beta_{1i}^2\eta_{yi}(t)+\beta_{1i}^4\eta_{yi}(t) = N_{yi}(t)$$

$$\ddot{\eta}_{yi}(t)+2\varsigma\beta_{2i}^2\dot{\eta}_{yi}(t)+\beta_{2i}^4\eta_{yi}(t)=N_{yi}(t) \qquad (6.1)$$

$$\ddot{\eta}_{yi}(t)+2\varsigma\beta_{3i}^2\dot{\eta}_{yi}(t)+\beta_{3i}^4\eta_{yi}(t)=N_{yi}(t)$$

In Z direction:

$$\ddot{\eta}_{z\,i}(t)+2\varsigma\beta_{1i}^{2}\,\eta_{z\,i}(t)+\beta_{1i}^{4}\,\eta_{z\,i}(t)=N_{z\,i}(t)$$

$$\ddot{\eta}_{z\,i}(t)+2\varsigma\beta_{2i}^{2}\,\dot{\eta}_{zi}(t)+\beta_{2i}^{4}\,\eta_{zi}(t)=N_{zi}(t) \qquad (6.2)$$

$$\ddot{\eta}_{z\,i}(t)+2\varsigma\beta_{3i}^{2}\,\dot{\eta}_{zi}(t)+\beta_{3i}^{4}\,\eta_{zi}(t)=N_{zi}(t)$$

where,

$$N_{y\,i}(t)=F_{y}(t)\left[\int_{0}^{\bar{L}_1} v_{1\,yi}(\bar{x})\,d\bar{x}+\int_{\bar{L}_1}^{\bar{L}_2} v_{2\,yi}(\bar{x})\,d\bar{x}+\int_{\bar{L}_2}^{1} v_{3\,yi}(\bar{x})\,d\bar{x}\right]$$

$$N_{z\,i}(t)=F_{z}(t)\left[\int_{0}^{\bar{L}_1} v_{1\,zi}(\bar{x})\,d\bar{x}+\int_{\bar{L}_1}^{\bar{L}_2} v_{2\,zi}(\bar{x})\,d\bar{x}+\int_{\bar{L}_2}^{1} v_{3\,zi}(\bar{x})\,d\bar{x}\right]$$

The force term with the electrodynamic suppression forces is:

$$F_{y}(t)=\frac{1}{EI_{1}}v_{1\,yi}(a)P_{y}(t) \qquad 0\langle\bar{X}\langle\bar{L}_1$$

$$=-\left[G_{2\,y\,i}^{*}F_{cy}(t)+G_{2\,y\,i}\ddot{F}_{cy}(t)\right] \qquad \bar{L}_1\langle\bar{X}\langle\bar{L}_2$$

$$=-\left[G_{3\,y\,i}^{*}F_{cy}(t)+G_{3\,y\,i}\ddot{F}_{cy}(t)\right] \qquad \bar{L}_2\langle\bar{X}\langle 1$$

and

$$F_z(t) = \frac{1}{EI_1} v_{1zi}(a) P_z(t) \qquad 0 \langle \overline{X} \langle \overline{L}_1$$

$$= -\left[G^*_{2zi} F_{cy}(t) + G_{2zi} \ddot{F}_{cz}(t)\right] \qquad \overline{L}_1 \langle \overline{X} \langle \overline{L}_2$$

$$= -\left[G^*_{3zi} F_{cz}(t) + G_{3zi} \ddot{F}_{cz}(t)\right] \qquad \overline{L}_2 \langle \overline{X} \langle 1$$

The final solution with the electrodynamic forces in the Y direction, using the integrals in Appendix A, is

$$W_{1y}(\overline{x}, t) = \sum_{i=1}^{\infty} v_{y1i}(\overline{x}) \left\{ \frac{1}{\omega_i} \int_0^t \left( \begin{array}{l} \frac{1}{EI_1} v_{1yi}(\overline{a}) P_y(\tau) \\ -\left[G^*_{2yi} F_{cy}(\tau) + G_{2yi} \ddot{F}_{cy}(\tau)\right] v_{2yi}(\overline{x}) d\overline{x} \\ -\left[G^*_{3yi} F_{cy}(\tau) + G_{3yi} \ddot{F}_{cy}(\tau)\right] v_{3yi}(\overline{x}) d\overline{x} \end{array} \right) e^{-\varsigma w_i (t-\tau)} \sin \omega_i (t-\tau) d\tau \right\},$$

in the range of $0 \langle \overline{X} \langle \overline{L}_1$

$$W_{2y}(\overline{x}, t) = \sum_{i=1}^{\infty} v_{y2i}(\overline{x}) \left\{ \frac{1}{\omega_i} \int_0^t \left( \begin{array}{l} \frac{1}{EI_1} v_{1yi}(\overline{a}) P_y(\tau) \\ -\left[G^*_{2yi} F_{cy}(\tau) + G_{2yi} \ddot{F}_{cy}(\tau)\right] v_{2yi}(\overline{x}) d\overline{x} \\ -\left[G^*_{3yi} F_{cy}(\tau) + G_{3yi} \ddot{F}_{cy}(\tau)\right] v_{3yi}(\overline{x}) d\overline{x} \end{array} \right) e^{-\varsigma w_i (t-\tau)} \sin \omega_i (t-\tau) d\tau \right\},$$

$+ g_2(\overline{x}) F_{cy}(t)$, in the range of $\overline{L}_1 \langle \overline{X} \langle \overline{L}_2$

$$W_{3y}(\bar{x},t)=\sum_{i=1}^{\infty}v_{y3i}(\bar{x})\left(\frac{1}{\omega_i}\int_0^t\left(\begin{array}{l}\dfrac{1}{EI_1}v_{1yi}(\bar{a})P_y(\tau)\\ -\left[G^*_{2yi}F_{cy}(\tau)+G_{2yi}\ddot{F}_{cy}(\tau)\right]v_{2yi}(\bar{x})d\bar{x}\\ -\left[G^*_{3yi}F_{cy}(\tau)+G_{3yi}\ddot{F}_{cy}(\tau)\right]v_{3yi}(\bar{x})d\bar{x}\end{array}\right)e^{-\varsigma w_i(t-\tau)}\sin\omega_i(t-\tau)d\tau\right),$$

$$+g_3(\bar{x})F_{cy}(t),\ \text{in the range of}\ \ \bar{L}_2\langle\bar{X}\langle 1$$

and in the Z direction is :

$$W_{1z}(\bar{x},t)=\sum_{i=1}^{\infty}v_{z1i}(\bar{x})\left(\frac{1}{\omega_i}\int_0^t\left(\begin{array}{l}\dfrac{1}{EI_1}v_{1zi}(\bar{a})P_z(\tau)\\ -\left[G^*_{2zi}F_{cz}(\tau)+G_{2zi}\ddot{F}_{cz}(\tau)\right]v_{2zi}(\bar{x})d\bar{x}\\ -\left[G^*_{3zi}F_{cz}(\tau)+G_{3zi}\ddot{F}_{cz}(\tau)\right]v_{3zi}(\bar{x})d\bar{x}\end{array}\right)e^{-\varsigma w_i(t-\tau)}\sin\omega_i(t-\tau)d\tau\right),$$

in the range of $0\langle\bar{X}\langle\bar{L}_1$

$$W_{2z}(\bar{x},t)=\sum_{i=1}^{\infty}v_{z2i}(\bar{x})\left(\frac{1}{\omega_i}\int_0^t\left(\begin{array}{l}\dfrac{1}{EI_1}v_{1zi}(\bar{a})P_z(\tau)\\ -\left[G^*_{2zi}F_{cz}(\tau)+G_{2zi}\ddot{F}_{cz}(\tau)\right]v_{2zi}(\bar{x})d\bar{x}\\ -\left[G^*_{3zi}F_{cz}(\tau)+G_{3zi}\ddot{F}_{cz}(\tau)\right]v_{3zi}(\bar{x})d\bar{x}\end{array}\right)e^{-\varsigma w_i(t-\tau)}\sin\omega_i(t-\tau)d\tau\right),$$

$$+g_2(\bar{x})F_{cz}(t),\ \text{in the range of}\ \ \bar{L}_1\langle\bar{X}\langle\bar{L}_2$$

$$W_{3z}(\bar{x},t)=\sum_{i=1}^{\infty}v_{z3i}(\bar{x})\left(\frac{1}{\omega_i}\int_0^t\left(\begin{array}{l}\dfrac{1}{EI_1}v_{1zi}(\bar{a})P_z(\tau)\\ +\displaystyle\int_{\bar{L}_1}^{\bar{L}_2}-\left[G^*_{2zi}F_{cz}(\tau)+G_{2zi}\ddot{F}_{cz}(\tau)\right]v_{2zi}(\bar{x})d\bar{x}\\ +\displaystyle\int_{\bar{L}_2}^{1}-\left[G^*_{3zi}F_{cz}(\tau)+G_{3zi}\ddot{F}_{cz}(\tau)\right]v_{3zi}(\bar{x})d\bar{x}\end{array}\right)e^{-\varsigma w_i(t-\tau)}\sin\omega_i(t-\tau)d\tau\right),$$

$$+g_3(\bar{x})F_{cz}(t),\ \text{in the range of}\ \ \bar{L}_2\langle\bar{X}\langle 1$$

where,

$$\bar{a}=0.1789$$

$$P_y(t)=P_{0y}\cos(\omega t+\theta)$$

$$P_z(t)=P_{0z}\sin(\omega t+\theta)$$

$$F_{cy}(t) = \overline{F}_c + F_{c0}\cos(\omega t)$$

$$F_{cz}(t) = \overline{F}_c + F_{c0}\sin(\omega t)$$

The whirling motions at different sections of the boring bar-workpiece system are plotted at speed =60 rad/sec and with the external forces in the form of

$$P_y(t) = P_{0y}\cos(60t + \pi)$$

$$P_z(t) = P_{0z}\sin(60t + \pi)$$

Fig. 6.2 and 6.3 shows the plots of the two signals in the Y and Z coordinates and the corresponding whirling motion with and without the active suppression forces at $\overline{L}_1 = 0.41$. Fig. 6.4 is a one-figure plot of the system with and without the active suppression forces at $\overline{L}_1 = 0.41$, $\overline{L}_2 = 0.81$ and $\overline{L} = 0.91$.

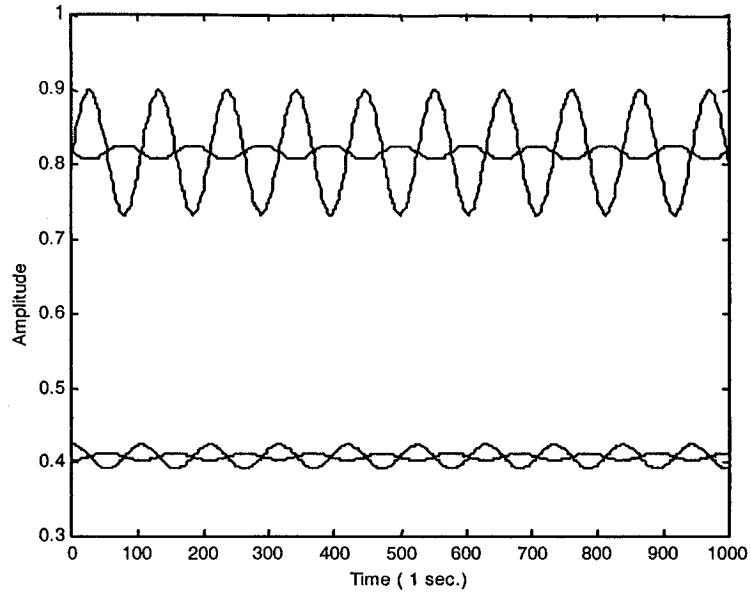


Fig. 6.2: Vibration of the bar in the Y and Z coordinates with and without the active suppression force at $\overline{L}_1 = 0.41$.

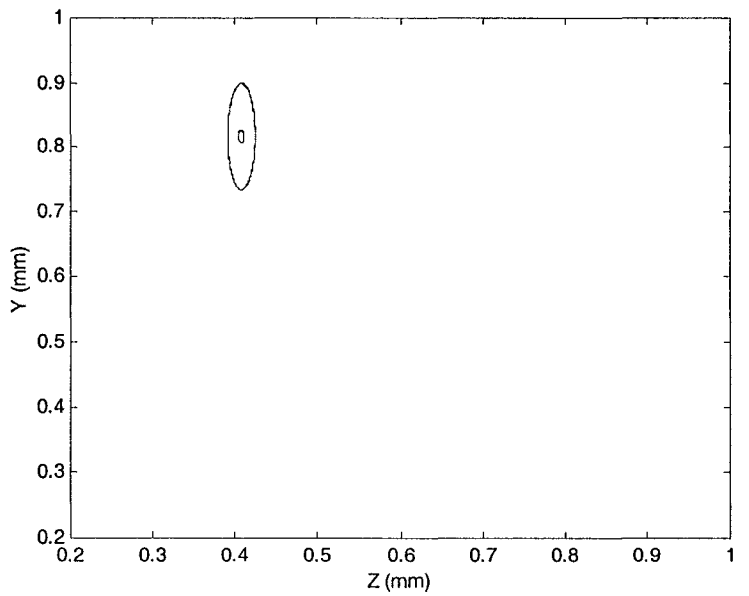


Fig. 6.3: Whirling motion with (____) and without (.....) the active suppression forces at $\overline{L}_1 = 0.41$.

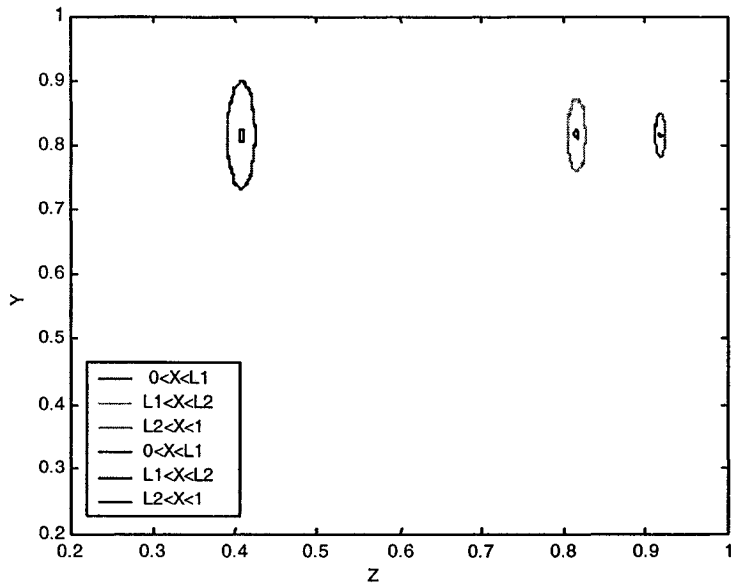


Fig. 6.4:Whirling motion with (____) and without (.....) the active suppression forces at $\overline{L}_1 = 0.41$, $\overline{L}_2 = 0.81$ and $\overline{L} = 0.91$.

## 6.2 Experimental set up

Active suppression of the whirling motion of deep hole boring-cutting head system is carried out experimentally. None of the previous studies reported on active suppression of whirling vibrations in the deep hole boring systems. Non-contacting type proximity pickups were used to measure the whirling motion of the boring bar before and after the experiment in order to compare between them. Two electrodynamic exciters were used with two force sensors or load cells to counter the vibrations of the bar. A schematic representation of the tools used in the active suppression of the whirling motion ar shown in Fig. 6.5.

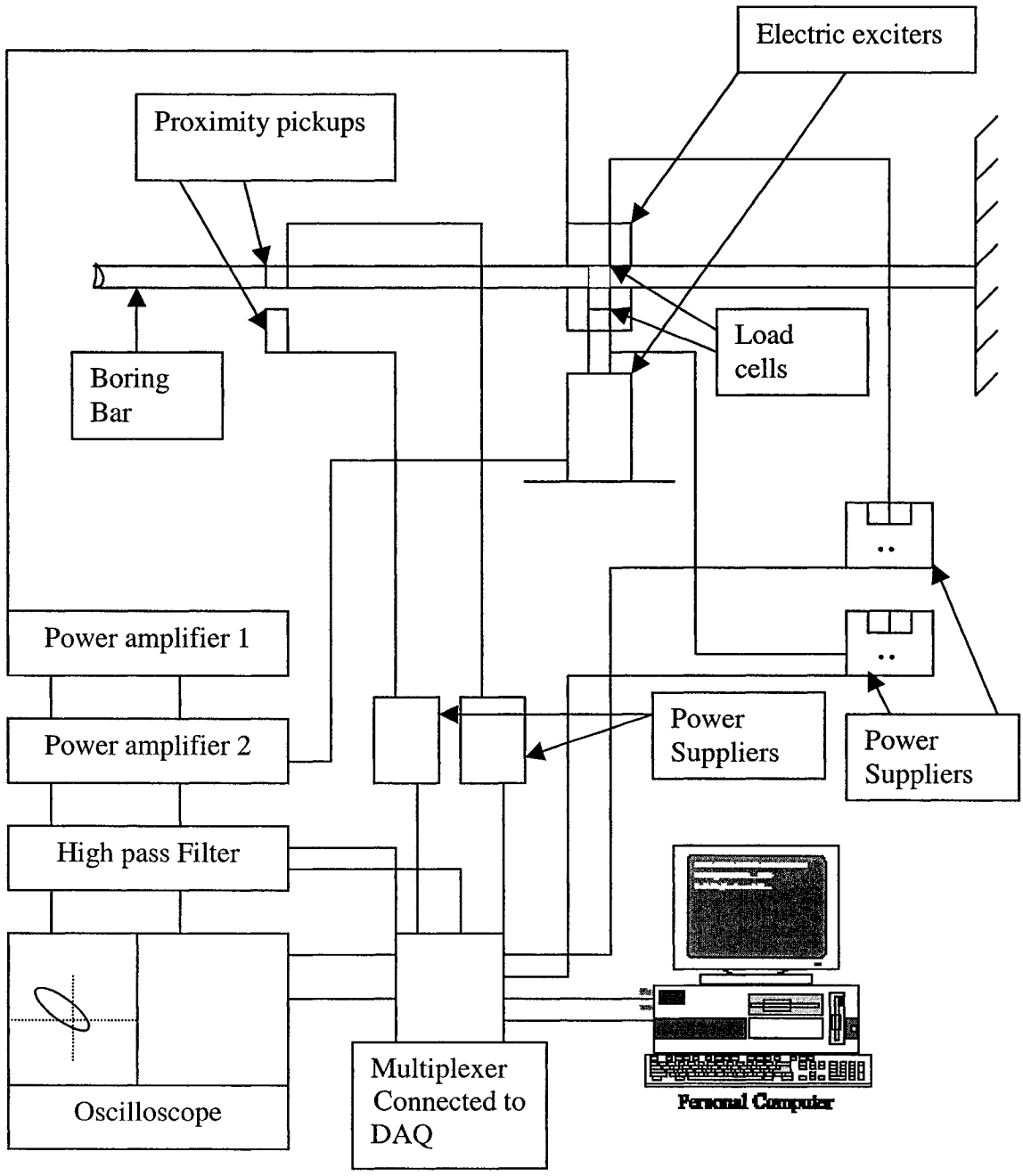


Fig. 6.5: A schematic representation of the tools used in the active suppression of the whirling motion.

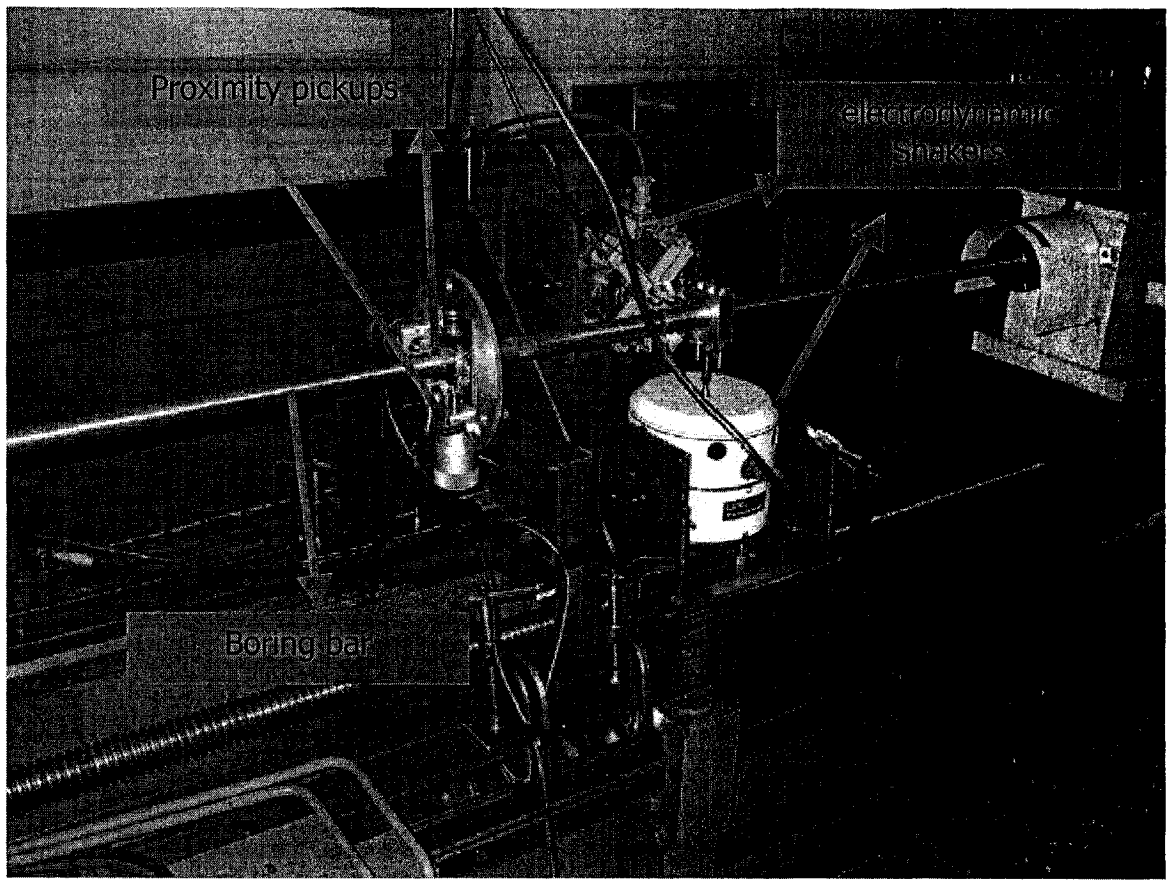


Fig. 6.6: A photograph of the equipments used in the active suppression of the whirling motion.

Fig. 6.6 shows the schematic of the experimental set up, which consists of the proximity sensors, the data acquisition system, the two electromagnetic shakers, the power amplifiers and the oscilloscope. Fig. 6.6 shows a photograph of the two electromagnetic shakers and the set up for the proximity pickups. A close-up figure of the housing, the bushing and the load cells are shown in Fig. 6.7. The bushing is of lubricated sintered bronze so that the boring bar will rotate and slide freely through it.

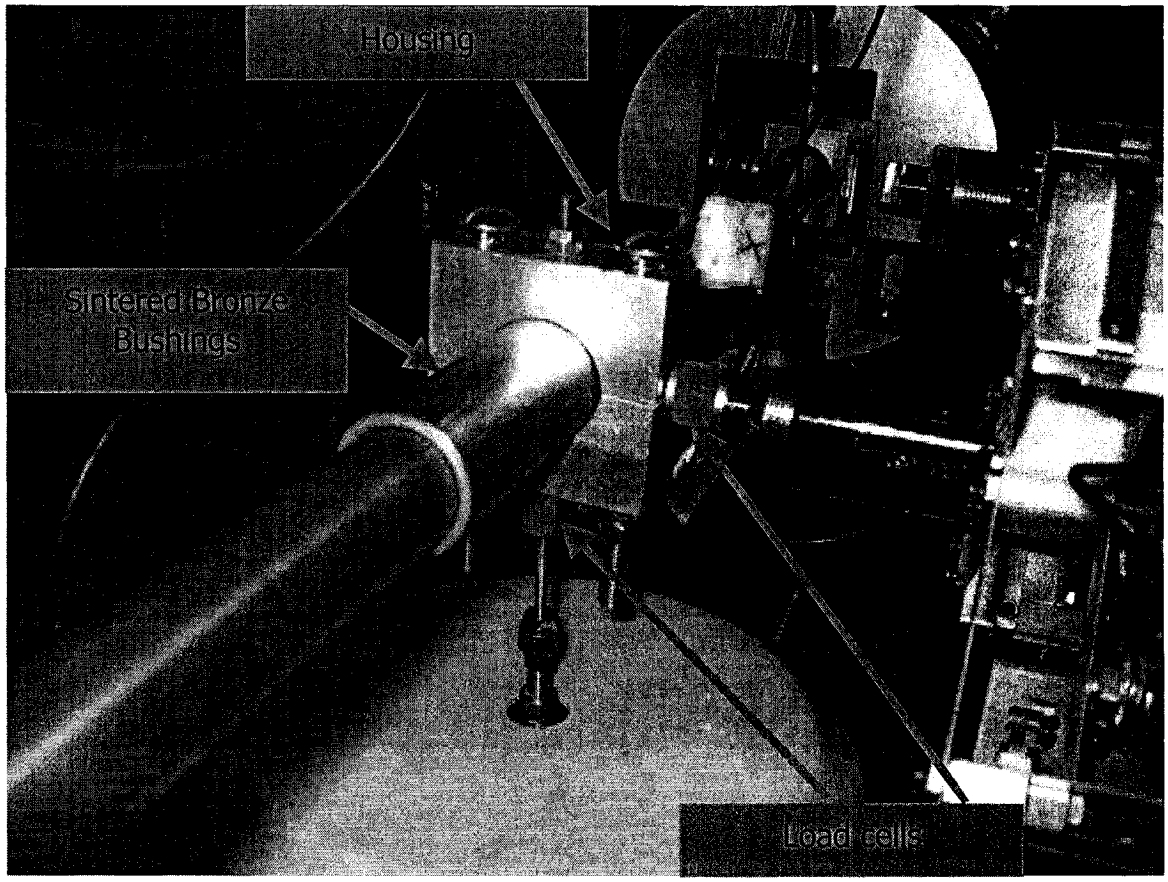


Fig. 6.7: photograph of the housing arrangement used in the active suppression of the whirling motion.

### 6.2.1 Calibration of the proximity pickups

The proximity pickups were calibrated again following the procedure explained in chapter 3. The two calibration figures are shown in Fig. 6.8.

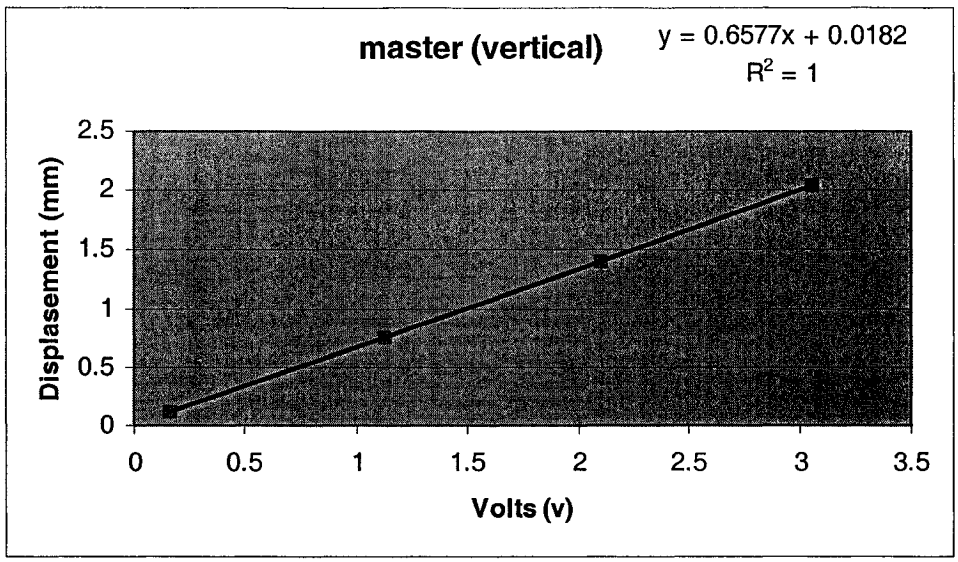


(a)

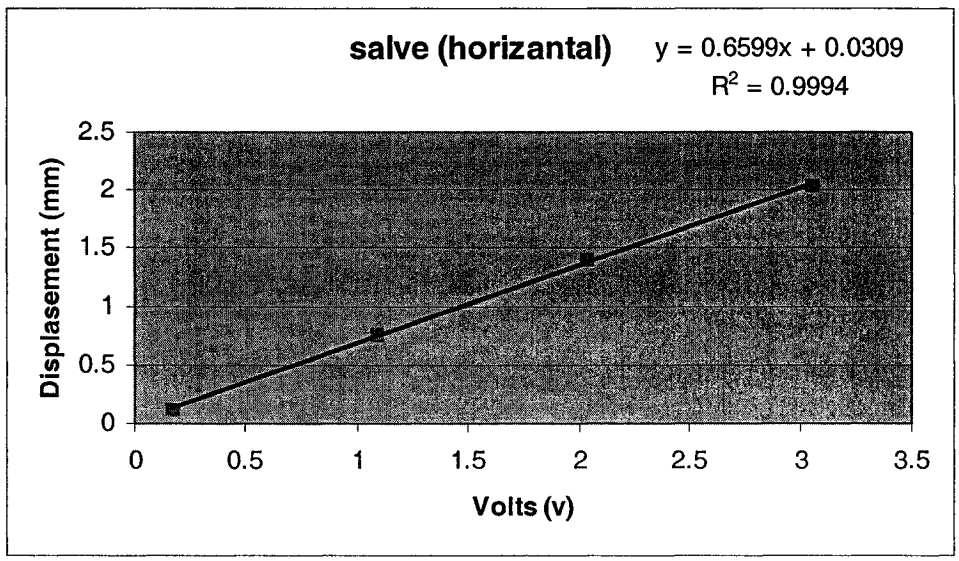


(b)

Fig. 6.8: Calibration figures for the proximity pick ups sensors, (a) the master or the vertical sensor, (b) The slave or the horizontal sensor.

## 6.3 Active vibration control scheme

### - Sensors location

The original or primary excitation in the deep hole boring which arises from the cutting process cannot be observed directly. The response of the boring bar is a measure of the tool-workpiece interaction while drilling and consequently such vibrations should be kept to a minimum.

Due to the movement of the whole feed unit and the special features of the BTA deep hole boring structure around the stuffing box, the location of the sensors were chosen close to the cutting tool-workpiece interaction.

The two electrodynamic shakers introduce the control forces to counteract the vibration resulting from the cutting action. Due to the size and weight of the shakers, a suitably designed fixture was used to keep it steady and as close as possible to the sensors.

### - System transfer function

To obtain the transfer function of the mechanical system and the controller, we need to find the Laplace transform of the equations of motion and solve the resulting algebraic equations for the relationship between the input and the output. In many control systems the system equation can be written so that their components do not interact except by

having the input of one part being the output of another part. In these cases it is easy to draw the block diagram that represents the mathematical relationships in a similar manner to that used for the component block diagram. The transfer function of each component is placed in a box, and arrows indicate the input-output relationships between components, as seen in Fig. 6.9 and Fig. 6.10.

The sensors in the Y –Z directions will measure the total response of the system, while the net excitations is the difference between the primary and secondary excitations.

To set the problem in general context, consider the system shown in Fig. 6.10, where:

$r_y$, $r_z$ : The reference signals in the Y and Z directions

$e_y$, $e_z$ : The error signals in the Y and Z directions

$H_1(s)$, $H_2(s)$ : The transfer function of the electrodynamic shakers

$F_{sy}(s)$, $F_{sz}(s)$ : The secondary excitations in the Y and Z directions

$\overline{F}_p(s)$ : The primary excitations

$\overline{\overline{G}}(s)$ : The transfer function of the mechanical system

$Y(s)$, $Z(s)$ : The output signals

$K_1$, $K_2$ : The gain

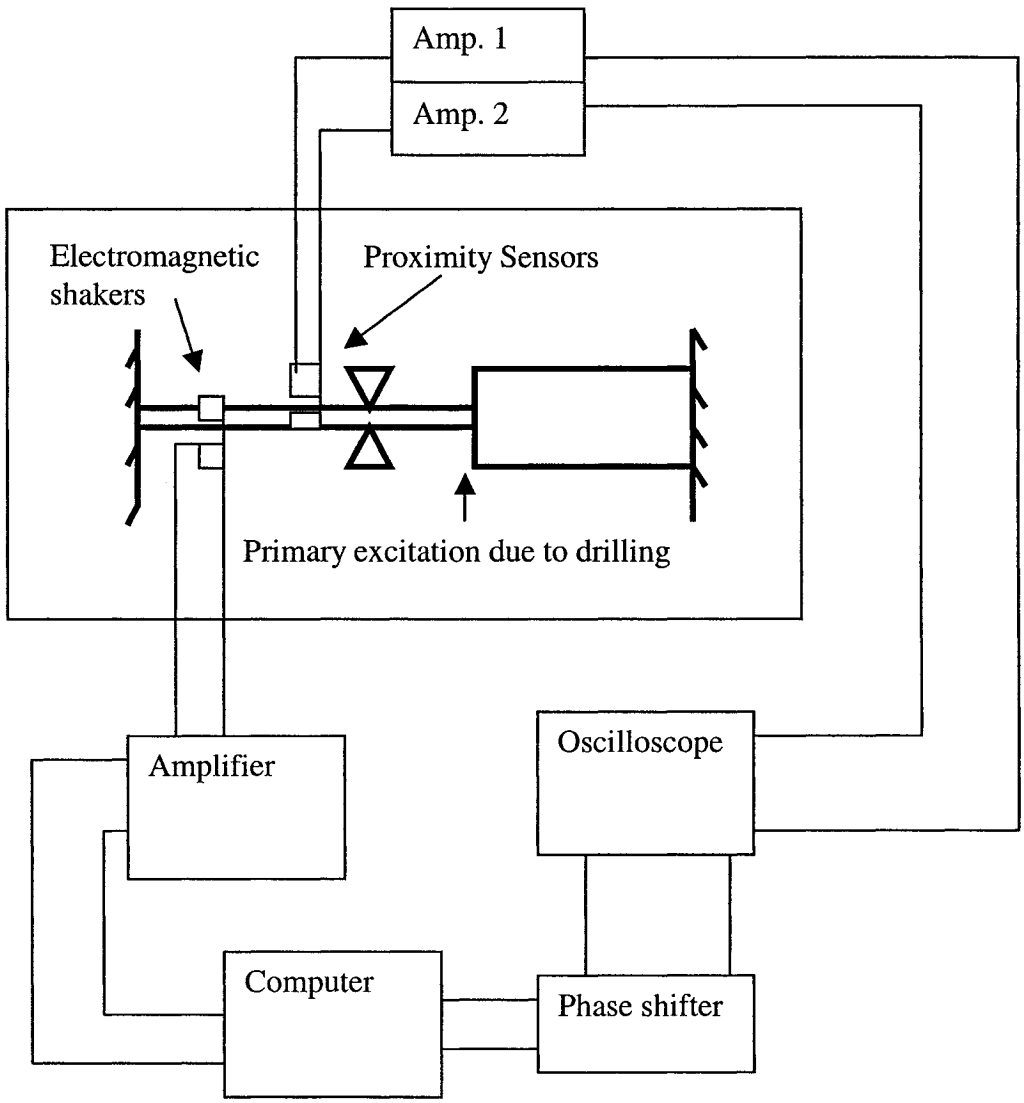


Fig. 6.9: A schematic presentation of the primary and secondary excitation of the system under study.

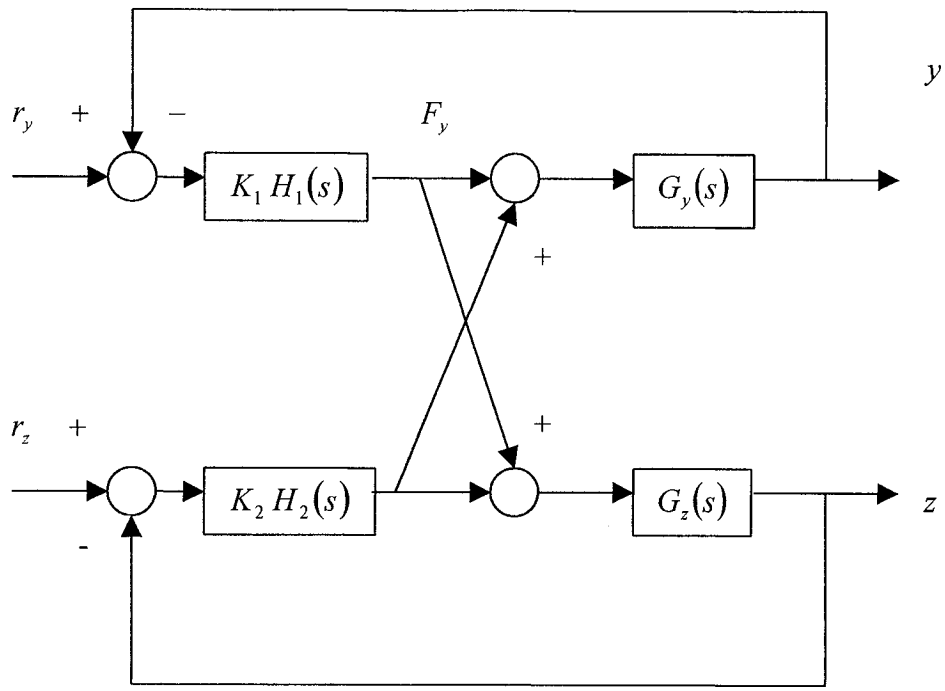


Fig. 6.10: The transfer function of the mechanical system and the controller.

Using Maison rule [151], we find the transfer function of the system as following:

$$Y(s) = \frac{[G_y(s)K_1H_1(s)][1+G_z(s)K_2H_2(s)]}{1+G_y(s)K_1H_1(s)+G_z(s)K_2H_2(s)+G_y(s)G_z(s)K_1H_1(s)K_2H_2(s)} r_y + \frac{G_y(s)K_2H_2(s)[G_z(s)K_2H_2(s)]}{1+G_y(s)K_1H_1(s)+G_z(s)K_2H_2(s)+G_y(s)G_z(s)K_1H_1(s)K_2H_2(s)} r_z \quad (6.3)$$

$$Z(s) = \frac{[G_z(s)K_2H_2(s)][1+G_y(s)K_1H_1(s)]}{1+G_y(s)K_1H_1(s)+G_z(s)K_2H_2(s)+G_y(s)G_z(s)K_1H_1(s)K_2H_2(s)} r_z + \frac{G_z(s)K_1H_1(s)[G_y(s)K_1H_1(s)]}{1+G_y(s)K_1H_1(s)+G_z(s)K_2H_2(s)+G_y(s)G_z(s)K_1H_1(s)K_2H_2(s)} r_y \quad (6.4)$$

which is a closed loop characteristic of any mechanical system and feedback controller .

Now if:

$$\left|1+G_y(j\omega)K_1H_1(j\omega)+G_z(j\omega)K_2H_2(j\omega)+G_y(j\omega)G_z(j\omega)K_1H_1(j\omega)K_2H_2(j\omega)\right| \gg 1$$

The response of the mechanical system is thus significantly reduced in this frequency region by the action of the feedback controller.

The form of the feedback controller should be known in order to determine the closed loop response of the system. The secondary force of the electronic response controller consists of three components, which are proportional to the acceleration, velocity and displacement of the mass with the gain constants $g_a$ , $g_v$ and $g_d$. But in practical case there is only one transducer to measure the acceleration, for example, and electronic integrators proportional to velocity and displacement obtain the others.

In the experiments, the simplest type of controller is used which depends on the operator to read and evaluate the feed back signal and adjust the amplifier signal input voltage. The approach followed to suppress the whirling motion is as if we have a sine wave signal generator and an accelerometer monitored by a voltmeter. It is left to the operator to manually make the necessary gain compensation for changes in frequency or desired level specification. The calibrated signals from the sensors which is seen on the oscilloscope made it easier to adjust the gain manually. Further extensive research study should be done to have a more sophisticated shaker controller.

## -Time delay:

Time delays often arise in control systems, both from delays in the process itself and from delays in the processing of the sensed signals. There is also a small time delay in any digital controller system due to the cycle time of the computer and the fact that the data is processed at discrete intervals. In the time domain it is $F(t-\tau)$, $\tau \geq 0$ in s domain it is $F(s)\,e^{-s\tau}$. This time delay or the unmodelled phase shift affects the performance of the feedback controller.

## - Electrodynamic shaker specifications

Generally, the structure of an electrodynamic shaker is similar to that of a common loudspeaker. In the shaker there is a coil, suspended in a fixed radial magnetic field. When the current is passing through this coil, an axial force is produced in proportion to

the current and this is transmitted to a table structure where the object is fixed. The force provided by the shaker is proportional to the magnetic flux passing through the coil, to the current flowing through the coil and the length of the wire.

The shaker type used in the experiment is LDS-V455/6 with a maximum force of 489 N, and a maximum continuous system displacement of 19 mm. The sensitivity of the load cells used to drive the shakers was of 44 mV/N (10 mV/Lb) with a low frequency response of 0.0003 Hz and upper frequency limit of 36 KHz.

## 6.4 Active suppression of whirling motion

Active control differs from the usual passive methods, such as a rubber damper between a structure and a frame. The rubber damper simply absorbs the vibrations, and does not directly control the motion of the structure. Active control, however, generates a response to counteract the unwanted vibration. Sensors in the active control system measure the vibrations and this information is used to direct the force sensors to apply forces on the structure and counteract the vibration and suppress them.

A lubricated sintered bronze bushing with a sliding fit was introduced into the boring bar so that it could rotate and slide freely through the bushings without exerting axial force on the exciter coupling rods. The bronze bushing also fitted from outside with a housing, which is, connected with the exciter coupling rods in the Z and Y directions.

As seen in Fig. 6.7, two load cells were placed between the housing and the coupling rods of the exciters. The housing was attached to the coupling rods in order to ensure that the exciters support the housing, and the weight of the housing does not affect the boring bar.

The complete experimental arrangement is shown in Fig. 6.5. The experimental equipment can be divided into two functional groups, the primary excitation system, i.e. the electrodynamic exciters and the displacement measurement system. The signal was acquired by the data acquisition system by means of the proximity pickups and then inverted and amplified to drive the electrodynamics exciters as shown in Fig. 6.6. The exciters acted on the housing through force transducers or load cells, and the magnitudes

of the forces were recorded using additional two channels in the labview from the data acquisition system.

The displacement signals from the two proximity pickups in Fig. 6.6 were passed to a high pass filter and to amplifiers, inverted and fed back to drive the electrodynamic exciters so as to minimize the displacement measured by the proximity sensors by counteracting the unwanted vibrations. The magnitude of the boring bar displacement and the force used to suppress the motion were recorded on a personal computer.

Figs. 6.6 - 6.7 show the photographs of the experimental setup. In Fig. 6.6, the housing and the bushing can be seen in the background with the proximity pickups, and the recording equipment, in foreground. Two electrodynamic exciters primary sources can be seen, as well as the housing and the bushing mounted across the boring bar. The housing set-up is shown in Fig. 6.7, with the two load cells.

The experiments were carried out with three speeds of rotation of the boring bar, 1040, 1237 and 1440 rpm. An experiment to suppress the whirling motion while cutting was done also. The cutting parameters chosen were at a speed of 1040 rpm, feed of 71 mm/min and 20 G/min starting from the beginning of the workpiece until 3.93 inches of tool penetration. For each experiment 10,000 data points were collected in 1 second. The time separation between each data point is 0.0001 second. At the minimum speed of 1040 rpm (17.33 Hz), 577 points are needed to complete one cycle. At the maximum speed

1440 rpm (24 Hz), 417 points is needed to complete one cycle. Hence, 1000 points were used for each experiment in 0.1 second.

### 6.4.1 Active suppression with free rotation of the boring bar

Fig. 6.11(a) shows the suppressed and unsuppressed whirling motions of the boring bar at 1040 rpm, where a reduction of 52.9 % was achieved in the maximum whirl amplitude. Fig. 6.11(b) shows the corresponding displacement signals from the master and slave sensors before and after suppression. Fig. 6.12 is the force-displacement characteristics for the vertical and horizontal motion. Also, the signal from the two sensors and the two force transducers are shown in Fig. 6.13. The amplitude of the displacement was multiplied by 100 for all force and displacement signals in order to magnify it so that it can be compared with the force signal on the same scale. From Fig. 6.13, it is found that when we take the difference between the two periods, the phase shift between the displacement and force in the vertical direction is 2.23° and 1.398° in the horizontal direction.

Fig. 6.14(a) shows the suppressed and unsuppressed whirling motion of the boring bar at 1237 rpm where a reduction of 69.2 % was achieved in the maximum whirl amplitude. The signals acquired from the two proximity pickups before and after applying the force from the two exciters are shown in Fig. 6.14(b). The force-displacement characteristics for the vertical and horizontal motion at this speed of rotation are shown in Fig. 6.15. Also, the signal form the two sensors and the two force transducers are shown in Fig.

6.16. From Fig. 6.16, it is found that the phase shift between the displacement and force in the vertical direction is 3.02° and 1.67° in the horizontal direction.

At 1440 rpm, the maximum speed of rotation for the boring bar under study, Fig. 6.17(a) shows the suppressed and unsuppressed whirling motion of the boring bar where a reduction of 75 % was achieved in the maximum whirl amplitude. Fig. 6.17(b) is the displacement signals from the master and slave sensors before and after suppression. Fig. 6.18 is the force-displacement characteristics for the vertical and horizontal motion. Also, the signal form the two sensors and the two force transducers are shown in Fig. 6.19. From Fig. 6.19, it is found that the phase shift between the displacement and force in the vertical direction is 5.72° and 7.63° in the horizontal direction.

From all these Figures it can be concluded that using the two electrodynamic exciters, the active suppression was able to reduce the displacement signal of the boring bar between 52.9-75 % of actual displacement at different speed of rotation. As the speed reaches toword the first natural frequency, the whirl amplitude decreases after suppression. It is not possible to eliminate the whirling motion completely, but it could be reduced as has been done in this research. Any reduction in the whirling motion is quite beneficial in order to improve the surface quality and to increase the life of the boring bar. The maximum force applied by the exciters in these cases was 45 N. Table 6.1 summarizes the whirl amplitude before and after suppression with the reduction percentage in the maximum whirl amplitude.

Table 6.1 The whirl amplitude before and after suppression.

| Speed (rpm) | Whirl radius before suppression (mm) | Whirl radius after suppression (mm) | Percentage of reduction (%) |
|---|---|---|---|
| 1040 | 0.425 | 0.2 | 52.9 |
| 1237 | 0.6 | 0.185 | 69.2 |
| 1440 | 1 | 0.25 | 75 |

### 6.4.2 Active suppression of the whirling motion while cutting

Experiments were carried out to suppress the whirling motion of the boring bar while cutting. The cutting parameters were at speed of 1040 rpm, feed of 71 mm/min and flow rate of 20 G/min. The results after suppression with these cutting parameters were compared with those without suppression under at the same conditions. Fig. 6.20 (a) and (b) shows the whirling motion before and after suppression at 76.2 mm (3 in) length of cut, respectively. The whirl radius before suppression was of 0.4 mm as shown in Fig. 6.20 (a), and of 0.312 mm as shown in Fig. 6.20 (b). A reduction of 22 % was achieved in the maximum whirl amplitude. Fig. 6.21 is all the data point while suppressing starting from the beginning of drilling at 76.2 mm (3 in) and ending at 100 mm (3.93 in). Within a tool penetration of 23.8 mm (from 76.2 mm to 100 mm) the whirl radius was reduced from 0.4 mm to 0.19 mm. A reduction of 52.5 % of the maximum whirl amplitude was achieved while penetrating the workpiece. Fig. 6.22 is a comparison between the power spectral densities before and after suppression at the same cutting parameters. Fig. 6.23 is the power spectral density after 76.2 mm (3 in) of tool penetration with the power

spectral density before suppression to show the continuous suppression of the motion while the tool penetrating the workpiece. Fig. 6.24 is the force-displacement characteristics for the vertical and horizontal motion while drilling the maximum force around 70 N.

## 6.5 Surface roughness

A surface roughness measurement was done on the specimen under active suppression of the whirling motion. Fig. 6.25 Shows the RMS values for the two specimens under the same cutting conditions. The cutting parameters were at speed of 1040 rpm, feed of 71 mm/min and flow rate of 20 G/min. From the Figure it is obvious that the surface roughness is better after applying active suppression. Table 6.2 shows the percentage of reduction in surface roughness at different lengths of the specimen.

Table 6.2 The surface roughness values at different lengths of the specimen before and after suppression.

| Tool penetration (mm) | Roughness before suppression (μm) | Roughness after suppression (μm) | Percentage of reduction (%) |
|---|---|---|---|
| 45 | 1.1 | 0.9 | 18 |
| 55 | 1.2 | 0.77 | 35.83 |
| 68 | 1.09 | 0.7 | 35.77 |

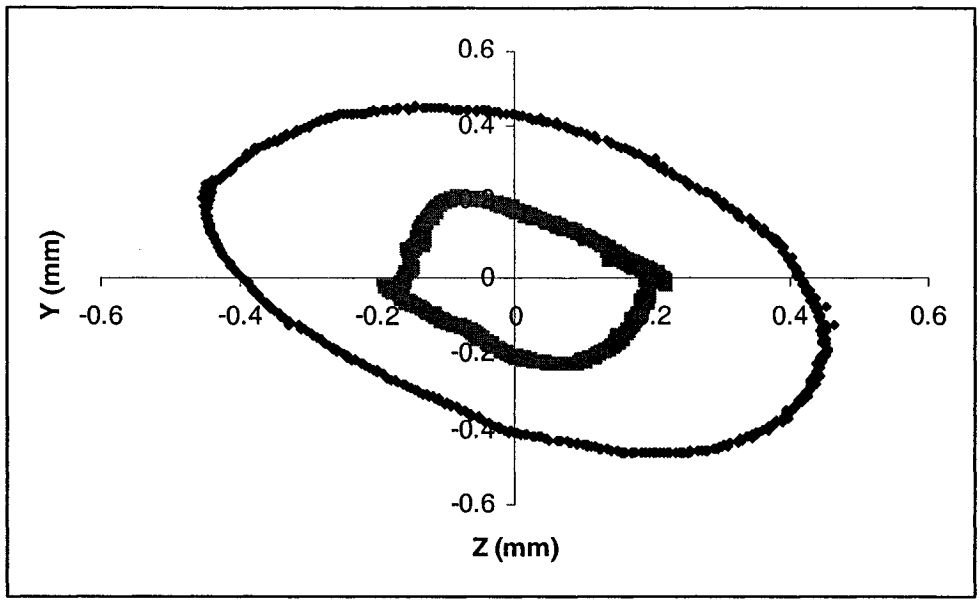


(a)

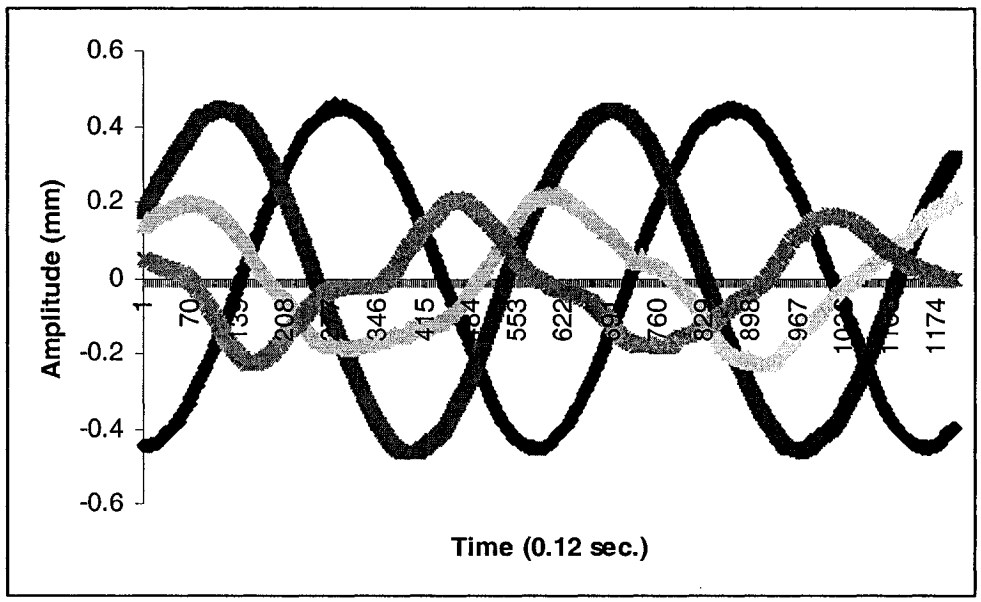


(b)

Fig. 6.11: (_____) Suppressed and (..... ) unsuppressed motion at 1040 rpm, (a) The whirl orbit, (b) The two displacement signals before and after suppression.

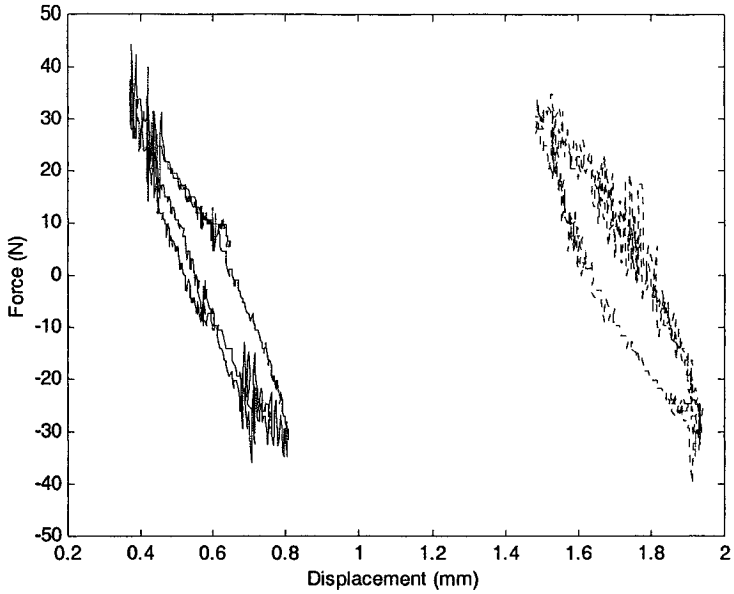


Fig. 6.12: The force displacement characteristics for: (.....) vertical Load cell and (____) horizontal load cell.

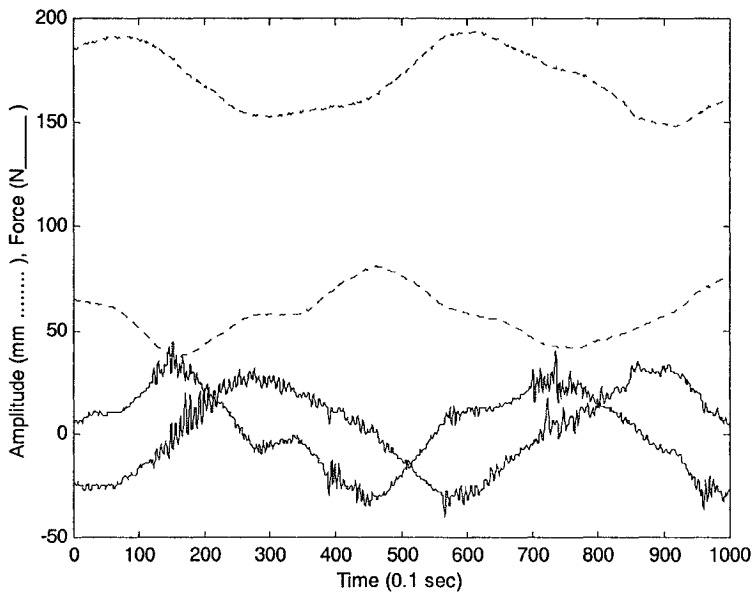


Fig. 6.13: Force and displacement signals: (____) force and (.....) Displacement.

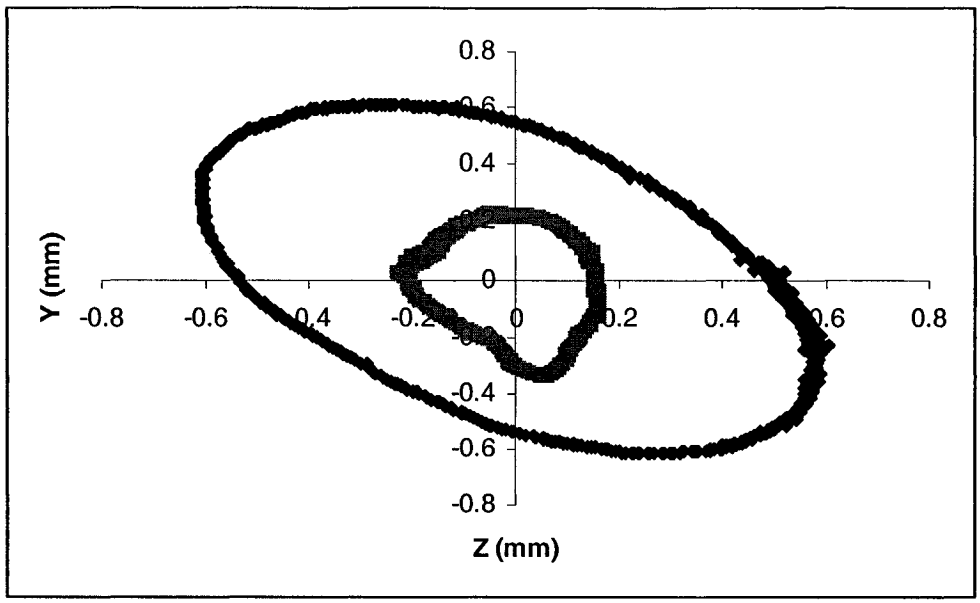


(a)

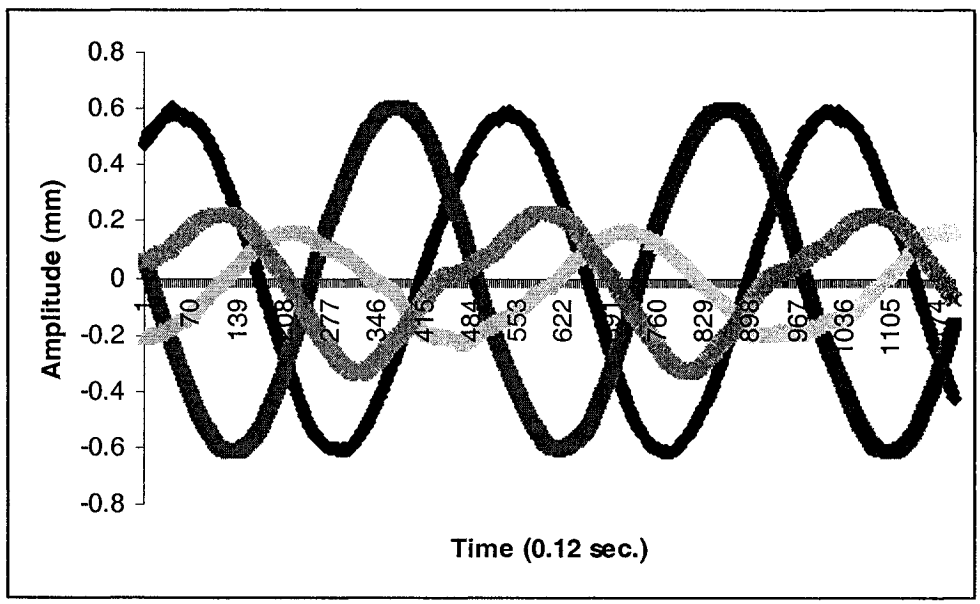


(b)

Fig. 6.14: (_____) Suppressed and (.....) unsuppressed motion at 1237 rpm, (a) The whirl orbit, (b) The two displacement signals before and after suppression.

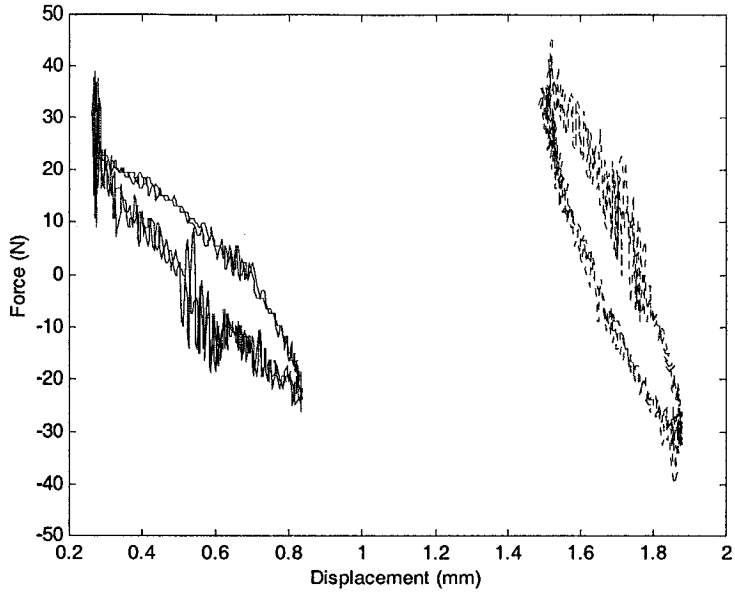


Fig. 6.15: The force displacement characteristics for: (.....) vertical Load cell and (____) horizontal load cell.

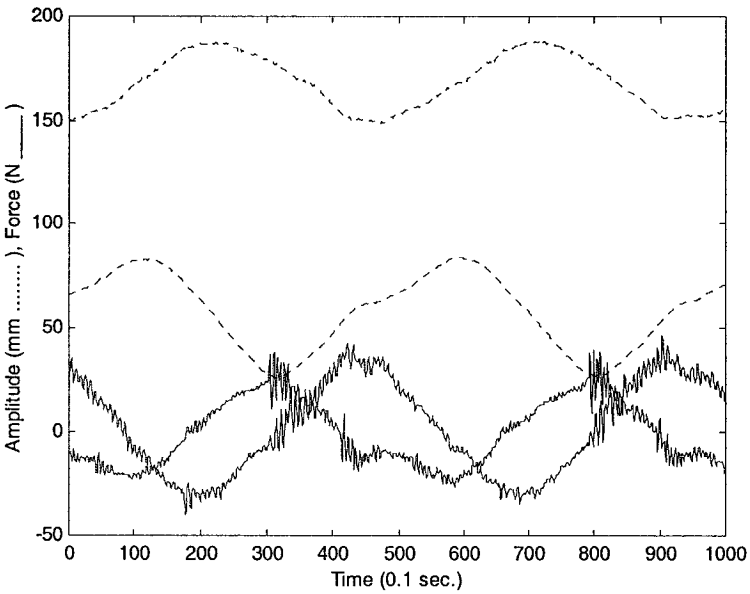


Fig. 6.16: Force and displacement signals: (____) force and (.....) Displacement.

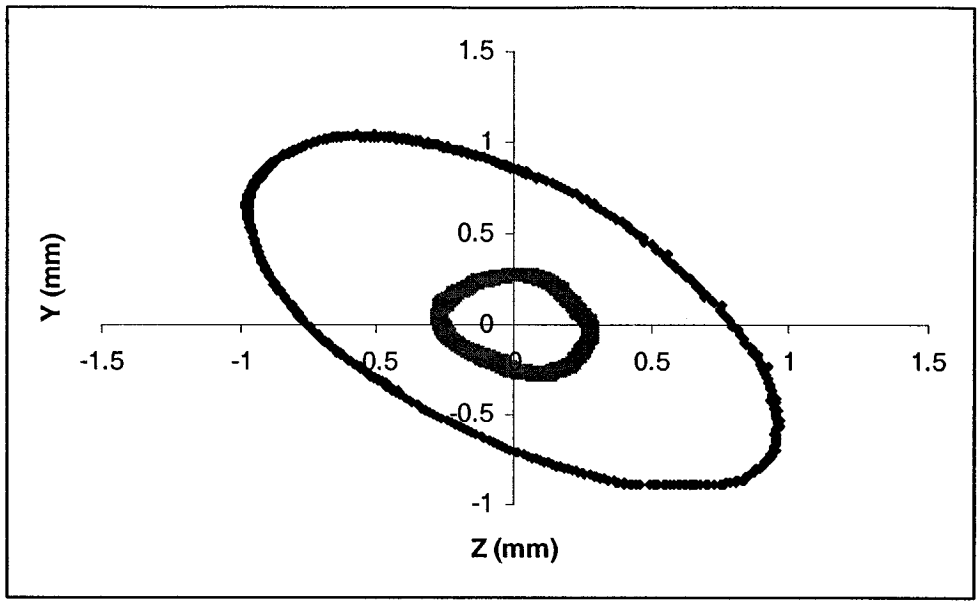


(a)

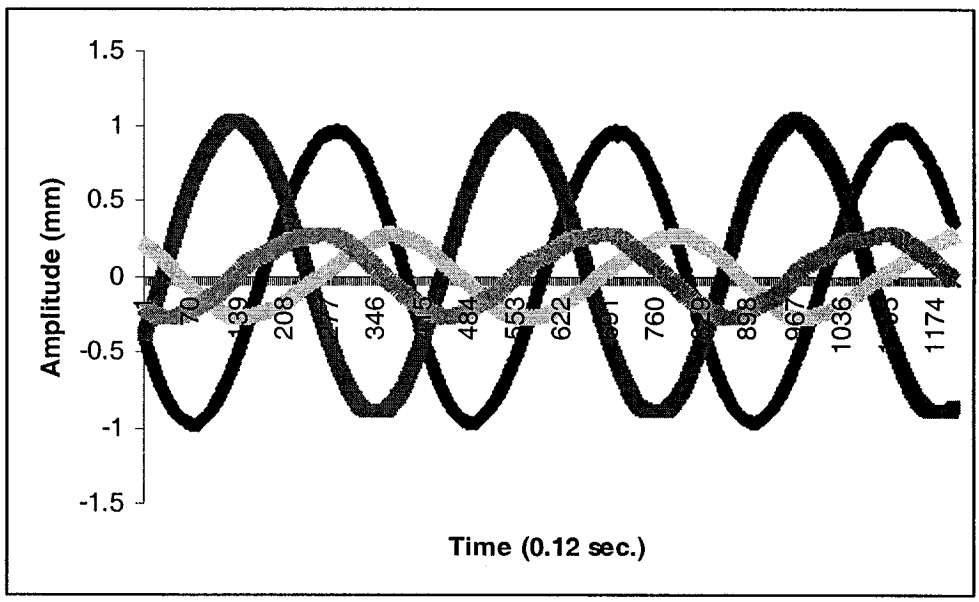


(b)

Fig. 6.17: (_____) Suppressed and (.....) unsuppressed motion at 1440 rpm, (a) The whirl orbit, (b) The two displacement signals before and after suppression.

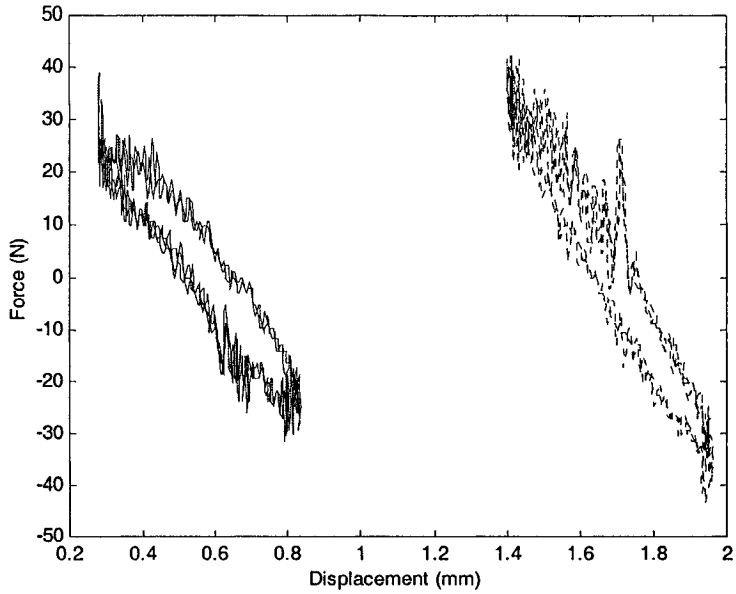


Fig. 6.18: The force displacement characteristics for: (……) vertical Load cell and (____) horizontal load cell.

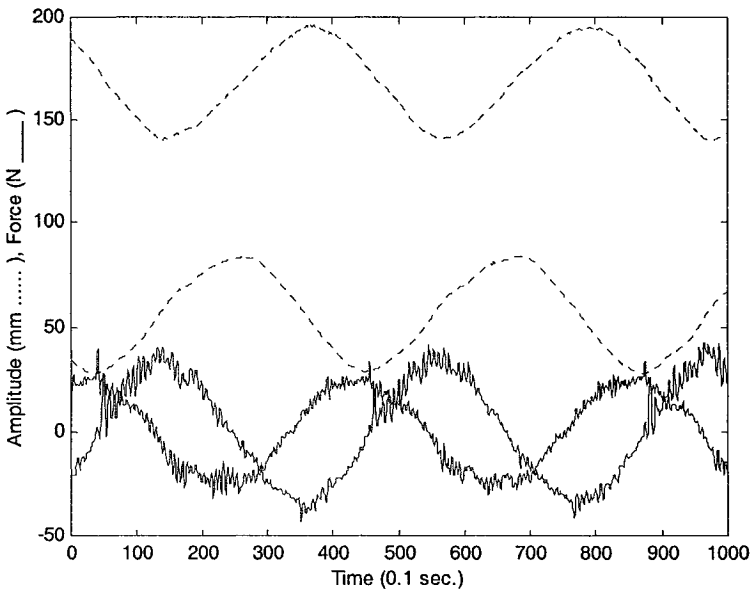


Fig. 6.19: Force and displacement signals: (____) force and (……) Displacement.

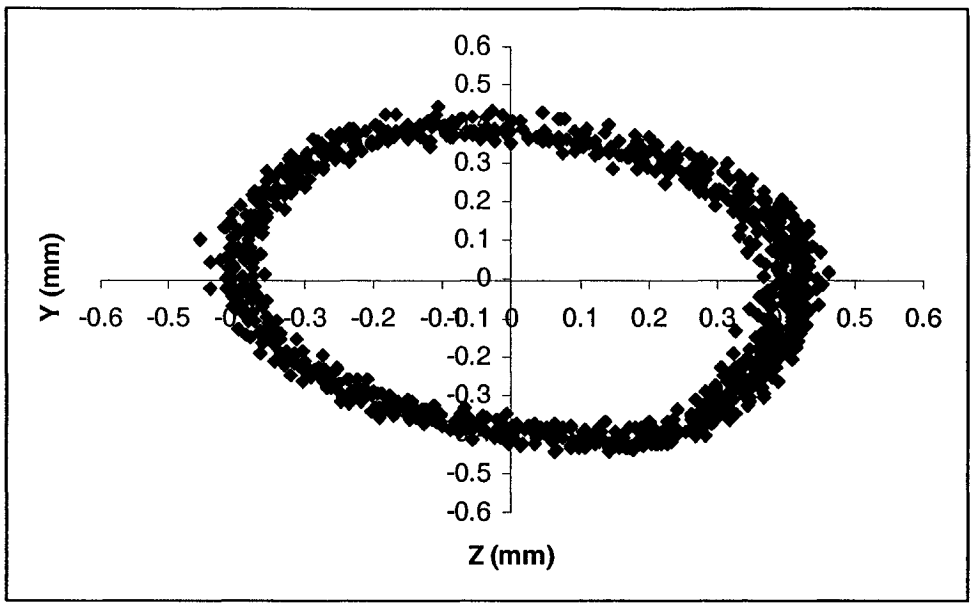


(a)

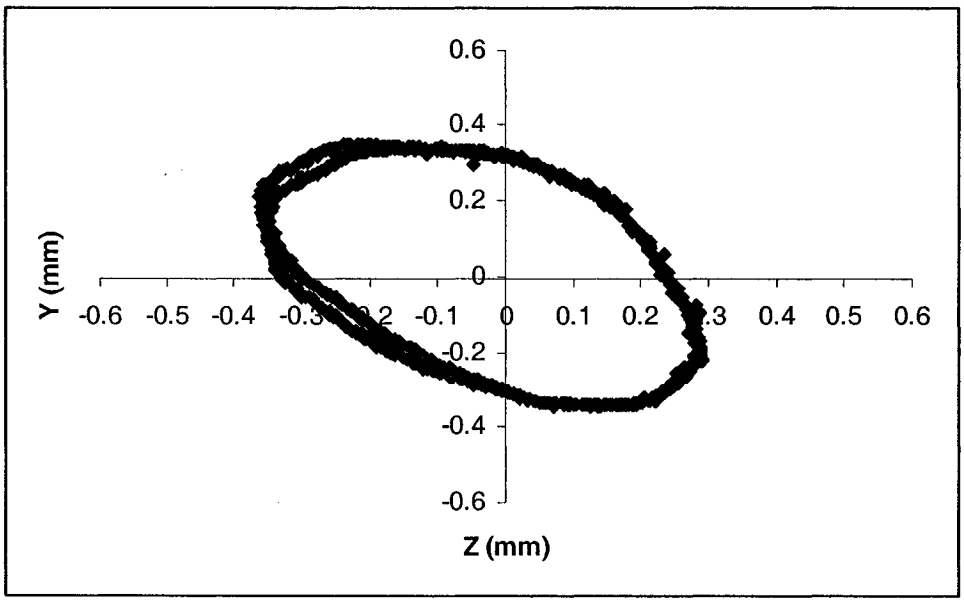


(b)

Fig. 6.20: (a) The whirl orbit before suppression at 76.2 mm (3 in), and (b) Active suppression while cutting at 76.2 mm (3 in) of tool penetration.

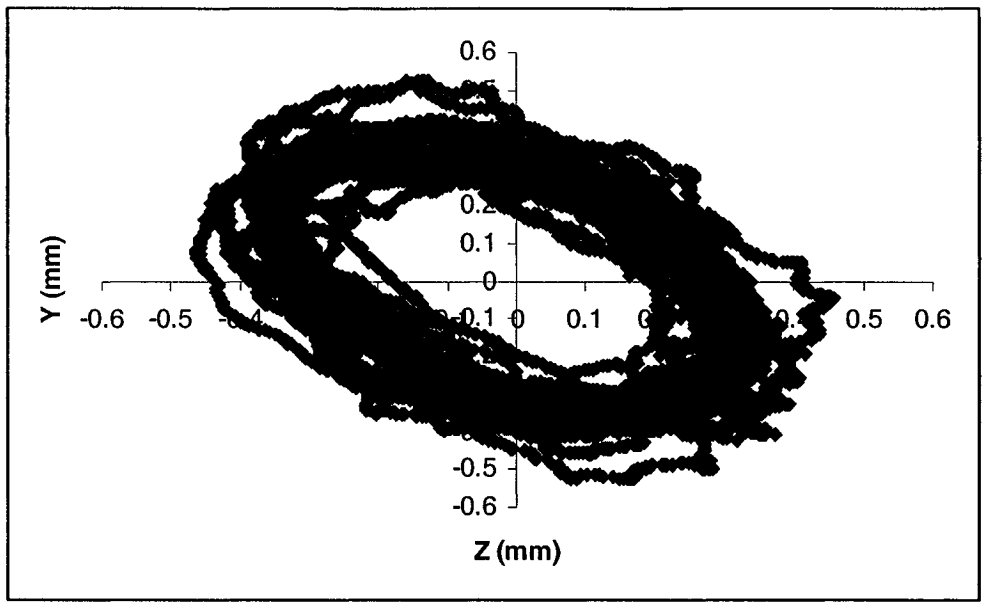


Fig. 6.21: Continuous suppression of the motion while the cutting head is penetrating the workpiece between 76.2 mm to 100 mm.

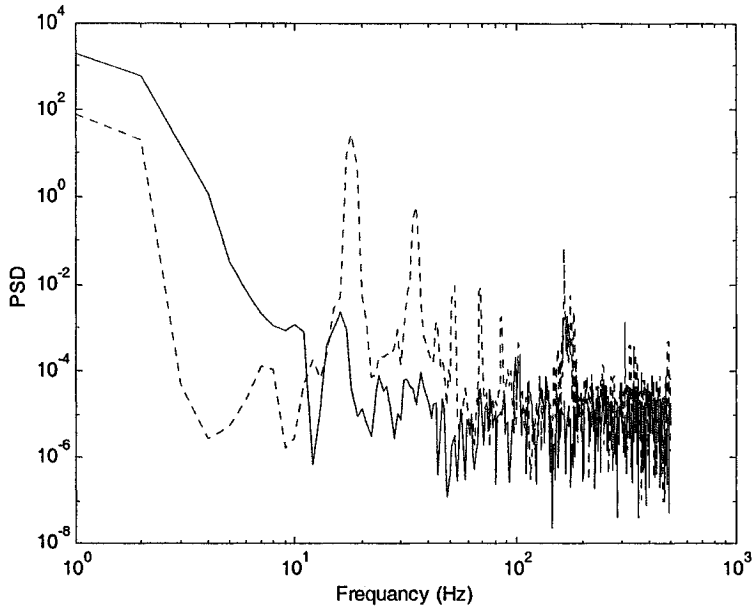


Fig. 6.22: (.....) with out suppression and (____) is with suppression at 3 inch of tool penetration.

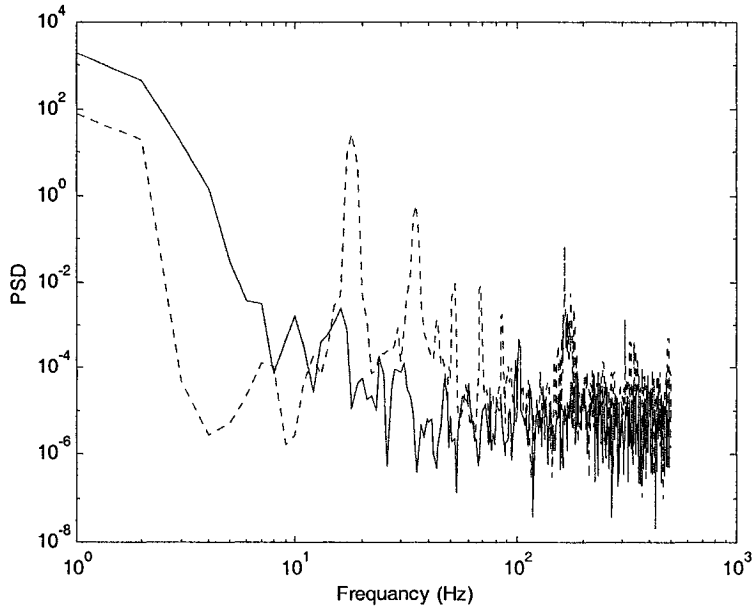


Fig. 6.23: (.....) with out suppression and (____) is with suppression after 3 inch of tool Penetration.

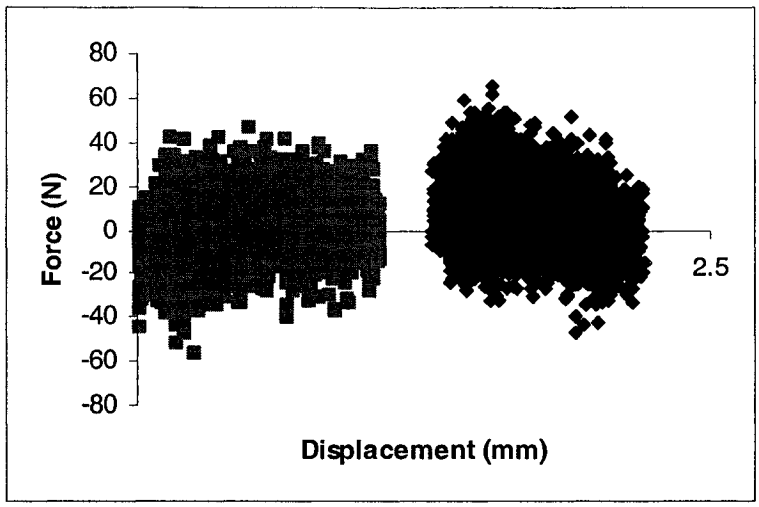


Fig. 6.24: The force displacement characteristics for vertical and horizontal load cells.

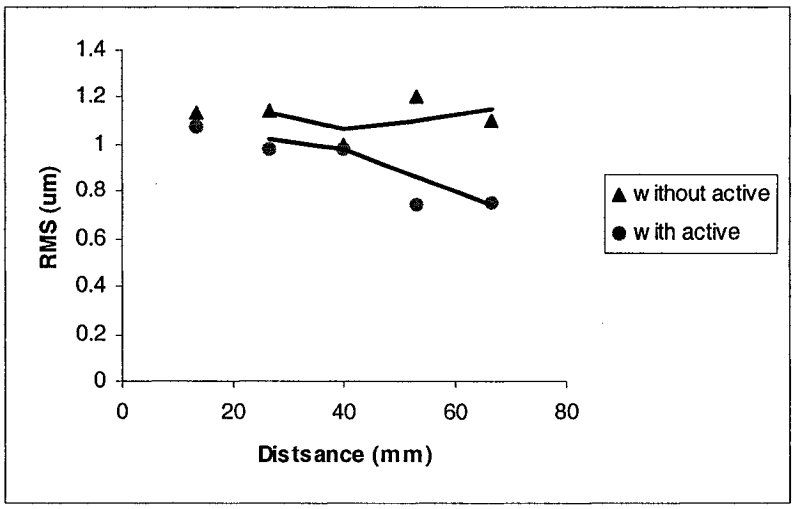


Fig. 6.25: Roughness measurement (RMS) without active suppression and with active suppression.

# CHAPTER 7

# CONCLUSIONS AND SUGGESTIONS FOR FUTURE WORK

## 7.1 Summary

A mathematical approach was developed to study the whirling motion of a continuous boring bar in a BTA deep hole boring process. Experimental investigations were carried out in order to validate the analytical model. This model has been used to simulate the whirling motion at different locations of the boring bar-workpiece system. A comprehensive study of the surface irregularities for different cutting parameters were carried out The best combinations of cutting conditions have been found using fuzzy logic model with ANFIS to improve the quality of the surface roughness and geometrical dimensioning and tolerances. Finally, an active control of the whirling motion has been carried out on the boring bar-workpiece assembly using control forces in the horizontal and vertical directions applied by electrodynamic exciters. Experiments were carried out with the boring bar rotating freely without cutting forces and with cutting forces.

A brief summary of each stage of the investigations are given below:

The mathematical model to study the whirling motion of the boring bar-workpiece assembly transformed the homogenous equations with nonhomogeneous boundary condition into a problem with nonhomogeneous equations with homogenous boundary conditions. The model included two external control forces in the Y and Z coordinate that were applied by two electrodynamic exciters. The frequency equation of the boring bar assembly has been found and the natural frequencies have been determined. The fundamental natural frequency of the boring bar was 9.149 Hz. The fundamental natural frequency of the boring bar-workpiece model was 11.23 Hz.

With a specially designed experimental set up, the whirling motion of the boring bar at different speeds of rotation has been measured and is in good agreement with the mathematical model. The fundamental frequency of the boring bar alone was found experimentally to be in the range of 6.97-10.38 Hz under different conditions. The first natural frequency of the boring bar-workpiece assembly was found to be in the range of 8.43-11.41 Hz.

The surface roughness and the surface geometrical dimensioning deteriorate due to the whirling vibrations. At any cutting parameters, speed of rotation, feed rate and flow rate of the coolant, the surface irregularities are different depending upon the tool penetration. The workpiece surface experiences various types of roundness. Basically, out of round surfaces are classified as surfaces having either an even or odd number of lobes that create out of roundness. Out of roundness with two, three, five, and seven lobes with roughness superimposed on the contour were noticed at different locations and for

different cutting parameters. Random irregularities occurred also, characterized by nonperiodic occurrence of significant departures from the basic round form. True roundness occurred also in some cases. At 76.2 mm (3 in) length of cut, the surfaces of different specimens were oval with 2 to 3 lobed out of roundness with random irregularities. At 228.6 mm (9 in) length of cut the surface was oval with two lobes out of roundness with true round cases. At 381 mm (15 in) of tool penetration the surface has mainly 3 lobed out of roundness with random irregularities. At 533.4 mm (21 in) of tool penetration the surface mainly has 4 lobes out of run and 7 lobes out of run in one case. At 685.8 mm (27 in) of tool penetration the surface mainly has 3 lobes out of roundness. At 838.2 mm (33 in) of tool penetration the surface has 3 lobes out of roundness with random irregularities.

Modeling and prediction of surface integrity of a workpiece in machining operation has been carried out by fuzzy logic analysis. Fuzzy logic is a powerful tool and was able to predict the best cutting parameters to minimize the range of size variation and surface roughness. Fuzzy logic principles have been applied for selecting best cutting conditions in deep hole boring. The basic principle of fuzzy systems, fuzzy connectives and fuzzy implication were able to mimic the actual behavior of the uncertain system such as the deep hole boring workpiece system. Subtractive clustering technique with adaptive neuro-fuzzy inference system (ANFIS) accurately established the relationship between the different cutting parameters and the resulting surface irregularities, and consequently, was able to successfully predict the surface irregularities using different cutting parameters involved in the study.

Active control of the whirling motion was successfully carried out on the bar freely rotating and during cutting operation. The whirling motion was reduced along the major and minor axes in the range of 52.9-75 % at different speeds of rotation of the boring bar freely rotating and in the range of 22-52.2 % while drilling. The PSD was reduced also in the case of cutting operations. The surface roughness in terms of RMS value was reduced as checked in the specimen drilled under active control of the whirling motion.

## 7.2 Conclusions

The main conclusions in this thesis are:

(i) The whirling motion experiments validated the mathematical model in BTA deep hole boring process. The radius of the maximum whirl amplitude was of 0.1 mm as found from the simulated mathematical model. At the same speed for the boring bar-workpiece assembly the maximum whirl amplitude was of 0.25 mm. A 60 % agreement was achieved between the model and the experimental results.

(ii) When the boring bar rotates freely at speed of 120 rpm, the whirl amplitude was of 200 μm. At speed of 240 rpm, the whirl amplitude was of 205 μm. At speed of 480 rpm the whirl amplitude was of 250 μm. The whirl amplitude increased as we approach the first natural frequency of the boring bar, which is around 550 rpm.

(iii) At 76.2 mm (3 in) of tool penetration, speed of 1040 rpm, feed of 117 mm/min and a flow rate of 40 G/min, the whirl amplitude was of 0.25 mm. At the same tool penetration, speed of 1240 rpm, feed of 117 mm/min and flow rate of 30 G/min, the whirl amplitude was of 0.3 mm. At the same tool penetration, speed of 1440 rpm, feed of 173 mm/min and flow rate of 20 G/min, the whirl amplitude was of 0.4 mm. The whirl amplitude increases when we approach the second natural frequency of the boring bar-workpiece assembly, which is around 1500 rpm.

(iv) The optimum cutting parameters to obtain a minimum cylindricity of 0.149 μm was at speed of 1406 rpm, feed of 126.3 mm/min, and flow rate of 40 G/min as the fuzzy model predicted. When the tool penetration of 76.2 mm is included in the model as a fourth input parameter, the minimum cylindricity was of 0.0527 μm at speed of 1440 rpm, feed of 71 mm/min and flow rate of 31.82 G/min. At 152.4 mm of tool penetration the optimum parameters were at speed of 1319 rpm, feed of 86.9 mm/min and flow rate of 27.58 G/min to get a minimum cylindricity of 0.0905 μm. A minimum cylindricity was of 0.0665 μm at tool penetration of 228.6 mm at a speed of 1440 rpm, feed of 71 mm/min and flow rate of 23.94 G/min. To obtain a minimum cylindricity while drilling a long workpiece, the cutting parameters should vary continuously as the boring bar penetrates the workpiece.

(v) The optimum cutting parameters to obtain a minimum straightness of 0.0001712 μm was at speed of 1218 rpm, feed of 138.6 mm/min, and flow rate of 31.08 G/min. When the tool penetration of 76.2 mm included in the

model as a fourth input parameter, the minimum straightness was of 0.0000655 μm at speed of 1440 rpm, feed of 131 mm/min and flow rate of 39.7 G/min. At 152.4 mm of tool penetration the optimum parameters were at speed of 1440 rpm, feed of 173 mm/min and flow rate of 39.7 G/min to get a minimum straightness of 0.000833 μm. This indicates that the cutting parameters should vary continuously as the boring bar penetrates the workpiece in order obtain a minimum straightness while drilling.

(vi) The optimum cutting parameters to obtain a minimum roughness of 0.00262 μm was at speed of 1245 rpm, feed of 121.4 mm/min, and flow rate of 32.77 G/min. When the tool penetration of 76.2 mm included in the model as a fourth input parameter, the minimum roughness was of 0.0178 μm at speed of 1258 rpm, feed of 120.7 mm/min and flow rate of 30.5 G/min. At 152.4 mm of tool penetration the optimum parameters were at speed of 1370 rpm, feed of 145 mm/min and flow rate of 25 G/min to get a minimum roughness of 0.0183 μm. At 228.6 mm of tool penetration the optimum parameters were at speed of 1313 rpm, feed of 124.5 mm/min and flow rate of 30 G/min to get a minimum roughness of 0.0121 μm. These findings indicate that the cutting parameters should vary continuously as the boring bar penetrates the workpiece in order obtain a minimum roughness while drilling.

(vii) By applying the two electrodynamic control forces along the Y and Z directions on the boring bar, a 52.9 % reduction was achieved in the maximum whirl amplitude at speed of 1040 rpm.

At speed of 1237 rpm a 69.2 % reduction was achieved in the maximum whirl amplitude. At the maximum speed of 1440 rpm a 75 % reduction was achieved.

(viii) A comprehensive study of the outcome surface irregularities, i.e., surface roughness and surface geometrical dimensioning and tolerances, roundness, straightness and cylindricity and explaining the main features of these irregularities under different machining conditions, speed of rotation, feed rate, flow rate of the coolant and tool penetration, reveal that the surface will experience different kind of irregularities due to whirling vibrations.

(ix) When active control of vibration was applied on the boring bar while drilling, at speed of 1040 rpm, feed of 71 mm/min, flow rate of 20 G/min, and 76.2 mm of tool penetration, a 22 % reduction of the whirl amplitude was achieved. While the boring bar continuously penetrating the work piece up to 100 mm the whirl amplitude was reduced form 0.4 mm to 0.19 mm. 52.5 % reduction was a achieved within 23.8 mm of tool penetration.

(x) The surface roughness reduction of 18 %, 35.83 %, and 35.77 % at specimen lengths of 45 mm, 55 mm, and 68 mm, respectively was achieved. Due to the fact that the maximum whirling amplitude was reduced in drilling while approaching the second natural frequency of the boring bar-workpiece system, which is around 1500 rpm.

## 7.3 Suggestions for future work

Some suggestions for future work are addressed below

(i) A separate simultaneous measurement of the whirling motion of the workpiece and the boring bar during cutting operations.

(ii) A continuous measurement of the whirling vibrations at one point of the boring bar while penetrating the workpiece by designing a special set-up so that the set-up will have the same feed rate of the boring bar assembly under different cutting conditions.

(iii) Design of a fuzzy controller using the suggested models to reduce the whirling motion by automatically changing the cutting parameters. Hence, the surface roughness is reduced and a better surface quality is obtained.

(iv) Development of a control system using two electrodynamic shakers to automatically control the whirling motion of the boring bar in the deep hole boring process.

(v) Measurement of cutting forces by directly mounting the piezoelectric transducers on the boring tool.

(vi) Identify the optimum position of the control forces on the boring bar.

## 7.4 Publications under preparation

**1- " Whirling vibrations in BTA deep hole boring process, Part1: Analytical and experimental investigations".**

A journal paper including the mathematical model of the whirling vibrations in BTA deep hole boring process with the internal cutting forces and the experiments done on the whirling vibrations of the boring bar-workpiece system at the beginning of drilling.

**2- " Active control of whirling vibrations in BTA deep hole boring process using two electrodynamic shakers, Part2: Analytical and experimental investigations".**

A journal paper including the mathematical model with the internal cutting forces and the electrodynamic shaker forces with the active suppression of motion experiments done in BTA deep hole boring process.

**3- "Fuzzy-logic modeling of different surface irregularities in BTA deep hole boring process".**

A journal paper for the fuzzy models of the outcome surface irregularities considering two models for each one, first model is without the tool penetration (3 inputs only, i.e., speed, feed and flow rate) and the second one when we consider the tool penetration i.e., (feed, speed, flow rate and tool penetration) to show the best combinations of the cutting parameters to improve the surface quality.

4- A journal or conference paper on the effect of the whirling motion on the outcome surface irregularities, roughness, geometrical dimensioning and tolerances (roundness, cylindricity and straightness) at different cutting parameters with tool penetration of 76.2, 228.6, 381, 533.4, 685.8, and 838.2 mm (3, 9, 15, 21, 27 and 33 inch).

**Published conference paper:**

1- H. Al-Wedyan, K. Demirli, and R. Bhat, "*A Technique For Fuzzy Logic Modeling Of Machining Process*", Joint 9th World Congress and 20th NAFIPS International Conference, Vancouver, British Columbia, Canada. July 25-28, 2001.

**Submitted conference papers:**

1- H. Al-Wedyan, R. Bhat, and K. Demirli, " *Whirling Motion in BTA Deep Hole Boring-Workpiece System Subjected to Cutting Forces*".

**The 2004 International Conference on Dynamics, Instrumentation and Control August 18-20, Nanjing, China**

2- H. Al-Wedyan, K. Demirli, and R. Bhat, " *Fuzzy-Modeling and Prediction of the Surface Irregularities in BTA Deep Hole Boring Process*".

**NAFIPS-04, Fuzzy sets June 27-30, 2004, Banff, Canada.**

# References


1. P. Bayly, M. Lamar and S. Calvert, "Low-Frequency Regenerative Vibration and the Formation of Lobed Holes in Drilling", Transactions of ASME, Journal of Manufacturing Science and Engineering, 2002, Vol. 124, pp. 275-285.

2. K. Weinert, O. Webber, M. Husken and J. Menen, "Statistics and Time Series Analysis of BTA Deep Hole Drilling", COST P4, Nonlinear Dynamics in Mechanical Processing, EU-Frame Work COST Action P4, University of Dortmund, Dortmund, Germany, 2001.

3. P. Bayly, S. Metzler, A. Schaut and K. Young, "Theory of Torsional Chatter in Twist Drilles: Model, Stability Analysis and Composition to Test", Transactions of ASME, Journal of Manufacturing Science and Engineering, 2001, Vol. 123, pp. 552-561.

4. S. Batzer, A. Gouskov and S. Vornov, "Modeling Vibratory Drilling Dynamics", Transactions of ASME, Journal of Vibration and Acoustic, 2001, Vol. 123, pp. 635-644.

5. J. Keraita, H. Oyango and G. Misoi, "Lathe Stability Charts Via Acoustic Emission Monitoring", African Journal of Science and Technology (AJST), 2001,Vol. 2, No. 2, pp. 81-93.

6. G. Litak, "Chaotic Vibrations in a Regenerative Cutting Process", Chaos Solitons and Fractals, 13, 2002, pp. 1531-1535.

7. P. Bayly, K. Young, S. Calvert and J. Hally, "Analysis of Tool Oscillation and Hole Roundness Error in a Quasi-Static Model of Reaming", Transactions of ASME, Journal of Manufacturing Science and Engineering, 2001, Vol. 123, pp. 387-396.

8. P. Huang, J. Chen, and C. Chou, "A Statistical Approach in Detecting Tool Breakage in End Milling Operations", Journal of Industrial Technology, 1999, Vol. 15, Number 3, pp. 1-7.

9. I. Kovacic, "The Chatter Vibrations In Metal Cutting-Theoretical Approach", The Scientific Journal FACTA Universitatis, Mechanical Engineering series, 1998, Vol. 1, No. 5, pp. 581-593.

10. E. Marui, S. Kato, M. Hashimoto and T. Yamado, "The Mechanism of Chatter Vibration in a Spindle-Workpiece System: Part 1: Properties of Self Exited Vibration in Spindle-Workpiece System", Transactions of ASME, Journal of Engineering for Industry, 1988, Vol. 110, pp. 236-241.

11. H. Fujii, E. Marui and S. Ema, "Whirling Vibration in Drilling. Part 1: Cause of Vibration and Role of Chisel Edge", Transactions of ASME, Journal of Engineering for Industry, 1986, Vol. 108, pp. 157-162.

12. H. Fujii, E. Marui and S. Ema, "Whirling Vibration in Drilling. Part 2: Influence of Drill Geometries, Particularly of the Drill Flank, on the Initiation of Vibration", Transactions of ASME, Journal of Engineering for Industry, 1986, Vol 108, pp. 163-1168.

13. H. Fujii, E. Marui and S. Ema, "Whirling Vibration in Drilling. Part 3: Vibration Analysis in Drilling Workpiece with a Pilot Hole", Transactions of ASME, Journal of Engineering for Industry, 1988, Vol. 110, pp. 315-321.

14. E. Edhi and T. Hoshi, "A New Mechanism Explaining High Frequency Chatter Vibration Involving Tool Tip X-Y Looping in Fine Boring", Transactions of ASME, Journal of Dynamic Systems, Measurement, and Control, 2001, Vol. 123, pp. 370-376.

15. K. Weinert, O. Webber, A. Busse, M. Husken, J. Mehnon and P. Stagge " Experimental Investigations of the Dynamics of the BTA Deep Hole Drilling Process", Journal of Production Engineering-Research and Development in Germany, 1999, VIII (2), pp. 925-935.

16. R. Landers and A. Ulsoy "Chatter Analysis of Machining Systems with Nonlinear Force Process", ASME International Mechanical Engineering Congress and Exposition, Atlanta, Georgia, November, 1996, Vol. 58, pp. 183-190.

17. E. Marui, S. Kato, M. Hashimoto and T. Yamado, "The Mechanism of Chatter Vibration in a Spindle-Workpiece System: Part 2: Characteristics of Dynamic Cutting Force and Vibration Energy", Transactions of ASME, Journal of Engineering for Industry, 1988, Vol. 110, pp. 242-247.

18. E. Marui, S. Kato, M. Hashimoto and T. Yamado, "The Mechanism of Chatter Vibration in a Spindle-Workpiece System: Part 3:Analytical Consideration", Transactions of the ASME, Journal of Engineering for Industry, 1988, Vol. 110, pp. 248-253.

19. S. Ema, H. Fujii and E. Marui, "Chatter Vibration in Drilling" Transactions of ASME, Journal of Engineering for Industry, 1988, Vol. 110, pp. 309-314.

20. F. Atabey, I. Lazoglu and Y. Altintas, "Mechanics of Boring Processes-Part I", International Journal of Machine Tools and Manufacture, 2003, Vol. 43, pp. 463-476.

21. F. Atabey, I. Lazoglu and Y. Altintas, "Mechanics of Boring Processes-part II: Multi-Insert Boring Heads", International Journal of Machine Tools and Manufacture, 2003, Vol. 43, pp. 477-484.

22. S. Vafaei, H. Rahnejat and R. Aini, "Vibration Monitoring of High Speed Spindles Using Spectral Analysis Technique", International Journal of Machine Tools and Manufacture, 2002, Vol. 42, pp. 1223-1234.

23. W. Yun, J. Ko, H. Lee, D. Cho and K. Ehmann, "Development of a Virtual Machining System, Part 3: Cutting Process Simulation in Transient Cuts", International Journal of Machine Tools and Manufacture, 2002, Vol. 42, pp. 1617-1626.

24. T. El-Wardany, D. Gao and M. Elbestawi, "Tool condition monitoring in drilling using vibration signature analysis", International Journal of Machine Tools and Manufacture, 1996, Vol. 36, pp. 687-711.

25. S. Smith and T. Tlusty, "An Overview of Modeling and Simulation of the Milling Process", Transactions of ASME, Journal of Engineering for Industry, 1991, Vol. 113, pp. 169-175.

26. D. Montgmery and Y. Altintas, "Mechanism of Cutting Force and Surface Generation in Dynamic Milling", Transactions of ASME, Journal of Engineering for Industry, 1991, Vol. 113, pp. 160-168.

27. Y. Matsumoto, D. Magda, D. Heoppner and T. Kim, "Effect of Machining Processes on the Fatigue Strength of Hardened AISI 4340 Steel", Transactions of ASME, Journal of Engineering for Industry, 1991, Vol. 113, pp. 154-158.

28. F. Kolarits and W. Devries, "A Mechanistic Dynamic Model of End Milling for Process Controller Simulation", Transactions of ASME, Journal of Engineering for Industry, 1991, Vol. 113, pp. 176-183.

29. I. Minis, E. Magrab and I. Pandelidis, "Improved Methods for the Prediction of Chatter in Turning, Part 1: Determination of Structural Response Parameters", Transactions of ASME, Journal of Engineering for Industry, 1990, Vol. 112, pp. 12-20.

30. I. Minis, E. Magrab and I. Pandelidis, "Improved Methods for the Prediction of Chatter in Turning, Part 2: Determination of Cutting Process Parameters", Journal of Engineering for Industry, 1990, Vol. 112, pp. 21-27.

31. I. Minis, E. Magrab and I. Pandelidis, "Improved Methods for the Prediction of Chatter in Turning, Part 3: A generalized Linear Theory", Transactions of ASME, Journal of Engineering for Industry, 1990, Vol. 112, pp. 28-35.

32. M. Rahman, K. Seah and V. Venkatesh, "Performance Evaluation of Endrills", International Journal of Machine Tools and Manufacture, 1988, Vol. 28, pp. 341-349.

33. S. Lee, K. Eman and S. Wu, "An Analysis of the Drill Wandering Motion", Transactions of ASME, Journal of Engineering for Industry, 1987, Vol. 109, pp. 297-305.

34. G. Zhang and S. Kapoor, "Dynamic Modeling and Analysis of the Boring Machining System", Transactions of ASME, Journal of Engineering for Industry, 1987, Vol. 109, pp. 219-226.

35. S. Kojic, "A Theoretical and Experimental Investigation of the BTA Deep Hole Tool Support in the Machining Zone", Master thesis, Concordia University, Montreal, Quebec, 1997.

36. M. Al-Ata, "An Investigation of the Surface Parameters in Self-Piloting Deep Hole Machining using A Developed Methodology of Statistical Design of Experiment", Master thesis, Concordia University, Montreal, Quebec, 1995.

37. R. Koganti, "Optimum Design of BTA Tools with Staggered Cutters by Probabilistic Approach and their Dynamic Stability", Master thesis, Concordia University, Montreal, Quebec, 1993.

38. S. Torabi, "Improved Version of BTA Deep-Hole Drilling Tools with Staggered Disposable Carbide Inserts", Master thesis, Concordia University, Montreal Quebec, 1990.

39. Y. Gessesse, "Stability of Deep-Hole BTA Machining Process", Master thesis, Concordia University, Montreal, Quebec, 1990.

40. S. Chandrashekhar, "An Analytical and Experimental Stochastic Modeling of The Resultant Force System in BTA Deep-Hole Machining and Its Influence on The Dynamics of the Machine Tool Workpiece System", PhD. thesis, Montreal, Quebec, Concordia University, 1984.

41. R. Hecker and S. Liang, "Predictive Modeling of Surface Roughness in Grinding", International Journal of Machine Tools and Manufacture, 2003, Vol. 43, pp. 755-761.

42. A. Hassui and A. Diniz, "Correlating Surface Roughness and Vibration on Plung Cylindrical Grinding of Steel", International Journal of Machine Tools and Manufacture, 2003, Vol. 43, pp. 855-862.

43. B. Muralikrishnan, J. Raja and K. Najarian, "Surface Wavelength Content Based Clustering Using Neural Networks for Manufacturing Process Mapping",

International Journal of Machine Tools and Manufacture, 2003, Vol. 43, pp. 272-281.

44. J. Rech and A. Moisan, "Surface Integrity in Finish Hard Turning of Case-Hardened Steels", International Journal of Machine Tools and Manufacture, 2003, Vol. 43, pp. 543-550.

45. E. Salisbury, K. Domata, K. Moon, M. Miller and J. Sutherland, " A Three-Dimensional Model for the Surface Texture in Surface Grinding, Part 1: Surface Generation Model", Journal of Manufacturing Science and Engineering, 2001, Vol. 123, pp. 576-581.

46. N. Lee, J. Chen and A. Joneja, "Effects of Surface Roughness on Multi-Station Mechanical Alignment Processes", Journal of Manufacturing Science and Engineering, 2001, Vol. 123, pp. 433-444.

47. D. Jang, Y. Choi, H. Kim and A. Hsiao, "Study of the Correlation Between Surface Roughness and Cutting Vibrations to Develop an On-Line Roughness Measuring Technique in Hard Turning", International Journal of Machine Tools and Manufacture, 1996, Vol. 36, pp. 453-464.

48. G. Zhang And S. Kapoor, "Dynamic Generation Of Machined Surface, Part 1: Description of a Random Excitation System", Transactions Of ASME, Journal of Engineering For Industry, 1991, Vol. 113, pp. 137-144.

49. G. Zhang and S. Kapoor, "Dynamic Generation of Machined Surface, Part 2: Construction of Surface Topography", Transactions of ASME, Journal of Engineering For Industry, 1990, Vol. 113, pp. 145-153.

50. L. Zhu and H. Ding, "Application of Kinematic Geometry to Computational Metrology: Distance Function Based Hierarchical Algorithms for Cylindricity Evaluation", International Journal of Machine Tools and Manufacture, 2003, Vol. 43, pp. 203-215.

51. P. Dhanish, "A Simple Algorithm for Evaluation of Minimum Zone Circularity Error From Coordinate Data", International Journal of Machine Tools and Manufacture, 2002, Vol. 42, pp. 1589-1594.

52. V. Astakhov, "The Mechanisms of Bell Mouth Formation in Gundrilling when the Drill Rotates and the Workpiece is Stationary. Part I: the First Stage of Drill Entrance", International Journal of Machine Tools and Manufacture, 2002, Vol. 42, pp. 1135-1144.

53. V. Astakhov, "The Mechanisms of Bell Mouth Formation in Gundrilling when the Drill Rotates and the Workpiece is Stationary. Part 2: The Second Stage of

Drill Entrance", International Journal of Machine Tools and Manufacture, 2002, Vol. 42, pp. 1145-1152.

54. J. Ko, W. Yun, D. Cho and K. Ehmann, "Development of a Virtual Machining System, Part 1: Approximation of the Size Effect for Cutting Force Prediction", International Journal of Machine tools and Manufacture, 2002, Vol. 42, pp. 1595-1605.

55. N. Cho and J. Tu, "Quantitative Circularity Tolerance Analysis and Design for 2D Precision Assemblies", International Journal of Machine Tools and Manufacture, 2002, Vol. 42, pp. 1391-1401.

56. E. Fung and S. Yang, "A New Method for Roundness Control in Taper Turning Using FCC Techniques", Journal of Manufacturing Science and Engineering 2001, Vol. 123, pp. 567-575.

57. S. Chou, S. Lin and C. Chen, "Assessing Circularity in Three Dimensions", Journal of Manufacturing Science and Engineering, 2001, Vol. 123, pp. 128-134.

58. N. Cho and J. Tu, "Roundness Modeling of Machined Parts for Tolerance Analysis", Journal of the International Societies for Precision Engineering and Nanotechnology, 2001, Vol. 25, pp. 35-47.

59. W. Jywe, C. Liu and C. Chen, "The Min-Max Problem for Evaluating the Form Error of a Circle", Journal of Measurement, 1999, Vol. 26, pp. 273-282.

60. R. Furness, C. Wu and A. Ulsoy, "Statistical Analysis of the Effects of Feed, Speed and Wear on Hole Quality", Journal of Manufacturing Science and Engineering, 1996, Vol. 118, pp. 367-375.

61. A. Shawky and M. Elbestawi, "In-process Evaluation of Workpiece Geometrical Tolerance in Bar Turning", International Journal of Machine Tools and Manufacture, 1996, Vol. 36, pp. 33-46.

62. Y. Gessesse, B. Latinovic and M. Osman, " On the Problem of Spiraling in BTA Deep-Hole Machining", Transactions of ASME, Journal of Engineering for Industry, 1994, Vol. 116, pp. 161-165.

63. T. Starbuck, "Software Techniques for Removing Unwanted Features on Components when Performing Automatic form Measurement", International Journal of Machine Tools and Manufacture, 1992, Vol. 32, pp. 101-108.

64. F. Parsons and Tabenkin, "The Theory and Development of User-Friendly Software for the Measurement of Surface Roughness and Geometrical Parameters", International Journal of Machine Tools and Manufacture, 1992, Vol. 32, pp. 255-262.

65. C. Cogun, "A Correlation Between Deviations In Circularity, Cylindricity, Roughness and Size Tolerance", International Journal Of Machine Tools And Manufacture, 1990, Vol. 30, pp. 561-567.

66. M. Shiraishi and S. Sato, "Dimensional and Surface Roughness Controls In a Turning Operation", Transactions of ASME, Journal of Engineering For Industry, 1990, Vol. 112, pp. 78-83.

67. S. Ema, H. Fujii, E. Marui and S. Kato, "New Type Drill With Three Major Cutting Edges", International Journal Of Machine Tools And Manufacture, 1988, Vol. 28, pp. 461-473.

68. K. Kim, "Cylindrical Accuracy Control Based on Stochastic Modeling and Forecasting Compensation", International Journal Of Machine Tools And Manufacture, 1988, Vol. 28, pp. 495-501.

69. P. Rao and M. Shunmugam, "Accuracy and Surface Finish in BTA Drilling", International Journal of Production and Research, 1987, Vol. 25, pp. 31-44.

70. K. Kim, K. Eman and S. Wu, "Analysis Of Alignment Errors in a Laser-Based In-Process Cylindricity Measurement System", Transactions of ASME, Journal of Engineering For Industry, 1987, Vol. 109, pp. 321-329.

71. K. Kim, K. Eman and S. Wu, "Development of A Forecasting Compensatory Control System For Cylindrical Grinding", Transactions of ASME, Journal of Engineering For Industry, 1987, Vol. 109, pp. 385-391.

72. F. Dweiri, M. Al-Jarrah and H. Al-Wedyan, "Fuzzy Surface Roughness Modeling of CNC Down Milling of Alumic-79", Journal Of Materials Processing Technology, 2003, Vol. 133, pp. 266-275.

73. S. Yang, V. Girivasan, N. Singh, I. Tansel and C. Kropas-Hughes, "Selection of Optimal Material and Operating Conditions in Composite Manufacturing. Part II: Complexity, Representation of Characteristics and Decision-Making", International Journal of Machine Tool and Manufacture, 2003, Vol. 43, pp. 175-184.

74. K. Demirli and M. Packirisamy "Higher Order Fuzzy System Identification with Subtractive Clustering", Journal of Intelligent Fuzzy Systems, 2001, Vol. 9, pp. 129-158.

75. S. Ying Ho, K. Chyi Lee, S. Shin Chen and S. Jang Ho, "Accurate Modeling and Prediction of Surface Roughness by Computer Vision in Turning Operations Using an Adaptive Neuro-Fuzzy Inference System", International Journal of Machine Tool and Manufacture, 2002, Vol. 42, pp. 1441-1446.

76. M. Jaulent, "Modeling Uncertainty in Computerized Guidelines Using Fuzzy Logic", Journal of The American Medical In Formations Association, 2001, Vol. 105, pp. 284-288.

77. H. Al-Wedyan, K. Demirli and R. Bhat, "A Technique For a Fuzzy Logic Modeling of Machining Process", IEEE, Joint 9th IFSA World Congress and 20th NAFIPS International Conference, British Columbia, Vancouver, July 24, 2001.

78. M. Alata and K. Demirli, "Fuzzy Prediction Model For BTA Deep-Hole Machining: Experimental Study", Ecole polytechnique University, Montreal, Quebec, Canada, May 2000.

79. H. Lou, and Y. Huang, "Fuzzy-Logic-Based Process Modeling Using Limited Experimental Data", Engineering Applications of Artificial Intelligence, 2000, Vol. 13, pp. 121-135.

80. J. Abonyi, R. Babuska, H. Verbruggen and F. Szeifert, "Incorporating Prior Knowledge in Fuzzy Model Identification", International Journal of Systems Science, 2000, Vol. 31(5), pp. 657-667.

81. G. Bontempi, M. Birattari and H. Bersini, "A Model Selection Approach for Local Learning", Journal of Artificial Intelligence Communication, 2000, Vol. 13, pp. 41-48.

82. S. Wu and M. J. Er, "Dynamic Fuzzy Neural Networks-A Novel Approach To Function Approximation", IEEE Transactions On Systems, Man And Cybernetics, 2000, Vol. 30, pp. 358-372.

83. K. Hashmi, M. El Baradie and M. Ryan, "Fuzzy-Logic Based Intelligent Selection of Machining Parameters", Journal of Materials Processing Technology, 1999, Vol. 94, pp. 94-111.

84. Y. Ali and L. Zhang, "Surface Roughness Prediction of Ground Components Using Fuzzy Logic Approach", Journal of Materials Processing Technology, 1999, Vol. 89-90, pp. 561-568.

85. G. Bontempi and M. Birattari, "Toolbox For Neuro-Fuzzy Identification and Data Analysis", Universite Libre De Bruxelles, Belgium, 1999.

86. C. Kim, "An Algorithm Approach For Fuzzy Inference", IEEE Transactions on Fuzzy Systems, 1997, Vol. 5, pp. 585-598.

87. H. Bersini and G. Bontempi, "Now Come the Time to Defuzzify Neuro-Fuzzy Models", Fuzzy Sets and Systems, 1997, Vol. 90, pp. 161-169.

88. W. Duch, R. Adamczak and K. Grabczewski, "Extraction of Logical Rules From Training Data Using Backpropagation Networks", First Polish Conference on Theory and Applications of Artificial Intelligent, Lodz, December 19-21, 1996, 163-170, Korea.

89. W. Pedrycz, "Fuzzy Multimodels, " IEEE Transactions On Fuzzy Systems, 1996, Vol. 4, No. 2, pp. 139-148.

90. S. Suharyanto, I. Goulter, and S. Wasimi, "Generation of Fuzzy Reservoir Operating Rules Under Imperfect Streamflow Data Condition", Symposium Of Postgraduate Student Association, Central Queensland University, Rockhampton, Australia, October, 2,1995.

91. K. Lee and Z. Bien, "A Corner Matching Algorithm Using Fuzzy Logic", Workshop on Soft Computing, Korea Advanced Institute of Science and Technology, August 19-30, 1996.

92. C. Stutz and T. Runkler, "Fuzzy C-Mixed Prototypes Clustering", 5th International Workshop Fns'98, Band7von Proceedings in Artificial Intelligence, 1998, S. 122-129.

93. C. Stutz, "Partially Supervised Fuzzy C-Means Clustering With Cluster Merging", Proceedings Of The 4th European Congress on Intelligent Techniques and Soft Computing (Eufit'98), Aachen, 1725-1729.

94. T. Ross and T. Hasselman, "Fuzzy Classification of Modal Vibration Data", ASCE Structure Congress, Boston, Ma, April 3-5, 1995.

95. J. Pyotsia, "Fuzzy Logic Expert System and Failure Analysis of Dynamic System", Industrial Computing Society's, ICSWEB, 1997, 1-8.

96. G. Bontempi, "Modeling With Uncertainty in Continuous Dynamical Systems: The Probability and Possibility Approach", Iridia-Ulb Technical Report, Bruxelles, Belgium. 1995, 95-16

97. P. Hsu and W. Fann, "Fuzzy Adaptive Control of Machining Processes with a Self-Learning Algorithm", Journal of Manufacturing Science and Engineering, 1996, Vol. 118, pp. 522-530.

98. R. Du, M. Elbestawai and S. Li, "Tool Condition Monitoring in Turning Using Fuzzy Set Theory", Journal of Manufacturing Science and Engineering, 1992, Vol. 32, No. 6, pp. 781-796.

99. L. Zadeh, "The Role of Fuzzy Logic in Modeling, Identification and Control", Modeling Identification and Control, 1994, Vol. 15, No. 3, pp. 191-203.

100. M. Xiao, S. Karube, T. Soutome and K. Sato, "Analysis of Chatter Suppression in Vibration Cutting", International Journal of Machine Tool And Manufacture, 2002, Vol. 42, pp. 1677-1685.

101. F. Ismail and R. Ziaei, "Chatter Suppression in Five-Axis Machining of Flexible Parts", International Journal of Machine Tool And Manufacture, 2002, Vol. 42, pp. 115-122.

102. S. Zhou and J. Shi, "Active Balancing and Vibration Control of Rotating Machinery: A Survey", The Shock And Vibration Digest, 2001,Vol. 33, No. 4, pp. 361-371.

103. S. Dyer, J. Ni, J. Shi and K. Shin, "Robust Optimal Influence-Coefficient Control Of Multiple-Plane Active Rotor Balancing Systems", Journal of Dynamic Systems, Measurement, and Control. 2002, Vol. 124, pp. 41-46.

104. Y. Altintas and P. Chan, "In-Process Detection And Suppression of Chatter in Milling", International Journal of Machine Tools and Manufacture, 1992, Vol. 32, pp. 329-347.

105. S. Lin, R. Devor and S. Kapoor, "The Effects of Variable Speed Cutting on Vibration Control in Face Milling", Journal of Engineering For Industry, 1990, Vol. 112, pp. 1-11.

106. K. Kim and J. Ha, "Suppression of Machine Tool Chatter Using Viscoelastic Dynamic Damper", Transactions of ASME, Journal Of Engineering For Industry, 1987, Vol. 109, pp. 58-65.

107. G. Agnes and D. Inman, "Nonlinear Piezoelectric Vibration Absorbers", Smart Material And Structure, 1996, Vol. 5, pp. 704-714.

108. J. Yellin and I. Shen, "A Self-Sensing Active Constrained Layer Damping Treatment for A Euler-Bernoulli Beam", Smart Material and Structure, 1996, Vol. 5, pp. 628-637.

109. A. Palazzolo, R. Lin, R. Alexander, A. Kascak and J. Montague, "Test and Theory for Piezoelectric Actuator-Active Vibration Control of Rotating Machinery", Journal of Vibration and Acoustics, 1991, Vol. 113, pp. 167-175.

110. A. Palazzolo, R. Lin, R. Alexander, A. Kascak and J. Montague, "Piezoelectric Pushers for Active Vibration Control of Rotating Machinery", Journal of Vibration, Acoustics, Stress and Reliability in Design, 1989, Vol. 111, pp. 298-305.

111. A. Palazzolo, R. Lin, R. Alexander, A. Kascak and J. Montague, "Active Control of Transient Rotordynamic Vibration and Optimal Control Methods", Journal of Vibration and Acoustics, 1991, Vol. 113, pp. 167-175.

112. J. Bennighof and L. Meirovitch, "Active Vibration Control of A Distributed System With Moving Support", Journal of Vibration, Acoustics, Stress And Reliability In Design, 1988, Vol. 110, pp. 246-253.

## Bibliography:

113. L. Meirovitch, "Analytical Methods in Vibrations", The Macmillan Company, New York, 1967.

114. E. Mamdani and S. Assillian, "An Experiment in Linguistic Synthesis with a Fuzzy Logic Controller", International Journal of Man Machine Studies, 1975, Vol. 7, No. 1, pp. 1-13.

115. J. Greve and F. Wilson, "Handbook of Industrial Metrology", Prentice-Hall, INC, England Cliffs, New Jersey, 1967.

116. A. Scarr, "Metrology and Precision Engineering", McGraw-Hill Publishing Company Limited, Maidenhead, Berkshire, England, 1967.

117. G. Thomas, "Engineering Metrology", Butterworth and Co. (Publishers) Ltd, Hungary, 1974.

118. L. Foster, "Geometric Dimensioning and Tolerancing", Addison-Wesley Publishing Company, Inc., Canada, 1972.

119. O. Devillers, and F. Prearant, "Evaluating the Cylindricity of a Nominally Cylindrical Point set", Center of Geometric Computing, Department of Computer Science, Brown University, 2000.

120. Taylor- Hobson, Talyrond model 262, operating instruction manual, The Rank Organization, Rank Taylor Hobson Division, Leicester, England.

121. R. Sundaram and B. Lambert, "Mathematical Model to predict Surface Finish in Fine Turning of Steel. Part I" International Journal of Production Research, 1981, Vol. 19, No. 5, pp. 547-556.

122. D. Whitehouse, "Surfaces-A Link Between Manufacture and Function", Journal of Mechanical Engineering Science, 1978, Vol. 192, pp. 179-192.

123. N. Demkin, I. Berkovich and M. Kourova, "Statistical Analysis of a Rough Surface Model", Journal of Mechanical Engineering Science, 1978, Vol. 20, No.6, pp. 315-318.

124. J. Peters, P. Vanherck and M. Sastrodinoto, "Assessment of Surface Typology Analysis Techniques", Annals of the CIRP, 1979, Vol. 28, No. 28/2/1979, pp. 539-554.

125. I. Loukjanov, "Evaluation of the Autocorrelation Functions Used when Investigating Surface Roughness", Journal of Mechanical Engineering Science, 1979, Vol. 21, No. 2, pp. 105-113.

126. A. Konczakowski, "The Matrix of Power Spectral Levels of Turned Surfaces Roughness", International Journal of Machine Tool Design Research, 1983, Vol. 23, No. 2/3, pp. 161-167.

127. W. North and A. Agrawal, "Surface Roughness Measurement with Fiber-Optics", Transactions of ASME, Journal of Dynamic Systems, Measurement, and Control, 1983, Vol. 105, pp. 295-297.

128. T. Watanabi and S. Iwa, "A Control System to Improve the Accuracy of Finished Surface in milling", Transactions of ASME, Journal of Dynamic Systems, Measurement, and Control, 1983, Vol. 105, pp. 192-199.

129. D. Whitehouse, "An Easy to Measure Average Peak/Valley Parameters for Surface Finish", Journal of Mechanical Engineering Science, Vol. 197C, pp. 205-207.

130. M. Hasegawa and T. Tsukizoe, "The Generating Mechanism of Surface Roughness By Random Cutting Edges", Journal of Mechanical Engineering Science, 1978, Vol. 20, pp. 197-200.

131. N. Demkin and M. Korotkov, "Calculation of the Topographic Characteristics of Rough Surfaces By Virtue of Profile", Journal of Mechanical Engineering Science, 1978, Vol. 20, No. 6, pp. 303-307.

132. J. Raja and V. Radhakrishnan, "Filtering of Surface Profiles Using Fast Fourier Transform", International Journal Machine Tool Design Research, 1979, Vol. 19, pp. 133-141.

133. R. Sayles and T. Thomas, "Measurement of the Statistical Micro Geometry of Engineering Surfaces", Journal of Lubrication Technology, 1979, Vol. 101, pp. 409-418.

134. S. Uchida, H. Sato and M. O-Hori, "Two Dimensional Measurement of Surface Roughness by the light Sectioning Method", Annals of the CIRP, 1979, Vol. 28/1/1979, pp. 419-423.

135. F. Hirano, Y. Yamamoto, T. Kawazoe and S. Watanabe, "The Effect of Surface Roughness On Scoring Part1: Under Starved Lubrication Condition", Bulleting of the JSME, Vol. 21, No. 155, pp. 893-898.

136. P. Basuray, B. Sahay and G. Lal, "A Simple Model For Evaluating Surface Roughness In Fine Grinding", Journal Machine Tool Design Research, 1980, Vol. 20, pp. 265-273.

137. V. Loukyanov and D. Whitehouse, "Local Irregularities of the Surface and their Influence on Surface Roughness Parameters", Annals of the CIRP, 1980, Vol. 29/1/1980, pp. 423-428.

138. A. Villa, S. Rosseto and R. Levi, "Surface Texture and Machining Conditions Part 1: Model Building Logic in View of Process Control", Transactions of ASME, Journal of Engineering for Industry, 1984, Vol. 105, pp. 259-269.

139. D. Jansson, "High-Speed Surface Roughness Measurement ", Transaction of the ASME, Journal of Engineering for Industry, 1984, Vol. 106, pp. 1-6.

140. M. Osman and T. Sanker, "Profile Characterization of Manufactured Surfaces Using Random Function Excursion Technique, part 1: Theory", Transactions of ASME, Journal of Engineering for Industry, 1974, February Vol., pp. 196-202.

141. M. Osman and T. S. Sanker, "Profile Characterization of Manufactured Surfaces Using Random Function Excursion Technique, part 2: Application", Transactions of ASME, Journal of Engineering for Industry, 1975, pp. 196-202.

142. R. Brodmann, O. Rodenstock, Munich, T. Gast, and G. Thurn, "An Optical Instrument for Measuring the Surface Roughness In Production Control", CIRP Annals Manufacturing Technology, 1984, Vol. 33/1/1984, pp. 403-406.

143. K. Creath and J. Wyant, "Absolute Measurement of Surface Roughness", Journal of Applied Optics, 1990, Vol. 29, No. 26.

144. P. Chandley, "Surface Roughness Measurements from Coherent Light Scattering", Optical and Quantum Electronics, 1976, Vol. 8, pp. 323-327.

145. A. Elgabry, M. Osman and T. Sankar, "On the Use of the Ra, AMS, and RMSS Values for the Simulation of Fine Machined Surfaces, " International Journal Production Research, 1980, No. 5, pp. 571-581.

146. R. Young, T. Vorburger and E. Teague, "In-Process and On-Line Measurement of Surface Finish", Annals of the CIRP, 1980, Vol. 29/1/1980, pp. 435-440.

147. K. Struik and A. Prakash, "Surface Roughness: The Measurement of Deformed Surfaces", International Journal of Production Research, 1980, No. 5, 559-569.

148. W. Devries, "Autoregressive Time Series Models for Surface Profile Characterization", Annals of the CIRP, 1979, Vol. 28/1/1979.

149. H. Sato and M. O-Hori, "Characteristics of Two Dimensional Surface Roughness-Taking Self-Exited Chatter Marks as Objectives", Annals of the CIRP, 1981, Vol. 30/1/1981, pp. 481-486.

150. E. Thwaite, "The Extension of Optical Angular Scattering Techniques to the Measurement of Intermediate Scale Roughness", Annals of the CIRP, 1982, Vol. 31/1/1982, pp. 463-465.

151. J. Jang, C. Sun and E. Mizutani, "Neuro-Fuzzy and Soft Computing", Prentice-Hall International, INC., U.S.A, 1997.

152. S. Chiu, "Fuzzy model identification based on cluster estimation", Journal of Intelligent and Fuzzy Systems, 1994, Vol. 2, pp. 267-278.

153. Noncontacting Displacement Measuring System, Instruction Manual of KD-2300, Kaman Instrumentation Operations, 3450 North Nevada Avenue, Colorado Springs, CO 80907, 1989.

154. L. Zadeh, "Fuzzy Sets", Journal of Information and control, 1965, Vol. 8, pp. 338-353.

155. G. Franklin, J. Powell and A. Emami-Naeini, "Feedback Control of Dynamic Systems", Addison-Wesley Publishing Company, Massachusetts, 1994.

156. D. Dubois and H. Prade, "Fuzzy Sets in Approximate Reasoning, Part 1: Inference with Possibility Distributions", Fuzzy Sets and Systems, 1991, Vol. 40, pp. 143-202.

# Appendix A

Integrals

$$\int_0^t \cos(\omega\tau+\theta)\, e^{-\varsigma\omega(t-\tau)} \sin\omega(t-\tau)d\tau = -\frac{1}{2\omega\varsigma(\varsigma^2+4)}\begin{pmatrix} -4\sin(\omega t+\theta)-2\varsigma\cos(\omega t+\theta) \\ +\varsigma^2 e^{-\varsigma\omega t}\sin(\omega t+\theta)+ \\ 4e^{-\varsigma\omega t}\sin(\omega t+\theta)+ \\ 2\,\varsigma e^{-\varsigma\omega t}\cos(\omega t-\theta)+ \\ \varsigma^2 e^{-\varsigma\omega t}\sin(\omega t-\theta) \end{pmatrix}$$

$$\int_0^t e^{-\varsigma\omega(t-\tau)} \sin\omega(t-\tau)d\tau = -\frac{1}{\omega(\varsigma^2+1)}\left(-1+e^{-\varsigma\omega t}\cos(\omega t)+e^{-\varsigma\omega t}\sin(\omega t)\right)$$

$$\int_0^t \cos(\omega\tau)\, e^{-\varsigma\omega(t-\tau)} \sin\omega(t-\tau)d\tau = -\frac{1}{\omega\varsigma(\varsigma^2+4)}\begin{pmatrix} -2\sin(\omega t)-\varsigma\cos(\omega t)+ \\ \varsigma^2 e^{-\varsigma\omega t}\sin(\omega t)+ \\ 2e^{-\varsigma\omega t}\sin(\omega t)+\varsigma\, e^{-\varsigma\omega t}\cos(\omega t) \end{pmatrix}$$

$$\int_0^t \sin(\omega\tau+\theta)\, e^{-\varsigma\omega(t-\tau)} \sin\omega(t-\tau)d\tau = -\frac{1}{2\omega\varsigma(\varsigma^2+4)}\begin{pmatrix} -2\varsigma\,\sin(\omega t+\theta)+4\cos(\omega t+\theta)+ \\ \varsigma^2 e^{-\varsigma\omega t}\cos(\omega t-\theta)- \\ 2\,\varsigma e^{-\varsigma\omega t}\sin(\omega t-\theta)- \\ \varsigma^2 e^{-\varsigma\omega t}\cos(\omega t+\theta)- \\ 4\, e^{-\varsigma\omega t}\cos(\omega t+\theta) \end{pmatrix}$$

$$\int_0^t \sin(\omega\tau)\, e^{-\varsigma\omega(t-\tau)} \sin\omega(t-\tau)d\tau = \frac{1}{\omega\varsigma(\varsigma^2+4)}\begin{pmatrix}\varsigma\sin(\omega t)-2\cos(\omega t)+\varsigma e^{-\varsigma\omega t}\sin(\omega t)+\\ 2\varsigma e^{-\varsigma\omega t}\cos(\omega t)\end{pmatrix}$$

## A1-Data acquisition system (DAQ)

The DAQCard-6025E series board which are high in performance multifunction analog, digital, and timing I/O boards for PCI, PXI, PCMCIA, and CompactPCI bus computers. The 6025E features 16 channels (eight differential) of analog input, two channels of analog output, a 100-pin connector, and 32 lines of digital I/O. The 6025E features 16 channels of analog input, two channels of analog output, a 68-pin connector and eight lines of digital I/O.

These devices use the national instruments DAQ-STC system-timing controller for time-related functions. The DAQ-STC consists of three timing groups that control analog input, analog output, and general-purpose counter/timer functions. These groups include a total of seven 24-bit and three 16-bit counters and a maximum timing resolution of 50 ns. [153]

## A2- Noncontacting displacement measuring system (KD-2300)

Kaman instrumentation's family is of displacement measuring systems, which uses inductive technology to determine the position of the target relative to the system sensor.

There are many sensor's model available for use with KD-2300 electronics and the standard performance. The specification of the sensors used in this study is listed in table A1.

Table A1: The standard performance specifications for 2S model [153].

| Sensor models<br>Model | Measuring range<br>Inch (mm) | Typical offset<br>Inch (mm) | Linearity<br>% FS* | Analog voltage<br>Vdc | Displacement sensitivity<br>mV/mil (mm) |
|---|---|---|---|---|---|
| 2S | 0.100 (2.5) | 0.010 (0.25) | 1.00% | 1.00 (2.5) | 10 (1000) |

* Full scale.

## A3-Reference cylinders used

1- **Least squares cylinder**: The least squares cylinder is constructed from the average radial departure of all the measured data from the least squares axis. See Fig. 7 for example.

2- **Minimum Zone cylinder**: The minimum zone cylinder can be described as the total separation of 2 concentric cylinders, which totally enclose the data and are kept to a minimum separation; this kind of reference is used in our measured data. See fig. 7 for example.

3- **Minimum Circumscribed cylinder:** The minimum circumscribed cylinder is a cylinder of minimum radius that totally encloses the data. See Fig. 7 for example.

4- **Maximum Inscribed cylinder:** The maximum inscribed cylinder is the largest cylinder that is enclosed by the data. See Fig. 7 for example.

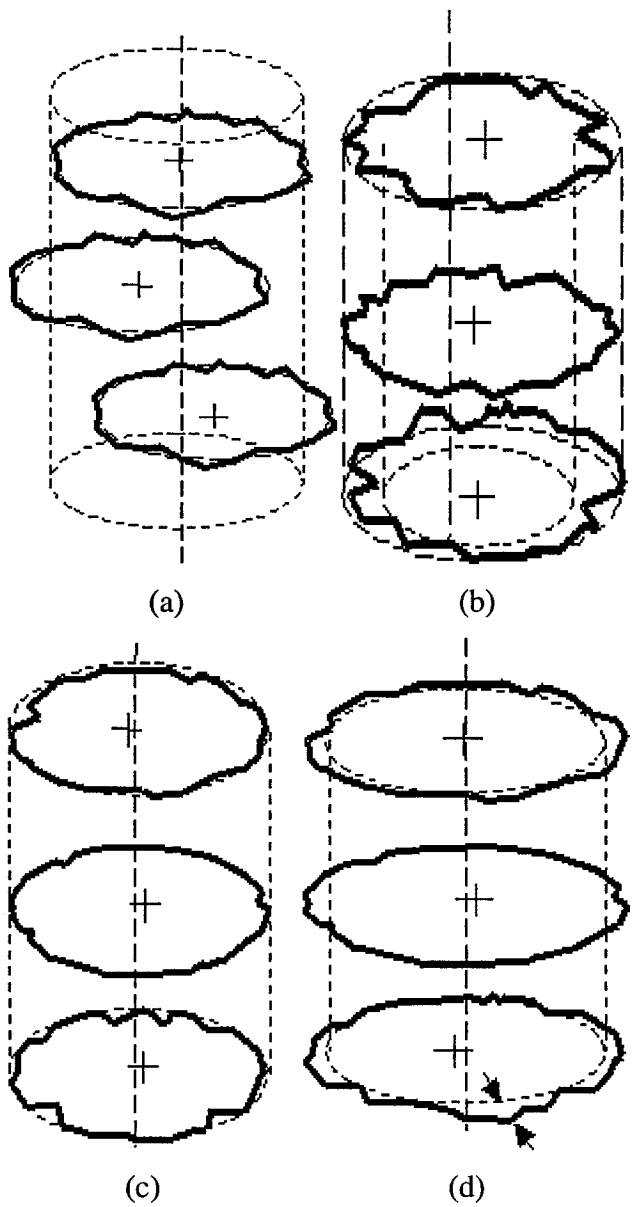


Fig. A1: Example of (a) least squares cylinder, (b) minimum zone cylinder, (c) minimum circumscribed cylinder and (d) maximum inscribed cylinder [117].

**Roughness** – this is usually the process mark or witness marks produced by the action of the cutting tool or machining process, but may include other factors such as the structure of the material [115].

**Waviness** – this is usually produced by instabilities in the machining process, such as an imbalance in a grinding wheel, or by deliberate actions in the machining process. Waviness has a longer wavelength than roughness, which is superimposed on the waviness [115].

## A5- Labview program

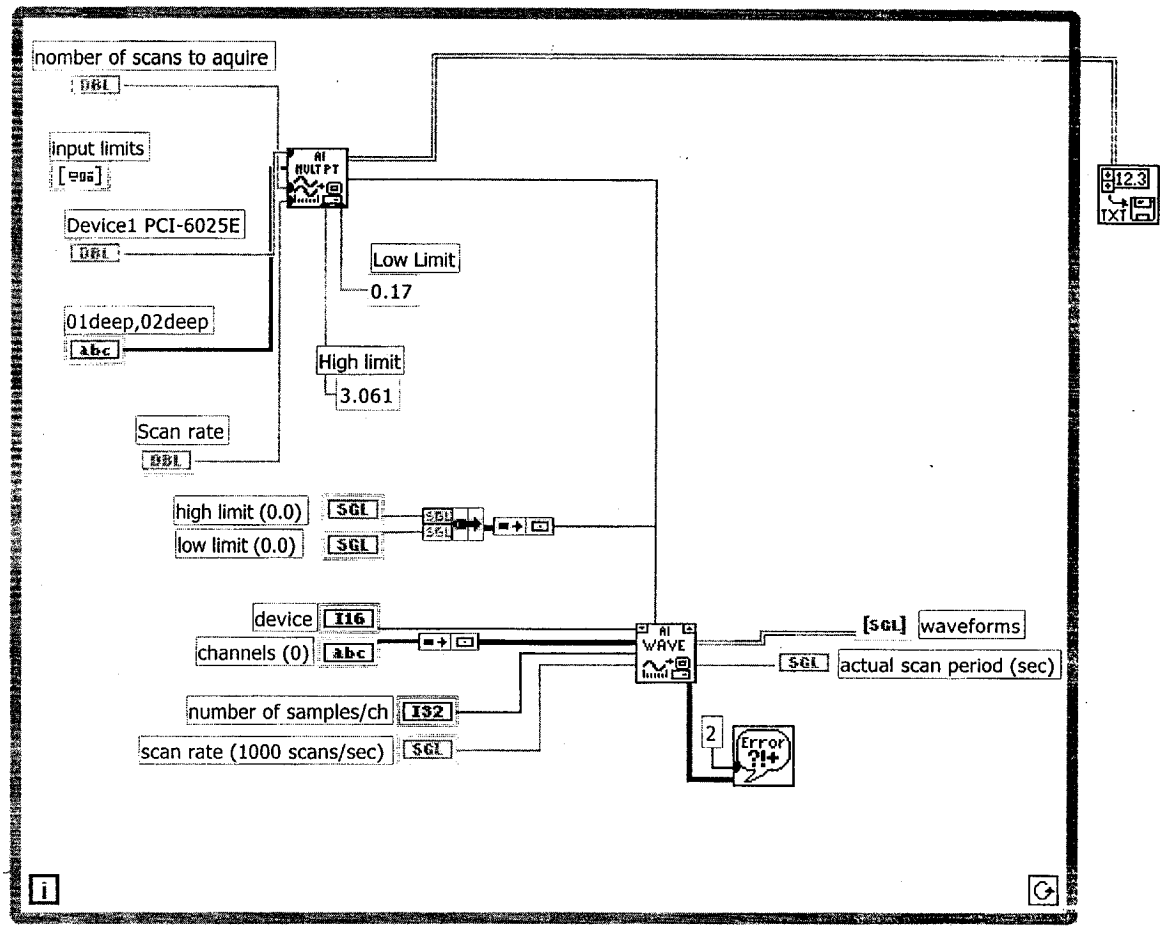


Fig. A2: Program used in Labview.

Table A2: Input-output data used in fuzzy modeling.

| Speed (rev/min) | Feed rate (mm/min) | Flow rate (G/min) | Tool penetration (inch) | Tool penetration (mm) | Cylindricity error (μm) | Straightness error (μm) | Roughness error (μm) |
|---|---|---|---|---|---|---|---|
| 1040 | 71 | 20 | 3 | 76.2 | 0.204851 | 0.124968 | 0.579 |
| 1040 | 117 | 20 | 9 | 228.6 | 0.239522 | 0.239522 | 0.823 |
| 1040 | 173 | 20 | 15 | 381 | 0.010455 | 0.102362 | 0.655 |
| 1240 | 71 | 20 | 21 | 533.4 | 0.174752 | 0.15494 | 0.5 |
| 1240 | 117 | 20 | 27 | 685.8 | 0.25019 | 0.150876 | 0.951 |
| 1240 | 173 | 20 | 33 | 838.2 | 0.08901 | 0.00963 | 0.708 |
| 1440 | 71 | 20 | 3 | 76.2 | 0.176657 | 0.176657 | 0.629 |
| 1440 | 117 | 20 | 3 | 76.2 | 0.239522 | 0.121158 | 0.678 |
| 1440 | 173 | 20 | 9 | 228.6 | 0.236728 | 0.126238 | 0.873 |
| 1040 | 71 | 30 | 15 | 381 | 0.219202 | 0.10795 | 0.472 |
| 1040 | 117 | 30 | 21 | 533.4 | 0.224536 | 0.14097 | 0.622 |
| 1040 | 173 | 30 | 27 | 685.8 | 0.178054 | 0.107696 | 0.479 |
| 1240 | 71 | 30 | 3 | 76.2 | 0.0235 | 0.0835 | 0.546 |
| 1240 | 117 | 30 | 9 | 228.6 | 0.152654 | 0.012802 | 0.375 |
| 1240 | 173 | 30 | 15 | 381 | 0.237744 | 0.099695 | 0.34 |
| 1440 | 71 | 30 | 21 | 533.4 | 0.136398 | 0.096266 | 0.879 |
| 1440 | 117 | 30 | 27 | 685.8 | 0.252222 | 0.093853 | 0.86 |
| 1440 | 173 | 30 | 33 | 838.2 | 0.189611 | 0.127635 | 0.58 |
| 1040 | 71 | 40 | 3 | 76.2 | 0.200152 | 0.138303 | 0.517 |
| 1040 | 117 | 40 | 9 | 228.6 | 0.244221 | 0.10668 | 0.688 |
| 1040 | 173 | 40 | 15 | 381 | 0.184277 | 0.119507 | 0.555 |
| 1240 | 71 | 40 | 21 | 533.4 | 0.211328 | 0.157226 | 0.433 |
| 1240 | 117 | 40 | 27 | 685.8 | 0.197866 | 0.137668 | 0.608 |
| 1240 | 173 | 40 | 33 | 838.2 | 0.001345 | 0.082347 | 0.493 |
| 1440 | 71 | 40 | 3 | 76.2 | 0.1002 | 0.096774 | 0.448 |
| 1440 | 117 | 40 | 9 | 228.6 | 0.150368 | 0.154432 | 0.488 |
| 1440 | 173 | 40 | 15 | 381 | 0.180467 | 0.168148 | 0.885 |

## A6-Proof of the least squares centre formulas [115]

Consider Fig. A3, where the rectangular coordinates $x_i$ and $y_i$, originating at O. Take a number of points $n$ of radii $r_i$ at equal angular spacings about O, which meet the trace at points given by $(r_i \phi_i)$, where

$$i = 1,2,3,\cdots,n \quad \text{and} \quad \phi_i = \frac{2\pi i}{n}$$

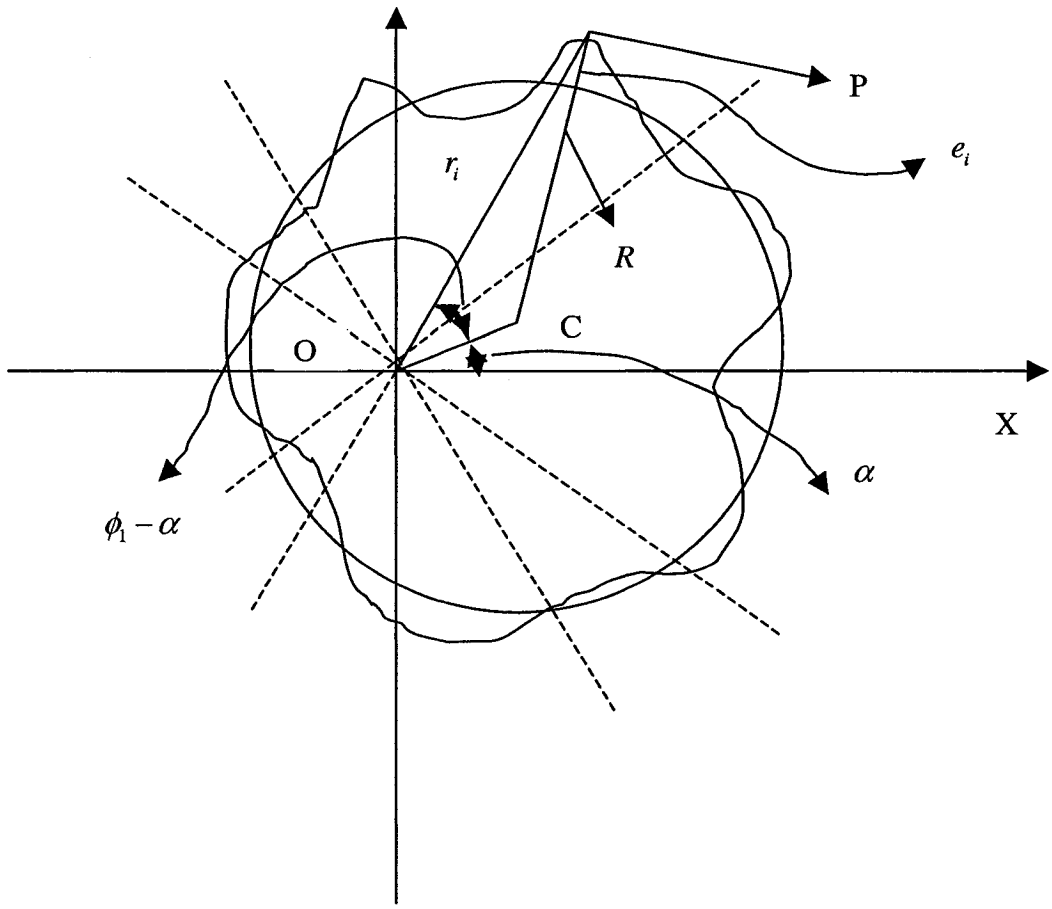


Fig. A3: Diagram for determination of the least squares centre [115].

C : is the least squares circle centre,

$(a,b)$: are the rectangular coordinates,

$R$ : is the radius,

$c$ : is the distance form origin O to the centre C.

$\alpha$ : is the angle which OC makes with the x−axis be. Then,

$$c^2 = a^2 + b^2 \quad \text{and} \quad \tan\alpha = \frac{b}{a}$$

The triangle OPC gives:

$$r_i = c\cos(\phi_i - \alpha) + \sqrt{\{(R+e_i)^2 - c^2\sin^2(\phi_i - \alpha)\}}$$

where $e_i$ is the deviation from the least squares circle along the radius $r_i$. or approximately

$$r_i = c\cos(\phi_i - \alpha) + R + e_i$$

By the principle of least squares $\sum e_i^2$ is a minimum , i.e., $\sum[r_i - R - c\cos(\phi - \alpha_i)]^2$ is a minimum and so

$$\frac{\delta\sum e_i^2}{\delta R} = 0 \qquad \frac{\delta\sum e_i^2}{\delta c} = 0 \qquad \frac{\delta\sum e_i^2}{\delta\alpha} = 0$$

$$\frac{\delta\sum e_i^2}{\delta R} = -2\sum[r_i - R - c\cos(\phi_i - \alpha)]$$

which gives,

$$\sum r_i - nR - c\sum\cos(\phi_i - \alpha) = 0$$

$$\frac{\delta\sum e_i^2}{\delta c} = -2\sum[\cos(\phi_i - \alpha)(r_i - R - c\cos(\phi_i - \alpha))] = 0 \qquad \text{(a1)}$$

which gives

$$\sum r_i \cos(\phi_i - \alpha) - R\sum\cos(\phi_i - \alpha) - c\sum\cos^2(\phi_i - \alpha) = 0$$

$$\frac{\delta\sum e_i^2}{\delta\alpha} = -2\sum[c\sin(\phi_i - \alpha)(r_i - R - c\cos(\phi_i - \alpha))] = 0 \qquad \text{(a2)}$$

which gives

$$\sum r_i \sin(\phi_i - \alpha) - R\sum\sin(\phi_i - \alpha) - c\sum\cos(\phi_i - \alpha)\sin(\phi_i - \alpha) = 0 \qquad \text{(a3)}$$

Now expressing

$$\frac{\sum f(\phi)}{n} \; as \; \frac{1}{2\pi}\int_0^{2\pi} f(\phi)d\phi$$

gives

$$\sum\cos(\phi_i - \alpha) = 0,$$

$$\sum\cos^2(\phi_i - \alpha) = \frac{n}{2}$$

and

$$\sum\cos(\phi_i - \alpha)\sin(\phi_i - \alpha) = 0,$$

also,

$$\sum r_i \cos(\phi_i - \alpha) = \cos\alpha\sum x_i + \sin\alpha\sum y_i$$

$$= \cos\alpha\, n\bar{x} + \sin\alpha\, n\bar{x}$$

since

$$\bar{x} = \frac{\sum x_i}{n} \; and \; \bar{y} = \frac{\sum y_i}{n}$$

similarly,

$$\sum r_i \sin(\phi_i - \alpha) = \cos\alpha \sum y_i - \sin\alpha \sum x_i$$

$$= \cos\alpha n\bar{y} - \sin\alpha n\bar{x}$$

Applying these results to Eqs. (a1), (a2), and (a3) gives:

$$\sum r_i - nR - 0 = 0 \qquad \text{from (a1)}$$

i.e.,

$$R = \frac{\sum r_i}{n}$$

$$\cos\alpha n\bar{x} - \sin\alpha n\bar{y} - 0 - \frac{cn}{2} = 0 \quad \text{from (a2)}$$

i.e.,

$$c = 2(\bar{x}\cos\alpha + \bar{y}\sin\alpha) \qquad \text{(a4)}$$

and

$$\cos\alpha n\bar{y} - \sin\alpha n\bar{x} - 0 = 0 \quad \text{from (a3)}$$

i.e.,

$$\tan\alpha = \frac{\bar{y}}{\bar{x}}$$

Hence

$$\sin\alpha = \frac{\bar{y}}{\sqrt{(\bar{x}^2 + \bar{y}^2)}} \quad \text{and} \quad \cos\alpha = \frac{\bar{x}}{\sqrt{(\bar{x}^2 + \bar{y}^2)}}$$

which substituted in (a4) give

$$c = \frac{2\left(\bar{x}^2 + \bar{y}^2\right)}{\sqrt{\left(\bar{x}^2 + \bar{y}^2\right)}}$$

i.e.,

$$c = 2\sqrt{\left(\bar{x}^2 + \bar{y}^2\right)}$$

now

$$c = \sqrt{\left(a^2 + b^2\right)} \text{ and } b = a\tan\alpha = \frac{a\,\bar{y}}{\bar{x}}$$

therefore

$$\sqrt{\left(a^2 + \frac{a^2\bar{y}^2}{\bar{x}^2}\right)} = 2\sqrt{\bar{x}^2 + \bar{y}^2} \text{ from (a5)}$$

$$\sqrt[a]{\left(\frac{\bar{x}^2 + \bar{y}^2}{\bar{x}^2}\right)} = 2\sqrt{\bar{x}^2 + \bar{y}^2}$$

which gives

$$a = 2\bar{x}$$

$$b = \frac{a\,\bar{y}}{\bar{x}} = 2\,\bar{y}$$

i.e.,

$$a = \frac{2\sum x_i}{n}$$

*and*

$$b = \frac{2\sum y_i}{n}$$